AN ELECTROMAGNETIC ACTUATED MICROVALVE FABRICATED ON A SINGLE WAFER

A Dissertation Presented to
The Academic Faculty

By

Jemmy Sutanto Bintoro

In Partial Fulfillment
Of the Requirements for the Degree
Doctor of Philosophy in Mechanical Engineering

Georgia Institute of Technology

December, 2004

AN ELECTROMAGNETIC ACTUATED MICROVALVE FABRICATED ON A SINGLE WAFER

Approved by:

Dr. Peter J. Hesketh, Chairman
Professor of Mechanical Engineering
Director of MEMS Research Laboratory

Dr. Paul Kohl
Regent Professor of Chemical and Biomolecular Engineering

Dr. Levent Degertekin
Assistant Professor of Mechanical Engineering

Dr. Andrei Fedorov
Assistant Professor of Mechanical Engineering

Dr. Mark G. Allen
Joseph M. Pettit Professor of Electrical and Computer Engineering
Director of Microsystems Group

Dr. Bruno Frazier
Associate Professor of Electrical and Computer Engineering

Date approved: November 18, 2004

ACKNOWLEDGEMENTS

I believe life is like a series of dreams, dream of love, joy, and peace that GOD has installed for us. I am so glad and thankful to GOD in Jesus Christ, who is my savior, because HE has given me the dream to pursue my PhD degree. In this page I would like to present my first and special acknowledgment to Jesus Christ who through my spirit has given me strength and enormous patience in the journey of my PhD work. It was indeed a combination of joyful and tough time; and I completely enjoyed the challenges of this work. There is one verse in the bible that always gives me strength when I am down:

> ***But those who wait on the LORD, shall renew their strength; They shall mount up with wings like eagles, They shall run and not be weary, They shall walk not faint (Isaiah 40:31)***

I believe it is GOD who gives and brings me to my dreams. I do not have to worry in my tough time because HE is the one that holds my future.

My second acknowledgment is for my lovely girlfriend, Wendy Tse. I met her in the first day of class in spring 2004 and we felt in love at the first sight. At the time that I write this PhD dissertation, I propose to engage her and marry her in year 2005. She is indeed a gift from GOD to me; she represents the love of Christ in physical and emotional forms. She gave me strength when I was weak and she spoke about positive things to encourage me.

There is always an important person behind the success of a research work. In this case, the person is my dearest friend and advisor, Dr. Peter J. Hesketh. I am just so thankful to him for the greatest three years time that I have worked with him. He is an excellent professor who is always open-minded and supportive to his students. His brilliant ideas and great advice are indeed the reasons behind the success of this work.

I would like to acknowledge the committee members of this PhD dissertation their time, supports, and ideas. They are: Dr. Paul Kohl, Dr. Levent Degertekin, Dr. Andrei Fedorov, Dr. Mark G. Allen, and Dr. Bruno Frazier.

Last but not the least, I want to acknowledge the followings for their contribution:

- My precious parents, Mr. Yahya Bintoro and Mrs. Sienny Gwattiningrum, and sisters, for their love and caring during my PhD study.
- The financial support from DARPA MTO-MPG office, Dr. Clark Nguyen, contract no. F33615-01-2173
- All staff in the Department of Mechanical Engineering and in Microelectronics Research Center (MiRC) at Georgia Institute of Technology
- Dr. Neil Manning and Mr. Jim Rooze from Arnold Engineering for their help in aligning the permanent magnet and very useful advice.
- Dr. Stanko Brancovic from Seagate Research Laboratory for the useful advice and help in aligning the permanent magnet.
- Dr. Kenneth Cunefare and all of his students for their courtesy in letting us to use their laser vibrometer and carry out experiments in their lab
- All the cell group members, Penabur, in IFGF (Indonesian Full Gospel Fellowship) for their prayer and friendship.

TABLE OF CONTENTS

LIST OF FIGURES

LIST OF TABLES

SUMMARY

Microvalves are essential components of the miniaturization of the fluidic systems to control of fluid flow in a variety of applications as diverse as chemical analysis systems, micro-fuel cells, and integrated fluidic channel arrangements for electronic cooling. Using microvalves, these systems offer important advantages: they can operate using small sample volumes and provide rapid response time.

This PhD dissertation presents the world first electromagnetically actuated microvalve fabricated on a single wafer with CMOS compatibility. In this dissertation, the design, fabrication, and testing results of two different types of electromagnetic microvalves are presented: the on/off microvalve and the bistable microvalve with latching mechanism. The microvalves operate with power consumption of less than 1.5 W and can control the volume flow rate of DI water, or a 50% diluted methanol solution in the range 1 – 50 μL/min. The leaking rate of the on/off microvalve is the order of 30 nL/min. The microvalve demonstrated a response time for latching of 10 ms in water and 0.2 ms in air. This work has resulted in a US patent, application no. 10/699,210.Other inventions that have been developed as a result of this research are bidirectional, and bistable-bidirectional microactuators with latching mechanism, that can be utilized for optical switch, RF relay, micro mirror, nano indenter, or nano printings.

CHAPTER 1

LITERATURE REVIEW

1.1 Introduction

The manipulation of fluid flow is a fundamental function that has a wide range of applications from precision manufacturing to drug delivery and miniaturization of chemical and bioanalysis systems. Microvalves are essential components of these miniaturized fluidic systems. Microvalves provide control of fluid flow in a variety of applications as diverse as chemical analysis systems, micro-fuel cells, and integrated fluidic channel arrangements for electronic cooling. Using microvalves, these systems offer important advantages: they can operate using small sample volumes, provide rapid response time, and function with low power consumption [1-5].

Various approaches and methods of manufacture of MEMS devices have been studied over the past 10 years. A comprehensive review of the earlier work is given by Shoji and Esachi [1,2,3] Yen *et al*.[4] and Nguyen and Wereley [5]. These reviews show that substantial work has been done on the use of macroscopic actuators that are assembled with microfabricated diaphragm or membranes to provide valve like functions. However, the real advantage of microvalves lies in the integration of the actuation mechanism with the microvalve components at the microscale. It is not only power efficient, but also helps in miniaturization and packaging.

This chapter presents an overview of the design approaches, fabrication methods, and testing of membrane-type microvalves. Various mechanisms used to actuate the membrane are described such as thermal, piezoelectric, electrostatic, thermopneumatic, electromagnetic, shape memory alloy, and hydrogel actuations.

In general, a membrane-type microvalve consists of three main parts: the flow channel, the membrane/diaphragm, and the actuator. Two types of mechanisms can be considered, the membrane closing over a channel, or a membrane closing off flow from an orifice. The base of the valve, known as the valve seat, interfaces with the membrane to provide a leak-free seal in the closed state. The actuator provides the necessary force to actuate/deflect the membrane to close or open the fluid flow. The valve may be powered so that it is normally open or normally closed however, latching valves have overall lower power consumption because the power is only applied to change the state of the valve.

In general, bulk micromachined microvalves typically use a micromachined flow channel and a membrane that is deflected over the opening to modulate the flow. However, significant advances have been made over the past several years, making available deep reactive ion etching (DRIE) for the flow channels, which produce membranes or channels without the limitations of bulk anisotropic etching based upon the crystal planes, in addition to surface micromachining of thin membranes, plates, cantilevers and flexures for valve components. The reader is referred to text by Madou [6] and Elwenspoek and Jansen [7] for further information and a comprehensive review.

Fluidic connections to the microvalve are also a big challenge in the design. In order to simplify the fabrication, most microvalves have been built with two or three

wafers bonded together, simply to define the inlet and outlet channels. Even though wafer bonding is simple, it is generally not desirable, because it reduced yield and limits the scope for integration with the electrical circuit on a single wafer. Therefore, microvalve fabrication on a single wafer is highly desirable and demanded, because of its simplicity and higher efficiency.

In a miniature gas chromatograph the valve is necessary for injection of the sample into the carrier gas and through the separation column. Typical operating flow rates of ~1sccm and pressure of 5 psi are used in miniature GC systems [8]. The valve should also be built from temperature stable materials and be inert and corrosion resistant. In a bioanalysis system the valve is required to dispense bioreactants necessary to complete an assay protocol. This may include enzymes, buffer and fluids containing magnetic beads for introduction of labeled immunochemicals [9]. These applications also require minimal temperature rise that could adversely affect the biological activity. In a fuel cell the valve remains normally closed until the delivery of the fuel to the fuel cell is required [10] and it is an essential requirement to use as little electrical power as possible to maintain high fuel cell efficiency. Microvalves could also useful for regulation of the fuel concentration in a direct methanol fuel cell.

There have been a number of different actuators developed for the operation of a microvalve. Different techniques have been introduced to produce force to actuate the membrane and a thorough review on microfabricated microactuators is given by Thielicke and Obermeier [11]. So far, there have been seven major actuations for the microvalve in the MEMS applications, they are: piezoelectric, electrostatic, electromagnetic, thermal, thermo pneumatic, shape memory actuators and hydrogel. In

this chapter the various designs have been collected together based upon the actuator drive technique employed.

1.2 Fluid Flow

The flow characteristic of fluid in microstructures, which inevitably occurs in a microvalve, is a topic of considerable interest. In most of the microvalve designs, fluid flow can be modeled using continuum theory with appropriate modifications to include the effects of small size, compressibility of working fluid, and geometry. The continuum model, embodied in the Navier-Stokes equations, assumes the medium to be continuous and indefinitely divisible. However, in microstructures, the characteristic length (L_c) of the flow channels may be comparable to the mean free path (l) of the fluid molecules. Therefore, under such an assumption, the molecular distribution of properties is considerably disturbed by its frequent interactions/collisions with the wall of the microchannels. Such a phenomena is predominantly seen in rarefied (low pressure) gas flow or flow channels of extremely small characteristic lengths (< 1 μm). For ideal gases, the mean free path (l) is given by

$$l \approx \frac{1}{\sqrt{2}\pi n d^2} = \frac{k_B T}{\sqrt{2}\pi d^2 P} \tag{1.1}$$

where, n is the molecular density, d is the molecular diameter, k_B is the Boltzmann's constant, T is the temperature, and P is the pressure [12].

The ratio of the mean free path and characteristic length, known as Knudsen number Kn ($= \frac{l}{L_c}$), is used as a measure of flow characteristic. As the Kn increases, the

rarefaction effects become more important and the fluid properties deviate from local equilibrium. The different flow regimes are depicted in Table 1.1 [13]:

Table 1.1. Flow regime as a function of Knudsen number

Knudsen Number (Kn)	**Flow Regime**	**Modeling Method**
$Kn \leq 0.001$	Continuum	Navier-Stokes equation with no-slip boundary conditions
$0.001 < Kn \leq 0.1$	Slip Flow	Navier-Stokes equation with slip boundary conditions*
$0.1 < Kn \leq 10$	Transition	Boltzmann Transport Equation (BTE), Direct Simulation Monte Carlo(DSMC)
$Kn > 10$	Free Molecular Flow	BTE, DSMC
* slip b. c. provided in equations 2 and 3		

The mean free path of air at STP is approximately 64nm. As shown in the table, the continuum model with no-slip boundary condition can be used for Kn number less than 0.001. Therefore, the model can be used if the characteristic length of the flow channel in a microvalve design is greater than 64μm. The governing equations for continuum model are derived from the mass, momentum and energy conservation principles, which can be found in standard fluid mechanics and heat transfer text books [14, 15].

Typically, the no-slip conditions at a fluid-solid interface are applied in the momentum and energy balance equations, which means that the fluid velocity and temperature at the wall is equal to that of the wall, respectively. However, at Kn less than 0.001, the above condition no longer holds. There is a relative tangential fluid velocity

and a temperature jump at the wall given by the following equations, which are first order approximation [16]

$$u_{gas} - u_{wall} = \frac{2-\sigma_v}{\sigma_v} Kn \frac{\partial u}{\partial n} \tag{1.2}$$

$$T_{gas} - T_{wall} = \frac{2-\sigma_T}{\sigma_T} \left[\frac{2\gamma}{\gamma+1} \right] \frac{Kn}{\mathrm{Pr}} \frac{\partial T}{\partial n} \tag{1.3}$$

where, u is the velocity, σ_v is the tangential momentum transfer coefficient, T is the temperature, σ_T is the energy accommodation coefficient, n is the normal direction to the wall, γ is the gas constant, and Pr is the Prandtl number.

Biological applications of microvalves require separate considerations to model the proteins, nucleic acids and cell, which can modify the flow characteristics. Such application of microfluidic devices has been reviewed by Beebe *et al.* [17]. The design considerations for a microvalve include the working fluid, flow rates, leakage rate, operating pressure, and power consumption. Fluid flow analysis is required to determine the optimum orifice size, membrane gap size, the necessary closing force and hence type of actuator required for the device. As discussed earlier, the flow analysis largely depends on the nature of the operating fluid. Important considerations required to model flow for incompressible and compressible fluids are presented in the following two sections.

1.3 Incompressible Flow Analysis

Incompressible flow in microvalves can be analyzed using standard equations derived for internal flow. Some of the common geometries encountered in modeling fluid flow in microvalves and related equations are depicted in Figure 1.1 and 1.2 [18]

1.3.1 Case 1: Fixed Parallel Plates

If we assume a steady laminar flow through fixed parallel plates, the volumetric flow rate per unit length of width can be obtained as follows by solving the above Navier-Stokes equation.

$$Q = \frac{2h^3}{3\mu}(-\frac{dP}{dx}) = \frac{2h^3}{3\mu} \cdot \frac{(P_o - P_i)}{L} \tag{1.4}$$

Where Q is volumetric flow rate, μ is viscosity, $2h$ is the gap between the plates, L is the length of the plates, and P_i, P_o are the inlet, outlet pressure.

1.3.2 Case 2: Circular Tube

For a fluid flow through a straight circular tube whose radius is r_o, the flow rate vs. pressure drop relationship for incompressible, laminar, fully developed flow can be obtained as follows.

$$Q = \frac{\pi r_o^4}{8\mu}(-\frac{dP}{dx}) = \frac{\pi r_o^4}{8\mu} \cdot \frac{(P_o - P_i)}{L} \tag{1.5}$$

1.3.3 Case 3: Rectangular Tube

For steady-state parallel flow through a rectangular tube as shown below ($-a \le y \le a$, $-b \le z \le b$), the average flow rate is given by

$$Q = \frac{4ba^3}{3\mu}(-\frac{dP}{dx})[1 - \frac{192a}{\pi^5 b}\sum_{i=1,3,5\ldots}^{\infty}\frac{\tanh(i\pi b/2a)}{i^5}] \tag{1.6}$$

It must be noted that these equations assume a fully developed internal flow in the microvalve, which seldom happen due to small channel lengths. Thus, the above equations are expected to provide a conservative value for the pressure drop for a given

flow rate. Also, sudden expansion in cross-section area is inevitable in most of the membrane type microvalve designs. Therefore, at high flow rates, the head loss due to sudden change in area and bends should be accounted for. For an example, pressure drops in the system will arise from the flow channels connected and the flow around the diaphragm and any support structure. The inlet hole pressure drop is calculated from the standard equation of flow through pipes. The inlet head loss is calculated using the following equation:

$$\Delta P = K\frac{V^2}{2g} \tag{1.7}$$

where, K is 0.5 for inlet and V is the fluid velocity.

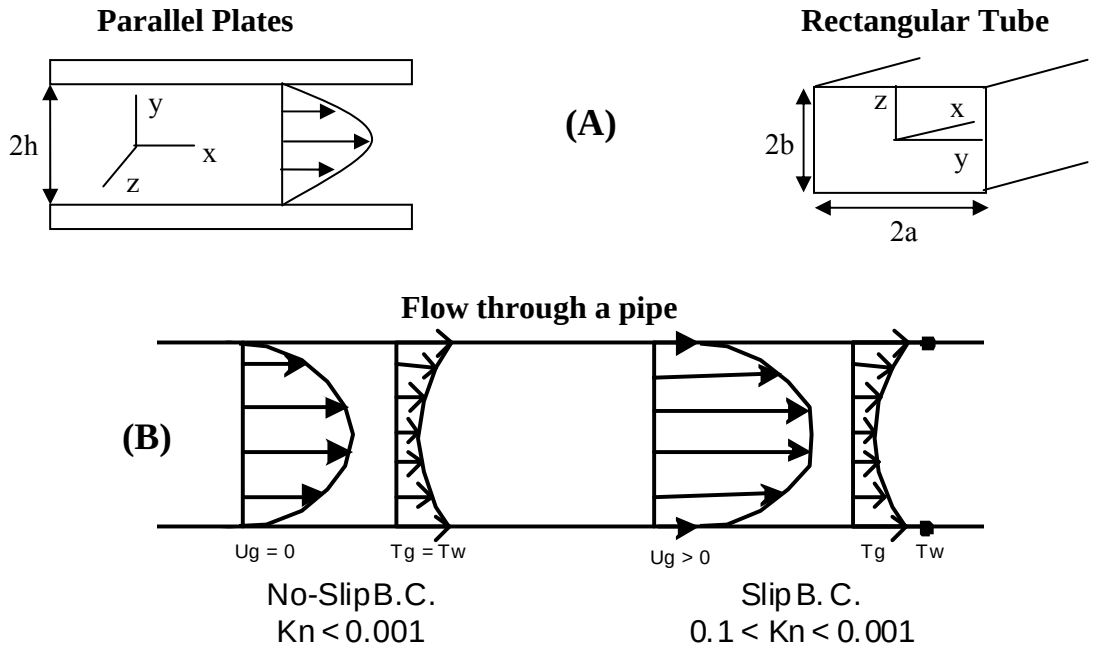

Figure 1.1. (A) Velocity profile under laminar flow conditions between parallel plates and geometry of a rectangular tube; (B) Schematic diagram of possible velocity profile that can occur in microvalves

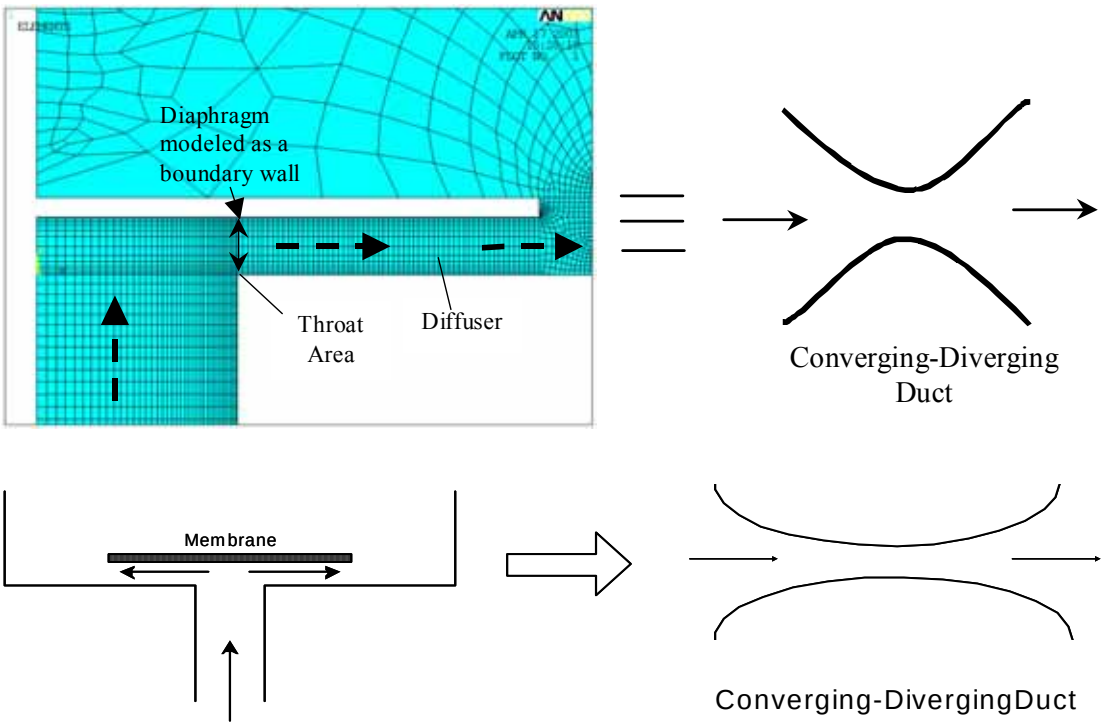

Figure 1.2. Finite element model of the pressure and velocity through the orifice and beneath the membrane in a microvalve

It is much easier to model incompressible flow as compared to the compressible flow, where variations in pressure and temperature cause appreciable variation in the gas density. Gas flow can be assumed incompressible if change in density is small compared to its initial density i.e. $\Delta\rho/\rho_o << 1$. A conventional criterion to determine whether a flow is compressible or incompressible is Mach number (Ma), which is defined as flow velocity over the velocity of sound. However, this criterion is no longer valid in flow through micro structures. For gas flow in a long and narrow microchannel, the viscous effect, which was neglected in the derivation of the above density equation, can become dominant; it scales inversely to the square of the characteristic length. Thus as the size of channel decreases, it is necessary to consider the pressure term versus the viscous term. It

is necessary to consider a modified criterion, $(L/d_o)(Ma^2/Re) << 1$, in order to determine whether the fluid can be treated as incompressible [19].

1.4 Compressible Flow

If the density change is significant as compared to the initial density of the gas, then the gas should be modeled as a compressible medium. Compressible flow of gas in simple and complex microgeometries with and without slip has been modeled using both analytical and numerical techniques. For further details on this topic, the reader is referred to the research work published by various groups [20, 21]. Typically a membrane-type microvalve geometry is similar to a converging-diverging duct, which is of greater significance in a compressible flow. Because the flow channel is small diameter, although the Reynolds number is low, the flow is not developed and the peak magnitude of the velocity can be quite high. Therefore it is necessary to check for choked flow resulting from velocities approaching sonic valves. A theoretical upper limit to the mass flow rate though the microvalve can be calculated from a choked flow analysis. The throat of the duct is the entrance gap area as shown in the Figure 1.2. For a gap, g and inlet radius, r_i, the throat area, a_{th} is given by:

$$a_{th} = 2\pi r_i g \qquad (1.8)$$

The air entering the microvalve is accelerates towards the throat region (minimum area) and then decelerated in the diffuser. As the back pressure is lowered sufficiently, the fluid velocity reaches the speed of sound at the throat (Ma = 1) and at this point the flow is choked. Beyond this, the mass flow rate of air does not increase with any further

lowering of the back pressure. Assuming an isentropic flow though the though the microvalve, the mass flow rate of air at choked condition is given by:

$$\dot{m} = \rho^{*}.A_{th}.c \qquad (9)$$

where, ρ^{*} is the air density at the throat under choked flow condition A_{th} is the throat area, and c is the speed of sound in air. Modeling of fluidics in microstructures are discussed by Gravesen *et al.* [22] along with the issues of scaling to nanoscale fluidics, i.e. dimensions over which non-continuum effects take place becomes important and nano-meter size scales.

1.5 Actuators for Microvalves

1.5.1 Introduction

In the following section selected examples of microvalves that have been built with micromachining fabrication techniques will be described and discussed. The various methods of providing actuation to the microvalve will be described. The examples include microvalves based upon: piezoelectric, electrostatic, electromagnetic, thermal, thermo pneumatic, shape memory actuators and hydrogel actuators.

1.5.2 Piezoelectric Actuated Microvalve

This type of microvalve utilizes the piezoelectric behavior of the material that is the mechanical deformation induced due to a change in the electrical polarization of the material. The membrane actuator can be made directly from a piezoelectric material or

layers of piezoelectric material can be attached onto the membrane. Figure 1.3 shows two commonly used piezoactuators.

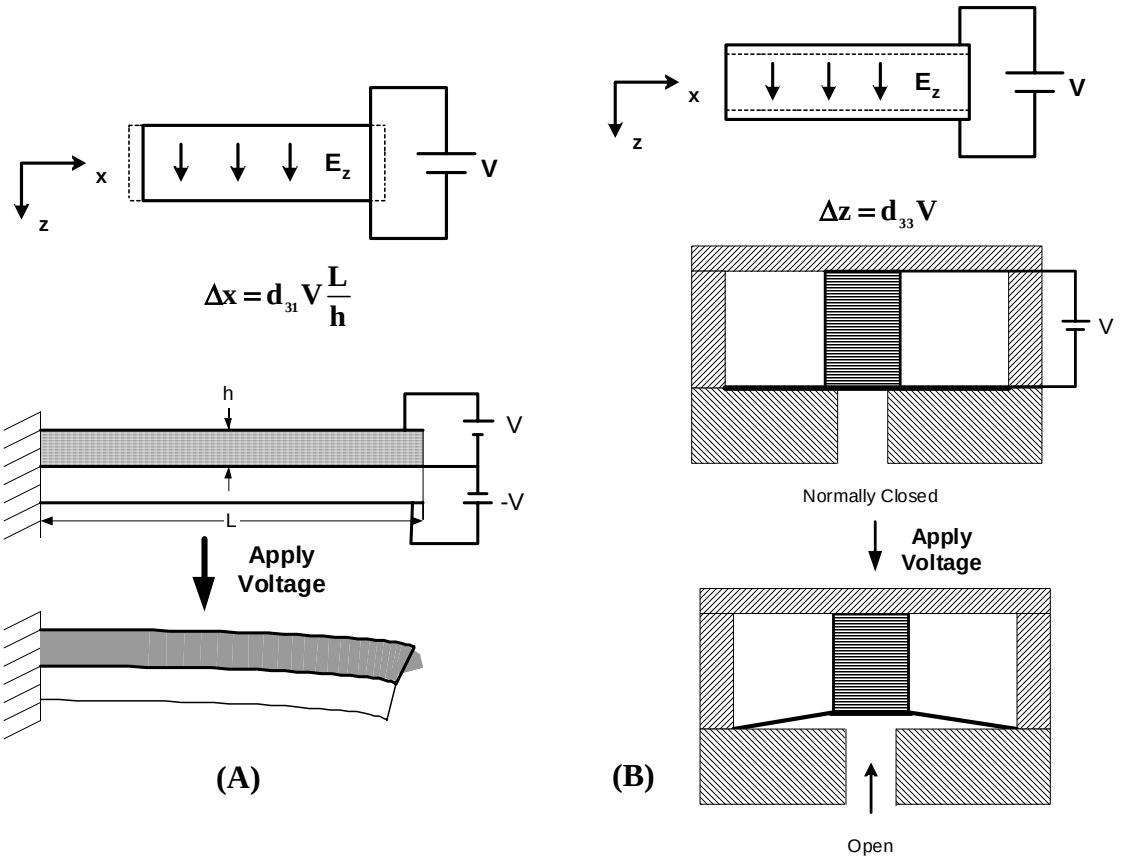

Figure 1.3. Schematic diagrams of (A) piezobimorph cantilever actuator and (B) piezo-stack actuator indicating its location in a microvalve

The z-displacement of a piezoelectric actuator is typically small, as indicated by the piezoelectric coefficient, as follows:

$$\Delta z = d_{33} V \qquad \varepsilon_z = \Delta z / d \qquad \varepsilon_x = \varepsilon_y = d_{31} V / d \tag{1.11}$$

Where V is the applied voltage, and d is the piezoelectric film thickness. The force is typically large (>MPa x Area), since a membrane structural design is very important in order to produce large displacement. A piezostack of N layers, or a bimorph built with oppositely poles films, is utilized in which case a displacement of several micrometers is typical:

Bimorph: $$\Delta z = 3d_{31}V\frac{L^2}{h^2} \quad (1.12)$$

Piezostack: $$\Delta z = Nd_{33}V \quad (1.13)$$

Where L is the length, h the thickness and V is the applied voltage. Finally, a Moonie which uses a poled composite piezoelectric transducer sandwiched between metal end cap structures to produce some mechanical displacement amplification results in deflections of the order of 10-20 times that of a single disk actuator [23] see Figure 1.4. Piezoelectric materials also have intrinsic hysterisis properties that must be taken into account when designing the actuator.

Esashi *et al.* [24, 25] has developed a normally closed microvalve with a silicon diaphragm and stacked with a piezo-disk actuator and glass support wafer, as shown in Figure 1.5. The structure is bulk micromachined with a membrane area of 300 μm and anodically bonded to the glass substrate wafer. A nitrogen gas flow rate of 0.1 ml/min to 85 ml/min at a gas pressure of 7.5 kPa, with a leakage rate of less than 0.1ml/min when an applied force of 0.45 kgf was provided by the piezo-stack. The valve could also operate with a liquid medium. There was however hysterisis present in the piezoactuators which resulted in hysterisis in flow versus voltage curves of the valve. Shoji [26] has also demonstrated normally closed valves utilizing a stacked piezoactuators, however, the external actuator was quite large measuring 2 x 3 x 9 mm.

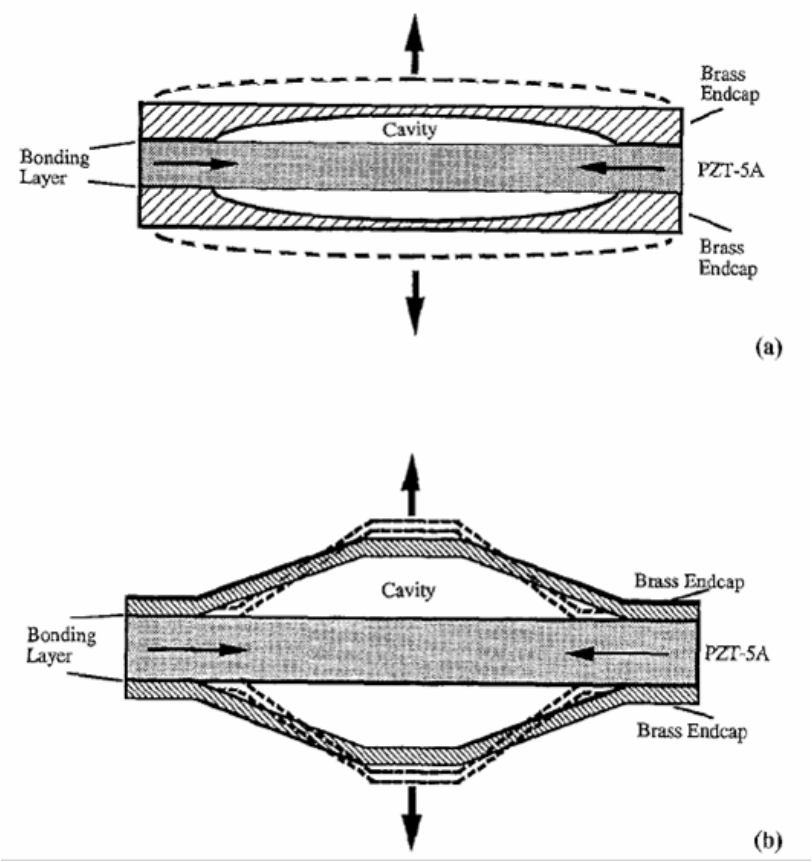

Figure 1.4. Schematic cross section of Moonie bimorph actuator [23]

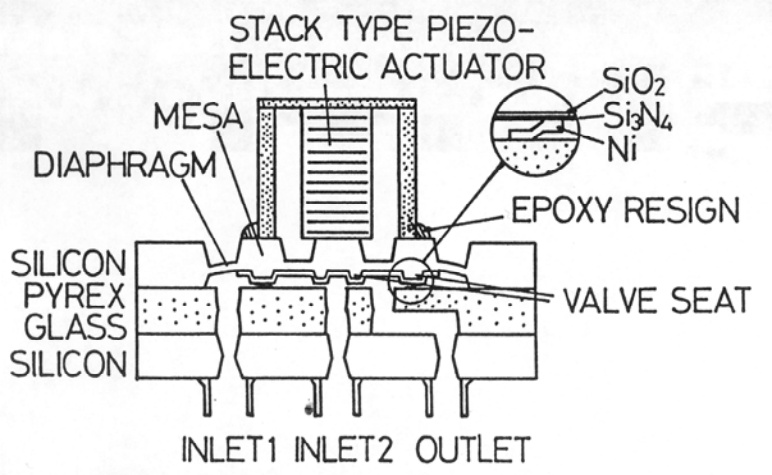

Figure 1.5. Schematic diagram showing the structure of the microvalve [24]

A novel disk shaped microvalve has been modeled by Watanabe and Kuwano [27] as shown in Figure 1.6. It comprises a thin piezo-film actuator suspended over a circular orifice.

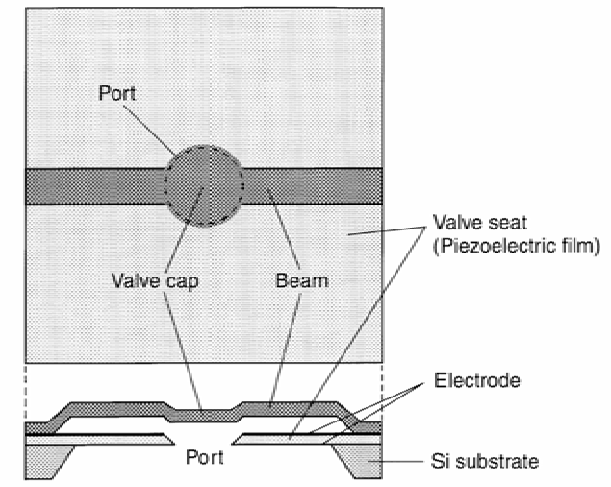

Figure 1.6. Schematic diagram of a surface micromachined piezodisk actuator [27]

When a voltage is applied to the valve seat the piezodisk shrinks, and because the outside of the disk is clamped to the substrate, the result is modulation of the opening port. Calculations indicate that the 1x1 mm valve can control air flow at a rate of 10^{-4} Pa m^3/s.

The developments by Chakroborty *et al.* [28] reports a piezovalve in which the piezostack is integrated into the wafer stack, see Figure 1.7. Here a corrugated diaphragm is utilized to extend the range of linear motion for the diaphragm and a stacked 100 μm thick PZT layers to produce 10 μm of displacement. In addition, a series of rings, 20 μm apart, are defined around the orifice to decrease the leakage rate and make the valve more tolerant to particulate contamination in the seal region. The valve is defined by DRIE etching and then the pieces bonded together with Ti/Pt/Au diffusion bonding at elevated temperatures (350-400^{o}C) and pressure (10-200 bars). Aerospace is a challenging application in which the valve must meet the rigorous requirements, including extremely low leak rates (<0.3 scc/h He) long shelf life, radiation and vibration resistant, and ability to operate over a wide temperature range (-120 to 200 ^{o}C).
The compact high differential pressure (>300kPa) microvalve described by Roberts *et al.* [29] is shown in Figure 1.8. It utilizes hydraulic amplification to improve the performance of the valve, a technique first pioneered by Huff *et al.* [30] and depicted in Figure 1.9. The differential pressure across the valve in the open and closed state are applied to each side of the disk shaped piston, so that there is an additional downward force due to the fluid present in the channel. By changing the ratio of diameter of the piston '*b*' to the diameter of the membrane *(b-a)* the force can be altered to the required range. Figure 1.9c shows the hysteresis produced in the flow characteristics of the valve.

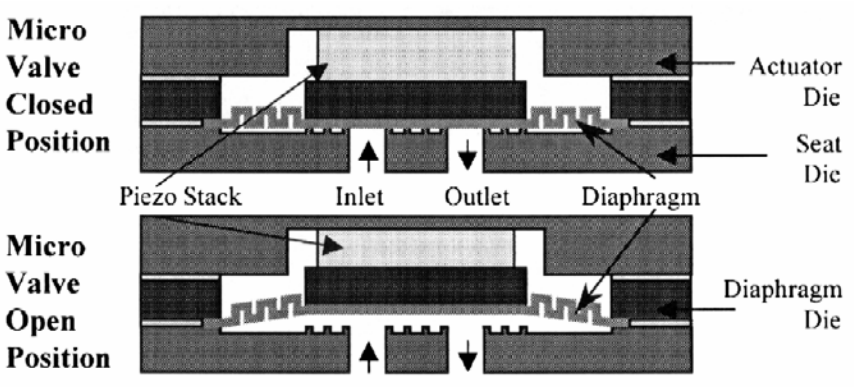

Figure 1.7. Schematic diagram of the microvalve, where the application of a voltage will cause the piezostack to contract, lifting up the diaphragm from the valve seat and creating a channel for the fluidic flow

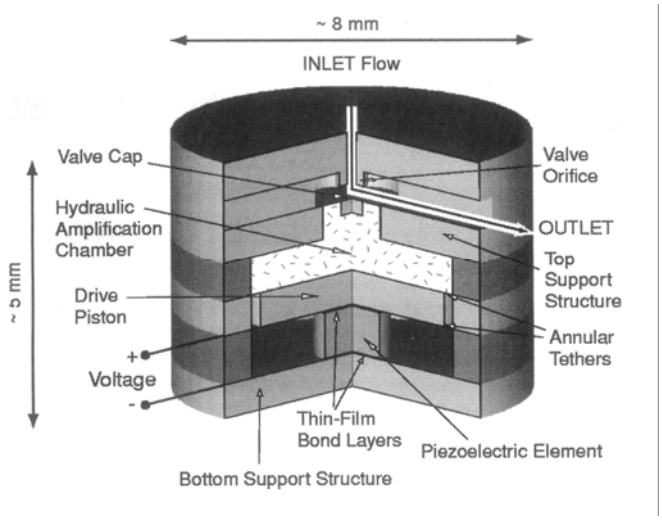

Figure 1.8. Schematic diagram of the piezoelectrically drive, hydraulically amplified microvalve [29]

In Roberts design a large valve stroke of 20-30 μm is achieved . Also, high frequency operation of up to 1 kHz provide a short closing time (< 1 ms). The silicon wafers are micromachined with DRIE etching, bonded together with silicon fusion

bonding and the glass to silicon bonding is anodic (at 300 ^{o}C) with the 4-layer piezo-stack embedded inside the structure, bonded with a AuSn eutectic bond. Following assembly the piezoelectric material is polled by applying 1000 V/cm electric field across the stack. The large deflection from a short Piezo-stack is achieved by utilizing a stiff membrane and hydraulic amplification to move a small area piston with a large diameter piezostack. This technique is well know in vibration control [31] and here the piston motion of the actuator is hydraulically amplified by the flow channels connected to the smaller area valve cap, displaced against the valve orifice. The results in Figure 1.10 show the regulation of fluid flow as a function of the differential pressure with silicon oil (hexamthydisiloxane) with low viscosity 0.65 centistokes as a function of the piston drive frequency and displacement. In these measurements the piston is first statically deflected to Z_{VC} = 11 μm, then up to 500 V peak-peak is applied to modulate the flow. The error bars indicate the range of measurement error in the flow data. Yang *et al.,* [32] developed an analysis of the pressure balanced approach for this valve, modeling both the static and dynamic motion. Results of the model indicate that valve will operate normally provided the pressure difference across the valve is positive, however there is a range of instability when the pressure difference is negative, such that the diaphragm may produce rapid oscillations. Modeling will enable the designs for different operating pressure ranges and with suitable damping introduced.

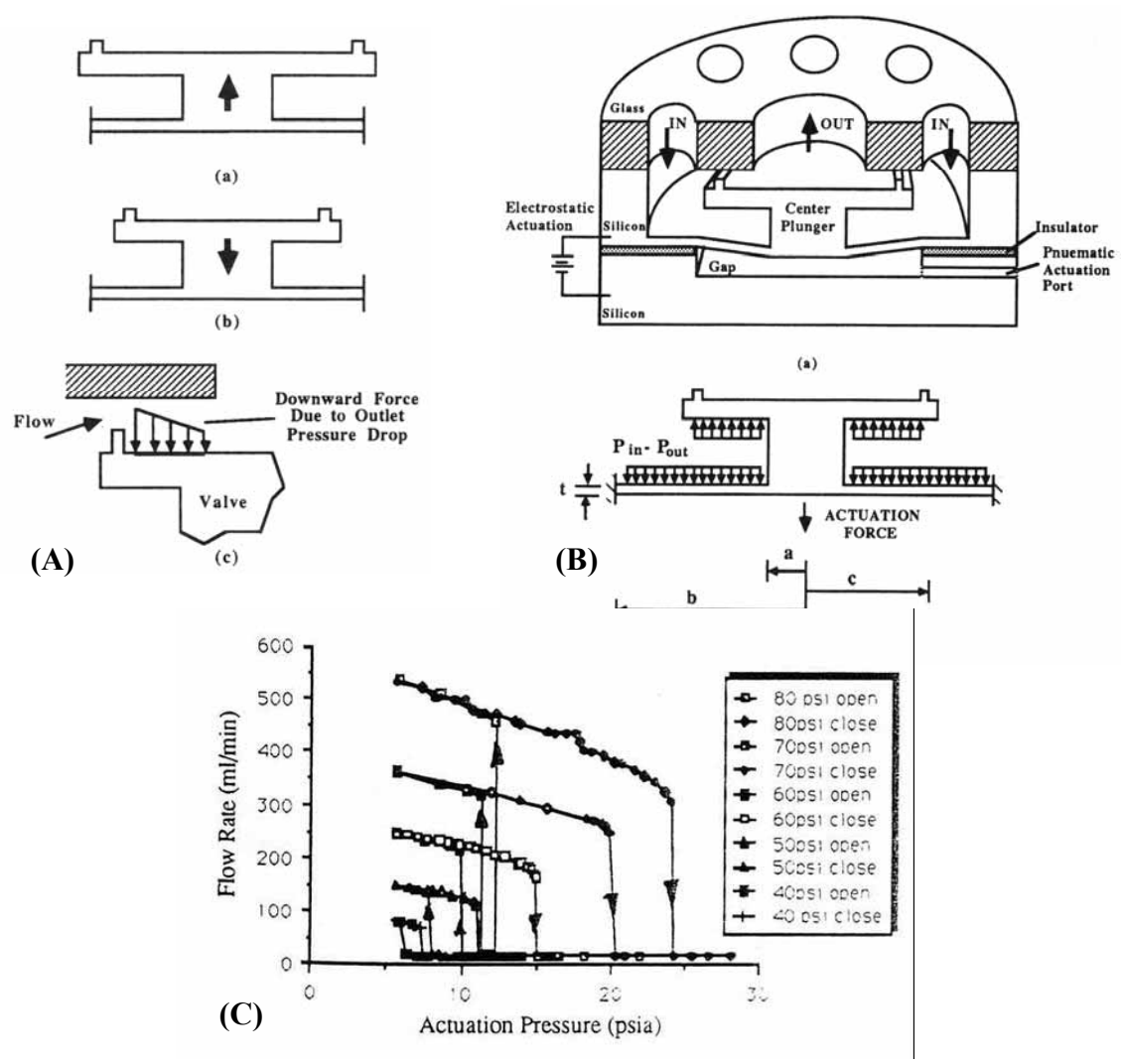

Figure 1.9. :(A)(a) Upward force on a valve with an oversized cap; (b) downward force on a valve with an undersized cap; (c) additional downward force on a open valve. (B) Schematic diagram indicating the principle of the pressure balanced microvalve. (C) Flow behavior for c = 1.4 mm, t = 15 μm, and a stroke of 5 μm. Proper pressure balance requires c = 1.41 mm, hence the cap is undersized in this case [30]

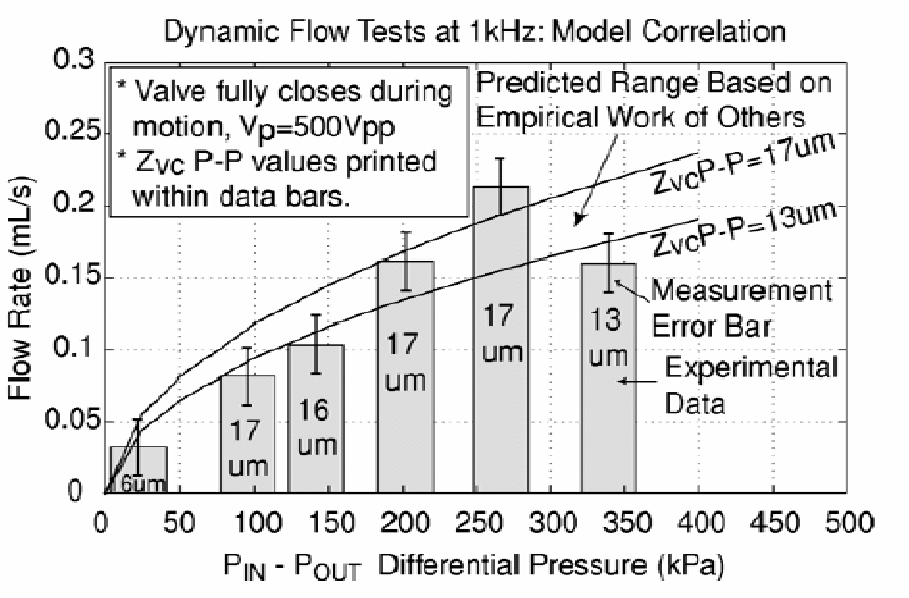

Figure 1.10. Dynamic flow regulation model and measurement at 1 kHz, as a function of the differential pressure, for silicone oil as the working fluid [29]

1.5.3 Electrostatic Actuation

Electrostatic actuation is commonly reported in microvalve design. The amount of electrostatic force generated between two conductors depends on the gap-distance between the surfaces and the applied voltage.

$$F = \frac{1}{2}\varepsilon\varepsilon_0 A\left(\frac{V}{d}\right)^2 \qquad (1.14)$$

where V is the voltage, d is the plate separation, A is the area and ε the relative dielectric constant, and ε_0 the dielectric constant of free space. The pull-in voltage is the voltage necessary to collapse two plates together and represents the minimum required to overcome the spring constant, k, of the membrane.

$$V_{PI} = \sqrt{\frac{8kd^3}{27\varepsilon A}} \qquad (1.15)$$

The electrostatic force is generally small, therefore high voltages are applied and small distance defined between the two conductive surfaces. However, one has to be very careful because a small displacement may limit the microvalve performance due high pressure drop or due to the clogging possibility from particulates in the flow. A novel S-shaped design developed by Sato and Shikida [33] and Shinkida *et al* [34] demonstrates fast response time and large displacement because the membrane distance from the actuator plate is a function of location, producing a rolling motion, as shown in Figure 1.11.

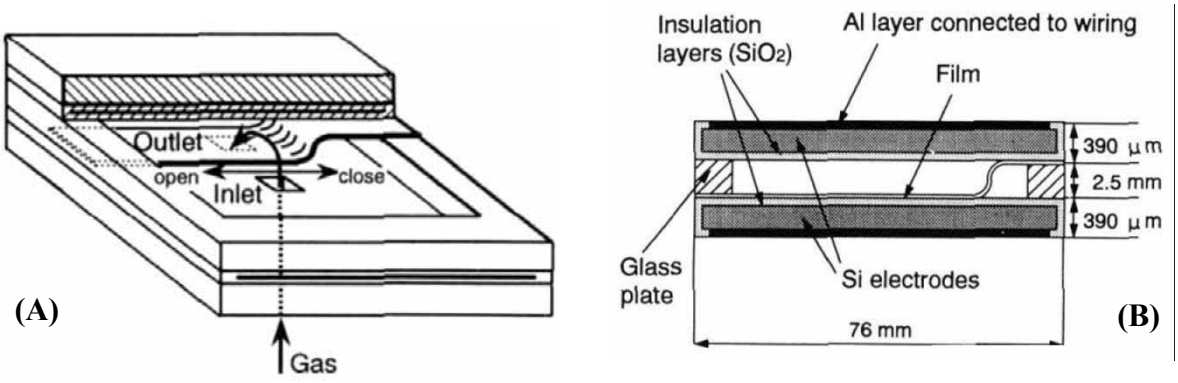

Figure 1.11. (A) Schematic diagram of a two-port electrostatic valve where the valve ports pass through the electrode plate. (B) Side view of the electrode plate with a 5 μm thick NiFe alloy rolled membrane [33]

The substrate is bulk micromachined, and electrode plates are defined by a silicone resin spacer gap of 2mm. Experiments with air indicate a working pressure of less than 100kPa, and switching of 0.4s with 125V applied. The application is for gas

flow control in a Molecular Beam Epitaxy system where the gas pressure is low, and rarified gas present, so that a large orifice size is required for small pressure drop. Further, work by Cabuz *et al.* [35] on electrostatic actuators demonstrated low power operation over many millions of cycles. A high-stroke, high pressure electrostatic actuator has been demonstrated on the similar principles by Goll *et al.* [36] made by thermal injection molding of conductive polyamide with a volume resistivity of ~ 1k Ohm-cm. The movable membrane acts as an electrode of 3 μm thickness: the membrane is spin-coated and patterned on a silicon wafer with gold electrodes defined. A voltage of 60-150 V is able to modulate the membrane to close the valve and flow rates of 12 mL/min at a differential pressure of 110kPa. Curvature of the silicon substrate can aide in the force displacement characteristics of the actuator (Nguyen *et al.*) [37]. An oxide nitride insulation film and the n-type Si fixed electrode are assembled into a three wafer stack. The valve operated with a back pressure of 10kPa with DC voltage of 162V and flow rate of 40 – 60 μl/min.

Ohnstein *et al.* [38] developed a normally open cantilever valve with a silicon nitride metallized membrane in which the conductor is embedded in the membrane by surface micromachining (see Figure 1.12). The valve could operate against a pressure of 12.9 kPa and provide flow rate up to 150 sccm nitrogen with a 30 V drive voltage. This is a single wafer fabrication process, which has been extended to arrays of valve by Vandelli [39] for fluid flow control. The valves are composed of square triple layer diaphragms, polysilicon - silicon nitride – polysilicon, of dimensions 300, 400 or 500 μm on a side, with a fluid channel air gap of 5 μm. They are normally open, operating at

250V to the closed state to control air-flow at a rate of 150 ml/min at a pressure differential of 10 kPa.

Novel bulk micromachined curved actuators which are an extension of the variable gap actuators have been demonstrated for a brail keyboard application by Yobas *et al.* [40], see Figure 1.13.

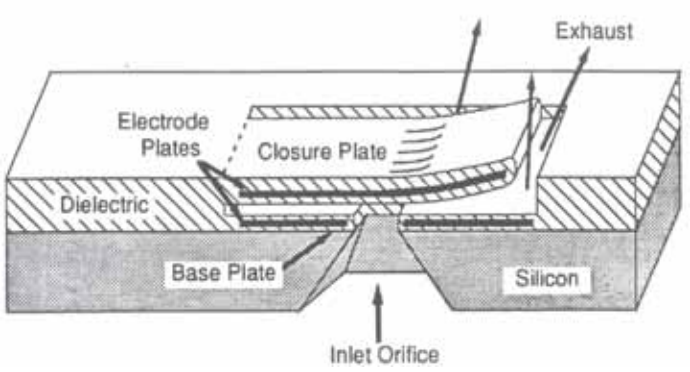

Figure 1.12. Schematic diagram of the thin-film surface micromachined electrostatic actuator [38]

Each brail dot of 1.5 mm diameter and height 0.5mm requires a closing voltage of 72.9V for 19.3kPa pressure difference across a 200 μm orifice in the silicon wafer. The curved-compliant doped silicon membrane 4 μm thick was defined by heavily doped p+ etch stop method on the upper wafer. The lower wafer has the flow orifice and the two are bonded together to complete the valve. Leakage rates are less than 1 mL/min is observed with the electrostatic drive voltage of 72.9V DC applied against a 13.8kPa back pressure of air.

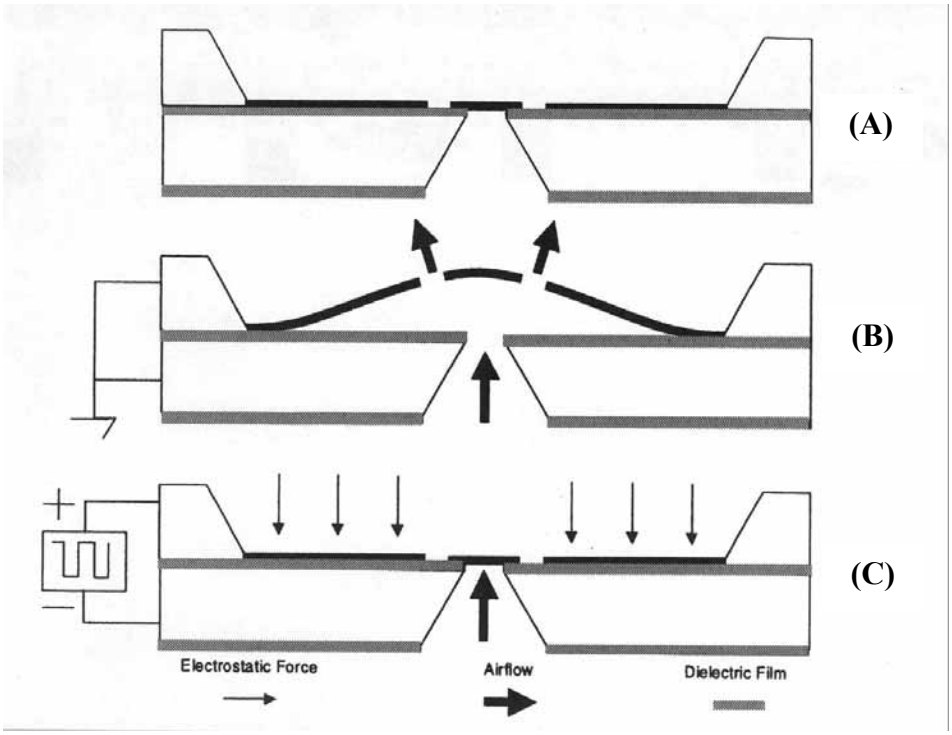

Figure 1.13. Cross sectional layout of the microvalve: (A) no pressure and no voltage applied; (B) open position, where the elastic diaphragm is deformed under an applied differential pressure, no voltage applied; (C) closed position, where the diaphragm is pulled flat and block the flow channel. Here the applied voltage is greater than the pull-in voltage [40]

Ph. Dubois [41] developed a valve that is composed of a vertically moving, double-clamped Ta-Si-N membrane, located over a small (10 μm) round orifice that is machined by deep reactive ion etching through the silicon substrate.

Finally a pressure balanced approach similar to Huff *et al.* [**Error! Bookmark not defined.**], was developed by van der Wijngaart *et al.* [42] for novel large stroke electrostatic actuators. The radii of the membrane and the actuator must be selected to demonstrate the correct back pressure stability for the valve and the electrostatic breakdown voltage through the dielectric film, in this case silicon dioxide. Bulk

micromachining was used to build the structure in a two wafer stack. However, the device was susceptible to instabilities due to parasitic charges trapped in the dielectric film. Performance based upon the modeling indicates it will be possible to control a 100 kPa pressure with a 5 μm diaphragm using only 24V dc bias.

1.5.4 Electromagnetic Actuation

An electromagnetically actuated microvalve utilizes the force generated from the magnetic field either through the magnetic induction or the Lorenz force [43], as indicated in Figure 1.14. Microvalve actuators can be based upon the forces generated from "coil to coil" or "magnet to coil". Magnitude of the Lorenz force is given by:

$$dF = \frac{\mu_0 I_1 d\ell_1 \times I_2 d\ell_2}{4\pi r} = B \times I_2 d\ell_2 \qquad (1.16)$$

where B is the magnetic field, I is the current and r is the distance between the wires.

The magnetic field may also be generated by a coil or a permanent magnet. In the case of a magnetostatic actuator the induction through the magnetic material results is a change in the stored energy, W_m, the sum of the energy stored in the magnetic core and the air gap. Hence an attractive force follows:

$$F = \frac{\partial W_m}{\partial x}; \text{ where: } \quad W_m = W_{core} + W_{airgap} = \frac{1}{2} L I^2 \qquad (1.17)$$

where L is the inductance of the coil and I is the current energizing the coil. The reader is referred to a review is given by Ari and Honda [44] and text on microactuators [45].

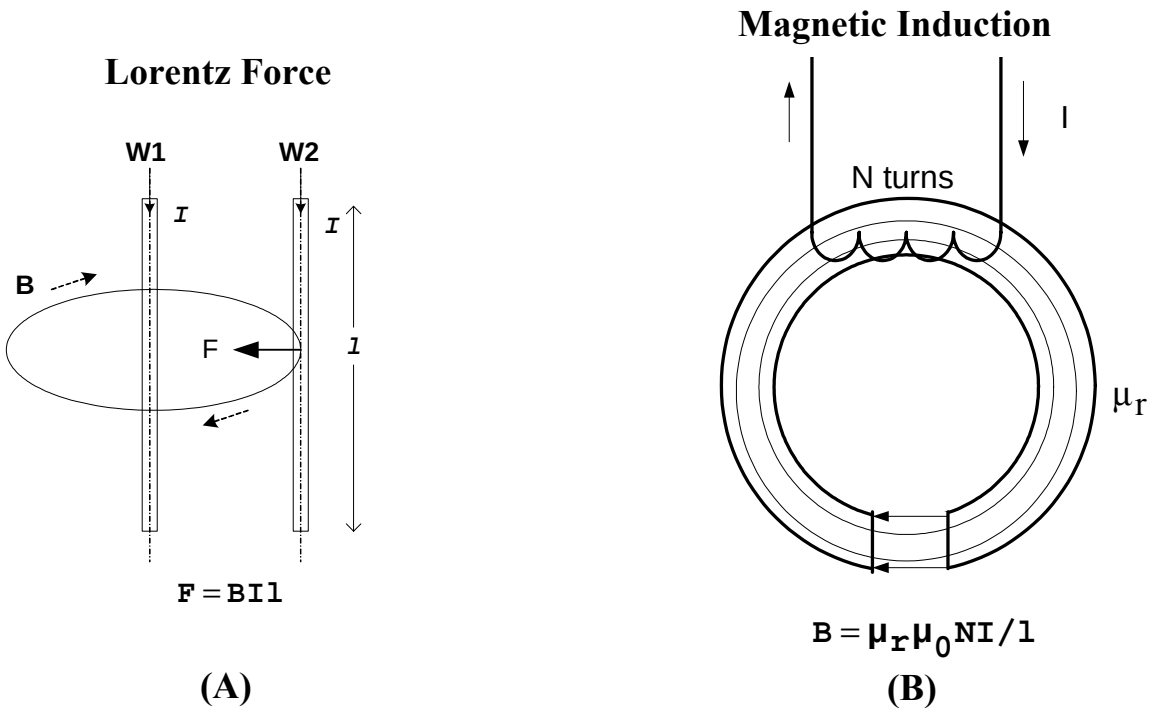

Figure 1.14. Electromagnetic forces generated by (A) Lorentz force and (B) magnetic induction

An early example of magnetically actuated device is described by Smith *et al.* [46] consisting of a polysilicon/magnetic material plug that is positioned in a flow channel between two bulk micromachined silicon. One of the benefits for magnetic devices is that thin films of high permeability materials, such as Permalloy (80% Ni 20% Fe), can be deposited by electroplating into a photoresist mould.

A combined electrostatic and magnetic actuation principle has been employed by Bosch *et al.* [47] in which a planar coil is lithographically defined on a membrane defined in a bulk etched silicon wafer. A second wafer is bonded to locate the flow channel beneath the membrane and define the electrode for the microvalve. Figure 1.15 shows a schematic diagram of the valve. The valve could operate against a static gas pressure of

16 kPa (2.4psi) and flow rate up to 3 ml/min. The magnetic actuator typically required current pulses of 200 mA and the electrostatic actuator, necessary to keep the valve in the closed state, required 30V dc. A switching time in under 0.4 ms was achieved and the static power consumption was reduced with the use of a short current pulse to provide an impulsive force to the membrane.

Other electromagnetic valves based upon microfabricated elements and use an external multi-turn coil to increase the magnitude of the actuator electromagnetic force, are shown in Figure 1.16. The design described by Yanagisawa *et al.* [48] for gas flow control uses a thin NiFe membrane (thickness 2 μm) supported by an angular-spiral spring with beam width 20 μm over a 30 μm diameter orifice, in the silicon wafer. The control of vacuum pumping was demonstrated with a operating pressure in the 10^{-7} torr range, and has demonstrated flow modulation over a range of frequencies from 0.1 to 100Hz.

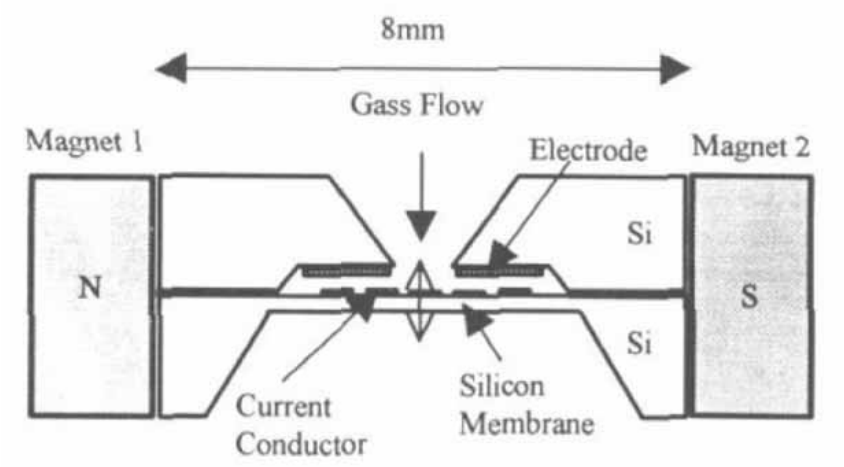

Figure 1.15. Schematic view of the silicon microvalve with electromagnetic/electrostatic actuation [47]

The latching principle can be applied to reduce the power consumption with a permanent magnet. Shinozawa [49] developed a valve with a micromachined coil, vertical displacement of 5 μm, and a permanent magnet. The overall valve dimensions including the actuator were about 5 x 5 x 5 mm^3. The smallest controllable amount of fluid (water) was 0.7 μl/min. An external 60 turn coil was utilized by Ren *et al.* [50] with a microfabricated flow channel, large air gap of 100 μm, to generate a comparatively large 5mN closing force. With a current pulse of 1.25 A of duration 0.3ms successfully demonstrates rapid closing time. Finally, Meckes [51, 52] developed a coil-to-coil design with the integrated gold microcoil defined on the membrane and the external magnetic coil generates sufficient flux (~310 T/m) to deflect it over the orifice producing a closing force of 800 mN at a current of 25mA.

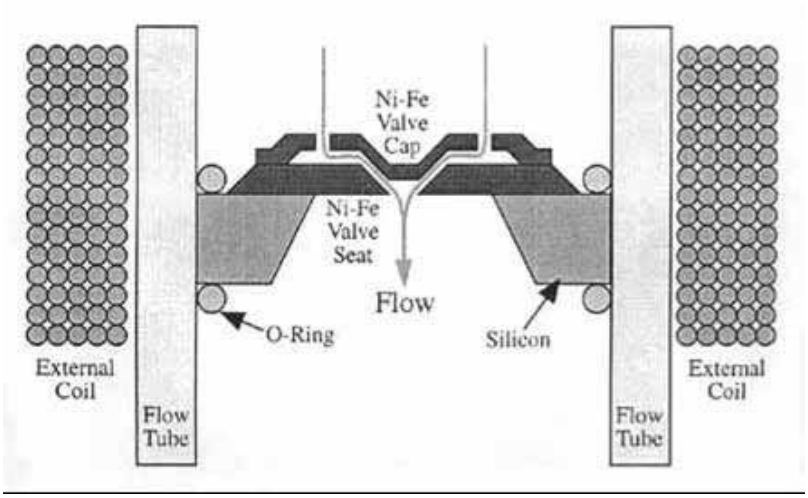

Figure 1.16. Schematic diagram of a microvalve activated by an external coil, the valve is normally in open condition [48]

Sadler *et al.* [53, 54] developed a 3-wafer design with magnetic flux coupling through the top wafer to the NiFe membrane, as shown in Figure 1.17. The valve components were bonded together, a glass orifice plate with inlet and outlet channels and valve seat, a silicon membrane with an electroplated film of NiFe, and a top layer with horseshoe-shaped inductor including a 25 μm thick magnetic core. Gas flow rates of 0.6ml/min at a pressure drop of 9.6 kPa, leakage rate of 10 μL/min, with power consumption of 300 mW was reported. With deionized water as the working fluid the flow rate was 0.85 μL/min at 5 kPa and the leakage rate was 0.3 μL/min.

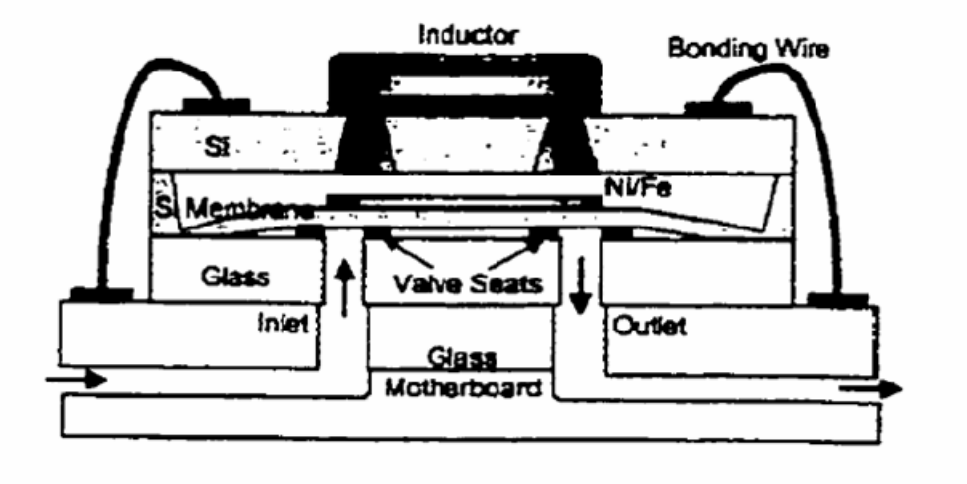

Figure 1.17. Schematic diagram of the microvalve with separate inductor and magnetic field coupling to the diaphragm in the flow channel [53]

Bohm *et al.* [55] designed a microvalve that consisted of two separated parts and were fabricated in two-separated processes, see Figure 1.18. The silicon-valve part with the overall dimensions of 7 x 7 x 1 mm^3 was made by a sandwich construction of two etched silicon wafers, where a silicon rubber membrane achieved improved sealing. The

external NeFeB permanent magnet, 800 turn coil with a soft magnetic circuit and integrated spring, provides a bi-directional actuator with 200 μm of displacement. The calculated forces on the actuator are designed by FEA of the magnetic fields, where the flux is confined to the soft magnetic material with a maximum flux density of 1.56 - 1.9 T present.

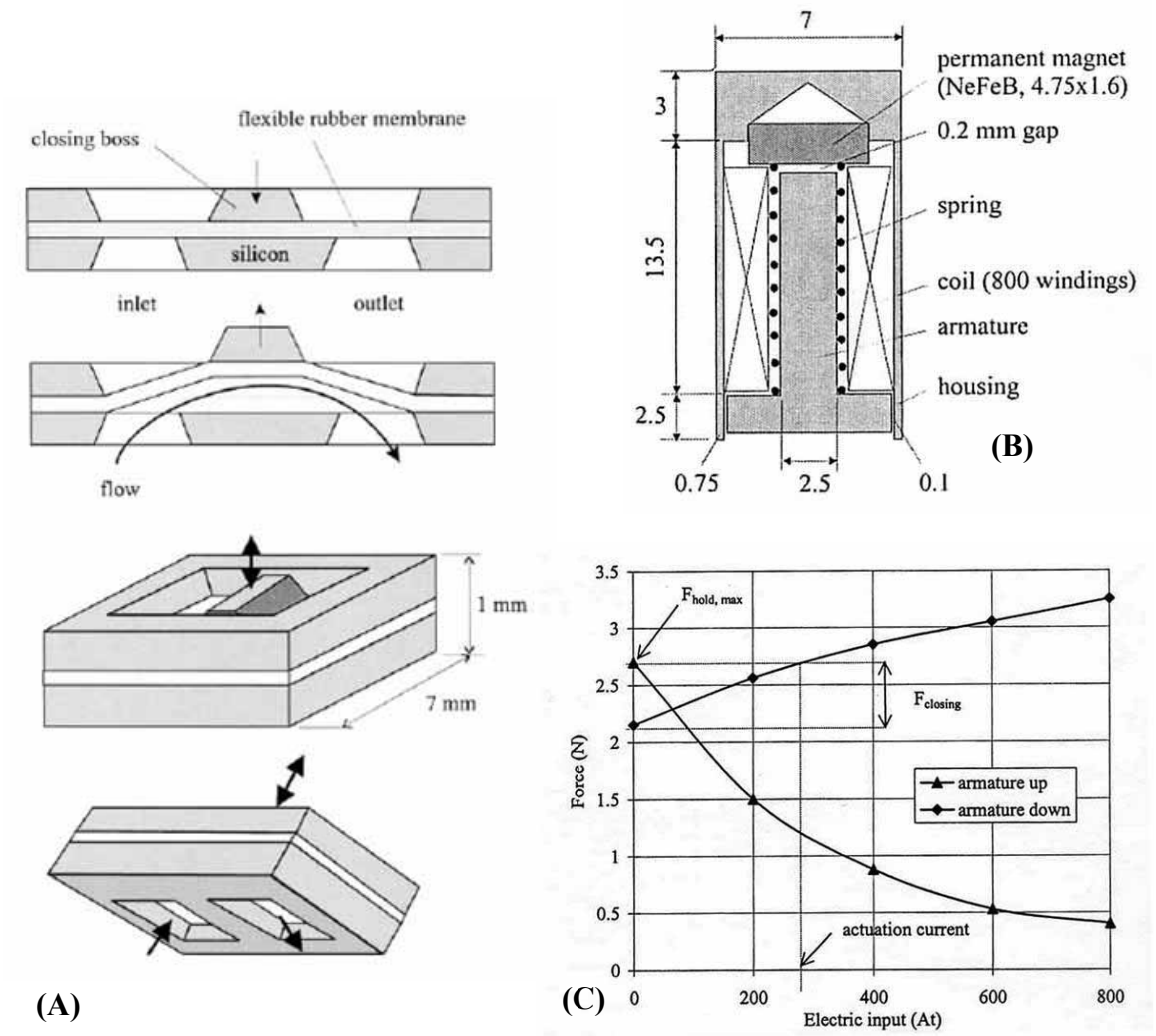

Figure 1.18. (A) Cross section of the silicon micromachined parts of the valve; (B) cross section of the bi-stable electromagnetic armature with integrated magnet, spring, and coil; (C) calculated forces on the armature as a function of the armature position and electric input [55].

When the current is applied to the coil to oppose the magnet the holding force is diminished and hence the spring force releases the armature downwards closing the valve. Hence for a force of 2.7 N, which is greater than the spring force is able to change the state at a required current of 300 mA, as indicated on the figure. The difference between the armature up and armature down force is 0.55 N.

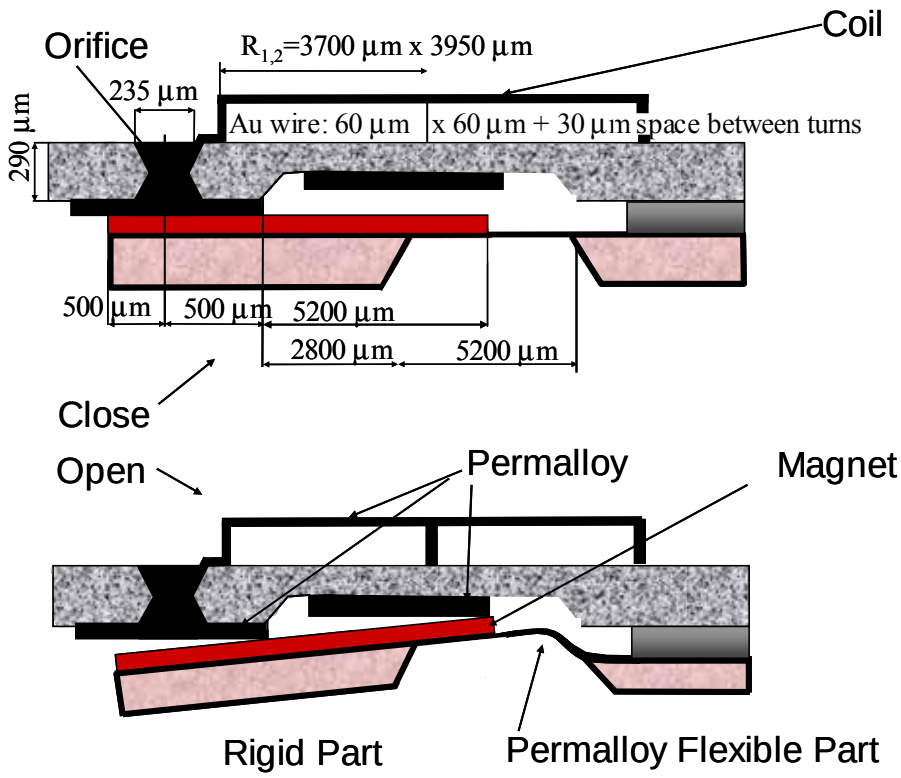

Figure 1.19. Schematic cross sectional diagram indicating the operating principle and general dimensions of the latching microvalve [56]

The combination of both forces generated from coil to coil and magnet to coil were utilized by Capanu *et al.* [56]. The valve is fabricated from three layers, the flow

channel, coil and a permanent magnetic Arnokrome Cr/Co/Fe rolled alloy foil to form the cantilever, see Figure 1.19. Bulk micromachining defines the orifice and electroplating into a photoresist mold for the planar coil and thin film Permalloy film required to complete the magnetic circuit.

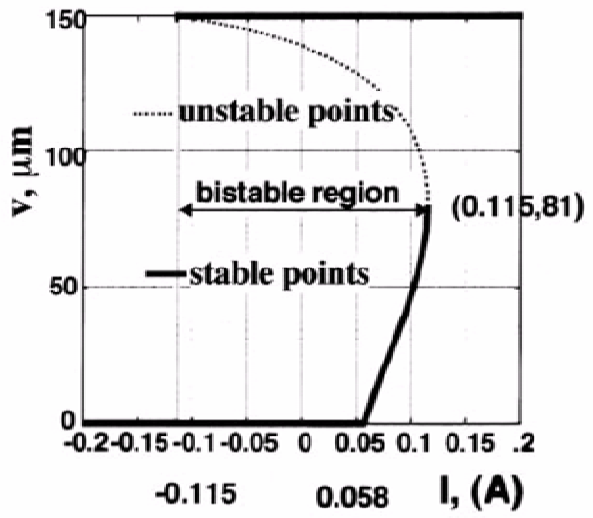

Figure 1.20. Stable and unstable equilibrium positions of the cantilever as a function of the DC current in the coil [56]

Figure 1.20 indicates the stable regions of operation for the valve actuator, when the current is between 0.06 and 0.12 A. There are two equilibrium points, one stable and one unstable as represented by the continuous and dotted lines, respectively. The stable and unstable points meet when the displacement of the cantilever tip is 81μm at a current of 0.12A. For I > 0.06A the stable position is deflected (open valve), and for I < -0.11A undeflected (closed valve). Actuation at 1-2 V occurs with a pulse width of 50-80 ms. Hence, when the current is zero the valve actuator has two stable locations between

which it is switched by reversing the direction of current pulse. In air, it was demonstrated that the valve opened with a 5.3 ms pulse of 1.38V; it closed with a pulse of 1.26V for 38ms. Performance in air was more rapid that in water. With the valve open water flow of 0.05-0.5 μL/s at a pressure up to 2,000 Pa was achieved.

An electromagnetic device described for Glaucoma treatment by Boe *et al.* [57] uses a multi turn coil, a miniature membrane and permanent magnet. These components are assembled into a cavity bulk micromachined into the silicon wafer together with a PDMS microchannel. Current pulse operation of the valve produced deflection of the membrane thereby modulating the pressure release rate from the eye.

1.5.5 Thermal Actuation

Bimetallic actuators are well known in miniature electro-mechanical systems because of their simplicity, and the large forces that can be generated, rapidly with modest temperature changes. The valve design is therefore much simpler than the electromagnetic actuator, as there is only a thin film heater required to deflect the membrane based upon a difference in thermal expansion coefficient. However, the drawbacks are the relatively high power consumption and that the structure is sensitive to ambient temperature. For two layers of equal thickness shown in Figure 1.21, we have the following deflection:

$$\delta \approx \frac{6L^2(\alpha_2 - \alpha_1)\Delta T}{t(E_1 + E_2 + 14E_1E_2)} \tag{1.18}$$

where E is the Young's Modulus, w the width of the beam, t the thickness, L the length, α the thermal expansion coefficient and ΔT is the temperature change.

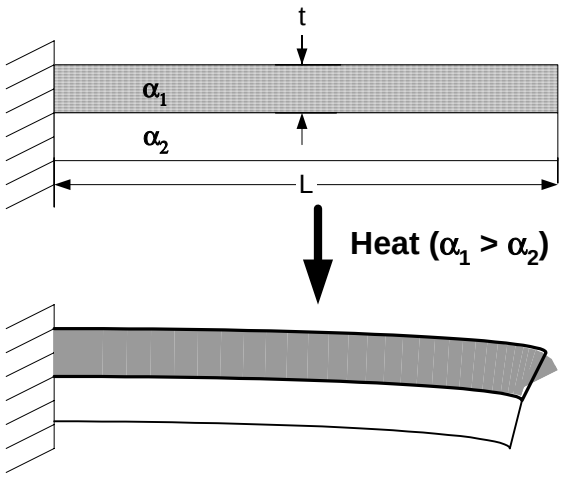

Figure 1.21. Cross section of a thermal bimorph actuator

The schematic of the thermally actuated microvalve developed by Jerman *et al.* [58, 59] is shown in Figure 1.22. It had a bossed silicon membrane to keep the valve piston separate from the thin film actuator which bends when heated. The bimetallic films comprise a 5 μm thick film of aluminum on the p+ silicon membrane with embedded diffused heating resistor. The membrane moves up providing a normally closed valve at a power level of 0.5 W and flow rate of 0.1 lpm nitrogen.

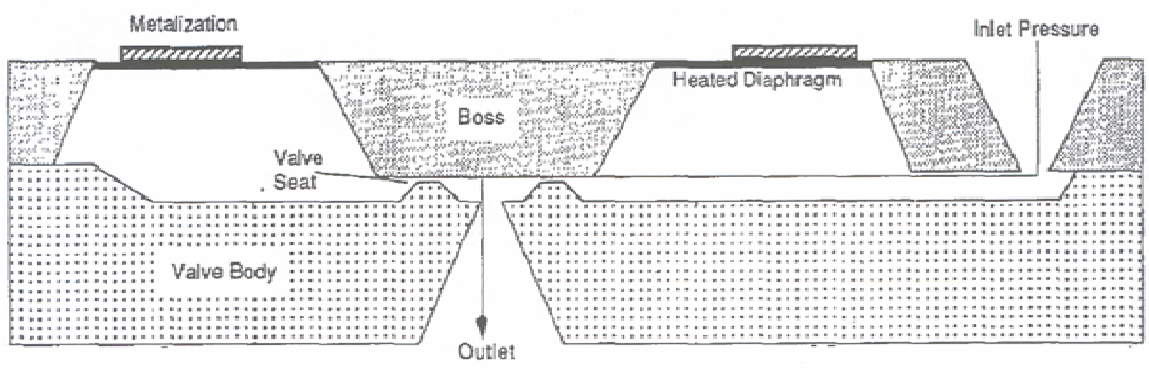

Figure 1.22. Schematic diagram of a normally closed thermal bimorph-actuated microvalve

A micromachined bimorph pressure driven actuated valve developed by Trah *et al.* [60] is shown in Figure 1.23. A jet of fluid is directed by a bimorph actuated flap such that the flow is re-directed due to the Coanda effect, resulting in pressure modulation. The Coanda effect observed when a fluid steam passed through an orifice into another fluid, it will tend to carry along with it a fraction of the surrounding fluid. This tendency results in the fluid jet attachment to the bimorph surface. A pressure difference across the valve membrane normally keeps the valve closed, however when the fluid jet is diverted a pressure difference ($p_2 - p_1$) develops. Here silicon and aluminum are used in the bimorph and a power input of ~8W was required to open the valve with air as the working fluid.

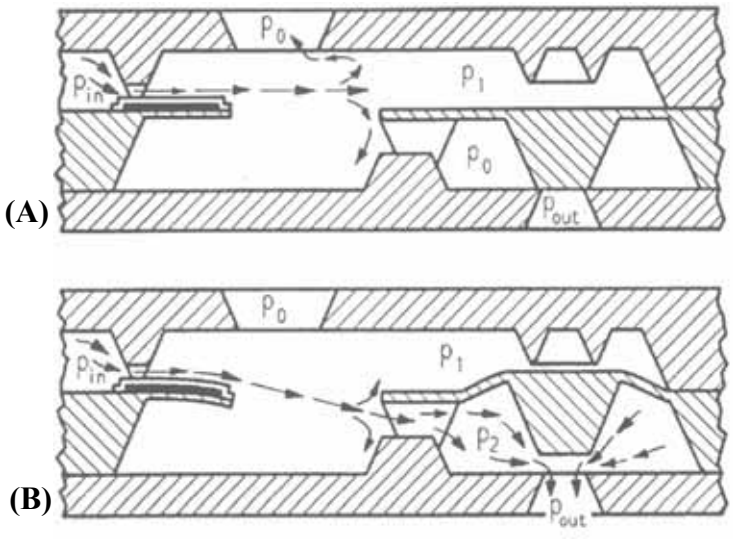

Figure 1.23. Schematic view and principle of the hydraulic actuated microvalve. (A) the valve without actuation of the bimorph; (B) heating of the bimorph redirects the flow to create a pressure difference which pushes the piston away from the orifice [60]

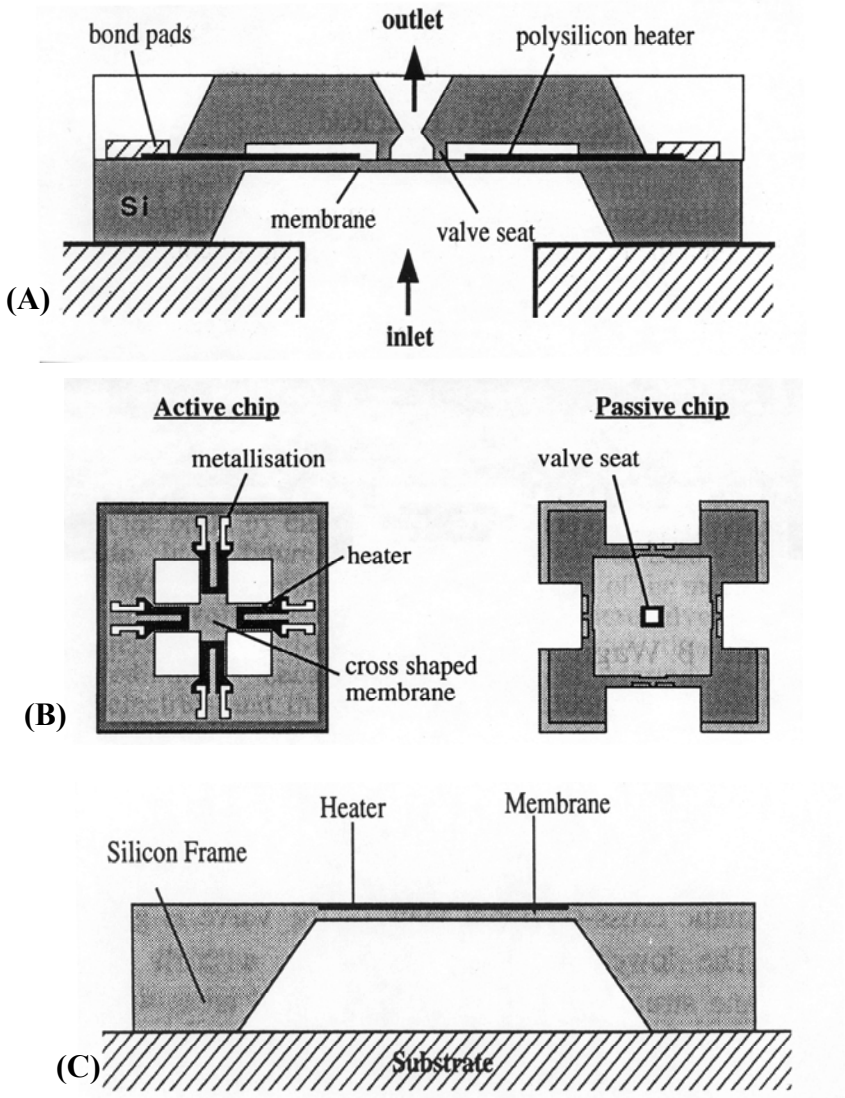

Figure 1.24. (A) Cross section of the bimorph microvalve; (B) plan view of the active chip with membrane and embedded heaters and passive chip containing the valve seat and orifice; (C) basic silicon structure of the valve [61]

T. Lisec [61] developed a normally closed design based upon buckling of the support beams attached to a mesa. A schematic diagram of the valve is given in Figure 1.24. The support beams 12 μm thick, 600 μm long surround the orifice size, which is 360 x 360 μm^2 and is included in an overall chip size of 2.6 x 2.6mm^2. For pressure of 100 kPa it delivers a flow rate of 0.7 lpm. The switching time is about 15 ms, which is

rapid for thermal actuation. The thin film polysilicon heaters are defined on the cantilever beams so that they are thermally isolated from the substrate and the estimate temperature of ~130^{o}C is reached with a power input of 1 - 4W.

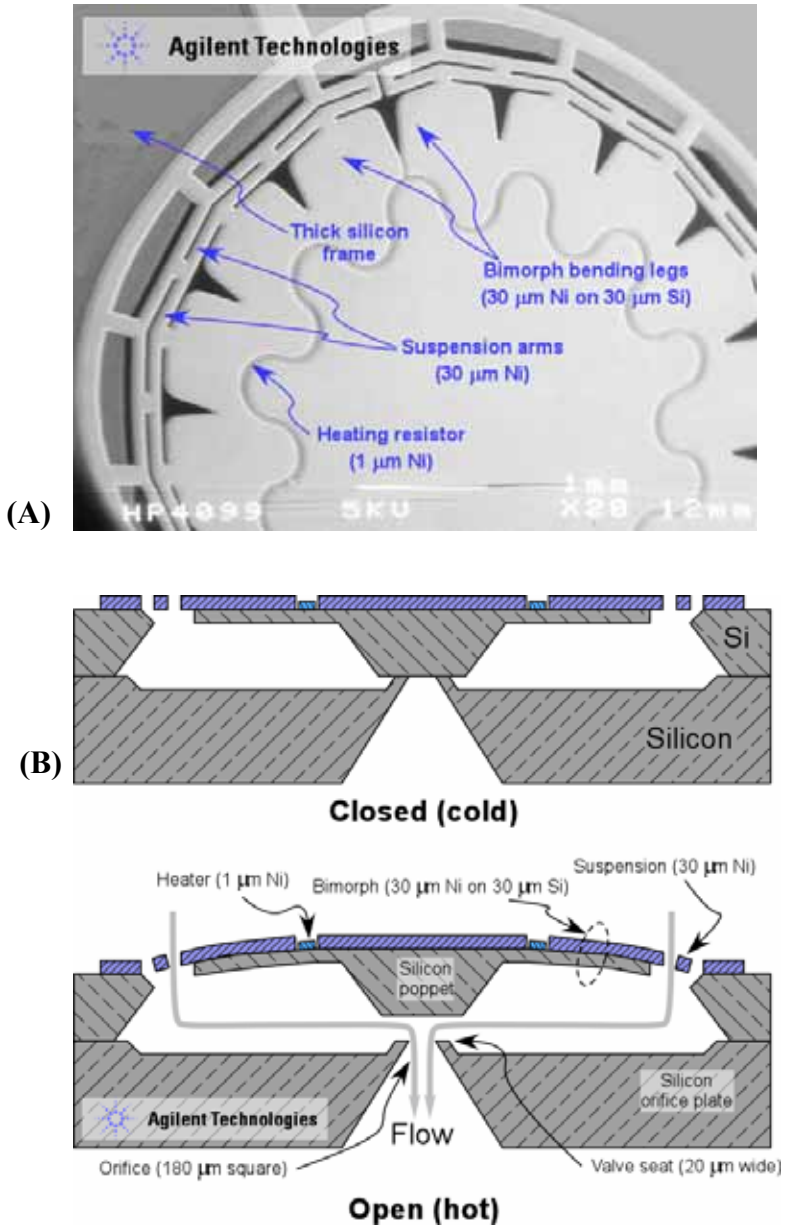

Figure 1.25. Top view of the thermal bimorph mechanism illustrating the leaf-like structure and thin-film heater; (B) cross-sectional diagram indicating the principle of operation for the normally closed bimorph valve [62]

The Barth *et al.* [62] developed a microvalve which includes a novel bimetallic actuator consisting of a 30μm thick Ni film deposited on the silicon structure, shown in Figure 1.25. The set of radial legs have an integrated heating element consists of a 1 μm thick Ni serpentine conductor.

Upon an increase in the temperature of approximately 100 ^{o}C above the ambient, the legs flex upward and lift the valve mesa to open the valve. The maximum pressure is ~ 680kPa, flow rate < 1 lpm and power consumed is less than 1 W with and response time is 0.2 s. The stable operating temperature range for the valve is 0 to 55^{o}C ambient.

1.5.6 Thermo Pneumatic Actuation

A valve that utilizes the actuation generated from the thermo-pneumatic force can be operated with gas, liquid or solid. The change in volume of the fluid includes the volumetric thermal expansion, plus any phase change phenomena. This type of actuator requires relatively more power consumption than those discussed due to the specific heat of the material and the latent heat in any phase change. In a volumetric change in density we can calculate the volume change with:

$$\Delta V = V_o \alpha_f \Delta T \tag{1.19}$$

where V_o is the initial volume, μ_f is the thermal expansion coefficient and ΔT is the temperature change. When vaporization occurs the vapor pressure in the gas must be in equilibrium at the working temperature, hence the volume is approximated by:

$$\Delta V = \frac{nRT}{p_v} \tag{1.20}$$

Where n is the number of moles of material vaporized and R it the universal gas constant.

Here the pressure of any superheated vapor is given by the following term:

$$p_v = p_o e^{\left(-\frac{L_H}{RT}\right)} \tag{1.21}$$

Where L_H is the latent heat of vaporization and p_0 is the initial pressure of the vapor.

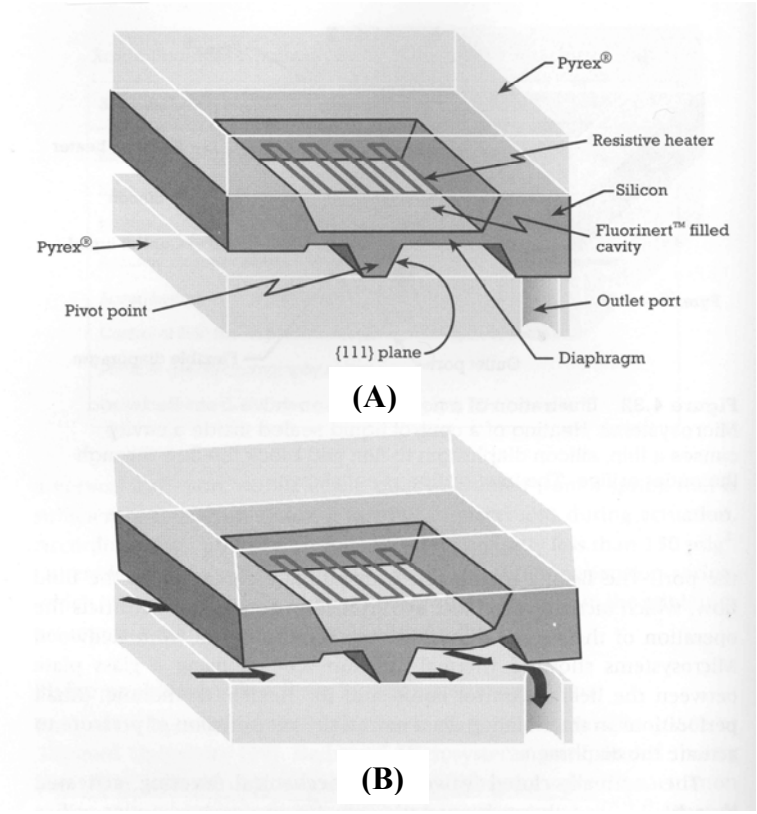

Figure 1.26. Schematic diagram indicating basic operating mechanism of the Redwood Microsystems thermopneumatic valve. (A) The silicon mesa covers the flow channel through the Pyrex support chip resulting in a valve that is normally closed. (B) Heating of the Fluorint™ liquid results in expansion in the sealed cavity such that the diaphragm is bent, lifting the silicon from the orifice channel [63, 99].

This type of valve typically has a longer response time due to the thermal time constant, however the membrane deflection is generally larger. The fabrication processes

are complicated due to the necessity to fill the chamber with fluid and provide a hermetic seal over the lifetime of the valve. The valve commercialized by Redwood Microsystems was developed by Zdeblick *et al.* [63], shown schematically in Figure 1.26. Here a fluid selected with a large volume expansion which when heated expands to push open the valve.

The properties of the Fluorinert^{TM} a perfluorocarbon from 3M, boiling pt. can be in range 56-260 ^{o}C, this fluid has a large expansion coefficient, the order of 0.13%/^{o}C and is electrically insulating. The normally closed has a bulk silicon micromachined diaphragm 2.5 mm diameter and 10 μm thick, with an Al heater requiring a power 1.5 W to produce a switching time ~ 1s. The valve has a maximum operating pressure of 170kPa.

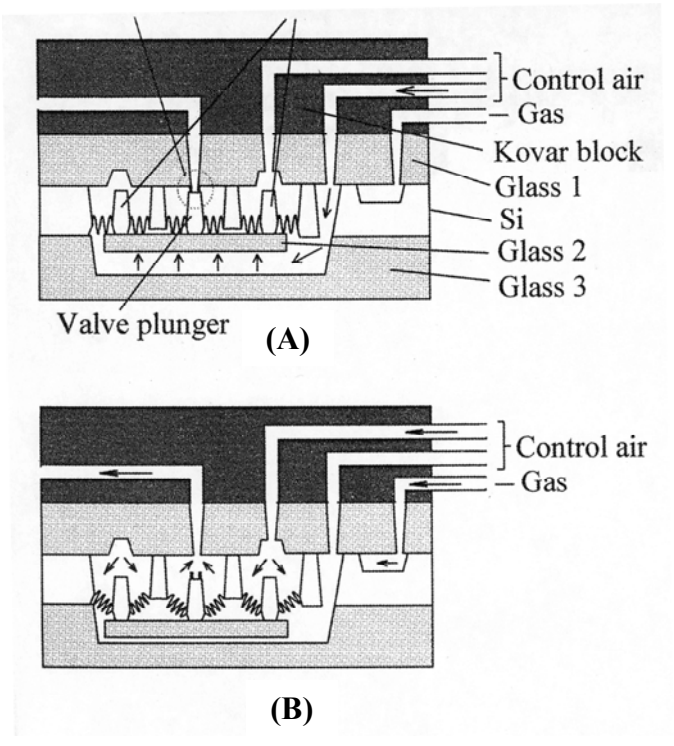

Figure 1.27. Working principle of the bakeable microvalve with (A) closed condition and (B) open condition indicated after the pneumatic control line is pressurized [64].

Pneumatic valves can be also be driven from an external source of pressure, as demonstrated by Sim *et al.* [64] and shown in Figure 1.27. This design is a three valve arrays that are buckled at higher temperatures ~125^{o}C, and utilize a silicon/glass/kovar stacked structure. A nitrogen gas flow of 0.1 to 35 sccm was controlled with the inlet pressure of 1-4 kPa.

A silicon rubber based thermo pneumatic actuated membrane valve, with a composite membrane comprising silicon rubber and Parylene was developed by Yang et al. [65].

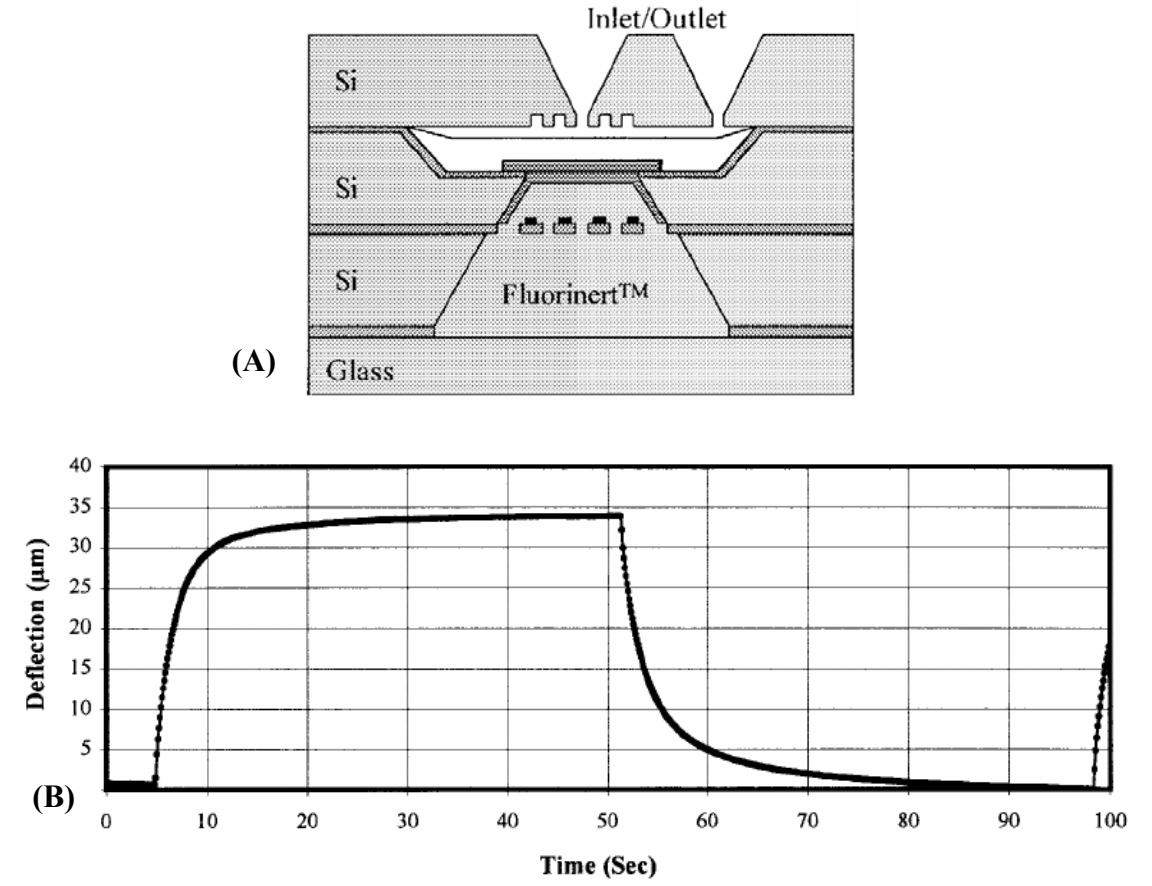

Figure 1.28. (A) Cross-sectional diagram through the thermopneumatic valve with silicone rubber-Parylene C membrane. (B) Observed deflection time response of the membrane when PF 5060 is used as the expansion fluidic with a power input of 42 mW [65]

The requirements for the valve membrane are small size, impermeability to the working fluid, large deflection, and an adhesive compatible surface for bonding the seat chip. Parylene C forms an effective vapor barrier, while the silicon rubber is very soft and elastic. The Young Modulus of the MRTV1 silicon rubber is 0.51 MPa while that of Parylene C is 4.5 GPa. Therefore, the composite membrane built from these two materials has great flexibility and impermeability. In order to keep the membrane soft, a very thin Parylene layer was used compared to the silicon rubber layer. Figure 1.28 shows a schematic cross-section through the valve which is built from three silicon wafers. The Fluorinert^{TM} is the working fluid. A thin film Cr/Au heating element is defined on a thin (0.5μm thick) silicon nitride membrane, such that the fluid can be heated effectively with low power consumption, ~ 40 mW.

Rich [66] developed a more complex thermo pneumatic microvalve, shown schematically in Figure 1.29A. The valve is a three wafer stack, the middle layer containing the corrugated diaphragm, 10 μm thick p+ silicon with a thick silicon mesa. A sealed cavity is defined below the diaphragm by anodic bonding to Pyrex glass. On top of this, the thin film suspended heating element has been defined. The heating element is positioned 9 μm from the cavity base thus minimizing heat loss to the package. The cavity contains a volatile fluid, in this case pentane, which is vaporized with resistive heating to deflect the diaphragm, thus closing the valve.

Figure 1.29B shows typical data indicating the pressure increase at power levels between 100 and 300mW. The actuator can generate a 2000 torr pressure rise with 500 mW input for 1s, while the closed state of the membrane can be maintained with just 30mW steady input power.

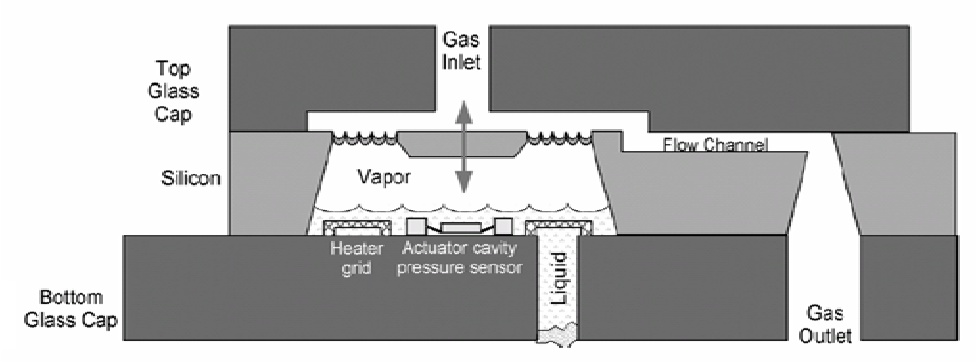

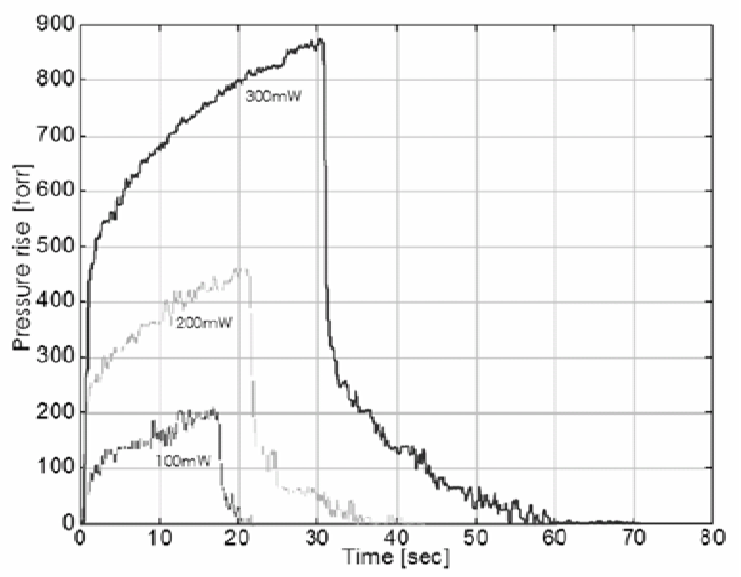

Figure 1.29. (A) Schematic diagram of the thermopneumatic valve. (B) Transient response of one actuator on a thermally insulating base, as a function of the electrical power input to the heater [66]

Carlen [67] developed a slightly different design for the valve, which used a paraffin micro actuator as the active element. The entire structure with nominal dimension of diameter 600 μm x 30 μm was batch: fabricated by surface machining. For gas flow rates, the actuation power ranged from 50 to 150mW with the leak rate of 500 μsccm.

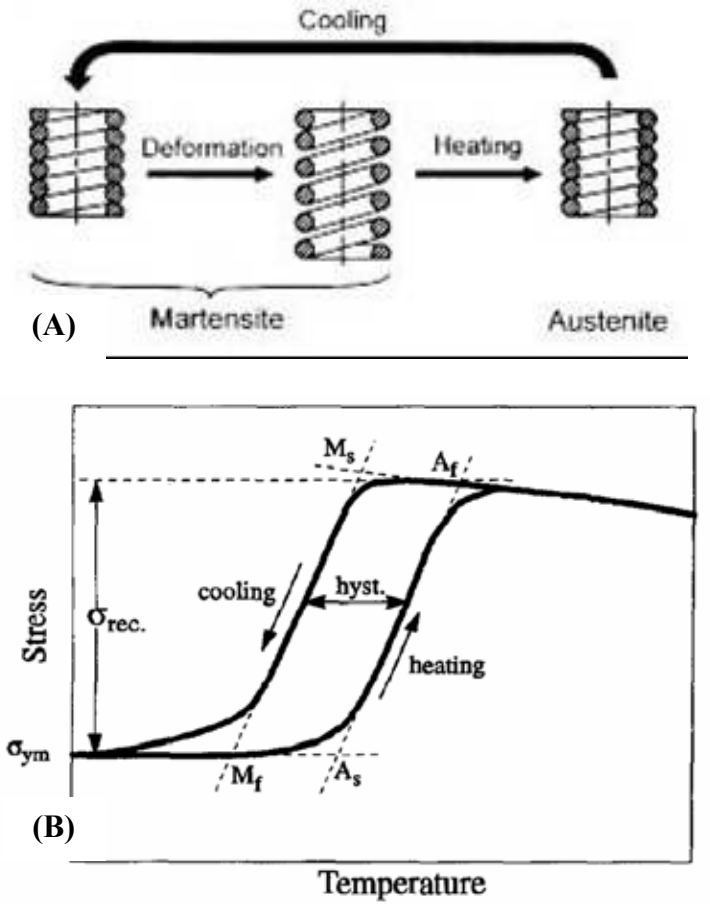

Figure 1. 30. (A) Principle of the shape memory actuator, where the spring recovers its original strain on heating above the transition temperature [68]. (B) Stress plotted as a function of temperature for NiTi material, indicating the recoverable stress resulting from the phase transformation. On heating, A_s is the beginning of the austenite transformation and A_f the final temperature, and on cooling, M_s indicates the onset of transformation to martensite and M_f the end of transformation [69]

1.5.6 Shape Memory Alloy Actuation

Shape memory actuators are reviewed by Buttgenbach *et al.* [68]. The shape memory effect as illustrated in Figure 1.30, is due to a crystalline transformation between a high temperature austenite phase and a low temperature martensite phase. The desired shape is memorized in the material at higher temperature, and when cooled below the

transition temperature the high ordered austentite state is transformed into the twinned martensite structure which can be easily deformed.

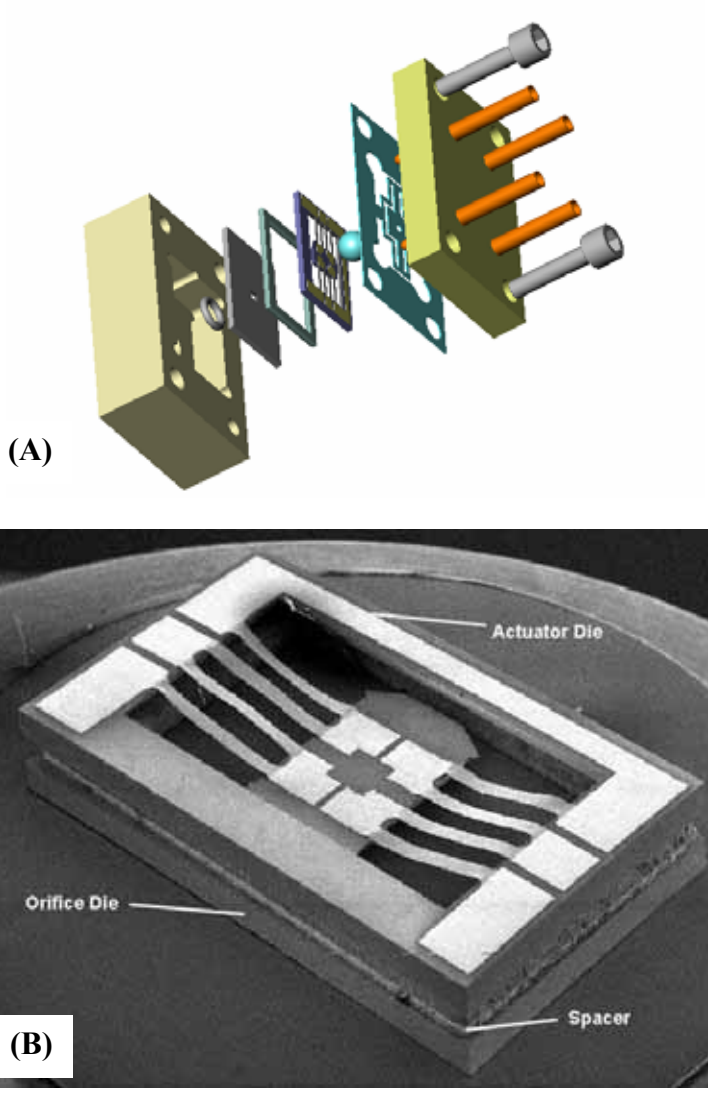

Figure 1.31. (A) Assembly of the micromachined components a TiNi Alloy Company microvalve. The beryllium-copper spring pushes a sapphire ball against the silicon over the spacer to close the flow orifice. Resistive heating of the NiTi spring results in results in recovery of the original undeflected state, hence moving the silicon back from the orifice and allowing flow [70]. (B) Actuator and orifice die after assembly

The mechanism is illustrated in Figure 1.31, in which the spring shows transitions above room temperature. SMA actuators offer high force capability and have been developed widely for microgrippers, artificial muscle actuators and can be supplied in wire or thin film foils. The foils can be laser cut or chemically etched into geometries useful for microactuators. Actuators based upon this effect can have various geometries, some of which are shown in Figures 1.31 - 1.33. There are many materials that exhibit the shape memory effect, and in particular NiTi alloy, know commercially as Nitinol is commercially available. More recent work on micro-shape memory actuators is reported by Kreulevitch *et al.* [69] and Johnson [70]. The use of NiTiCu alloys provides a higher recoverable stress as compared to the Nitinol alloy. A review of such an actuation for MEMS applications is provided by Wolf and Heuer [71].

The early work on this type of valve actuator in thin film format led to the first commercial microvalve from the TiNi company Johnson [72] see Figure 1.31. The power consumption is 0.5 W and the actuator is assembled onto the microfabricated flow channels such that a sapphire ball applies the pressure to the close the flow channel. An external actuator was employed by Kahn *et al.* [73] that deflects a diaphragm structure, as shown in Figure 1.32. The modulation of flows of nitrogen and water have been demonstrated at flow rates of lpm. Power consumption is approximately 100 mW for the $8.4x8.4mm^2$ valve. A miniature pinch valve developed by Pemble and Towe [74] in which the SMA wire squeezes down onto a thin-walled silicone tube effectively blocking the flow. The device although simple provides flow regulation at current levels between 260 and 320 mA with a maximum pressure of 3 psi. (20kPa).

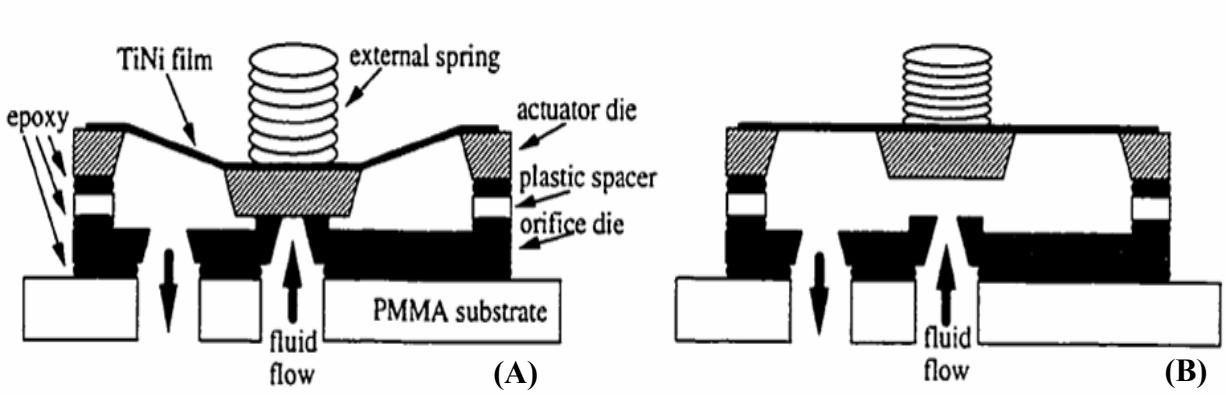

Figure 1.32. Schematic of the SMA actuated microvalve, (A) in normally closed state [73]. (B) In open state.

Thin foil based SMA actuated microfabricated membrane valve has been studied in detail by Kohl *et al.* [75, 76, 77]. A study of the possible size effects on the transformations was carried out down to foil thicknesses of 20 μm, which revealed enhance transformation hysterisis and strain [78]. Gas microvalves are shown in Figure 1.33 where a polyimide spacer defined the deflection of the membrane and tension in the SMA film prior to actuation.

Kohl *et al.* [79] used cold rolled films of NiTi (20 μm thick) and sputtered TiNiPd and TiNiCu (10 μm thick) which have phase transformations near room temperature over the range 30 to 120^{o}C. Magnetron sputtering was used for fabrication of the films of 10 μm thickness control of stoichiometry that is critical in defining the transition temperature, here mainly influenced by the amount of Pd in the film. Figure 1.34 shows data for the flow rate as a function of the pressure and applied temperature rise in the SMA actuator. The valves operated with a maximum pressure difference of 250 kPa and flow of up to 360 sccm.

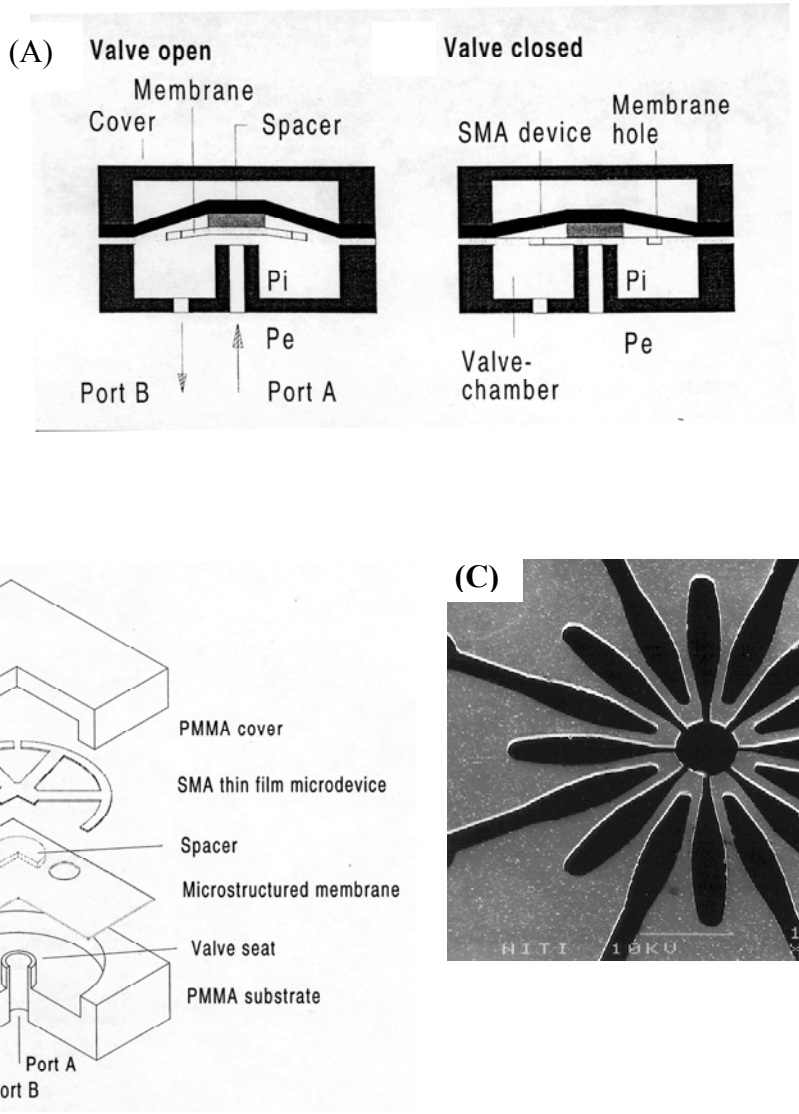

Figure 1.33. (A) Operating principle of SMA microvalve [78]. (B) Schematic cross section of a thin-film SMA microvalve [78]. (C) Photograph of the etched thin-film NiTi alloy SMA actuator, 2 mm diameter

1.5.7 Hydrogel Actuation

The actuation of the Beebe [80] and Yu *et al.*, [81] microvalve is due to the response to the changes in the concentration of specific chemical species in an external liquid environment. Baldi [82] made a valve that consists of a hydrogel disc sandwiched between porous plates and a flexible silicone rubber membrane. The swelling of the

hydrogel that is produced by diffusion of chemical species through the porous plate results in the deflection of the membrane and closure of the valve intake orifice. Baldi's valve is based on a phenylboronic acid hydrogel and it is used to construct a valve that responds to changes in the glucose concentration and pH. However the response time is comparatively slow, with the most rapid time response achieved being 16 minutes, using a 70 μm thick hydrogel and a 60 μm porous back plate.

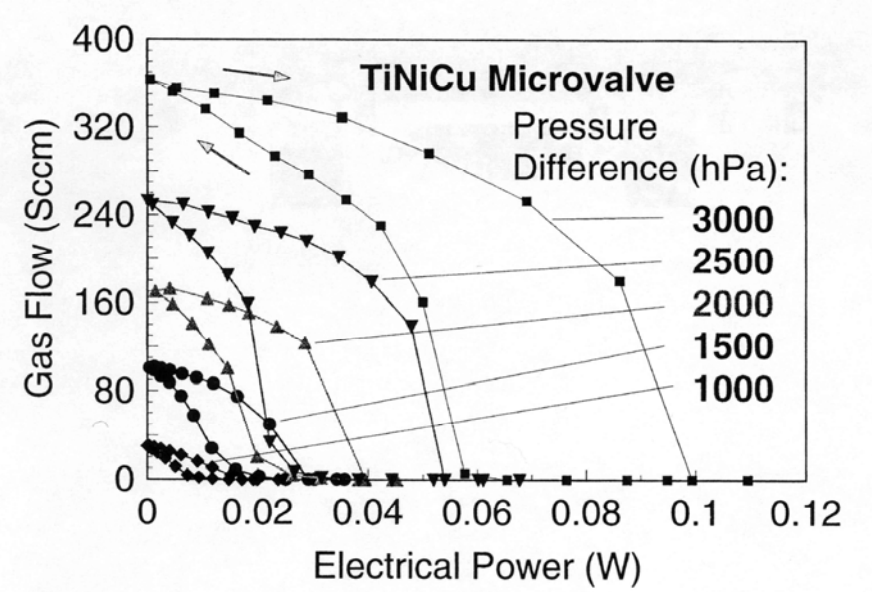

Figure 1.34. Gas-flow characteristics of a TiNiPd thin-film microvalve [79]

Robin H. Liu [83] has developed a valve based on hydrogel actuation, which has the closing and opening time on the order of several tens of seconds, and can operate at a differential pressures as high as 300 kPa. Figure 1.35 shows the data collected after a 30 s reaction in a 2-D valve implemented in a 300 μm wide channel. Figure 35B shows a schematic diagram of the 3-D valve that can route fluid in the miniature analysis system.

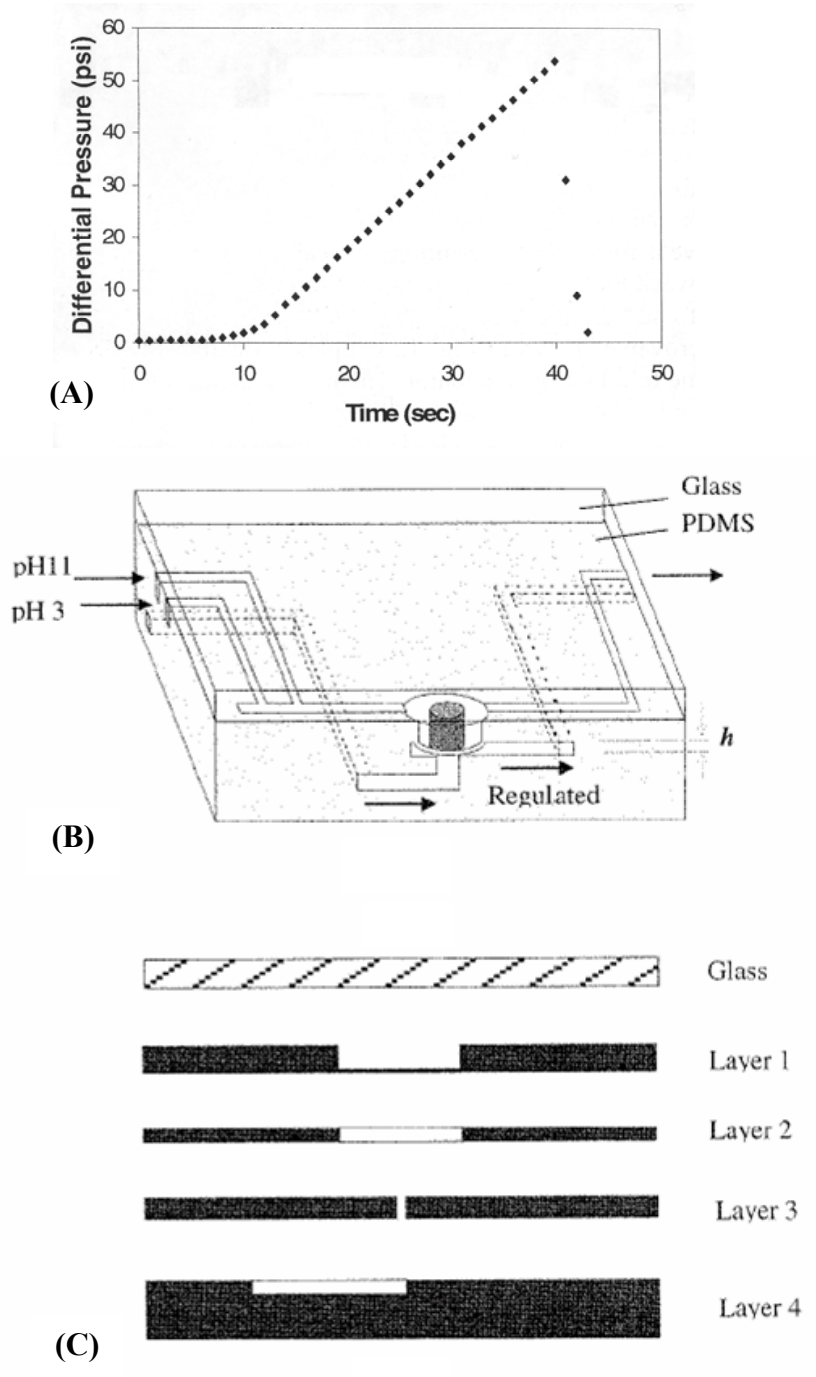

Figure 1.35. (A) Pressure drop measurements for a 2D post valve to illustrate the response time and the pressure after the swelling process. The transition to a linear response takes about 12 s, indicating valve closure. At 41 s the pressure dropped substantially owing to the failure of the external tubing connections in the experiment. (B) Schematic diagram of the D hybrid microvalve and (C) PDMS multilayer stacking method of fabrication [83]

CHAPTER 2

MICROVALVE DEVELOPED IN THIS RESEARCH

2.1 Introduction

Chapter 1 has given detailed discussion about the fluid flow in the microvalve and several different kinds of actuators for microvalves. Obviously, the choice of an actuator is very important to meet the design parameters of the microvalve. This chapter discusses the function of the fabricated microvalve and the challenges of the microvalve developed in this research.

2.2 Function of the Microvalve

The microvalve developed in this PhD research is proposed to be a part of a complete fuel cell system as shown in Figure 2.1 below [10]. As shown in Figure 2.1, the complete fuel cell unit has three main components: a pressurized chamber, a microvalve, and a micro fuel cell. The chamber holds a pressurized mixture of water and methanol fuel; it has an integrated constant force spring that delivers the fuel to the micro fuel cell at a constant rate.

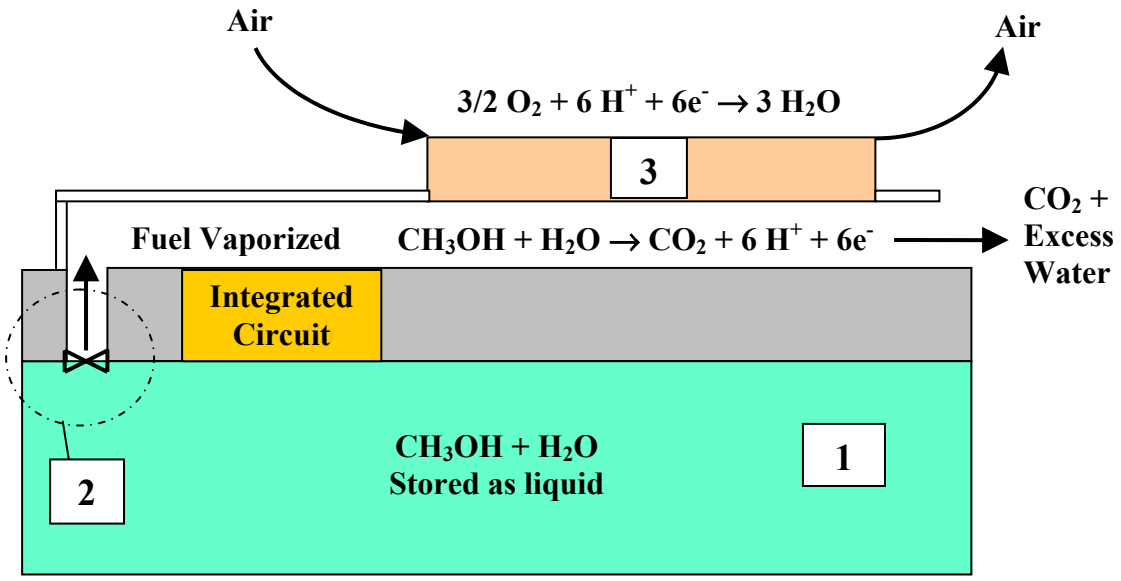

Figure 2.1. Schematic of a complete fuel cell unit [10]; it consists of three main parts: 1 = a pressurized chamber, 2 = A microvalve; 3 = fuel cell microchannels

The function of the microvalve is to control the fuel flow from the pressurized chamber to the micro fuel cell channels by opening or closing its membrane. The microvalve should deliver the fuel of diluted methanol and water, at 1 – 2 Molar concentration, at the flow rate of 1 μL/min for the power production ≈ 10 mW [120].

Since the energy produced from the fuel cell unit is used to charge a battery unit, the frequency of the microvalve operation is low. There are two types of operation for the microvalve:

1. The microvalve is required to open the flow from the pressurized chamber for the first time and then the fuel is delivered to the micro fuel cell to charge a battery unit. The initial power is provided from an external resource, not from the fuel-cell unit to close the microvalve when the fuel chamber is installed. The flow continues until the fuel chamber is empty. For this kind of application, the microvalve should not consume

any power when it is fully open. Thus, for this operation it is required an on/off and normally open microvalve.

2. The microvalve is to open the fuel flow for the first time, once the fuel chamber is installed, and then to close the flow when the battery is fully charged. The elapse time between open and close operations can be in the duration of several days. For this kind of application, the microvalve should not consume any power when it is fully open or closed. In addition, for opening or closing the flow the microvalve should consume a minimum energy, at sufficient time for the membrane to latch or unlatch respectively. Thus, for this operation a latching microvalve with bistable positions is required.

Because there are two different microvalve operations as explained above, two types of microvalve are designed in this dissertation: 1 = an on/off and normally open microvalve; and 2 = a latching microvalve with bistable positions.

2.3 The Design Parameters of the Microvalve

The microvalve is designed for integration with the fuel cell unit, where power is the final product. Thus, the design parameters for the microvalve are:

1. Has to be inert and non-reactive in the operation

The chemical reaction inside the microchannels of the fuel cell, as shown in Figure 2.1 produces electrical power. It is not desirable to have any reaction or phase change in the microvalve operation. This requirement eliminates the possibility of using a

thermally actuated microvalve because the heating process from the heating element/electrode may introduce an additional heating in the fluidic flow. Other actuators that may be suitable for the microvalve are electromagnetic, piezoelectric, and electrostatic actuators.

2. Fabrication process has to be CMOS compatible

One of the biggest challenges in the microvalve design is to have its fabrication process be CMOS compatible. The microvalve has to be entirely fabricated by bulk or surface micromachining processes and the fabrication temperature must be less than 400 °C [84, 54]. More details regarding this issue are discussed in Chapter 5, section 5.2.

3. Fabricated on a single wafer process

Most of the currently developed microvalves fabricated by surface micromachining involve the bonding of two or three wafers together to make the fluidic connections and the valve structure. Wafer bonding is generally not desirable for a microvalve that is used to control fluidic flow in a chemical analyzer, microchannels, or fuel cell. In this research, the microvalve must be fabricated on a single wafer that is the same wafer as the fuel-cell microchannels and other electrical circuits. More details regarding this issue are discussed in Chapter 5, section 5.2.

4. Minimum power consumption

Since the valve is a part of the fuel-cell unit, the power and energy consumption of the microvalve has to be as minimal as possible. The fuel-cell is designed for

generating power in the order of 10 mW [120] and the energy could be stored inside a battery unit. As mentioned before, because the frequency of the microvalve operation is pretty low, the duration between the opening and the closing time can be several days. In order to achieve minimum operational energy, the time required to open or close the microvalve should be minimal, in the order of ms. In this research, the microvalve is proposed to have the power consumption of 1 – 2 W for the on/off and bistable microvalves. The energy consumption of the bistable microvalve should be less than 20 mJ with the latching/unlatching time of several ms; this energy consumption can be supplied from the charged battery unit.

5. Minimum clogging effect due to impurities

There is always the possibility of some impurities in the fluid. For MEMS application, the impurity or particulate sizes may vary depending upon the application and the fluid type. A good microvalve should be designed to have an adequately large opening to prevent the clogging caused by the impurities. At the same time, valve size should be small for MEMS applications, since a large deflection in a small and compact volume will provide good characteristic in terms of the volumetric efficiency [55]. Generally, for a highly purified liquid flow, with the particulate size of less than 1 μm requires a microvalve opening of more than 10 μm [28, 55].

6. Low closing/opening time for the membrane/actuator

In most MEMS application, long closing and opening times for the microvalve are not desired. In the spacecraft application, the opening/closing speed has to be less

than 2 s [28]. Equal time for valve opening/closing may also be important in some other applications. For thermal actuated or hydrogel micro valve, this condition is generally does not exist. It can be achieved by other actuators such as piezoelectric, electrostatic, or electromagnetic actuator.

7. Capable to function at different environmental condition

There are other design parameters that can be considered for the microvalve design, which depend on the environmental condition of the operation. Since the microvalve is in function for a fuel cell unit, it may subject to minor shock, vibration, and temperature fluctuation.

2.4 Electromagnetic Microvalve

Selecting an actuator is an important part of the microvalve design. Table 2.1 below shows the summary of the advantages and the disadvantages of different kinds of actuators for the microvalve, which were discussed in Chapter 1. After careful consideration, the electromagnetic actuator was selected for the microvalve. The reasons for this selection are as follows: it has large displacement, CMOS compatibility, non-reactive operation, and fast actuation. Prior work on electromagnetic bidirectional actuator with the size of 6 mm x 1 mm has shown a large actuation in the order of ± 80 μm [54]. Thus electromagnetic actuator is suitable for the microvalve.

The electromagnetic microvalve structure can be fabricated by electroplating at low temperature and it is CMOS compatible. Soft magnetic material such as NiFe has

been widely used to fabricate MEMS devices and it can be electroplated at room temperature; more details are discussed in Chapter 5.

Unlike the thermal actuator that introduces local boiling to the working fluid and the hydrogel operated microvalve that is very sensitive to the environment changes. The electromagnetic operation is generally inert and non-reactive.

The response time of the electromagnetic force is very fast. It is reported in [56], that the electromagnetic response of less than 100 ms is achieved to open/close a microvalve that operate to control the flow of water.

Table 2.1. The advantages and disadvantages of different type of actuators

Type of Actuation	*Advantages*	*Disadvantages*
THERMAL	The amount of deflection can be adjusted from the amount of power inputted to the heating element.	Power consumption can be large and not applicable for application where the energy consumption is limited
	It is simple, basically the elongation of material due to the thermal expansion give the actuation to the membrane.	The thermal expansion may cause loosening to the support, which may introduce some leaking
	It can be integrated with the memory shape material in order to give pre-stress on the membrane for increasing closing force. [8]	The valve closing time may not be the same as the opening time
	Using the optimization of the flow back-pressure in closing the valve reduces the leaking possibility and improved the device crushing pressure.	The heating to fluid may not be applicable to some MEMS application. It may introduce some local boiling on the electrode.
PIEZO-ELECTRIC	Flexible, the amount of membrane deflection can be adjusted from the amount of potential voltage applied to the piezoelectric material.	It requires high power consumption. Recent piezoelectric valves require continuous power to keep the valve in the open/close position.
	It is pretty stable in the environmental condition that involves high thermal fluctuation, shock, and vibration. It may produce a reliable micro valve suitable for heavy-duty application.	It generally produces a small amount of deflection at a given amount of voltage.
	Typical piezoelectric disk requires high voltage to produce substantial deflection, the laminated piezostacks may mitigate this concern to produce larger displacement	The structure and fabrication processes may be complex, it requires enormous amount of time in to produce a reliable fabrication.

Table 2.1. (Continued)

ELECTRO-STATIC	It is simple in the structural system; the required components are not complex.	The electrostatic force is typically small. The greater the applied voltage, the greater the force is, but one has to be careful with the break down voltage.
	The response time to close and opening the valve is generally very small (~ms) when the gap distance is small (< μm)	The actuation distance is typically small (< 5 μm). Small distance between the membrane and insulation layer increases the clogging possibility.
	Force generated when the membrane touches the insulation layer is extremely large; this produces a high sealing force for a normally open valve.	The actuator dimensions are typically large to produce large deflection, this contradict to the MEMS application, where a small device is required.
THERMO-PNEUMATIC	Very flexible and adjustable, the amount of deflection can be adjusted from the amount of power given to the heating element. This gives the utilization for a variable valve.	The response time is very long for both opening and closing the valve. This valve is not suitable for high frequency cycle operation.
	Large displacement can be developed in a small valve package, since the fluid restriction (clogging) can be avoided.	Heating to the fluid may not be applicable to some application. Fluid with low boiling point, e.g. water, may experience local boiling.
	The implementation of the bistable principle is feasible and indicates a significant reduction in the power consumption [7].	The change in the vapor pressure of the fluid inside the chamber due to overheating by the heater may cause permanent damage to the membrane.

Table 2.1 (Continued)

ELECTRO-MAGNETIC	It can be integrated with other actuation techniques, such as pre-buckled membrane for bi-stable conditions [9] that may reduce the power consumption.	The design may be neat and complex, particularly for the membrane that involves bi-stable positions.
	It is flexible; the amount of actuation force depends on the amount of current applied to the coil. Large actuator-displacement and smaller closing time can be achieved by inputting bigger current.	The permanent magnet is usually demagnetized over the life of the application.
	The time required to open and close is similar; this is useful for the application where a reliable and exact closing time is required.	The magnet saturation of the structure limits the maximum amount of force produced by the coils.
	The combination between a permanent magnet and coils may increase the crushing pressure of valve. This is useful for the high duty valve, which expose in closing high-pressured fluid.	The application of the permanent magnet fabricated by traditional method may require a heat treatment up to the temperature of 600 °C to create magnetic anisotropy.
HYDROGEL	There is no power consumption is required and suitable for application of drug delivery or other chemicals on demand	The volume change of the Hydrogel is diffusion-limited and exceedingly slow when the path length us large
	Environmentally sensitive Hydrogel offer unique opportunities for active flow control in micro flow systems	Since it is relying on the change in environmental and chemical condition. It is not widely applicable for all applications
	The actuation dimension is extremely large can more than 100 μm	Because it is sensitive to the environmental condition. The opening/closing time may not be consistent through the operation life

CHAPTER 3

BASIC PRINCIPAL OF THE DEVELOPED MICROVALVE

3.1 Introduction

This chapter discusses the basic principal of the microvalves operation that are developed in this research. There are two types of microvalves: an on/off microvalve and a latching microvalve with a bistable mechanism. This chapter discusses about the main parts of each microvalve, the basic operation, and the basic design. At the end of this chapter, the bidirectional microactuator is also discussed.

3.2 On/Off Microvalve

3.2.1 Schematic of the On/Off Microvalve

The schematic of the on/off microvalve is shown in Figure 3.1 below. It shows that the microvalve consists of 7 main components: 1 = inlet orifice; 2 = base of the microvalve; 3 = gold (Au) microcoil; 4 = outlet orifice; 4* = gasket (which is the center of the microcoil); 5 = circular support; 6 = centered soft magnetic dome; 7 = membrane supported legs. In order to achieve an efficient magnetic circuit, all components of the microvalve, except the microcoil, are made of soft magnetic materials.

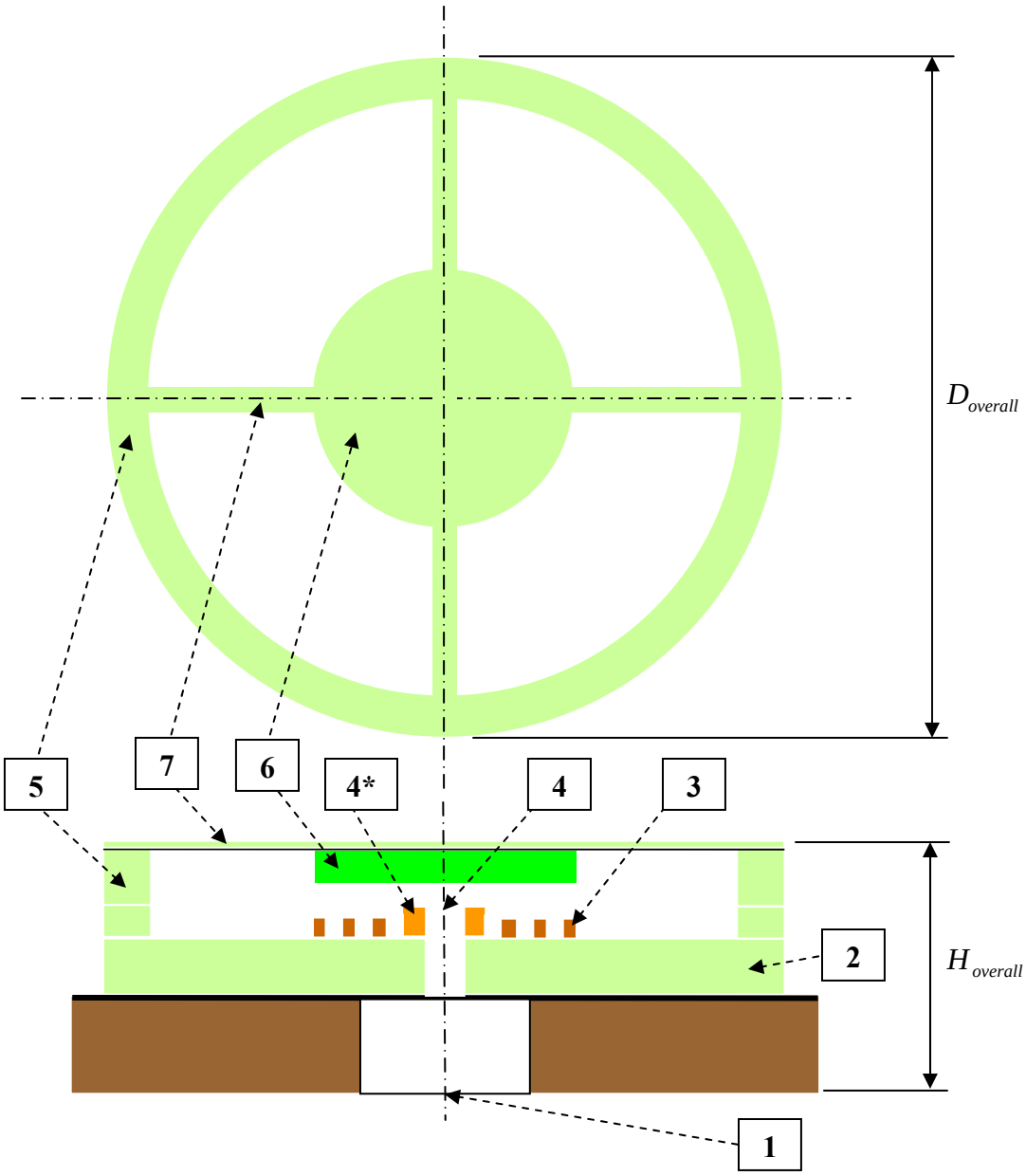

Figure 3.1. Schematic of the on/off electromagnetic microvalve; 1 = Inlet orifice; 2 = base of the microvalve; 3 = microcoil; 4 = Outlet orifice; 4* = Gasket (which is the center of the microcoil); 5 = Circular support; 6 = Center soft magnetic dome; 7 = Membrane supported legs. The components no. 6 and 7 forms the microvalve membrane.

Three different sizes of on/off microvalve have been built, with the overall diameter ($D_{overall}$) of 1,000, 1,500, and 2,000 μm. The overall height of the microvalve ($H_{overall}$) is approximately 600 μm including the thickness of the silicon substrate. The

microcoil is located at the center of the microvalve base. The center of the microcoil defines the microvalve gasket. The gap (g) distance between the bottom of the soft magnetic dome and the top surface of the microcoil is in the range of 12 – 20 μm. This defines the actuation distance where the membrane moves.

3.2.2 Basic Principal of the Mechanism

The basic mechanism of the on/off microvalve is shown in Figures 3.2a and 3.2b below. The microvalve is initially open, where the membrane is separated from the microcoil by a gap (g) distance in the range of 12 – 20 μm, depending on the design. There is no input current is required to the microcoil (I_{coil}) at this stage. The fluid from the pressurized chamber freely flows from the inlet orifice to the outlet orifice and then flows beneath the membrane. The fluid is then gathered and connected to the microchannels of the fuel cell.

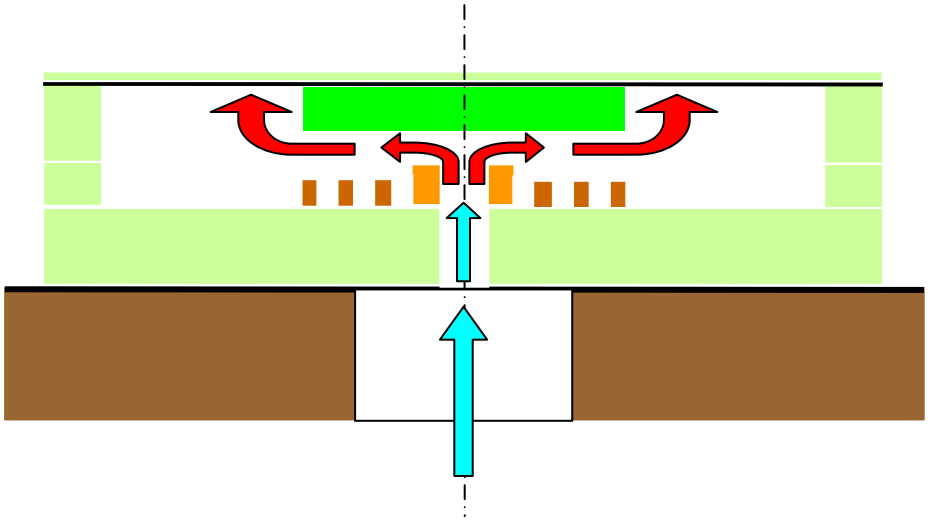

Figure 3.2a. The valve is normally open and there is no input current to the microcoil (I_{coil}). The fluid flow from the inlet orifice (blue line) to the outlet orifice and beneath the membrane (red line)

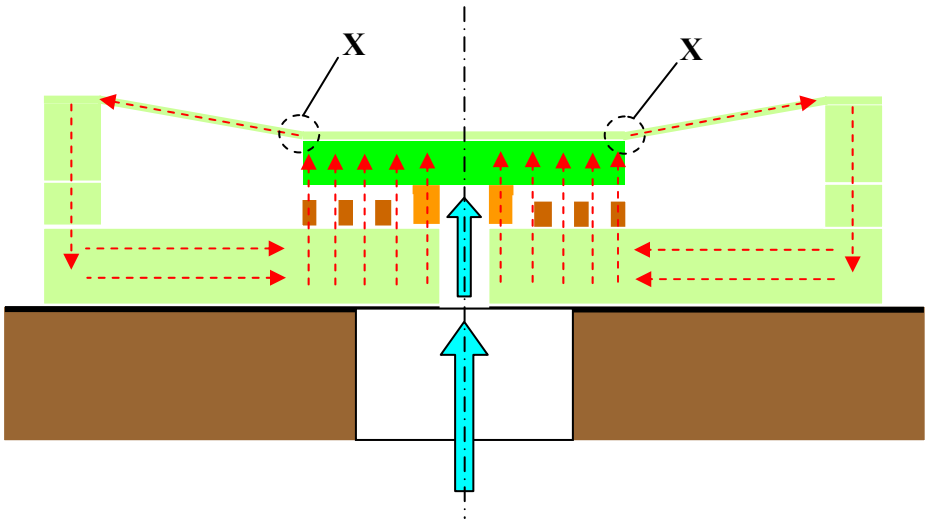

Figure 3.2b. Current (I_{coil}) is drawn to the microcoil and it produces an electromagnetic force that deflects the membrane downward. When the bottom of the membrane touches the gasket, the fluid flow is choked, e.g. the valve is closed. A closed loop electromagnetic field is formed when the valve is closed.

In order to close the valve, an electric current (I_{coil}) is input to the microcoil. The electric current (I_{coil}) produces an electromagnetic force (F_{EM}) that deflects the centered soft magnetic dome downward and closes the microvalve. The flow is then choked as the outlet orifice is closed. For the micro fuel application, the on/off microvalve is closed when it is required to charge the fuel inside the pressurized chamber or when the pressurized chamber is installed to the microvalve for the first time. When the valve is closed, current (I_{coil}) is continuously drawn to the microcoil and a close loop magnetic circuit is formed inside the microvalve structure. Close loop magnetic circuit means that all the magnetic field is directed inside the soft magnetic material structure, minimizes the possibilities of magnetic leakage through the air gap. A closed loop magnetic structure, as shown in Figure 3.2b minimizes the magnetic reluctance, which is equivalent to the electrical resistance in the electric circuit, this consequently increases

the efficiency of the magnetic flux in producing electromagnetic force that closes the microvalve. As shown in Figure 3.2b that the electromagnetic field produced by the microcoil flows to the centered soft magnetic dome; then flows through the membrane supported legs, the circular supports, it is finally collected in the microvalve base.

In the closing position of the microvalve as shown in Figure 3.2b, a small amount of magnetic field may also be presented in the air gap between the membrane supported legs and the base, however the majority of the field is properly guided by the soft magnetic structure of the microvalve.

In order to open the valve, the electric current to the microcoil (I_{coil}) is turned off. This stops the production of the electromagnetic force. The spring force of the membrane supported legs (F_S) moves the membrane upward back to its initial open condition.

3.2.3 Membrane Design with Centered Dome and Overhanging Leg

The membrane is an important part of the microvalve. The membrane's design is certainly challenging. It should be stiff enough to prevent buckling that is caused by the stresses arising from the fabrication process, and at the same time it should not be too stiff so that the electromagnetic force is insufficient to deflect the membrane. In order to achieve both requirements, the membrane is designed in such away that it consists of a centered soft magnetic dome as shown in Figure 3.1 that is supported by four legs comprising cantilever beams. The center dome is much thicker than the supported legs to prevent overstressing from the fabrication process. The thickness of the centered soft magnetic dome (t_1) is designed to be in the range of 10 – 15 μm. Meanwhile the thickness

of the membrane supported legs (t_2) is in the order of 3 μm. Because the center dome is much stiffer than the supported legs, it remains flat during its movement from the initial open position to the closed position and vise versa as shown in Figure 3.2a and 3.2b, at the same time the supported legs rotate on the so-called pin joint "X" as shown in Figure 3.2b during its downward movement.

3.2.4 Circular Microcoil for Magnetic Actuation

As shown in Figure 3.1, a circular membrane is implemented in the microvalve structure. The microcoil is patterned to define circular turns and it is designed with a rectangular cross sectional area. Different coil sizes, e.g. height (H) and width (W) and the number of coil turns (N_{coil}) are modeled in ANSYS 5.7 to obtain the best coil geometry; more details are discussed in Chapter 4, section 4.1.3. As shown in Figure 3.1, the center of the microcoil defines the microvalve gasket and the outlet orifice. In order to achieve an efficient magnetic field flow, from the microcoil to the center soft magnetic dome, the maximum number of coil turns is limited by the projected area of the centered dome. Additional coil turns outside the perimeter of the centered dome have less efficient coupling and produce little additional magnetic field.

3.2.5 Soft Magnetic Material Selection

Before a description of the magnetic materials used in MEMS and in particular for the microvalve, the units and fundamental equations of magnetism must first be

discussed. The relationship between magnetic field, H and magnetic flux density, B in free space is denoted by Equation 3.1:

$$B = \mu_0 . H \qquad (3.1)$$

With permeability of the free space is $\mu_0 = 4.\pi.10^{-7}$ V.s/A.m. The MKS units of the magnetic field are A/m and an older unit still commonly used is oersteds, which is 79.577 A/m = 1 Oe). The MKS units of the magnetic flux density are V.s/m^2 or Tesla (T) and an older unit still commonly used is gauss, which is (1 T = 1 V.s/m^2 = 10,000 gauss (G)). When the magnetic fields and flux densities of interest are inside magnetic materials, the equation of the free space must be adjusted to account for the magnetization, M, of the material. There are many forms of this equation, but one used here is:

$$B = \mu_0 . H + M = \mu_r.\mu_0 . H \qquad (3.2)$$

With relative permeability, μ_r, and the units of M are the same as B. Magnetic materials can be classified according to their magnetic susceptibility $\chi = M/H$ and relative permeability, $\mu_r = (\chi / \mu_0 + 1)$ into several categories: ferromagnetic, ferrimagnetic, anti ferromagnetic, paramagnetic, diamagnetic, and superconducting materials. Listed in Table 3.1 below is typical range of χ/μ_0 for each category of magnetic material and examples of each are identified [85].

Of those listed in Table 3.1, ferromagnetic materials have been found to be the most useful in magnetic microsensors, microactuators, and microsystems. When ferromagnetic materials are magnetized, demagnetized, and re-magnetized, they exhibit a hysteresis behavior as shown in Figures 3.3 and 3.8. Ferromagnetic materials can be divided into so-called soft magnetic materials (i.e. with small coercivity and low

saturation field) and hard magnetic materials (i.e. with a large coercivity and high saturation field)

Table 3.1. Magnetic material classification [85]

Category	χ/μ_0	Examples
Ferromagnetic	10^7 to 10^2	Ni, Fe, Co, NiFe, NdFeB
Ferrimagnetic	10^4 to 10^1	Fe_3O_4, ferrites, garnets
Anti ferromagnetic	Small	MnO, NiO, FeCO3
Paramagnetic	10^{-3} to 10^{-6}	Al, Cr, Mn, Pt, Ta, Ti, W
Diamagnetic	-10^{-6} to -10^{-3}	Ag, Au, C, H, Cu, Si, Zn
Superconducting	-1	$YbBa_2Cu_3O_x$

As mentioned before, in order to form a close loop magnetic circuit, all components of the microvalve, except the microcoil, are made of soft magnetic materials. A proper selection of the soft magnetic material is very important. An ideal soft magnetic material should have an infinite magnetic saturation (B_S) and zero coercivity (H_C) and zero hysteresis. Figure 3.3 shows the B-H curve for a soft magnetic material. It is preferable to select a soft magnetic material that has large B_S and small H_C, and also a material that can be fabricated by surface micromachining.

The most commonly used soft magnetic materials are NiFe alloys (e.g. permalloy or orthonol). The combination of relatively high saturation flux density (B_S), low hysteretic losses, and near zero magnetostriction (i.e., stresses in the device will not impact its magnetic performance) has driven their use in macroscopic and microscopic

sensors, actuators, and systems. Perhaps the most significant reason for their common use in magnetic MEMS is that these materials are used in magnetic recording heads and the technologies necessary for depositing and micromachining them have been well developed by that large industry [85]. Table 3.2 below shows the magnetic [86, 87] and mechanical [88] properties of some soft magnetic materials that can easily be deposited on the patterned photoresist mould by electroplating.

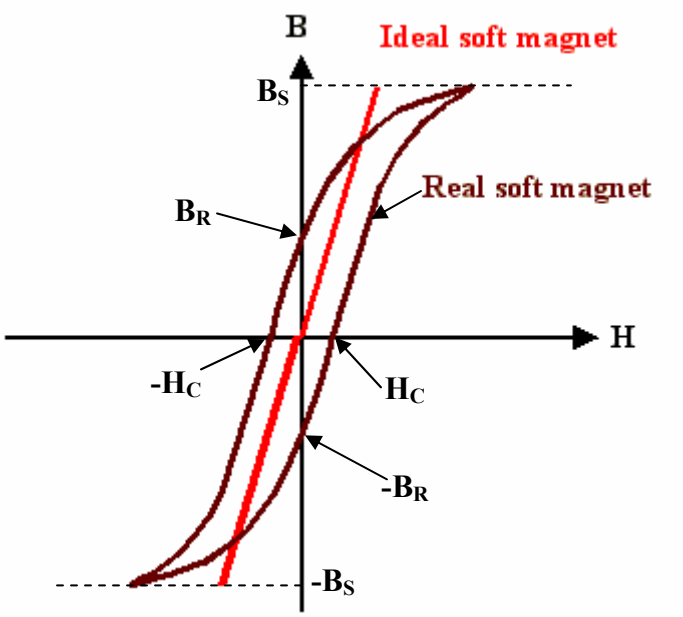

Figure 3.3. The B-H curve for a soft magnetic material

As shown in Table 3.1, permalloy and orthonol are more likely to be the candidates for the soft magnetic materials to build the valve structure because they have relatively high magnetic saturation (B_S) and small coercivity (H_C) compared to cobalt alloy, CoFeCu. Permalloy and orthonol have been as the soft materials for the microvalve

structure; they can easily be fabricated by electroplating at or near temperature (< 60 °C). For more details regarding the fabrication of the microvalve are described in Chapter 5.

Table 3.2. Properties of some soft magnetic materials [86 – 88]

Alloy	**Composition**	**Magnetic Saturation (B_S)**	**Coercivity (Oe)**	**E (GPa)**	**Yield Strength (GPa)**	**Ultimate Strength (GPa)**
NiFe, Permalloy	80% Ni, 20% Fe	0.9	0.65	65	0.93	1.034
NiFe, Orthonol	50% Ni, 50% Fe	1.41	1.3	119	0.73	0.62
CoFeCu	85% Co, 10% Fe, 5%Cu	1.8 - 2	4	-	-	-

3.3 Bistable Electromagnetic Actuated Microvalve

3.3.1 Introduction

The bistable mechanism is introduced for the microvalve operation in order to reduce the energy consumption. The membrane has two stable positions, the open and the closed positions. There is no input current (I_{coil}) that is required to maintain the membrane at either position; Contrasted with the on/off microvalve that has only one stable position, which is the open position, and continuously requires power to maintain its closed position. This section discusses two different methods used to achieve a bistable mechanism, their advantages and disadvantages; and the selection between these two methods for the operation of bistable microvalve.

3.3.2 Methods to Create Bistable Mechanism

3.3.2.1 Integrated Buckled Membrane

One method of creating a bistable mechanism for the microvalve operation is to have a buckled membrane. Figure 3.4a to 3.4c below illustrates the idea for integrating a buckled membrane:

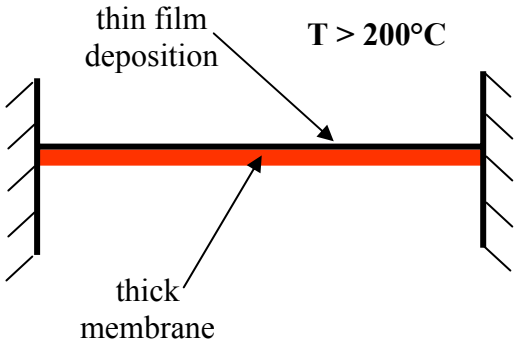

Figure 3.4a. Thin dielectric film under compressive stress is deposited on top of a membrane at high temperature. The membrane remains flat during deposition process.

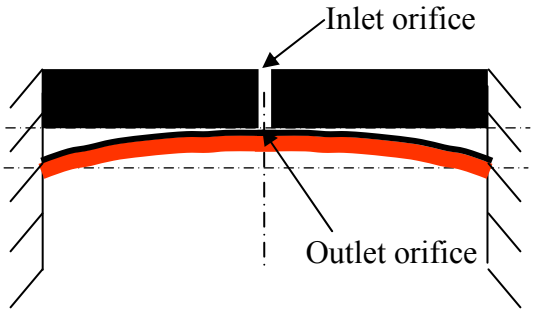

Figure 3.4b. When the membrane is brought back to room temperature, it buckles upward to accommodate the compressive stress in the film. This position is then called the 1st stable position of the membrane. This position is utilized to close the outlet orifice of the microvalve. There is no external force to maintain the membrane in this position.

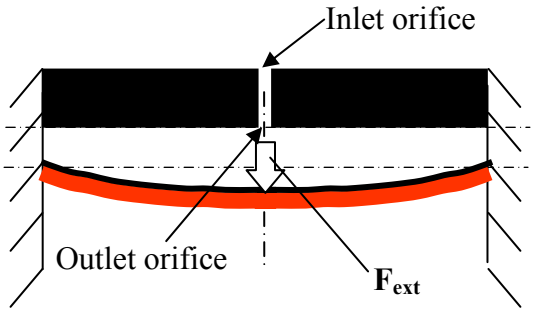

Figure 3.4c. In order to open the flow, an external force (F_{ext}) is applied to displace the membrane downward. Once the membrane come to its 2nd stable position, which is the symmetry of the 1st stable position in this case, no more force is required.

Based on the structural mechanics point of view, buckling is categorized as a type of failure that is caused by the loss of material stiffness and the occurrence of material instability [89, p740-741]. Buckling causes a beam or membrane to deflect in the lateral direction in order to come to the lowest energy state. Buckling can occur in the beam/membrane structure because of the large compressive stress. When the compressive stress is sufficiently large, the equilibrium of the beam is no longer straight but it is bent. Applying an external force to produce a buckled beam/membrane in the MEMS application is not desirable. However, the buckled membrane can be developed through design, as a result of the fabrication process. For example, two layers of bi-morph substrates at different thermal expansion coefficients (α_t) may buckle when one layer is deposited at higher temperature than the other one, i.e. the thermal stress causes the buckling.

Figure 3.4a above shows that a thin film (< 1μm) under high compressive stress (> 100 MPa) is deposited at high temperature (> 200 °C) on top of a membrane that is initially stress-free. Because of the intrinsic compressive stress in the film from the

fabrication process and the difference in the thermal expansion coefficients of the thin layer (α_L) and the membrane (α_B), e.g. $\alpha_L < \alpha_B$, the membrane is buckled upward when it is brought back to the room temperature.

The buckled membrane can be utilized for the microvalve operation. The membrane that is initially buckled upward as shown in Figure 3.4b can be used to close the outlet orifice and choke the liquid flow. This is called the first stable position. When an external downward force (F_{ext}) is applied, the membrane moves from the first stable position to the second stable position as shown in Figure 3.4c. This opens the flow of liquid; once the membrane arrives to the second stable position, no more external force is required. In this case, the second stable position is the symmetry of the first stable position. In order to bring the membrane back to the first stable position and choke the flow, an external upward force is required.

As shown in Figures 3.4b and 3.4c, an external force is required just to provide movement to open or close the orifice, there is no force required to maintain the membrane at the open/closed position. This bistable mechanism achieved by the buckling technique will save energy in the microvalve operation and appears quite feasible but is also complicated to control. It is a very challenging task to implement this technique for an electromagnetic microvalve, especially fabricated on a single wafer. The fabrication process can be very complex and does not seem to be feasible. The deposition process of the thin film at a temperature of more than 200 °C may cause some delamination of the microcoil and the soft magnetic structure.

3.3.2.2 Implementing a Permanent Magnet on the Membrane

As mentioned before, the electromagnetic force drives the actuation mechanism of the microvalve. A bistable mechanism can be developed for the microvalve operation by incorporating a permanent magnet on the membrane. This idea turns out to be the simplest way to implement the bistable mechanism utilizing the existing on/off microvalve, shown in Figure 3.1. Prior works [55, 56] have shown an integration of an external permanent magnet for bistable microvalve operation. Here, the external permanent magnet can be purchased separately and it can be attached on to the back of the silicon substrate, or attached on the actuator to produce a bistable mechanism. However, attaching an external permanent magnet on the back of the silicon substrate results in serious magnetic leakage, and an inefficient electromagnetic circuit that makes it hard to precisely control the membrane displacement. The serious magnetic leakage from the permanent magnet may also interfere with and could damage the electronic devices surrounding the actuator.

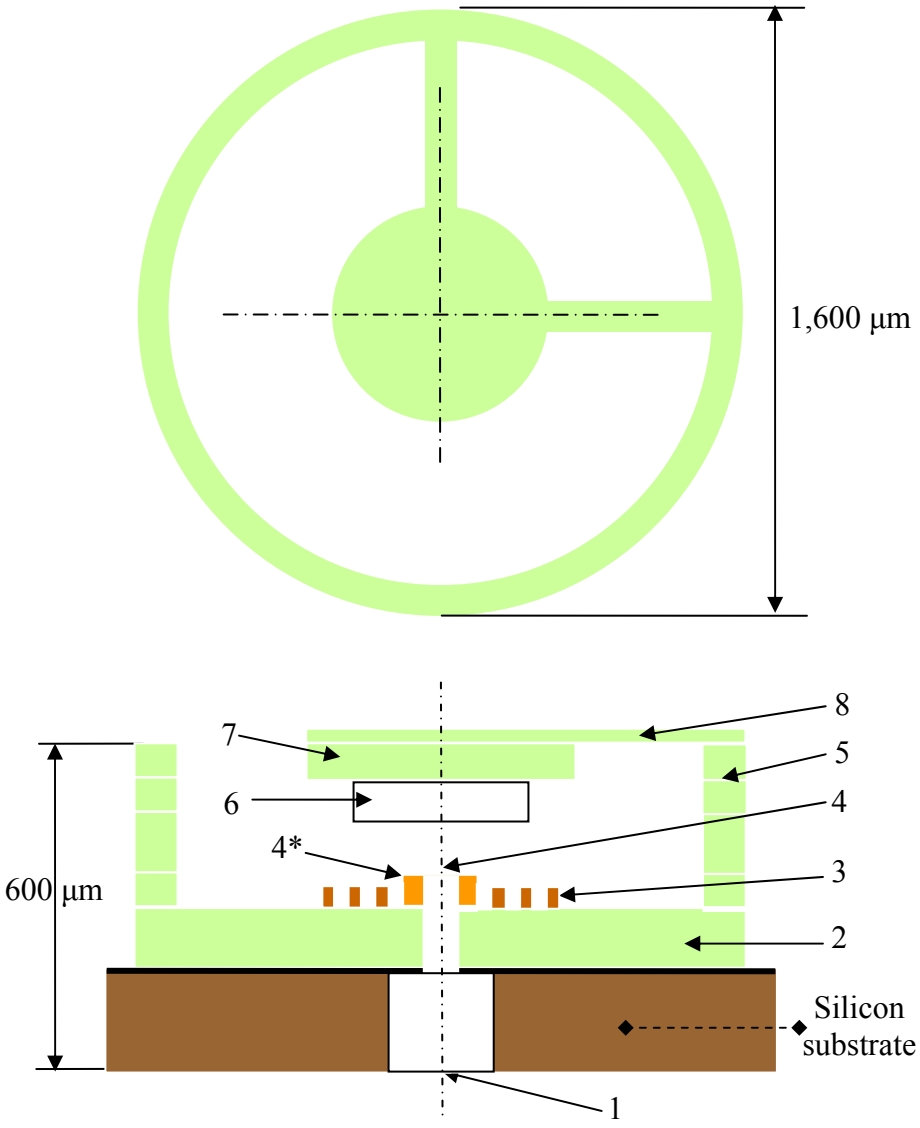

Figure 3.5. Schematic of the microvalve with bistable mechanism, implementing a permanent magnet on the soft magnetic dome, where: 1 = inlet orifice, 2 = base of the microvalve, 3 = Gold (Au) microcoil, 4 = outlet orifice, 4* = gasket (which is the center of microcoil), 5 = circular support, 6 = permanent magnet, 7 = center soft magnetic dome, 8 = 2 x 90° membrane supported legs. The microvalve has an overall diameter ($D_{overall}$) of 1,600 µm and the overall height ($H_{overall}$) of approximately 600 µm including the silicon substrate. The components no. 6, 7, and 8 forms the microvalve membrane.

In this research, the permanent magnet is incorporated on the center soft magnetic dome. This integration produces a very efficient electromagnet circuit that leads to the

lower power/energy consumption for the microvalve operation, and produces bidirectional movements for the membrane. More details regarding the bidirectional movement are discusses in section 3.4. A schematic of the bistable microvalve incorporating a permanent magnet is shown in Figure 3.5.

There are two possible ways to close and latched the microvalve's membrane as shown in Figure 3.5. The first one is to bring the membrane downward until it touches the microcoil, and latched because of the remanence force from the permanent magnet. The second one is to bring the membrane close enough to the microcoil and let the remanence force continuously pull the membrane downward, until it touches the microcoil and latches. In this PhD dissertation, the first latching operation is used for the design, and the details are shown in the following sections.

3.3.3 Bistable Mechanism

Figures 3.6a-3.6d below illustrate the mechanism of the bistable microvalve incorporating a permanent magnet, while Figure 3.7 describes the force versus membrane downward displacement diagram that characterizes the bistable operations.

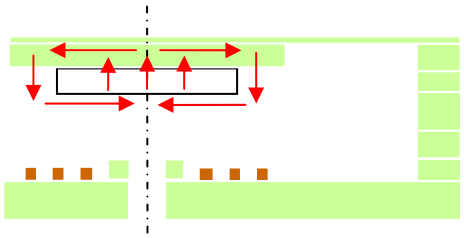

Figure 3.6a. Magnetic field produced by the permanent magnet in the 1st stable position, there is no input current (I_{coil}) to the microcoil required.

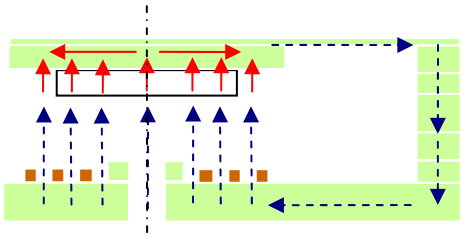

Figure 3.6b. Combined magnetic fields produced by the microcoil (dashed line) and the permanent magnet (solid line) just before membrane's downward movement. An input current (I_{coil}) is applied to the microcoil for a short time.

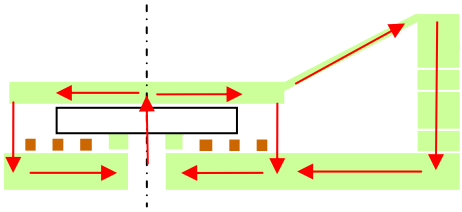

Figure 3.6c. Remanence magnetic field produced by the permanent magnet at the latching (2^{nd} stable) position. There is no input current (I_{coil}) to the microcoil required.

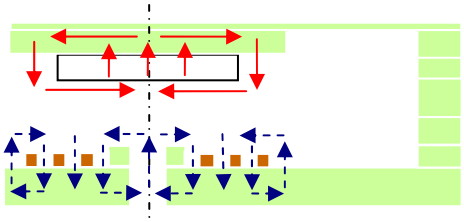

Figure 3.6d. Magnetic fields produced by the microcoil (dashed line) and the permanent magnet (dashed line), just after the membrane is unlatched. Both fields are at the opposite direction. There is an input current (I_{coil}) at the reversed direction as shown in Figure 3.6b applied to the microcoil for a short time.

Figure 3.6a shows that initially the membrane is flat (1^{st} stable position) when there is no current (I_{coil}) input to the microcoil. The remanence flux density (B_R) produced by the permanent magnet is not large enough to close the valve due to the large gap (g) between the membrane and the micro coil. This condition is shown by point A (1^{st} stable position) in Figure 3.7. The membrane is separated by a gap (g) distance,

which is designed to be 30 μm from the micro coil. This ensures that there is no clogging due to the presence of impurities that may be in the fluid. A slight downward movement, in the order of 0 – 1 μm, may be experienced by the membrane due to the remanence force. The membrane can not move further due to the remanence force (F_R) that is less than the membrane spring force (F_S). The initial displacement is neglected in the design compared to the large gap, g = 30 μm.

In order to fully close the microvalve and provide resistance to the fluidic flow, the membrane has to move downward until it touches the gasket, which is the center of the microcoil underneath. It requires an additional electromagnetic field in the same direction as the existing remanence field, as shown in Figure 3.6b. The combined magnetic densities (B_g) has to be large enough to overcome the magnetic reluctance across the gap and produce sufficient electromagnetic force (F_{EM}) to deflect the membrane. The attraction force (F_Z) and the magnetic flux density across the gap are related by Equation 3.3 below [90]:

$$F_Z = -\frac{A_g . B_g^2}{2.\mu_O} = -\frac{\Phi^2}{2.\mu_O . A_g} \qquad (3.3)$$

While the gap (g) does not appear explicitly in Equation 3.3, the magnetic flux density (B_g) depends on the gap (g), the current to the microcoil (I_{coil}), remanence (B_R) and the coercivity of the permanent magnet (H_C). The magnetic force, F_{EM} or F_Z increases as the gap decreases. Figure 3.7 shows F_{EM} as the current is applied to the coil. When a sufficient current is applied, the membrane closes the outlet orifice providing a closing force of F_C as shown in Figure 3.7. The current (I_{coil}) is then turned off and the membrane remains closed and latched (2nd stable position), shown by point B in Figure 3.7. The remanence force (F_R) from the permanent magnet is large enough to overcome

the membrane spring force (F_S), thus $F_R > F_S$ when the membrane downward displacement (d_m) is 30 μm. Figure 3.7 shows that the latching force (F_L) is determined by the resultant between these two forces, F_R and F_S. Figure 3.6c, shows the flow of magnetic field when the membrane is at the latching (2nd stable) position.

In order to unlatch the membrane and fully open the microvalve, a reversed (negative) current is required to produce an electromagnetic field in the opposite direc to the permanent magnet field. The interaction between these two opposite magnetic fields produces a repulsive force that finally opens the microvalve and moves the membrane upward back to the first stable position. Figure 3.6d shows the magnetic field produced by the microcoil and the permanent magnet just after the membrane is unlatched.

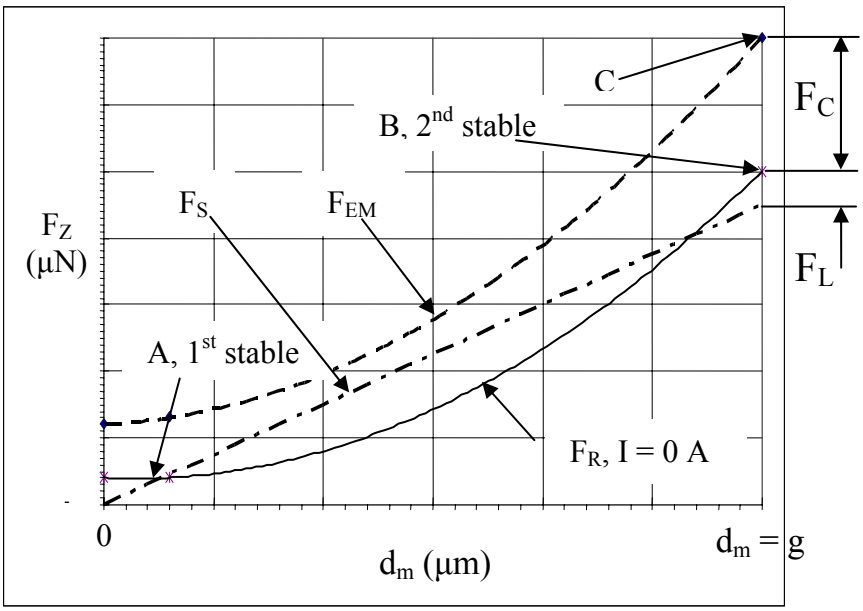

Figure 3.7. Force (F_Z) versus membrane downward displacement (d_m); Showing two stable positions of the membrane

The repulsive/attraction force between a permanent magnet and a coil located along a center line with a gap distance (g) is given by Equation 3.4 below [91]:

$$F_Z = V.M_Z.\frac{\partial B_Z}{\partial Z} \qquad (3.4)$$

Where: V is the volume of the magnet, M_Z is the saturation magnetization of the permanent magnet along z-direction, and B_Z is the flux density of the coil/electromagnet along z-direction. When the direction of the magnetic field produced by the coil is at the same direction as the permanent magnet alignment, the attraction force is produced and vise versa.

3.3.4 Review in Permanent Magnet

Although soft magnetic materials have been used widely in MEMS application to realize high-force actuators and sensitive magnetometers, permanent magnets would be more appropriate in some cases. For example it can be used to realize bidirectional microactuators [54, 92, 93]. In addition, microactuator driven by off-chip coils could be activated with lower field and hence lower power levels if a hard magnetic material is used. In spite of the advantages of permanent magnets, they have not been used widely in MEMS [94]. The primary reason for this has been the lack of readily available and reliable deposition and micromachining processes. Various hard magnetic materials can be prepared by traditional metallurgical processes (e.g. sintering, pressure bonding, injection molding, casting, extruding, and calendaring). Past work [95] has shown the process of assembling commercial magnets or screen printing of magnetic particles that result in significant field for micro actuators and micro motors. Even though the method

is simpler and the magnet has relatively high coercivity (H_C) and magnetization (M), the integration process of the permanent magnet with the micro actuators can be very tough and time consuming in particular the alignment. Further more, it is not efficient for batch fabrication process, and not compatible with the fabrication of other electronics devices such as CMOS circuits.

Other processes used to produce permanent magnets are vacuum processes (e.g., evaporation, sputtering, MBE (Molecular Beam Epitaxy), CVD (Chemical Vapor Deposition)) and electrochemical processes (e.g., electroless deposition and electrodeposition). These two processes are suitable for batch fabrication in MEMS application. The vacuum process such as sputtering is applicable for thin film deposition, < 1 μm. The electrodeposition or electroplating is more suitable for thick film deposition, > 10 μm. The magnets can be deposited on the photolithographically defined mould.

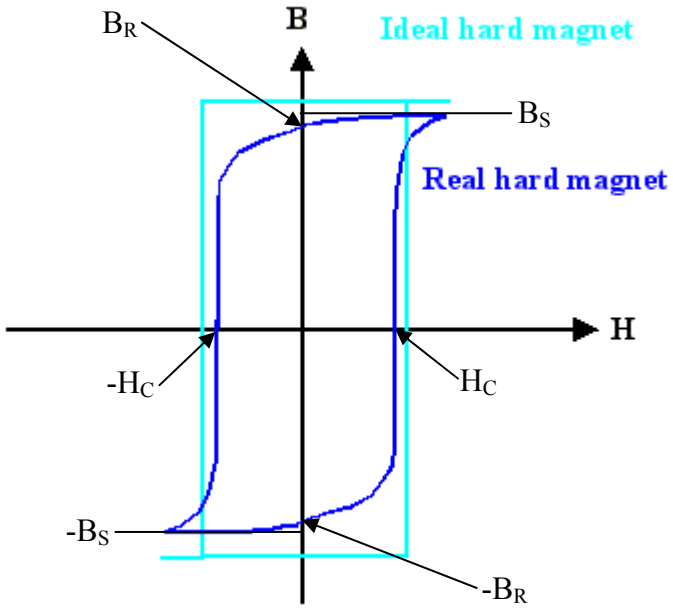

Figure 3.8. The B-H curve for a permanent magnet

The selection of the permanent magnet is based on the large magnitude of coercivity (H_C), the magnetic saturation (B_S), and magnetic remanence (B_R). Figure 3.8 shows the B-H curve of a permanent magnet. For an ideal permanent magnet, the magnitude of B_R is the same as B_S. The total area inside the permanent magnet loop indicates the total energy stored within the permanent magnet, and it is called $(B.H)_{max}$.

Originally, most hard magnetic materials have been based on cobalt alloys because its hcp structure has high crystal anisotropy, which results to high magnetic anisotropy. Thus the magnetic properties of a material are related its material properties. For the application in an actuator, it is always desirable to have a permanent magnet that has high magnetic anisotropy. So far Co-based alloys with P, As, Sb, Bi, W, Cr, Pd, Pt, Ni, Fe, Cu, Mn, and the associated entrapped gasses O and H, have been deposited by the above methods. Elements alloyed into Co tend to become concentrated at grain boundaries, which results in isolated magnetic Co particles, surrounded by non-magnetic or weakly magnetic boundaries [96]. Such materials formations create microscopic energy barriers that increase the coercivity (H_C) of the film. The exceptions are for Pt and Pd that are readily alloyed with Co or CoNi and have the effect of increasing the magnetocrystalline anisotropy [97]. Luborsky electrodeposited Co and CoNi with P, As, Sb, Bi, W, Mo, and Cr, and adjusted the amount of the alloying element required to achieve the maximum deposited coercivity. In this work, the coercivity is decreasing in the order P > As > Sb > Bi and W > Mo > Cr [96]. Another result is that the saturation magnetization, M_S, decreased with the increasing contents of the non-magnetic elements. Thus, it is preferable to have low deposit contents of P or W that results in high H_C while still maintain relatively high M_S.

Promising hard magnetic thin film materials include CoPt and FePt because of their high magnetocrystalline anisotropy and magnetic saturation [97]. Specifically, tetragonal L10 ordered phase materials with the composition of 50% Co – 50% Pt and 50% Fe – 50% Pt have shown very high coercivities (> 10,000 Oe) [17]. Most investigations of the CoPt and FePt deposits permanent magnet were conducted in vacuum processes (e.g., MBE [99] and sputtering [98-101]. In these processes, the CoPt and FePt were deposited in multilayered structures and then annealed to produce ordered phases. However the annealing process requires high temperature (e.g. 500 – 700 °C), this is a major disadvantage for MEMS application because the integrated circuits (ICs) and some materials commonly used in MEMS (e.g. Al, polymers, etc.) will not survive at these temperatures.

CoPt and Co/Pt multilayers have been electrodeposited at or near room temperature [102-105]. Cavalloti obtained hard magnetic Co-Pt by electroplating with the coercivity that reduced from 4,000 to 2,000 Oe. As the film thickness was increased from 50 nm to 10 μm [106]. Zana and Zangari show that in Co-Pt micromagnet formed by electrodeposition with thickness less than 1 μm, with B_R = 0.411 – 0.488 T and H_C = 3,497 Oe – 3,654 Oe. [107]

In 1983 Non-cobalt alloys, NdFeB permanent magnets, become commercially successful. They are produced by using sintering or melt spinning processes. These bulk NdFeB alloys represented an exciting new type of hard magnetic material because they do not contain expensive and rare elements, such as cobalt, and yet are able to produce a maximum energy product of up to 0.4 MJ/m^3 (50 MGOe)

Work on developing NdFeB permanent magnets for micromachining using injection molding and pressure bonding [108] has been reported; however it is not wafer integrated or a bath-fabrication process. Although thin films of NdFeB (<1 μm) can be vacuum deposited [97-98], in most cases the film is still amorphous as deposited and has very low coercivity (< 100 Oe), i.e. a soft magnet. In order to enhance the coercivity, high temperature annealing (> 400 °C) [97] or a high substrate temperature (>600 °C) during deposition was needed. Moreover these alloys have high corrosion rate means that they need to be coated with a protective layer before being exposed to the strong chemistries often used in micromachining (e.g. concentrated HF, KOH, etc).

3.3.5 Electrodeposited Permanent Magnet

Electrodeposition or electroplating is a very effective process for deposition of thick films (>10 μm) of permanent magnet materials. The electrodeposition can be done in a batch process that is preferable for MEMS application. Table 3.3 below, shows various hard magnetic materials that have been studied to evaluate their magnetic properties.

Table 3.3. Hard magnetic properties of electrodeposited alloys

Plated Alloys	Composition (wt. %)	H_C(Oe)		Thick-ness (μm)	M_S (T)	Squareness		Ref.
		Out of plane	In plane			Out of plane	In plane	
CoNi	20-40% Ni	100	-	2	1.4 - 1.6	0.6 - 0.78		[109-110]
CoP	2-4% P	1400	1300	2	1.5 - 1.6	0.2 - 0.5	0.1 - 0.3	[109-110]
CoPt	30-58% Pt	1653	2102	-	1.2 - 1.7	0.34 - 0.64	0.25 - 0.7	[105]
CoPt	20% Pt	2497 -2600	-	< 1	1	0.875	-	[107]
CoNiP	18-37% Ni, 1-3% P	926	2150	2	1.2 - 1.4	0.2- 0.45	0.1 - 0.3	[109-110]
CoMnP	2-4% P, <1% Mn	800	2000	2	1.4 - 1.5	0.1- 0.3	0.1- 0.2	[109-110]
CoPtP	58% Pt, 1% P	2887	3555	1	0.7	0.4 - 0.6	0.3 - 0.4	[109-110]
Co_3W or CoW	30-40% W	250		2	1.2 - 1.3	0.2 - 0.5	-	[109-110]
Co/Cu	5-50% Cu	340	650	2	0.7 - 1.3	0.6 - 0.7	0.1 - 0.2	[109-110]
CoNiMnP	83.5% Co, 10.57% Ni, 5.44% P, 0.49% Mn	710 - 1100	286	40	1.5	0.13	0.05	[54]

In order to integrate electrodeposited magnetic materials successfully with ICs and MEMS, the electrodeposited materials must have:

(1) low deposit stress to prevent film cracking; This is a very serious issue particularly for multilayer structure, which is the fabricated microvalve in this research; Moreover the film cracking is more pronounced as the thickness increases. Most of the electrodeposited Co alloys permanent magnets experience high tensional stress, this stress increases as the cobalt content increases.

(2) Good adhesion between the seed layer and the electrodeposited films; this requirement is very important to produce a solid structure integrated with the permanent magnet; Because of the frequent high tensional stress produced during the electrodeposition process, delamination may occur if the adhesion is poor.

(3) Corrosion resistance to HF and other acids that are frequently employed in MEMS to release micromechanical structures; This requirement is not very important for the microvalve fabrication in this research because we use sacrificial photoresist to build our membrane that can easily be released in a solvent such as acetone.

The selection of a permanent magnet is very important in order to produce high magnetic force. Permanent magnet should have high coercivity (H_C) and high saturation magnetization (M_S). A higher coercivity permanent magnet is preferred as it reduces the required thickness of the permanent magnet and the required electromagnet current needed in the coil to produce the same amount of actuation force. In this research, two electrodeposited permanent magnets, as shown in Table 3.3 are selected. They are Co-Pt and CoNiMnP alloy magnets. The fabrication of CoNiMnP alloy reported in [54] introduces an additional permanent magnet field during electroplating to increase the magnetic anisotropy and the coercivity. CoNiMnP has high saturation magnetization (M_S) as shown in Table 3.3 and can be electroplated at room temperature. The Co-Pt permanent magnet reported in [107] has a high coercivity (H_C) and moderate M_S, and it can be electroplated at or near room temperature (40 – 50 °C).

Unlike other candidates, such as CoPt reported in [105], the two permanent magnets, CoNiMnP and CoPt, do not require additional heat treatment after the electrodeposition process in order to align the magnetic moment in a hard magnetic film

through crystallization. The heat treatment at the temperature of 500 - 700 °C will cause delamination to the microvalve structure and it is not compatible for CMOS integrated circuits. More details magnetic properties of the chosen permanent magnets, CoPt and CoMnNiP, are tabulated in Table 3.4.

Table 3.4. Magnetic properties of CoPt and CoMnNiP permanent magnets

Magnet/ Reference	**Composition**	**B_R (T)**	**H_C (Oe)**	**$(B.H)_{MAX}$ (kJ/m^3)**	**Fabrication Comment**
Co-Pt/ [54]	80% of Co 20% of Pt	0.41 - 0.49	3,497 – 3,654	29.52 - 34.5	no Field
CoNiMnP/ [107]	83.5% of Co 10.57% of Ni 5.44% of P 0.49% of Mn	0.17 - 0.19	710 – 1,100	1.9 – 2.3	with Field

3.4. Bidirectional Microactuator

3.4.1 Introduction

Other than creating the first prototype of the bistable electromagnetic microvalve fabricated on a single wafer, another contribution of this research is the invention of a bidirectional microactuator with permanent magnet and a microcoil fabricated on a single wafer. The production of the bidirectional actuator is the result of the electroplated permanent magnet on the center soft magnetic dome as shown in Figure 3.5, which enables the membrane to move upward and downward because of the permanent magnet anisotropy along the vertical direction. In this section, we discuss the possible methods

used to create bidirectional actuators and the mechanism of the bidirectional actuator invented in this research.

3.4.2 Methods of Creating Bidirectional Actuator

There are many ways to develop bidirectional electromagnetic actuators. Figure 3.9 shows that a bidirectional actuator is created by having a cantilever beam made of soft magnetic material and two electromagnetic coils. The top and bottom coils provide electromagnetic forces that move the cantilever upward and downward respectively.

Another method is shown in Figure 3.10, which utilizes an external permanent magnet and a micro coil located on the bottom and the top of cantilever beam respectively. The cantilever beam is again made of soft magnetic material. The remanence field of the permanent magnet is large enough to gives initial deflection to the cantilever beam.

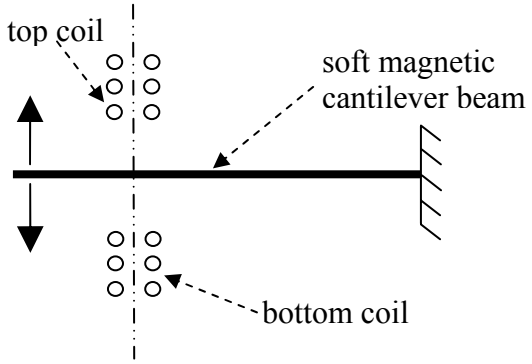

Figure 3.9. Bidirectional actuator with two coils design and a soft magnetic cantilever beam

The microcoil produces an additional electromagnetic field when a current (I_{coil}) is applied. In order to deflect the beam upward, an electromagnetic field in the opposite direction to the remanence field is required. The spring stiffness (k_S) of the beam and the resultant flux densities from the microcoil and the permanent magnet, define the amount of deflection (d_m). To moves the beam further downward, an electromagnetic field in the same direction as the remanence field is required.

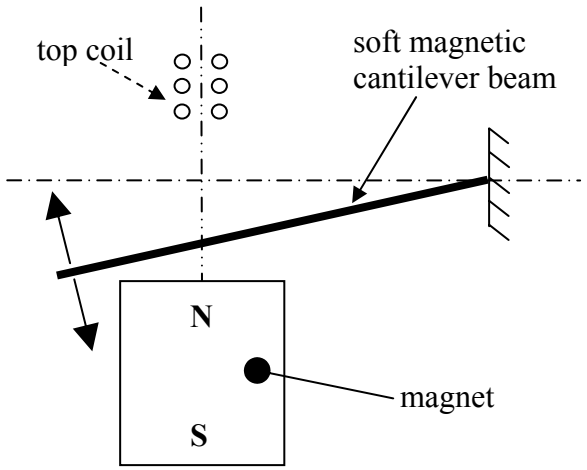

Figure 3.10. Bidirectional actuator with one coil and permanent magnet beneath the soft magnetic cantilever beam

For the methods shown in Figures 3.9 and 3.10, the cantilever beam must be made of a soft magnetic material such as (Ni, Fe, or NiFe alloy). Other methods for producing a bidirectional microactuator with no soft magnetic cantilever beam are shown in Figures 3.11 and 3.12. Figure 3.11 shows the same idea as shown in Figure 3.9 except that the cantilever beam is non-magnetic. As a result, a separate permanent magnet has to be integrated on the beam to produce a remanence field. The magnetic interaction between

the magnet and the top and bottom coils produces the upward and downward movements respectively.

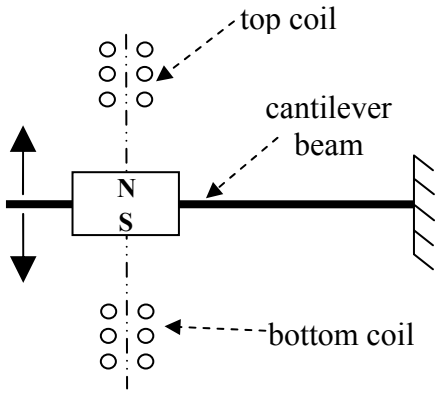

Figure 3.11. Bidirectional actuator with two coils design and an integrated permanent magnet on a cantilever beam

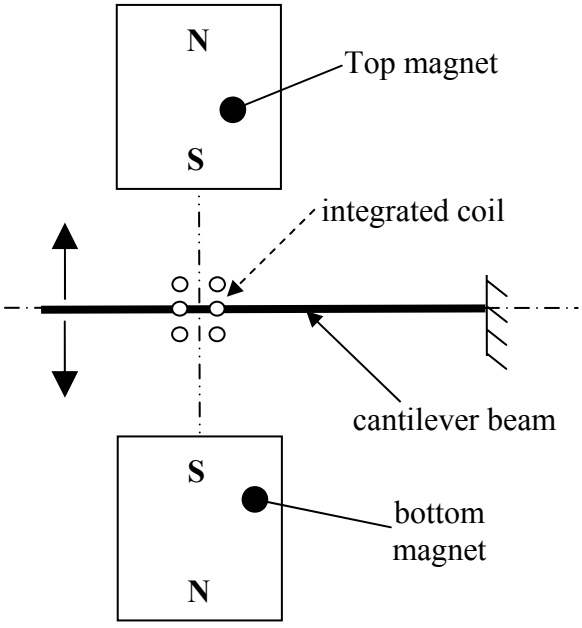

Figure 3.12. Bidirectional actuator with integrated coil design on a cantilever beam and two permanent magnets

Figure 3.12 shows a design of bidirectional actuator by having two permanent magnets and a non-magnetic cantilever beam. In order to move the beam; a separated coil is integrated on the beam. When the electromagnetic field produced by the coil is at the same direction as the top magnet, the beam moves upward and vise versa.

The idea shown in Figure 3.9 seems to be neat and simple in mechanism. However, the fabrication of two coils on top and bottom of the cantilever on a single wafer is a very challenging task and seems not to be realistic. The fabrication is much simpler if it is fabricated on two silicon wafers, and finally they are clamped by a bonding process. The idea shown in Figure 3.10 seems require a simpler fabrication process, where the system only has one coil and an external permanent magnet that can be glued on the back of the wafer. However, the system may have a serious magnetic leakage and inefficient electromagnetic flux, which makes it hard to precisely control the amount displacement of the beam. The additional complexity of the system as shown in Figure 3.11 of having a permanent magnet on the cantilever beam makes the fabrication process challenging on a single wafer. Figure 3.12 seems to be easier to fabricate than the method shown in Figure 3.11, however there is a serious magnetic leakage of the two magnets that are faced in the opposite field direction. Also, the magnetic field may interfere and damage the electronics devices surrounding the actuator.

By understanding the weaknesses of the four methods as shown in Figures 3.9, 3.10, 3.11, and 3.12, the new creation of a bidirectional microactuator has to have an efficient electromagnetic circuit and a simple mechanism. Based on the magnetic principal, bidirectional actuation can be achieved between a permanent magnet and an electromagnet [54, 91]. By reversing the current flowing through the electromagnet, the

magnetic field produced can be either in the same direction, or opposite to the remanence of the permanent magnet, this consequently produces either attractive or repulsive forces respectively. The permanent magnet can be attached on the membrane actuator that provides favorable scaling factors, much thinner dimension, more efficient magnetic field, and low power consumption compared to having external permanent magnet or a variable reluctance-type electromagnetic actuator [54].

In this report, a Co-Pt permanent magnet reported in [107] is introduced to the membrane actuator by electrodeposition at a temperature of 40 – 50 °C. The major invention of this work is a bidirectional actuator with a permanent magnet, a micro coil, and a membrane actuator fabricated in a single wafer process. The schematic of the bidirectional actuator is the same as the bistable microvalve as shown in Figure 3.5, except that the actuator does not have any flow orifices. Past work [54] integrated an external commercial electromagnetic coil to produce the membrane actuation. This process is not suitable for batch fabrication and requires additional work to manually align the center of the external coil and the center of the permanent magnet. The fabrication process involves the use of two silicon wafers. One wafer is to define the actuator and the other one is for the substrate and the attachment of external coil.

3.4.3 Principal of Bidirectional Mechanism

The principal of the bidirectional mechanism is shown in Figures 3.13a - 3.13d below. Initially the membrane is flat as shown in Figure 3.13a, the permanent magnet

produced a remanence field and there is no current input to the micro coil. The membrane is separated by a gap distance (g), that is designed in the range of 70 – 100 μm.

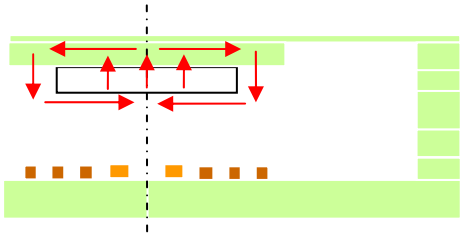

Figure 3.13a. The initial position of the membrane when there is no input current (I_{coil}) to the micro coil

When a current (I_{coil}) is input to the microcoil, an electromagnetic field (B_{EM}) is produced. When B_{EM} is in the opposite direction to the remanence field, the membrane deflects upward as shown in Figure 3.13b.When the direction of B_{EM} is the same as the remanence field, the membrane moves downward, as shown in Figure 3.13c. It shows that when the membrane moves downward, there is a misalignment between the center-line of the membrane with the center-line of the micro coil. This creates a resistance to the magnetic flow from the microcoil to the permanent magnet and soft magnetic membrane. Thus, the membrane supported legs are designed to be much thinner than the centered membrane to allow rotation on the so-called pin joint as shown in Figure 3.13d. When a part of membrane starts to touch the bottom coil, the membrane rotates on the pin-joint so that its bottom surface can fully touch the microcoil and create a close loop magnetic field as shown in Figure 3.13d.

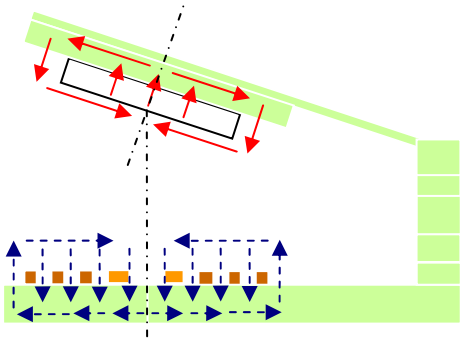

Figure 3.13b. The upward motion of the membrane because of the repelling force between the micro coil and permanent magnet. The magnetic field produced by the microcoil (blue-dashed line) is in the opposite direction to the magnet's field (red-solid line).

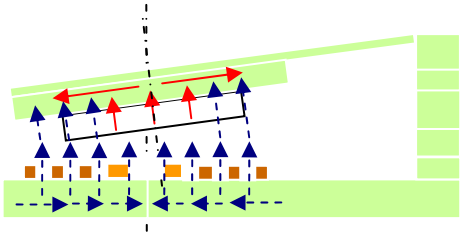

Figure 3.13c. The downward motion of the membrane because of the attraction force between the permanent magnet and micro coil. The magnetic field produced by the microcoil (blue-dashed line) is in the same direction as the magnet's field (red-dashed line).

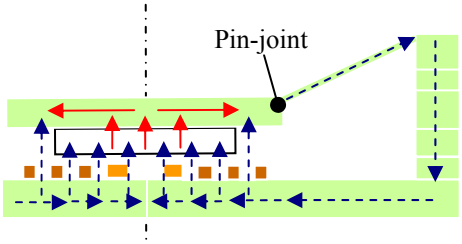

Figure 3.13d. The membrane touches the micro coil. Both magnetic fields are aligned to each other and form a closed loop magnetic field.

CHAPTER 4

DESIGN AND FINITE ELEMENT ANALYSIS (FEA)

4.1 On/Off Electromagnetic Microvalve

4.1.1 Introduction

This section discusses the design steps that have been carried out to create the on/off mechanism of the microvalve. During the designs, we found a lot of ideas and improvements for the microvalve operation, such as orthonol insertion in between the coil-turns and 3D analysis of the buckled membrane. This section also discusses briefly about these ideas.

4.1.2 Advantages of Orthonol Insertion

A simple 2D magnetic model has been studied in ANSYS in order to understand the amount of electromagnetic force produced by an electromagnetic actuator as well as to investigate the saturation and magnetic behavior. 2D Axisymmetric model has been utilized in ANSYS 5.7 using element PLANE 53. The schematic of the model is shown in Figure 4.1. *Note: This geometry is not the geometry of the fabricated on/off microvalve as shown in Figure 3.1.* The results of this model become the milestone for us to design the actual on/off microvalve.

Figure 4.1a shows that a soft magnetic material, orthonol, is inserted in between the coil turns in order to decrease the reluctance ($\Re$) of the microcoil. As mentioned before that $\Re$ is equivalent to the resistance in the electrical analogy, i.e. lowest value of $\Re$ is desirable to produce an efficient electromagnetic circuit. To understand better about this, please refer to the reluctance ($\Re$) of a micromachined inductors or transformers [86], as shown in Figure 4.1b, which composes a magnetic core and multilevel metal conductors (turns of microcoil). The reluctance ($\Re$) of the micromachined inductors, can be calculated by the following Equation 4.1:

$$\Re = \frac{l_C}{\mu_0 . \mu_r . A_C} \qquad (4.1)$$

Where: A_C = cross sectional area of the magnetic core, l_C = length of the closed magnetic core; μ_0 = permeability in vacuum; and μ_r = it is assumed to be permeability of the magnetic core.

It is clear from Equation 4.1 above, when there is no magnetic core inside the coil turns, $\mu_r = 1$, the total permeability ($\mu = \mu_r.\mu_0$) is the same as the air magnetic permeability (μ_0). By inserting a magnetic core, which can be made of Orthonol (50% Ni and 50% Fe) or Permalloy (80% Ni and 20% Fe) with $\mu_r = 6000$ [111]. $\Re$ of the microcoil is reduced significantly.

The same principal of reducing $\Re$ in the micromachined inductors by introducing a soft magnetic core, as shown in Figure 4.1b, is also applicable to the microcoil design of the microvalve actuator as shown in Figure 4.1a. However to see the advantages of the Orthonol insertion in between the coil-turns, we need to model the whole structure of the electromagnetic actuator and compared the produced electromagnetic force with and without Orthonol.

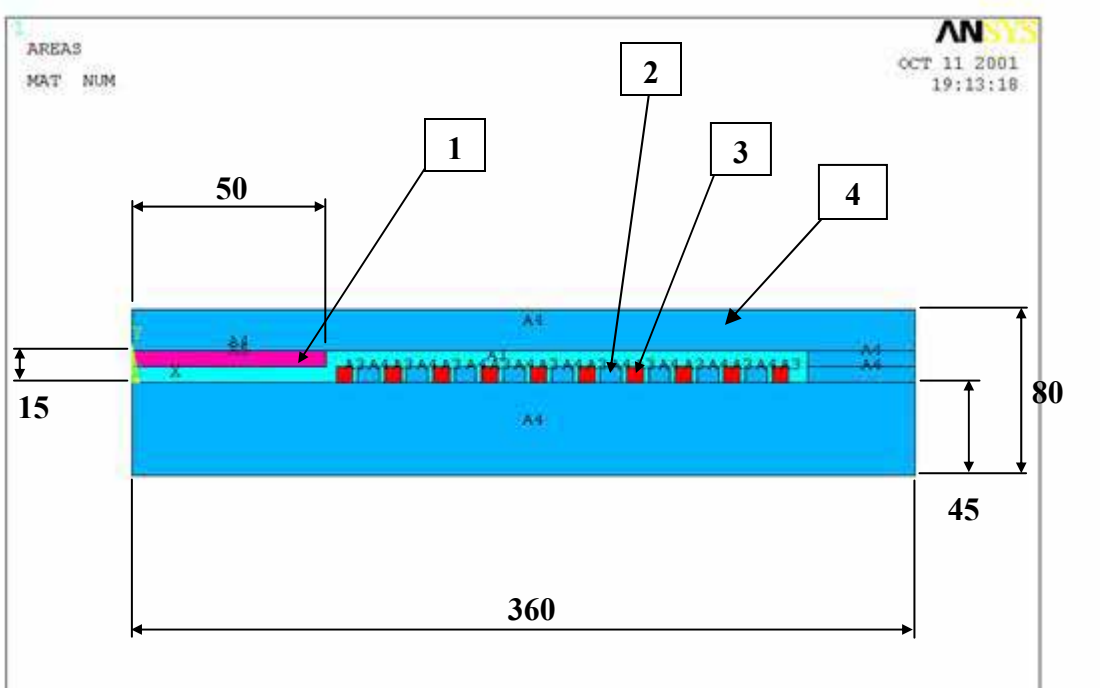

Figure 4.1a. 2D magnetic model for FEA in ANSYS 5.7, where: 1 = center soft magnetic dome, 2 = orthonol in between the coil turns, 3 = microcoil, made of gold (Au) with the dimensions of 7.5 μm (H) and 7.5 μm (W), and 4 = soft magnetic membrane. All dimensions are in μm.

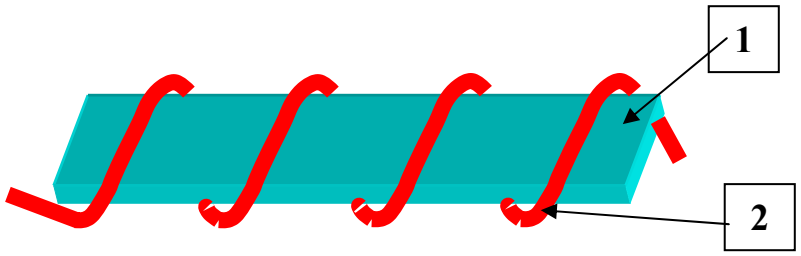

Figure 4.1b. Conceptual drawing of micromachined inductors and transformers, where: 1 = soft magnetic core, and 2 = microcoil turns, made of Au.

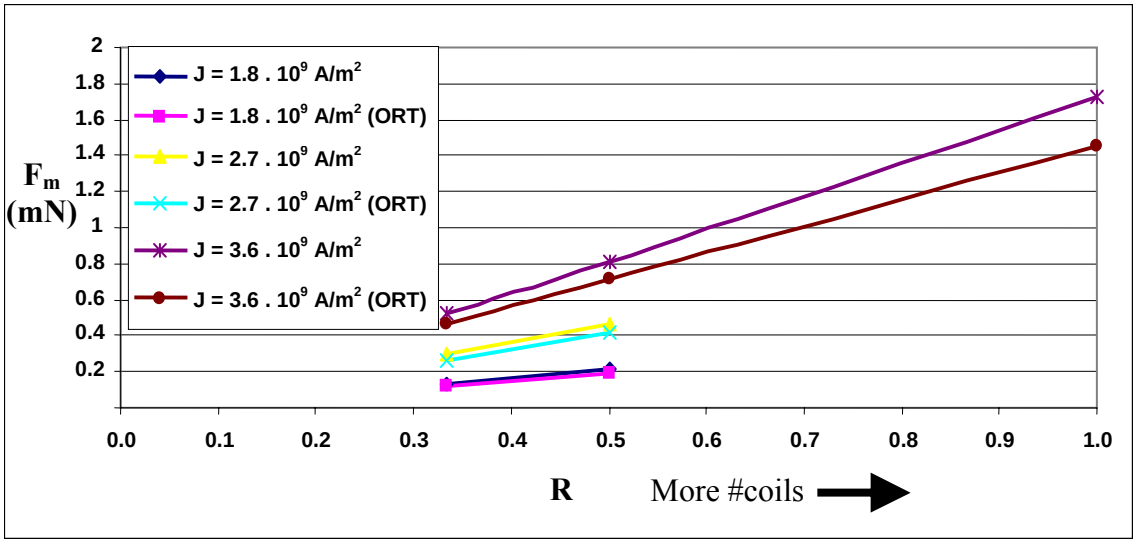

Figure 4.2. The variation of the downward force exerted by the membrane (F_m) and the ratio (R) = "coil height (H)"/"space between coil-turns (S)". It is plotted at different current densities (J) for with and without orthonol in between the coil-turns. Coil size = 7.5 µm (H) x 7.5 µm (W); J = 3.6 GA/m^2 is equivalent to 0.2 A.

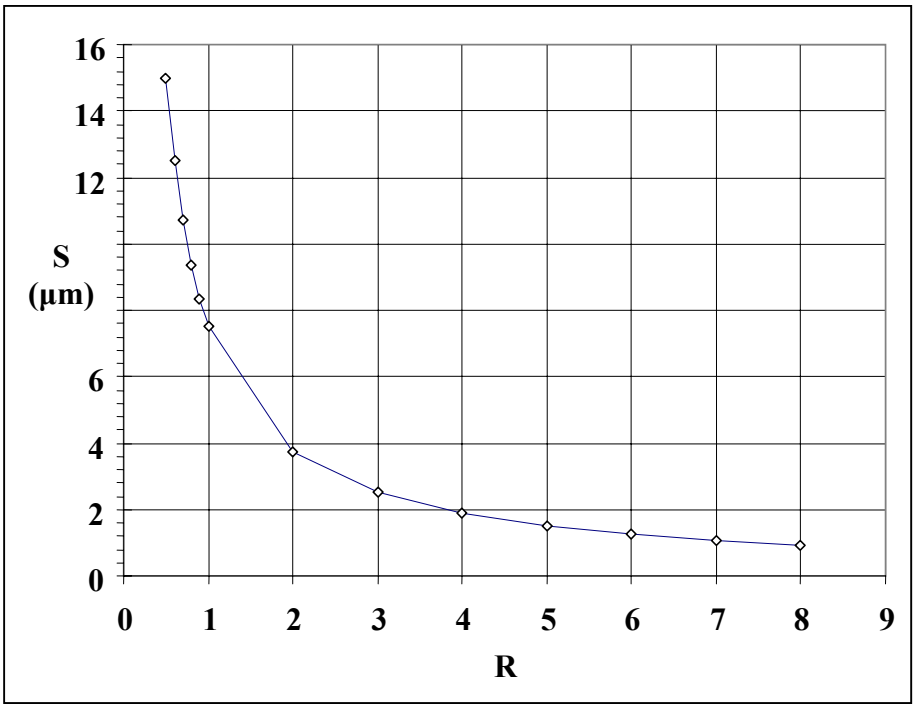

Figure 4.3. The corresponding spacing (S) between coil turns at different R (Ratio)

Figure 4.2 shows the variation of the downward force exerted by the membrane (F_m) and the ratio (R). Ratio (R) is defined as the "coil height (H)"/"space between coil-turns (S)". The corresponding spacing between coils at different R is shown in Figure 4.3. The coil size is 7.5 μm (H) x 7.5 μm (W), thus the increases of R result in more coil-turns (N). Figure 4.2 shows that the insertion of Orthonol in between the coil-turns has increased F_m. And also F_m increases with R and current densities (J).

It shows that when J = 3.6 GA/m^2 and R = 0.32, F_m increases from 0.48 mN to 0.55 mN with the addition of Orthonol, i.e. 15% increase. However, when R = 1, F_m increases from 1.42 mN to 1.75 mN with the additional of orthonol, i.e. 23.2 % increase.

4.1.3 Optimum Microcoil Design

The additional of Orthonol in between the coil-turns has shown some improvement in the downward force (F_m). The fabrication of microcoils with Orthonol in between the coil-turns seems to be very challenging and problematic. Thus this improvement is not implemented in the microvalve fabrication. More analysis has been done in order to find the optimum spacing (S) between circular coil-turns. By optimizing the maximum available area for the microcoil, we should be able to determine the optimum number of coil-turns (N). Analysis has been done using the same geometry as shown in Figure 4.1, except that there is no Orthonol in-between the circular coil-turns.

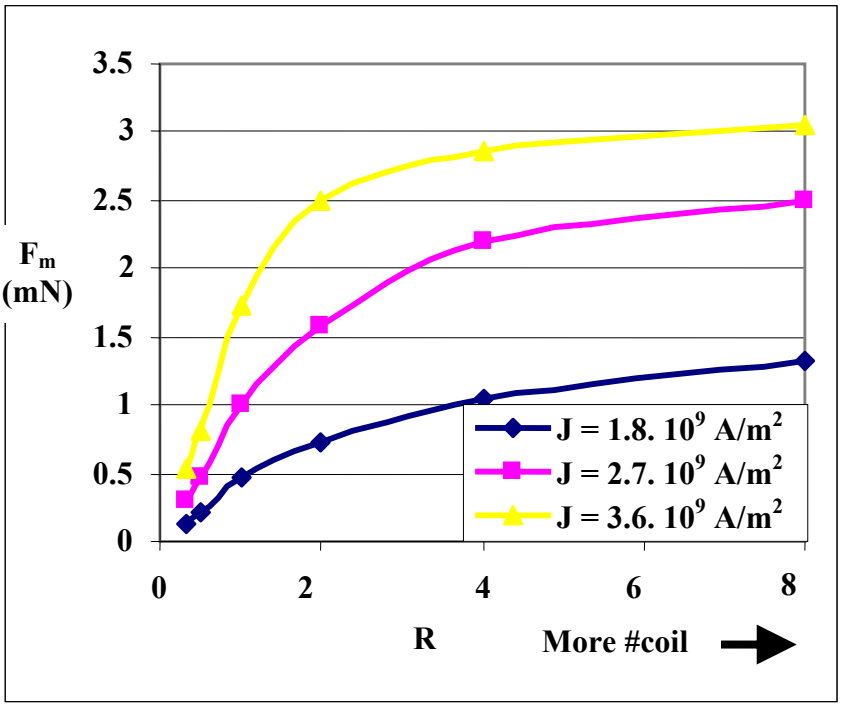

Figure 4.4. The force exerted on the membrane (F_m) versus the ratio (R) = "coil height (H)"/"space between coil-turns (S)" at different current density (J). Coil size = 7.5 µm (H) x 7.5 µm (W); J = 3.6 GA/m^2 is equivalent to 0.2 A.

Figure 4.4 shows the variation of the downward force exerted by the membrane (F_m) at different ratio (R) and current density (J). It shows clearly that at the same current density (J), the force exerted on the membrane (F_m) increases with R. It also means that F_m increases with number of coil-turns (N). Figure 4.4 shows that F_m saturates at a certain R, at this point the addition of N does not contribute to the increase of F_m. Figure 4.3 shows that when R gets larger, the space between coil-turns (S) becomes smaller. This saturation occurs because of the Eddy current presented in between the coil turns. Figure 4.4 shows that the saturation occurs at smaller R as J increases.

To achieve the best design, it is always desirable to have F_m at or closer to its saturation value at the same time that size of S has to feasible for the fabrication process.

Figure 4.4 shows that at J = 3.6 GA/m^2 or I = 0.2 A, F_m = 90% of its saturation when R = 4, F_m = 80% of its saturation when R = 2, and F_m = 60% of its saturation value when R = 1. Figure 4.3 shows that when R > 4, the size of S < 2 μm. It is very challenging to fabricate a feature that is smaller than 2 μm by ordinary photolithography process. It is also much easier in the fabrication process using thick positive photoresist, such as AZ4620, when R = 1. This means that the feature size is the same as the thickness of photoresist.

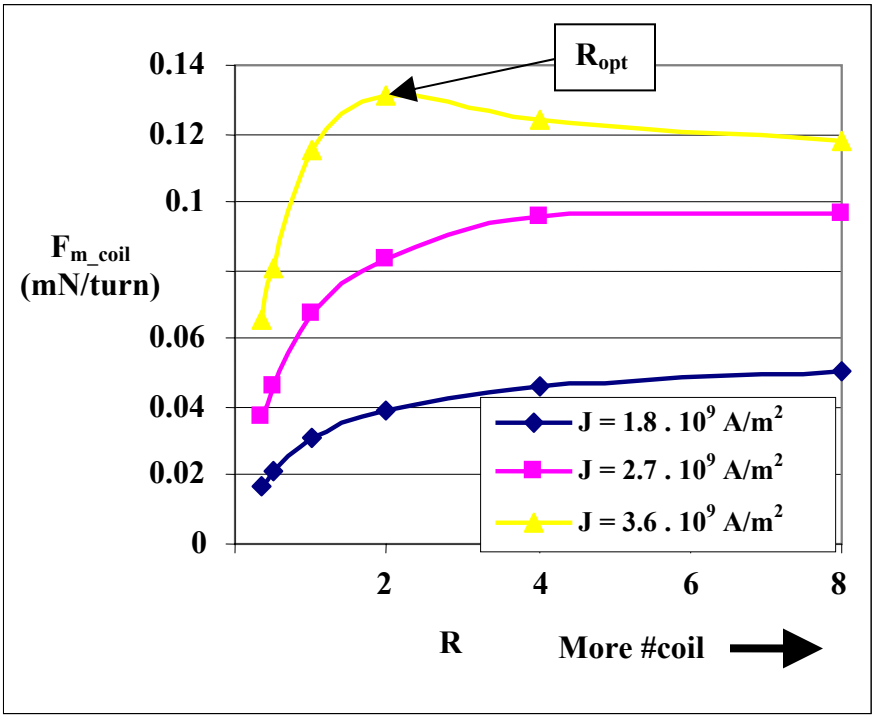

Figure 4.5. The force exerted on the membrane (F_m)/ number of coil-turns versus the ratio(R) = coil height (H)/space b/w coils (S) at different current density. Coil size = 7.5 μm (H) x 7.5 μm (W); J = 3.6 GA/m^2 is equivalent to 0.2 A.

Figure 4.5 shows the variation of "force exerted by the membrane divided by the number of coil-turns (F_{m_coil})". It shows that F_{m_coil} increases with R. F_{m_coil} saturates at lower value of R than the case for F_m as shown in Figure 4.4. It shows that for all current densities (J), when R > 1, F_{m_coil} has achieved more than 70% of the saturation value. At J = 3.6 GA/m^2 or I = 0.2 A, Figure 4.3 shows that there is an optimum or peak value of F_{m_coil} when R = 2. And F_{m_coil} goes to saturation as R continues to increase. However this peak value is not far different than the saturation value. Meanwhile when R = 1, F_{m_coil} has already achieved its saturation. Thus, it is still recommended to have R = 1 for optimum design and easy fabrication process.

4.1.4 Membrane Spring Force (F_S)

In order to achieve the on/off mechanism for the microvalve, shown schematic in Figure 3.1, it is required to understand the forces that are involved in the mechanism. In the design, it is assumed that the membrane actuates in the medium of air, where the squeeze film damping is insignificant and can be ignored. Thus there are two forces that are involved in the mechanism, the membrane spring force (F_S) that from the stiffness of the membrane supported legs, and the electromagnetic force (F_{EM}) that is produced by the microcoil.

In order to determine the membrane spring force (F_S), three approaches are carried out: beam theory, finite element analysis (FEA), and experiment. The analyses are carried out for the microvalve with the gap (g) distance of 12 μm.

4.1.4.1 Beam Theory

As mentioned before, and by referring to Figures 3.1 and 4.6, the thickness of the membrane supported legs (t_2, 3 μm) are thin compared to the thickness of the centered soft magnetic dome (t_1, 12 μm). Thus $E_1.I_1 >> E_2.I_2$ because I, which is the moment of inertia is determine by the following Equation 4.2:

$$I = \frac{w.t^3}{12} \tag{4.2}$$

This results in the centered soft magnetic dome remaining flat during its motion, as shown in Figure 4.6b. The membrane is supported with 4 legs, as shown in Figure 4.6a, and can be represented as 2 x statically indeterminate beams with total length of $2.L_2$, as shown in Figure 4.6c. According to beam theory, the spring force (F_S) can be determined by the following Equation 4.3 adapted from [89, p. 707]:

$$F_S = 2.\left(\frac{24.E_2.I_2}{L_2^3}\right) = \frac{4.E_2.w_2.t_2^3}{L_2^3} \tag{4.3}$$

Where: The value of E_2, w_2, t_2, and L_2 are 115 GPa, 50 μm, 3 μm, and 350 μm respectively. The value of Young's modulus of Orthonol, which is the material that made the membrane supported leg, is E_2 = 115 GPa; it is adapted from [88]. The results of the beam theory are shown in Figure 4.7.

4.1.4.2 Finite Element Analysis (FEA)

In order to determine F_S by finite element analysis (FEA), ANSYS 5.7 is used. 3D (three dimensional) shell element with nonlinear geometry and stress stiffening capabilities was used to build the model. The FEA results are shown in Figure 4.7.

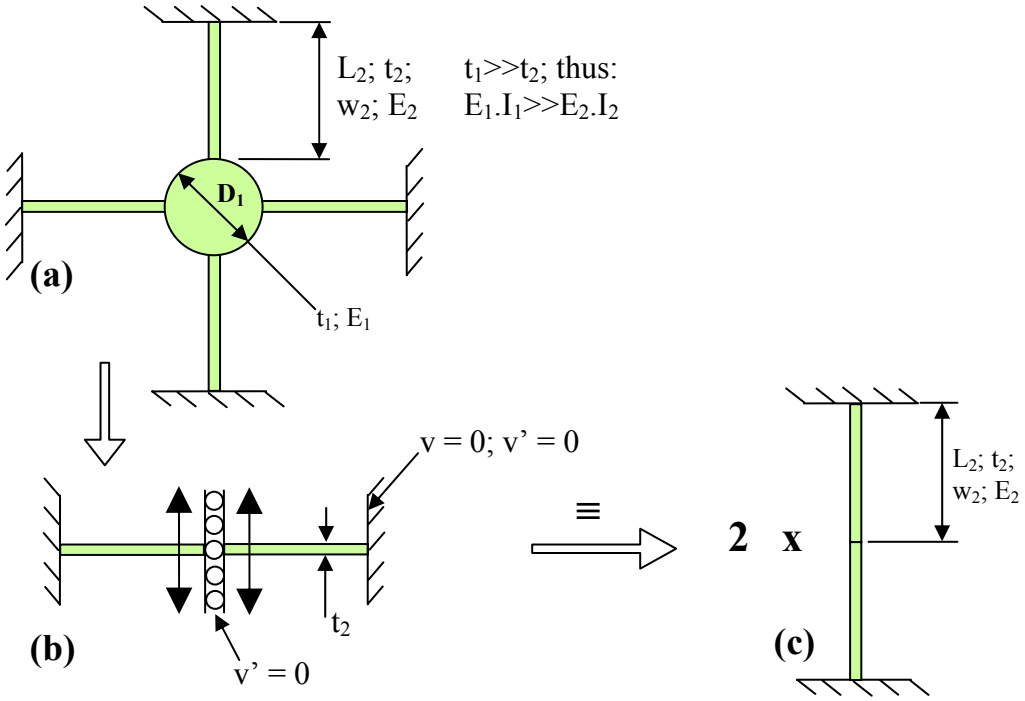

Figure 4.6. The application of the beam theory to predict the spring force (F_S) of the membrane: (a) the membrane with centered soft magnetic dome is supported by 4 legs, $t_1 >> t_2$ thus $E_1.I_1 >> E_2.I_2$; (b) the soft magnetic dome remains flat and does not deform during its motion, the leg-supports on the soft magnetic dome can be approximated by rollers, where the rotation (v') = 0; (c) the membrane supported with 4 legs can be simplified as 2 statically indeterminate beams with total length of $2.L_2$

4.1.4.3 Experiment

Experimental approach to measure the stiffness of the membrane is carried out in the machine called Tribo Indenter, Hysitron Inc., model 1BR-12. The device senses the membrane movement by a capacitive approach. The device has a sensing tip with a sphere diameter of 200 μm. During the testing, the tip-sensor is in contact with the membrane surface and displaces the membrane downward while at the same time it senses the experienced reaction force. The device has an accuracy of +/- 150 μN. The experimental results are shown in Figure 4.7.

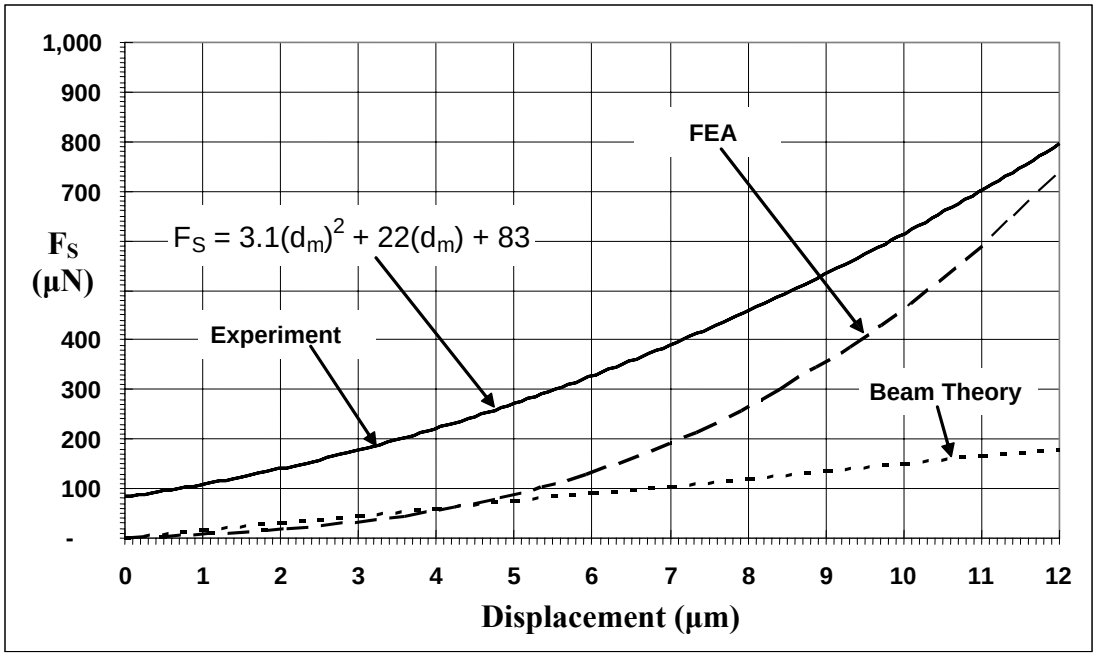

Figure 4.7. The combined results (experiment, finite element analysis (FEA), and beam theory) in the membrane spring force (F_S) for on/off microvalve. The accuracy of the experimental result is +/- 150 μN.

Figure 4.7 shows the combined theoretical, FEA, and experimental results in measuring F_S. It shows clearly that the beam theory does not give a good prediction of the membrane stiffness. The results show the membrane stiffness (k_S) is constant, which means that F_S has a linear relationship with the membrane displacement. This is not the case for a large deformation. The beam theory assumed that the plane stress remains planar during the deformation, which is also not the case for the deformation larger than the beam thickness. The FEA results show that F_S is not linearly related to the membrane displacement. It starts with a linear relationship at a small displacement, and becomes non-linear as the displacement increases. The nonlinearity occurs because of the stress stiffening effects in the membrane legs. The experimental results confirm the non-linear behavior of the membrane displacement as shown in FEA results.

4.1.5 Three Dimensional (3D) Modeling

It is not enough just to understand the required spring force (F_S) of the membrane; in addition, we need to understand the electromagnetic force (F_{EM}) that moves the membrane. In order to model more complex geometries of the microvalve and to investigate the combined structural and the magnetic behavior of the membrane actuation, a three dimensional (3D) model has been created in ANSYS 5.7. The structural analysis presents the results of the stress and membrane displacement (d_m). The magnetic analysis presents the electromagnetic force (F_{EM}) experienced by the membrane, the magnetic flux, and the magnetic field in the microvalve structure.

3D element, SOLID 98, is chosen to model the microvalve structure. This element has the capability to couple between the magnetic and structural analyses of the model. It has non-linear geometry, large deflection, and stress stiffening behaviors for the structural analysis. Unfortunately, ANSYS 5.7 does not have a direct macro command that couples the magnetic and structural analyses. Two separate physics environments (magnetic and structural) must be developed for the model and then the magnetic results are applied to the microvalve structural analysis.

Figure 4.8 shows schematically the sequential procedures that have been developed in this research in order to couple the magnetic and structural analyses for the on/off mechanism of the microvalve. As shown in Figure 4.8, the elements are re-meshed when the two analyses (magnetic and structural) are finished. The element remeshing is required to ensure that the analyses converge. A number of loops of analyses have been made to achieve the convergence results. The results are converged when the difference on the membrane maximum displacement between two consecutive loops is less than the

assigned tolerance, which is 0.01 μm. It may take more than 40 loops or about 24 hours to get the results to converge.

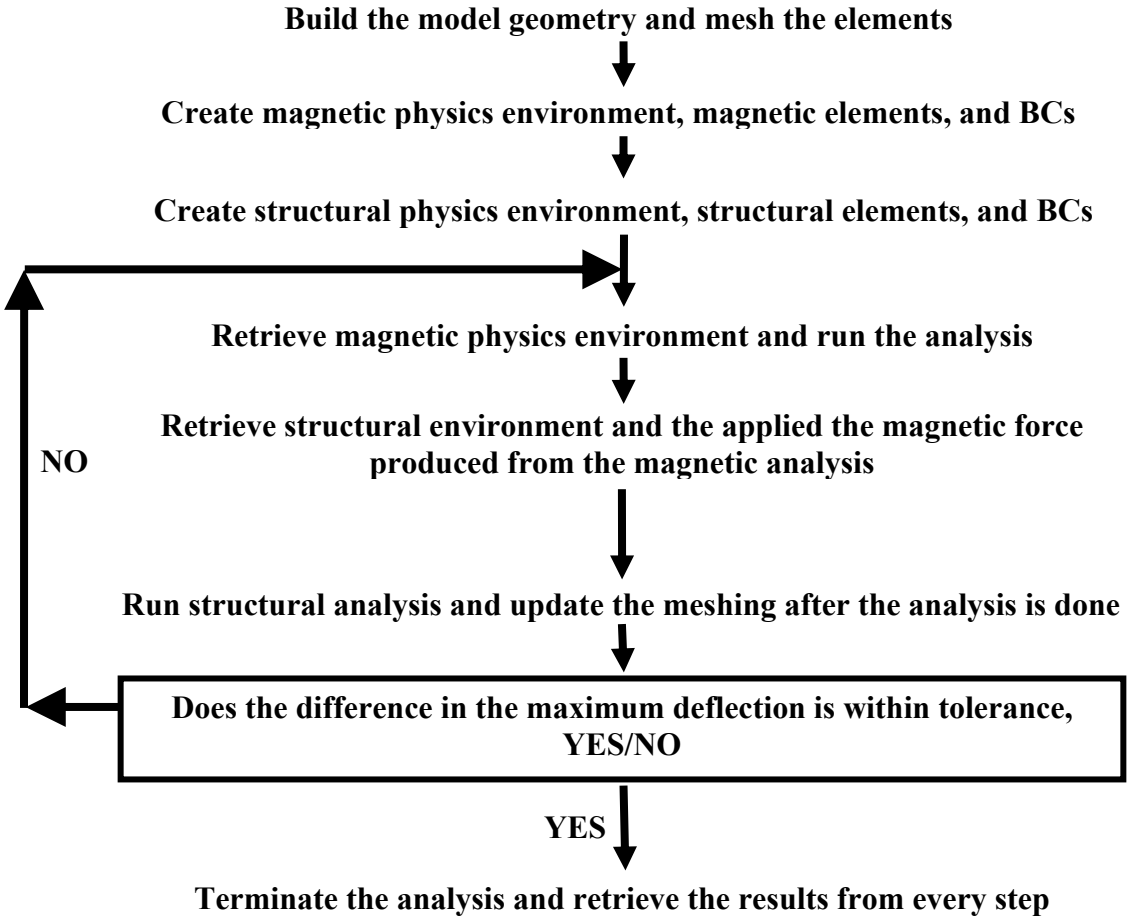

Figure 4.8. Schematic procedures to couple the magnetic and structural analysis in ANSYS 5.7; BC = boundary condition

Figure 4.9 shows the 3D geometry to model the on/off microvalve that has been developed in ANSYS 5.7 using SOLID 98 element. Because of the symmetry in the microvalve geometry as shown in Figure 3.1, only one quarter of the microvalve is

modeled. It is shown in Figure 3.1, the microvalve structure basically consists of a flat membrane with a thicker centered dome and 4 thin cantilever legs, a gold microcoil, a gasket, and a microvalve base.

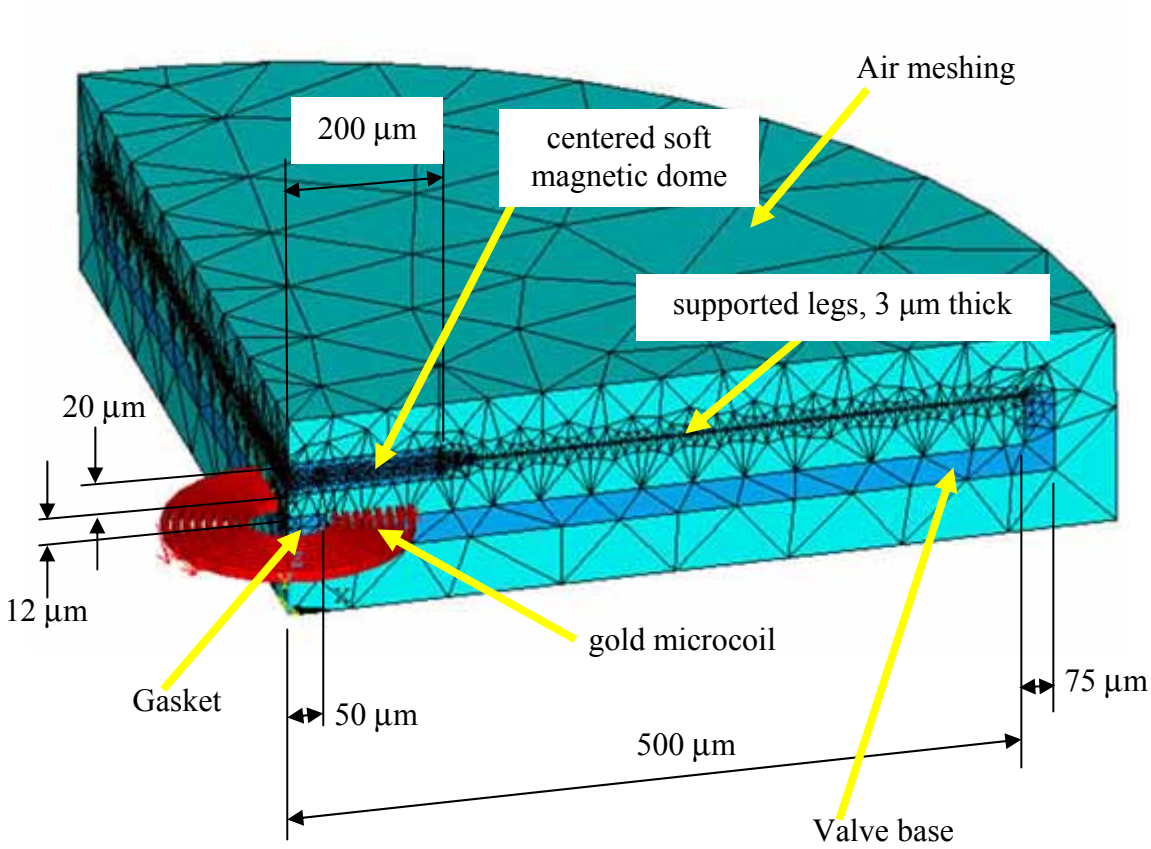

Figure 4.9. Three dimensional (3D) models that have been developed in ANSYS 5.7 to couple the magnetic and structural analyses of the on/off microvalve. Because of its symmetry, only one quarter of the microvalve is modeled.

A particular on/off microvalve with the geometry shown in Figure 4.9 was studied for the combine structural and magnetic analyses. The analyses were done at different input current to the microcoil (I_{coil}) and gap distance (g) between the centered soft

magnetic dome and the gasket. Instead of having a flat membrane, a different model with the buckled membrane was also developed for analysis. Another type of model, with Orthonol inserted between the coils was also developed.

4.1.5.1 Investigation of Orthonol Insertion in Between the Coil-turns

Figures 4.10a and 4.10b shows results from the magnetic analysis for the on/off microvalve with 8 turns of Au microcoil and an input current (I_{coil}) of 0.7 A. The initial gap (g) between the membrane and the microcoil is 12 μm. The membrane achieved its minimum downward deflection at this input current, with a downward electromagnetic force (F_{EM}) of 720 μN, as shown in Table 4.1. Thus, in order to close the microvalve it requires a current of 0.7 A. This is supports the experimental results, as shown in Figure 4.7 a force required to deflect the membrane by a distance of 12 μm is about 800 μN. The increase of I_{coil} to 0.8A increases the electromagnetic force (F_{EM}) to 951 μN as shown in Table 4.1.

Figure 4.10a shows that saturation (B > 1.4 T) has occurred when I_{coil} = 0.7 A. As mentioned before, 1.4 T is the B_{sat} of the Orthonol, which is the soft magnetic material of the membrane structure. The saturation, B > 1.4 T, mostly happen in or near to the gasket and the supported legs. Figure 4.10b shows the flow of magnetic flux density, it shows clearly that the flow is saturated in the area of the gasket. There is no saturation occurring beneath the soft magnetic dome. In order to achieve the optimum magnetic force and more efficient magnetic field applied to the membrane, it is necessary to distribute the saturation over a larger area of the microvalve.

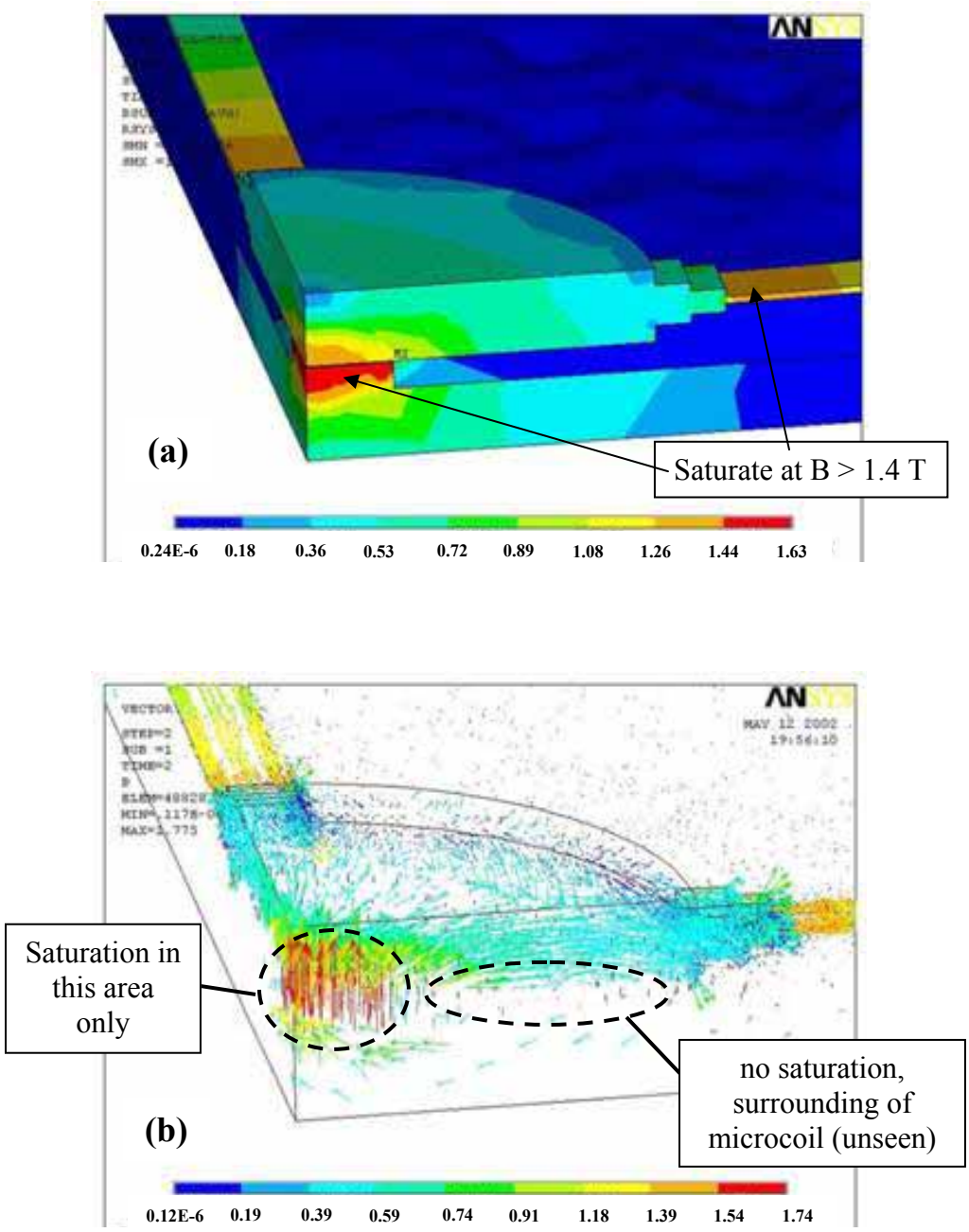

Figure 4.10. The magnetic results of the 3D model developed in ANSYS with the geometry as shown in Figure 4.9 with 8 coil-turns (not shown): (a) Showing the magnetic flux density (B, unit: T) and (b) Showing the flow of magnetic field (B)

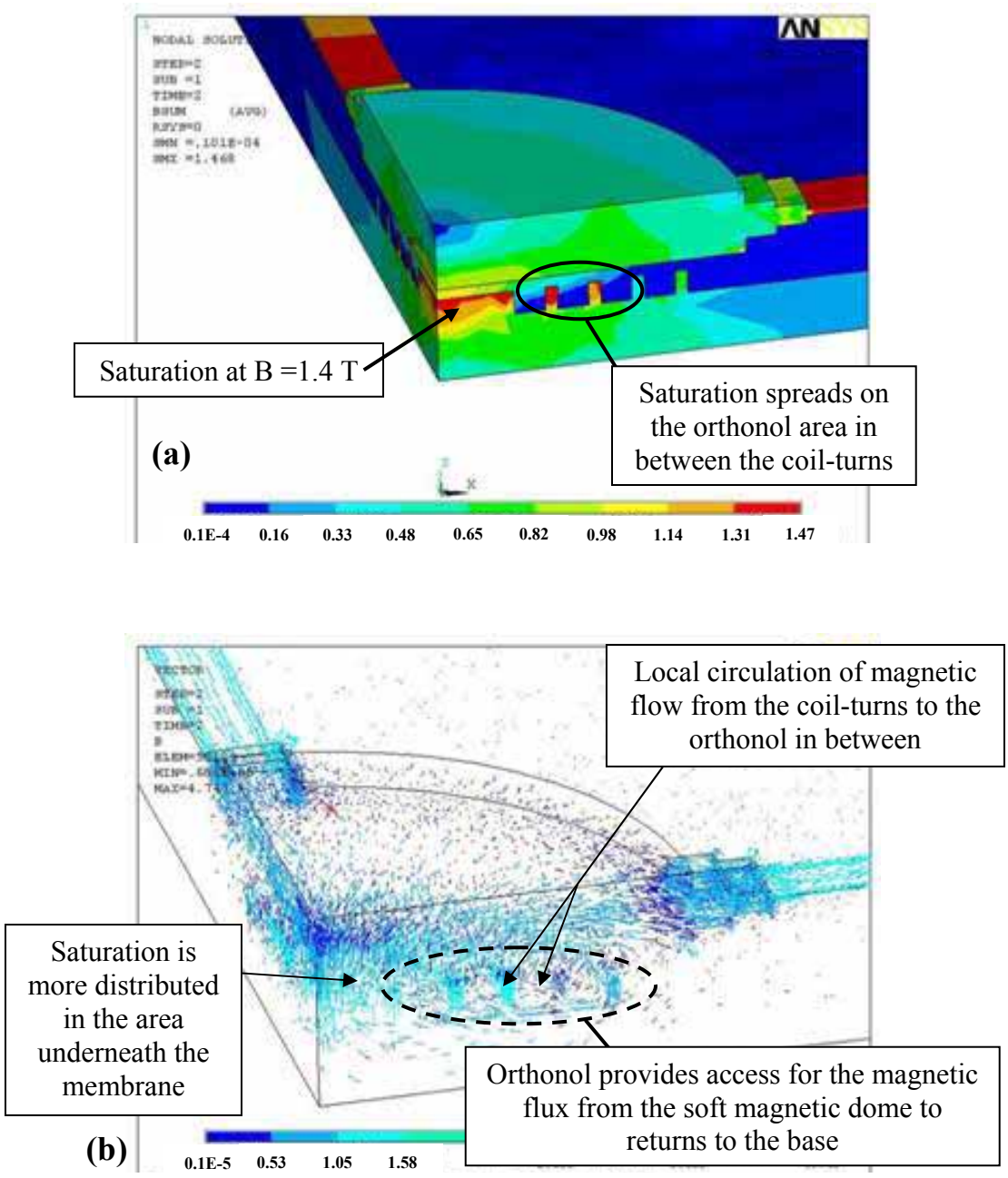

Figure 4.11. The magnetic results of the 3D model developed in ANSYS with the geometry as shown in Figure 4.9 with 5 coil-turns (not shown) and 4 turns of orthonol in between: (a) Showing the magnetic flux density (B, unit: T) and (b) Showing the flow of magnetic field (B)

Figures 4.11a and 4.11b show the magnetic results for 5 coils with 4 turns of Orthonol inserted inbetween the coil-turns. For this particular model a current (I_{coil}) of 0.8 A is input to the microcoil to fully deflect the membrane. As shown in Table 4.1, the produced electromagnetic force (F_{EM}) is 924 μN compare to F_{EM} = 951 μN for the case of 8 coil-turns without orthonol in between. This shows a significant improvement of the Orthonol insertion in between the microcoil, which confirms our previous results in 2D models. Hence to produce about the same amount of F_{EM}, only 5 coil-turns instead of 8 coil-turns are required. This reduces the coil resistance (R_{coil}) and the power concumptions (P_{coil}) approximately by 30% for the microvalve operation.

Figure 4.11a and 4.11b shows that the saturation, B > 1.4 T, occurs in more distributed area of the microvalve, compared to the results in Figures 4.10a and 4.10b. The saturation is no longer concentrated in the gasket but it is more distributed to the orthonol beneath the membrane.

Figure 4.11b shows that the additional of orthonol in between the coil-turns provides the access for the magnetic field from the centered soft magnetic dome to go directly to the mirovalve base, thus it reduces the magnetic reluctance of the air gap as indicated by Equation 4.1. There is a local circulation of the magnetic field from the coil turns directly to the orthonol. This results in more distribution of the magnetic field beneath the membrane. Eventhough it has been proven theoretically and supported by FEA that the orthonol insertition produces more efficient coupling to the microcoil and reduces the power consumtion, this idea was not implemented in the microvalve because the fabrication is complex.

Table 4.1 below summarize the results of the electromagnetic force (F_{EM}) produced from the 3D modeling, with the geometry as shown in Figure 3.9. It shows the results at different input current to the microcoil (I_{coil}) and the gap (g) distance.

Table 4.1. 3D (three dimensional) finite element analysis (FEA) results from ANSYS 5.7

Model: 12 µm initial gap distance with 8 turns of coils				
I_{coil} (A)	**F_{EM}, Magnetic Force (µN)**	**B_{max} (T)**	**Location of B_{max}**	**Membrane Condition**
0.4	504	1.47	Gasket	Is not fully deflected
0.5	530	1.6	Gasket	Is not fully deflected
0.6	582	1.62	gasket + cantilever	Is not fully deflected
0.7	720	1.65	gasket + cantilever	Full deflection
0.8	951	1.7	gasket + cantilever	Full deflection
Model: 12 µm gap distance with 5 turns of coils and 4 orthonols in between				
0.7	692	1.6	Gasket + Cantilever	Is not fully deflected
0.8	924	1.72	gasket + cantilever	Full deflection
Model: 17 µm gap distance with 8 turns of coils				
0.9	1,250	1.92	gasket + cantilever	Full deflection
Model: 17 µm gap distance with 5 turns of coils and 4 orthonols in between				
0.9	1,220	1.71	gasket + cantilever	Full deflection

4.1.5.2 On/Off Microvalve with Buckled Membrane

Figure 4.12 shows the structural results of the ANSYS 5.7 analysis, for the model with buckled membrane. The geometry of the microvalve is the same as in Figure 3.9,

except that the membrane is initially buckled upward with a distance of 15 μm from the horizontal/flat position. This is called 1st stable position as shown in Figure 4.12a. A current of I_{coil} = 1.0 A, is drawn to the microcoil until the membrane deflects and achieves its 2nd stable position, as shown in Figure 4.12d. Figure 4.12 shows the membrane displacement (d_m) at 4 (four) different iterations. In total of 43 iterations are required to finish the analysis.

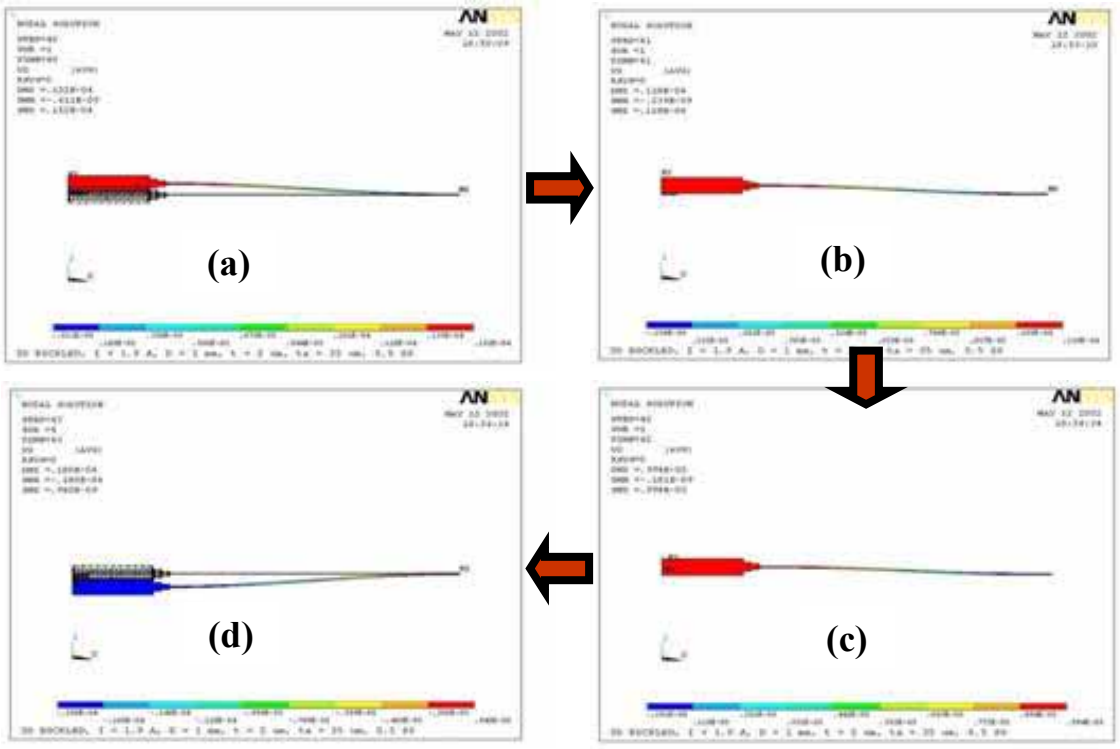

Figure 4.12. (ACW) The structural results of the buckled membrane produced by FEA using ANSYS 5.7, showing the membrane displacement (d_m): (a) The membrane is initially deflected upward, d_m = +15 μm. It is the first (1st) stable position. (b) The membrane deflected downward due to the electromagnetic force (F_{EM}) produced from the microcoil. (c) The membrane reaches its instability point and starts to lose its stiffness. (d) The membrane moves downward to achieve its 2nd stable position and regains its stiffness.

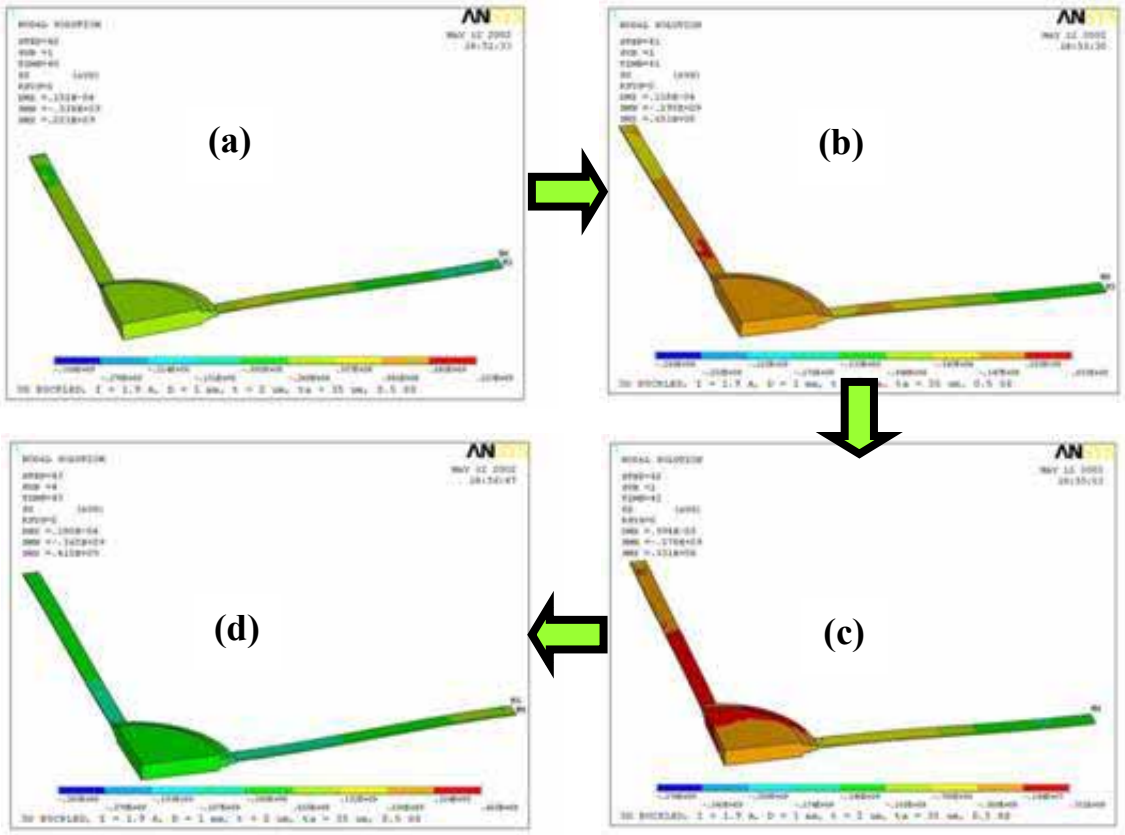

Figure 4.13. (ACW) The structural results of the buckled membrane produced by FEA using ANSYS 5.7, showing the lateral stresses (S_X). (a) The membrane is initially deflected upward, d_m = +15 μm. The membrane is at the first (1st) stable position and experiences compressive stresses. (b) The membrane deflected downward due to the electromagnetic force (F_{EM}) produced by the microcoil. (c) The membrane reaches its instability point and starts to loss its stiffness. The membrane is nearly at flat position and experiences the combination of compressive and tension stresses. (d) The membrane moves downward to achieve its 2nd stable position and regains its stiffness. The membrane experiences compressive stresses.

Figure 4.13 shows the lateral stress (S_X, Pa), experienced by the membrane at different iterations. As shown in Figure 4.13 that most of the stress is experienced by the elements on the supports, as expected. A combination of tensile and compression stresses are experienced in the centered dome as it comes to instability point as shown in Figure 4.13c. It is the point where the membrane supported legs loose its stiffness and try to

come to the second stable position. The membrane then suddenly moves to the 2nd stable position as shown in Figure 4.13d to regains its stiffness and the stresses becomes compressive.

4.2 Design of Bistable Mechanism

4.2.1 Introduction

This section discusses in detail the design of the bistable mechanism for the microvalve operation. The schematic of the microvalve with the bistable mechanism is shown in Figure 3.5. Figures 3.6 and 3.7 show the basic principle of the bistable operation. It indicates that extensive designs for the membrane spring force (F_S), the electromagnetic force (F_{EM}), and the remanence force of the permanent magnet (F_R) are required in order to achieve the bistable mechanism.

4.2.2 Membrane Spring Force (F_S)

The membrane spring force (F_S) comes from the stiffness of the membrane supported legs. In order to determine F_S, one has to determine the amount of membrane displacement (d_m) required to close the outlet orifice, which is located at the center of the microcoil, as shown in Figure 3.5. The initial gap (g) between the permanent magnet and the microcoil is designed to be 30 μm. F_S is determined by three approaches: beam theory, finite element analysis (FEA), and experiment.

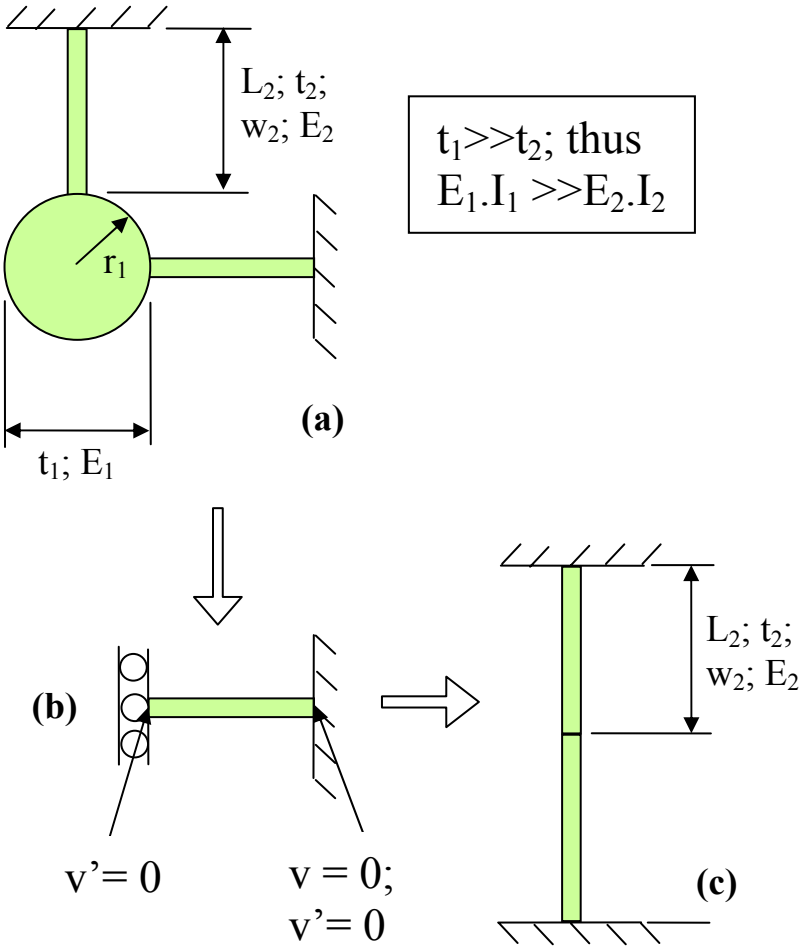

Figure 4.14. Simplified membrane geometry for the application of beam theory: (a) The membrane geometry of the bistable microvalve; (b) Because $E_1.I_1>>E_2.I_2$, the membrane supported leg can be approximated by a roller ($v' = 0$) and a fixed support ($v = 0$ and $v' = 0$); (c) The membrane geometry can be approximately by statically indeterminate beam with the length of $2.L_2$

As shown in Figures 3.5 and 4.14a because the thickness of the centered membrane (t_1) is much thicker than the legs thickness (t_2), the centered membrane remains flat during its motion. Thus the membrane geometries can be simplified into a statically indeterminate beam with fixed supports at both ends as shown in Figure 4.14c.

When the total length of the beam is $2.L_2$, the spring force (F_S) is determined from beam theory by Equation 4.4 [89, p.707]:

$$F_S = \frac{24.E_2.I_2}{L_2^3} = \frac{2.E_2.w_2.t_2^3}{L_2^3} \qquad (4.4)$$

Where: E_2, w_2, t_2, and L_2 are the Young's modulus, width, thickness, and length of the legs respectively. These values are 65 GPa [88], 60 μm, 4 μm, and 350 μm respectively. The value of the Young's modulus 65 GPa is for permalloy (80% Ni and 20% Fe). The F_S results from the beam theory [89, p.707] are shown in Figure 4.16.

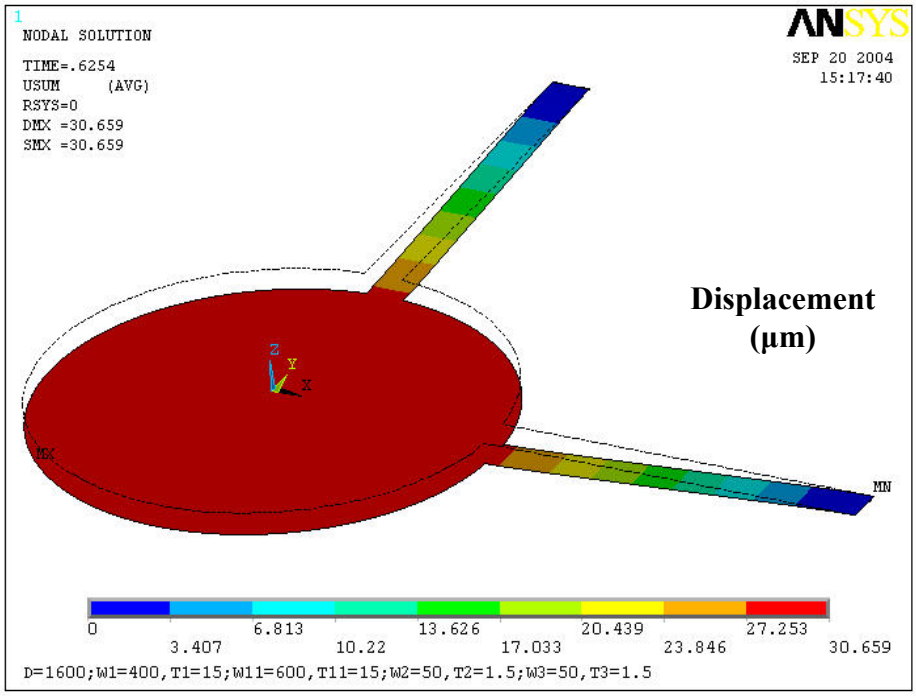

Figure 4.15. The FEA results from ANSYS 5.7 showing the membrane downward displacement at 30 μm

In order to determine F_S by finite element analysis (FEA), ANSYS 5.7 is used. 3D (three dimensional) shell element with nonlinear geometry and stress stiffening capabilities is used to build the model. The ANSYS 5.7 results showing the deformation of the membrane at the maximum deflection of 30 μm is shown in Figure 4.15. The FEA results on F_S are graphed in Figure 4.16. Another approach is to measure the stiffness of the membrane experimentally by Tribo Indenter, Hysitron Inc., model 1BR-12. The experimental results are also shown in Figure 4.16.

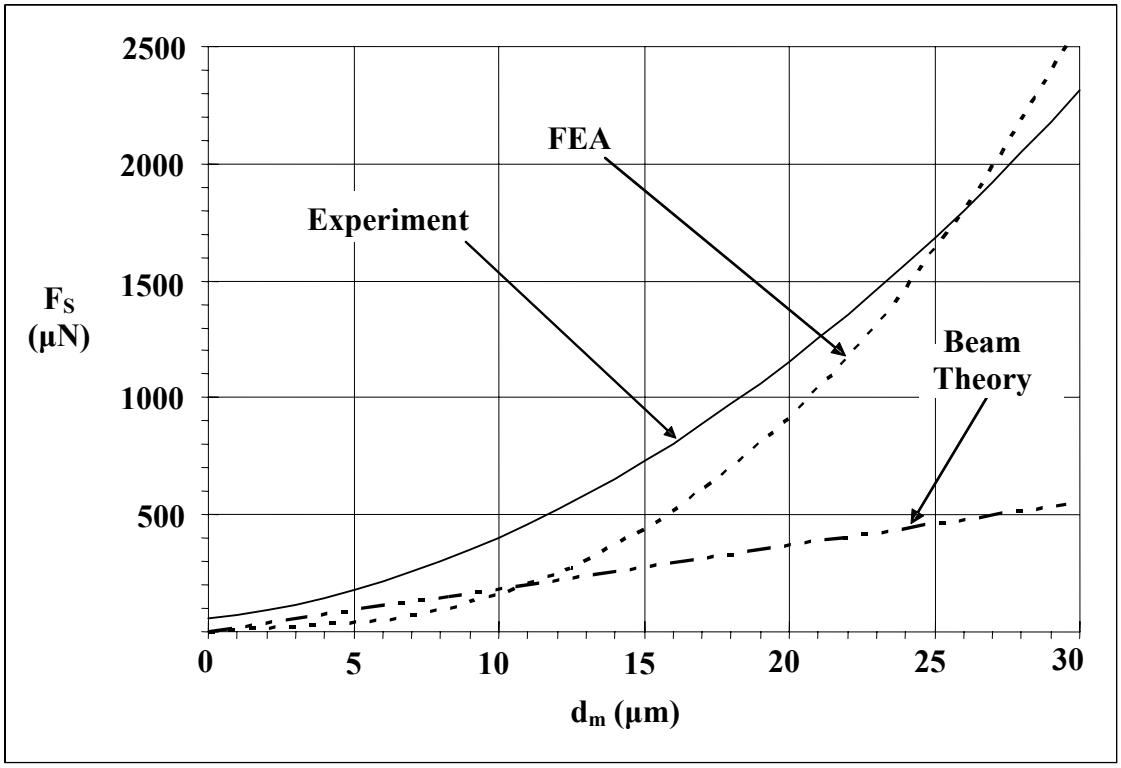

Figure 4.16. Combined results (beam theory, FEA, and experiment) on force versus displacement, it shows the variation of the membrane spring force (F_S) with the membrane displacement (d_m)

Figure 4.16 shows the combined theoretical, FEA, and experimental results in measuring F_S. It shows clearly that the beam theory does not give a good prediction of the membrane stiffness. The results show that the membrane stiffness (k_S) is constant. This is not the case for a large deformation. The FEA results show that F_S is not linearly related to the membrane displacement. It starts with a linear relationship at a small displacement and becomes non-linear as the displacement increases. The nonlinearity occurs because of the stress stiffening effects in the membrane legs. FEA results show that F_S is 2,502 μN at 30 μm displacement. The experimental results confirm the non-linear behavior of the membrane displacement. However the experimental results show higher values of F_S at the initial displacement and lesser stress stiffening behavior at higher displacement. The experimental results show that F_S is 2,312 μN at 30 μm. The experimental results are used as guidance in designing for the actuator magnetic forces.

4.2.3 Remanence Force of the Permanent Magnet (F_R)

An important component required for the bistable mechanism of the microvalve actuator is the permanent magnet that is attached on the soft magnetic dome. As shown in Figure 3.6c, the permanent magnet provides a remanence field during the latching (2^{nd} stable) position. In order to keep the valve closed, the remanence force (F_R) of the permanent magnet has to exceed the spring force (F_S) of the membrane at its minimum downward displacement, thus $F_R > 2{,}312$ μN.

In order to estimate F_R, Equation 3.3 is used. When the membrane is in the latching position, the gap (g) is zero and there is no input current (I_{coil}) to the micro coil.

By assuming that there is no magnetic leakage in the structure, $B_g \approx B_R$ (remanence flux density) of the permanent magnet. For the bistable operations, CoNiMnP has been selected as the permanent magnet material. It has the magnetic properties as shown in Table 4.2 below, adapted from [54] below:

Table 4.2. Magnetic Properties of CoNiMnP

Properties		**Unit**
H_C	57 – 88	kA/m
B_R	0.17 - 0.19	T
$(B.H)_{MAX}$	1.9 - 2.3	kJ/m^3

After substituting the value of B_R into Equation 3.3, the values of F_R are plotted against the radius of the permanent magnet (r_M) as shown in Figure 4.17. It shows that the minimum radius of the magnet to maintain the valve closed is 225 μm with the $F_R \approx 2312$ μN. For this application, the microvalve is designed to provide the burst pressure (dP_{burst}) of 10 kPa against the fluidic flow. For the bistable microvalve as shown in Figure 3.5, the outer radius of gasket (r_G), which is the center of the Au microcoil, is designed to be 100 μm. For this size of gasket, the latching force (F_L) is equivalent of 315 μN. Thus the minimum required remanence force (F_R) to achieve the valve design is $F_S + F_L = 2{,}627$ μN. The r_M is designed to be 250 μN, which has F_R of 2,820 μN.

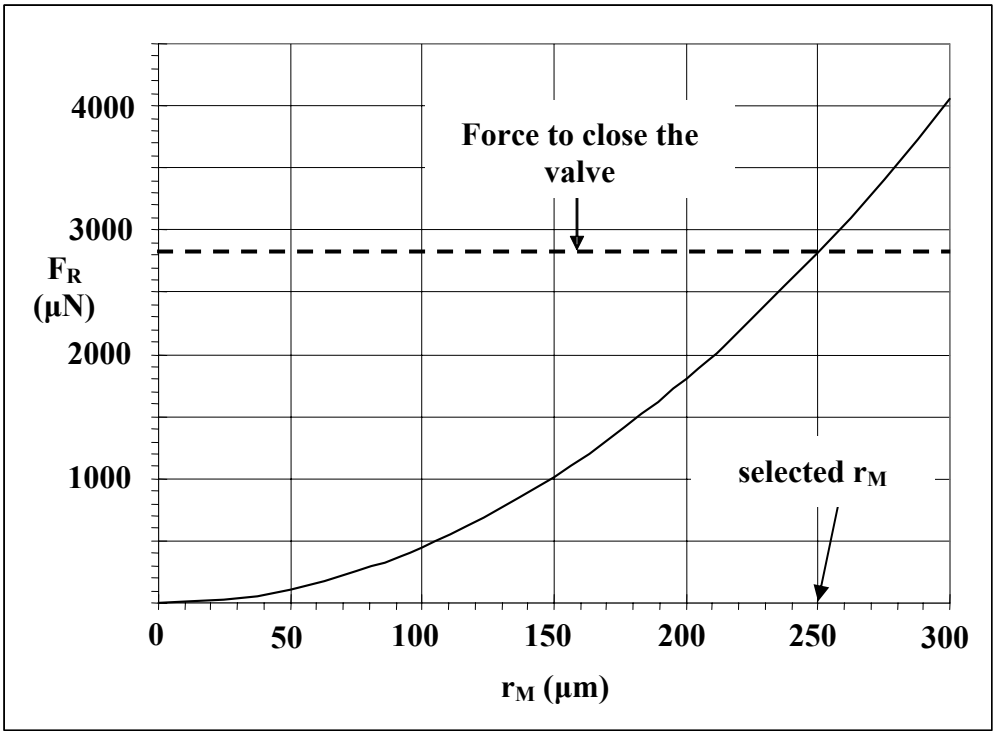

Figure 4.17. The variation of the remanence force (F_R) with the size of the magnet (r_M); the permanent magnet with r_M = 250 µm is selected to provide the burst pressure (dP_{burst}) of 10 kPa for the microvalve operation

4.2.4 The Electromagnetic Force (F_{EM})

As mentioned before, the membrane will not move from the flat (1st stable) position, Figure 3.6a, to the latching (2nd stable) position, Figure 3.6c, unless an additional electromagnetic field in the same direction as the permanent magnet alignment is presents. The additional flux density across the gap (B_g) is produced when a current (I_{coil}) flows in the micro coils beneath the membrane. In order to design the electromagnetic force (F_{EM}), Equation 3.4 is used. The amount of F_{EM} is proportional to the change in the flux density of the microcoil/electromagnet along the z-direction $\left(\frac{dB_Z}{dz}\right)$. The value of $\left(\frac{dB_Z}{dz}\right)$ depends on the amount of current (I_{coil}) drawn into

the electromagnet and the gap (g). The value of $\left(\frac{dB_Z}{dz}\right)$ is determined from ANSYS 5.7 simulation, where we use 2D axisymmetric magnetic model. Figure 4.18 below shows a sample of the FEA results from ANSYS 5.7, it shows the variation of $\left(\frac{dB_Z}{dz}\right)$ along the gap distance.

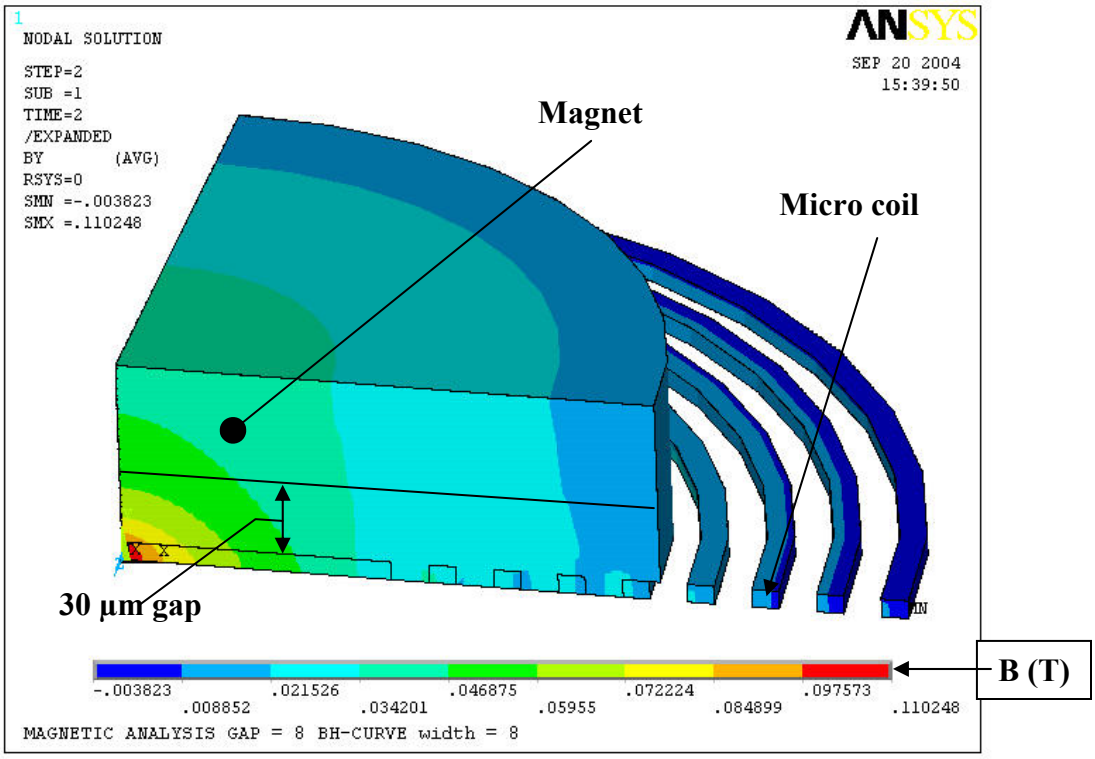

Figure 4.18. FEA results by ANSYS 5.7, showing the variation of magnetic flux density (B_Z) produced by the electromagnetic coil. The gap (g) distance between the permanent magnet and the microcoil is 30 µm and there is no input current to the microcoil.

As shown in Equation 3.4, the magnitude of F_{EM} is proportional to the volume of the magnet (V_M). Thus the thickness of magnet (t_M) has to be properly designed. The way

that t_M is designed is based on the required current (I_{coil}) to the microcoil in order to fully displace the membrane downward and close the microvalve. In order to determine the membrane displacement (d_m) because of the applied F_{EM}, the experimental results on the membrane stiffness as shown in Figure 4.16 are used. The FEA results showing d_m versus I_{coil} plotted at different t_M are shown in Figure 4.15. It shows that smaller t_M produces a significant decrease in the magnitude of d_m.

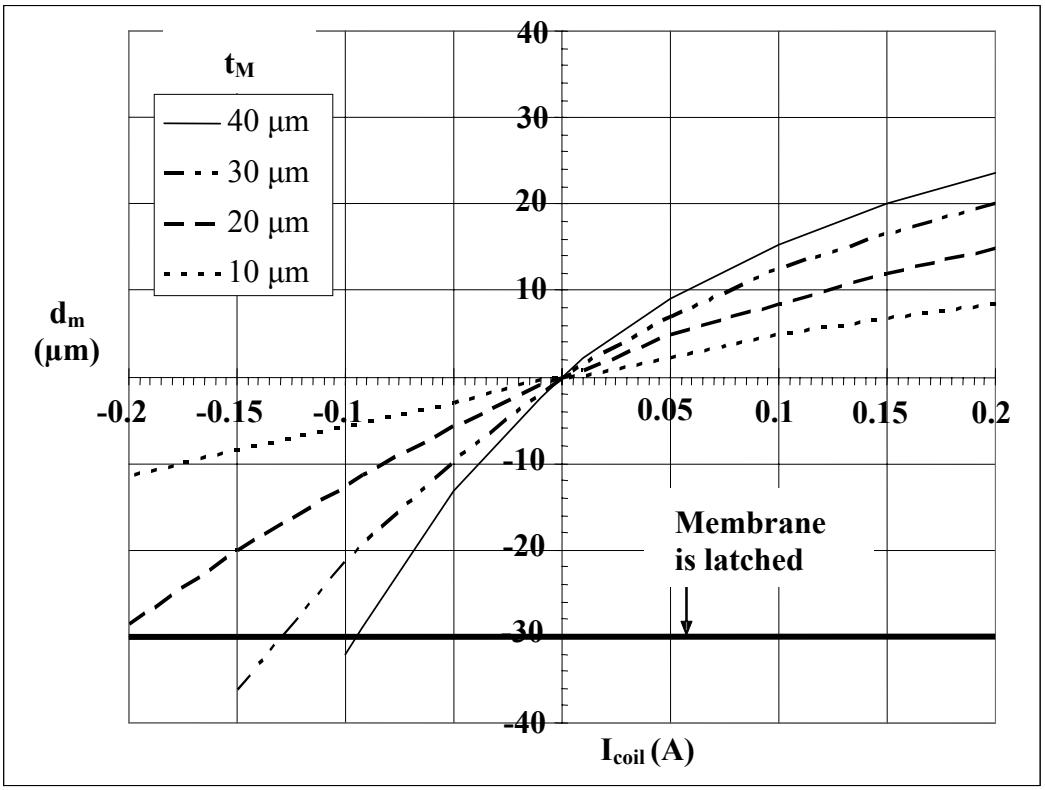

Figure 4.19. The membrane displacement (d_m) versus input current (I_{coil}) to the micro coil, plotted at different permanent magnet thickness (t_M)

In order to latch the membrane, d_m has to achieve its minimum displacement of -30 μm. Figure 4.20 shows the required input current (I_{coil}) at different t_M, to produce d_m =

-30 μm. It shows that I_{coil} decreases significantly when t_M increases from 10 to 20 μm. For further increases in t_M, the slope continues to decrease and saturate at a certain magnitude. The valve is designed so that the required I_{coil} to latch the membrane is less than 0.1 A. Figure 4.20 shows that when t_M = 40 μm, the required current to latch the membrane is 0.094 A. Thus CoNiMnP magnet is designed to have the thickness of 40 μm.

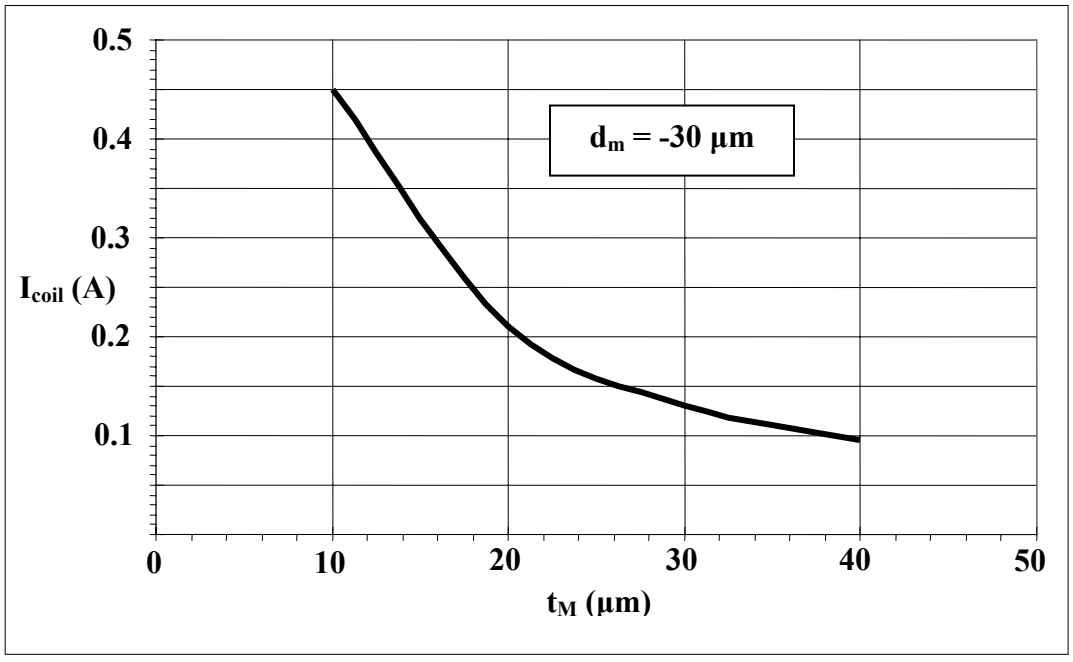

Figure 4.20. The required input current (I_{coil}) to the microcoil at different permanent magnet thickness (t_M) in order to produce d_m = -30 μm and latch the membrane.

It should be noted that FEA results shown in Figures 4.19 and 4.20 are for the membrane displacement (d_m) in the free air medium. The results should be different when the displacement is performed inside the liquid (water) medium where the squeeze film

damping produces significant forces that hinder the fluidic movement. Thus more current (I_{coil}) is required in water than air to produce the same amount of displacement.

4.3 Design of Bidirectional Actuator

4.3.1 Introduction

This section discusses the steps that have been taken to design large displacement bidirectional actuator. In order to produce a bidirectional actuation, we need to determine the force required to deflect the membrane or the membrane spring force (F_S) and the electromagnetic force (F_{EM}) produced by the interactions between the permanent magnet and the microcoil. Two types of membrane are designed for the bidirectional micro actuators. A membrane with 2 legs-design separated by 90° angle, as shown in Figure 3.5 (except that there is no inlet/outlet orifices), and single-leg design. The double-legs design has the initial gap (g) distance of 70 μm and the single-leg design has the gap (g) distance of 100 μm. The thickness (t_2) and width (w_2) of each leg are 2 μm and 60 μm respectively.

4.3.2 Membrane Spring Force (F_S)

In order to determine the spring force (F_S), three approaches are used: beam theory, FEA, and experiment. As mentioned before, there are two types of membrane support, double-legs design and single-leg design. The designs of each type are discussed separately.

4.3.2.1 Double-legs Design

Because the thickness of the centered membrane (t_1) is designed to be much thicker than the legs thickness (t_2), the centered membrane remains flat during its motion. Thus Equation 4.4 is used to determine the spring force (F_S), where the values of E_2, w_2, t_2, and L_2 are 65 GPa, 60 μm, 2 μm, and 350 μm respectively. The results of the beam theory are plotted in Figure 4.22.

4.3.2.2 Single-leg Design

For a single-leg design, the theoretical F_S is determined by using a beam theory as shown in Figure 4.21 and Equation 4.5 in Reference [89, p. 655]

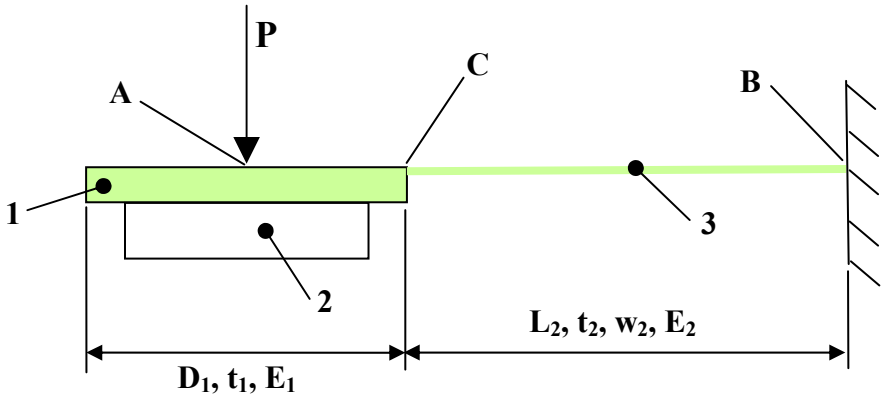

Figure 4.21. Application of the beam theory to determine the deflection of the membrane with single-leg design; 1 = centered soft magnetic membrane; 2 = permanent magnet; 3 = a membrane leg

The deflection (δ_A) of a cantilever beam ACB, which have two different moments of inertias, I_1 and I_2, due to a concentrated load P can be divided into three main parts [89, p.655] as shown in Equation 4.5. Where: δ_1 is the deflection due to bending of part AC of the beam, δ_C is the deflection due to the downward motion of point C, and $\theta_C.L_1$ is the deflection due to the rotation of point C. The results of beam theory as shown in Equation 4.5 are plotted in Figure 4.23.

$$\delta_A = \delta_1 + \delta_C + \theta_C.L_1 =$$
$$\left(\frac{F_S.L_1^3}{3.E_1.I_1}\right)+\left(\frac{F_S.L_2^3}{3.E_2.I_2}+\frac{(F_S.L_1).L_2^2}{2.E_2.I_2}\right)+\left(\frac{F_S.L_2^2}{2.E_2.I_2}+\frac{(F_S.L_1).L_2}{2.E_2.I_2}\right).L_1$$
$$F_S = \qquad (4.5)$$
$$\delta_A.\left(\left(\frac{L_1^3}{3.E_1.I_1}\right)+\left(\frac{L_2^3}{3.E_2.I_2}+\frac{L_1.L_2^2}{2.E_2.I_2}\right)+\left(\frac{L_2^2}{2.E_2.I_2}+\frac{L_1.L_2}{2.E_2.I_2}\right).L_1\right)^{-1}$$

Where: δ_1 is the deflection due to bending of part AC of the beam, δ_C is the deflection due to the downward motion of point C, and $\theta_C.L_1$ is the deflection due to the rotation of point C. The results of beam theory as shown in Equation 4.5 are plotted in Figure 4.23.

In order to determine F_S by finite element analysis (FEA), ANSYS 5.7 is used. 3D shell element with nonlinear geometry and stress stiffening capabilities was used to build the model. The membrane stiffness is experimentally measured with Tribo Indenter, Hysitron Inc., model 1BR-12. The FEA and experimental results of double-legs and single-leg designs are shown in Figures 4.22 and 4.23 respectively.

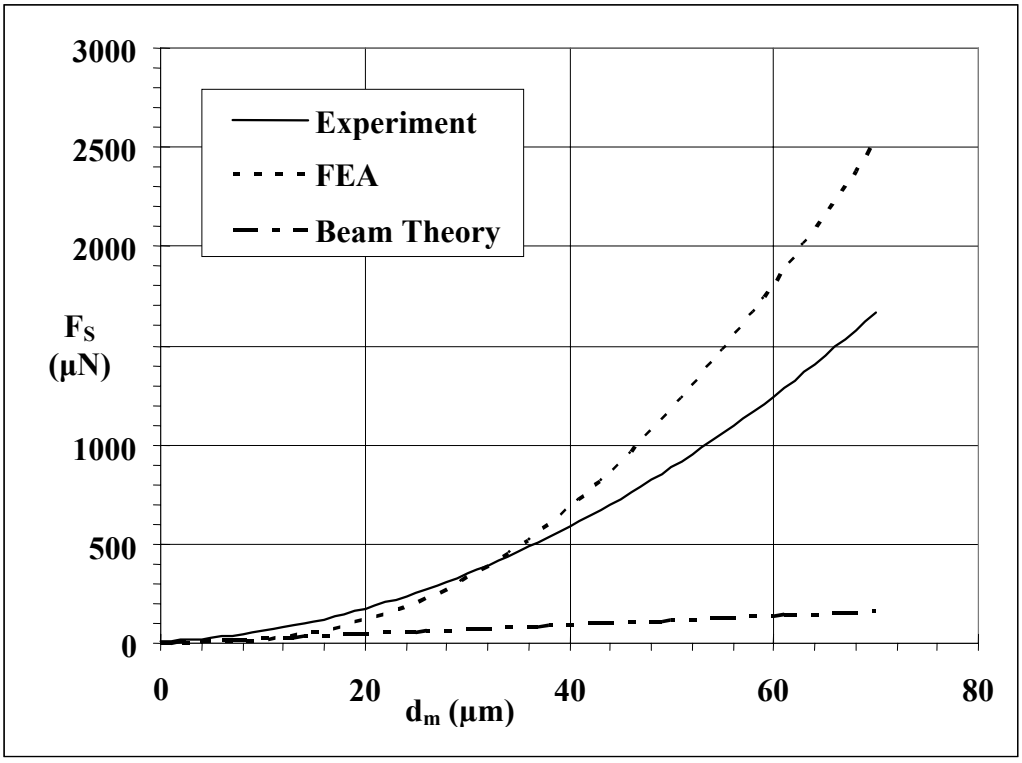

Figure 4.22. The combined results (Theory, FEA, and Experiment) of the membrane spring force (F_S) for double-legs design at different membrane displacement (d_m)

Figure 4.22 shows that there is a good agreement between FEA and experimental results at small d_m, $d_m < 30$ μm. However as d_m increases, FEA shows much larger F_S than the experiment. FEA presents more stress stiffening effect on the membrane legs than the experiment. Meanwhile the beam theory results do not agree with the experiment. It is shown in Figure 4.23 for the single-leg design that the results from beam-theory are much smaller than the FEA and experiment, and do not show any stress stiffening behavior at all. The experimental results as shown in Figures 4.22 and 4.23 are then used for designing the electromagnetic force (F_{EM}) of the bidirectional microactuator.

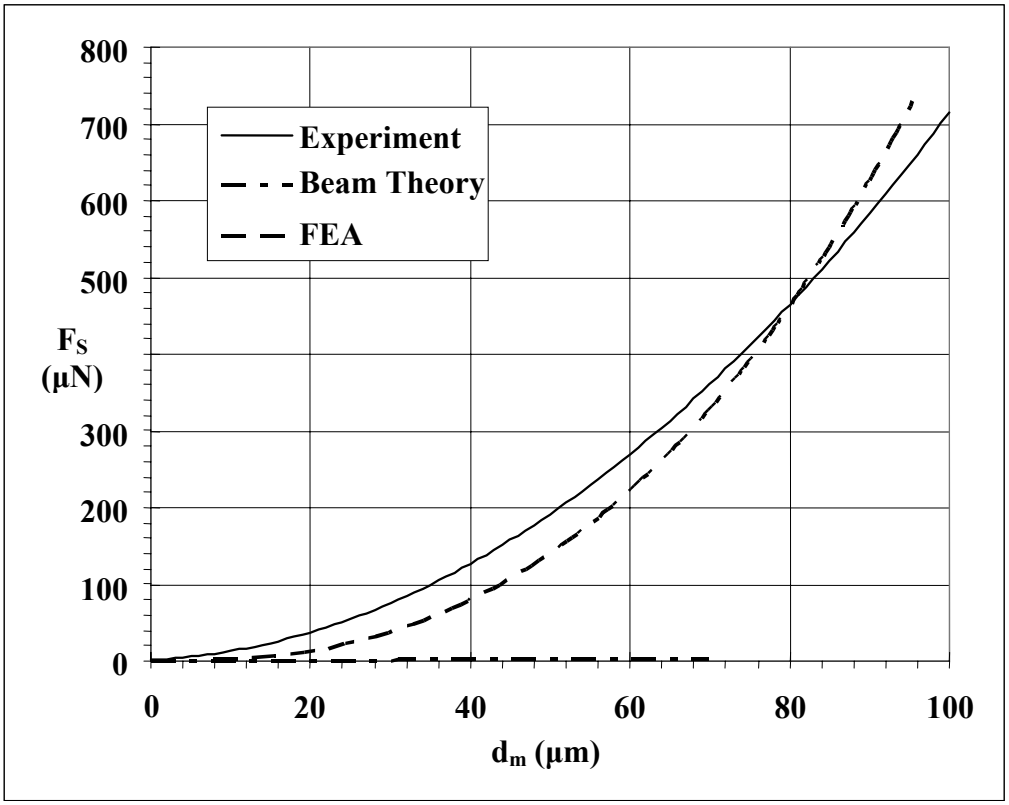

Figure 4.23. The combined results (theory, FEA, and experiment) of the membrane spring force (F_S) for single-leg design at different membrane displacement (d_m)

4.3.3 The Electromagnetic Force (F_{EM})

In order to determine the electromagnetic force (F_{EM}) produced, Equation 3.4 is used. The F_{EM} is proportional to the change in flux density of the microcoil along the z-direction $\left(\frac{dB_Z}{dz}\right)$. The value of $\left(\frac{dB_Z}{dz}\right)$ depends on the amount of current drawn into the microcoil (I_{coil}) and the gap (g) between the magnet and the microcoil. In order to determine, B_Z, finite element analysis (FEA) by ANSYS 5.7 is used. Figure 4.24 shows FEA results for B_Z from ANSYS 5.7 at different g and I_{coil}.

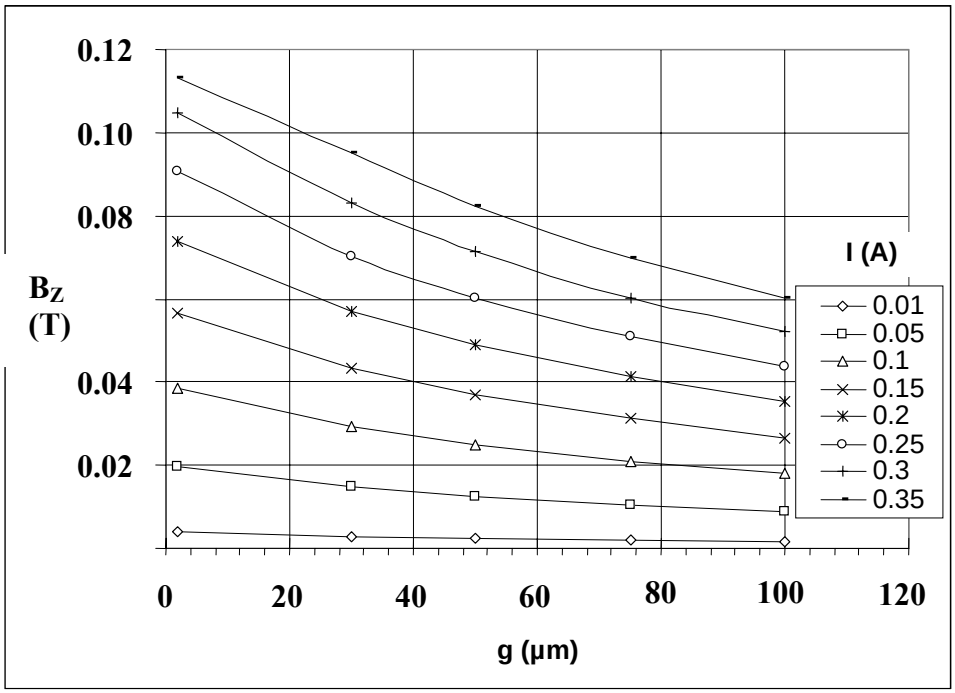

Figure 4.24. The variation of magnetic flux density (B_Z) of the micro coil at different gap (g) distance. Plotted at various input currents (I_{coil})

Co-Pt is selected as the material for the permanent magnet in the bidirectional microactuator. The magnetic properties of the Co-Pt magnet are shown in Table 4.3 below [107].

Table 4.3. Magnetic properties of CoPt

Properties		Unit
H_C	279 – 292	kA/m
B_R	0.411 - 0.488	T
$(B.H)_{MAX}$	29.52 – 34.5	kJ/m^3

Equation 3.4 shows that F_{EM} is also proportional to the volume of the Co-Pt magnet. Figure 4.25 shows the combined FEA results for d_m at different thickness of magnet (t_M) for double-legs design. The circular diameter of magnet (D_M) is designed to be 500 µm. The experimental results of F_S as shown in the Figure 4.22 are used in order to determine the membrane deflection (d_m) due to the applied F_{EM}.

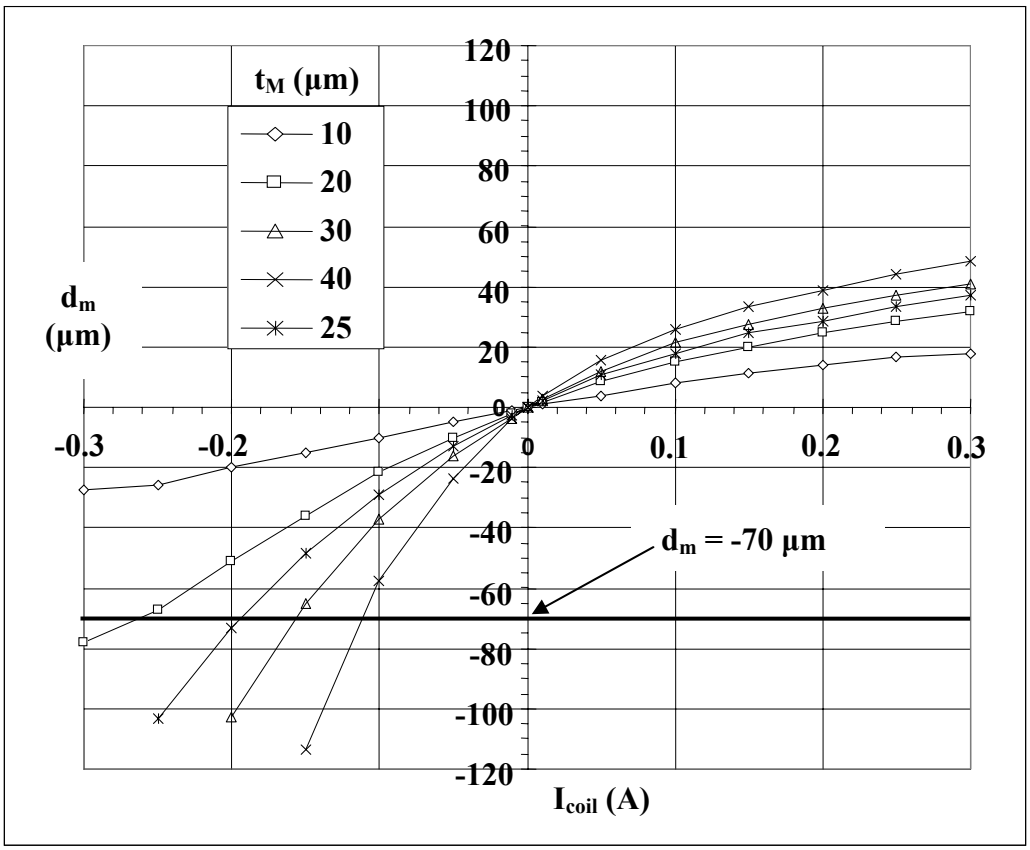

Figure 4.25. FEA results for the membrane displacement (d_m) at different input current (I_{coil}) of the bidirectional microactuator with double-legs design. The results are plotted at various thicknesses of permanent magnet (t_M).

Figure 4.25 shows that when t_M = 10 μm, d_m is pretty much linearly related to I_{coil}, and the upward d_m is similar to the downward d_m at the same magnitude of I_{coil}. At larger t_M, e.g. t_M > 10 μm, d_m shows to be non-linear with I_{coil}, and the magnitude of the downward d_m is larger than the magnitude of upward d_m at a given I_{coil}. The slope of downward d_m keeps increasing as the magnitude of I_{coil} increases; meanwhile the slope of upward d_m keeps decreasing. The upward d_m seems to saturate at a certain maximum value (d_{max}). The thickness of magnet (t_M) is designed so that the microactuator achieves its minimum deflection (d_{min}), which is -70 μm at I_{coil} = -0.2 A. Figure 4.25 shows that when t_M = 25 μm, the required I_{coil} = -0.19 A to achieve d_{min} = -70 μm. This thickness is then selected as the designed thickness of CoPt magnet both for double-legs and single-leg design.

CHAPTER 5

FABRICATION

5.1 Introduction

This chapter discusses the fabrication steps that have been developed to build the microvalves. There are two different designs of microvalve that have been fabricated: an on/off microvalve and a latching bistable microvalve. The microvalve with the bistable mechanism requires an additional component: an electroplated permanent magnet. Figure 5.1 below shows a schematic of the major challenges that the fabrication processes have to overcome.

As shown in Figure 5.1, the microvalve has 6 (six) components that have to be integrated to fabricate on a single microvalve with an overall size of less than 2000μm in diameter. The components are: a micro coil, a membrane, a permanent magnet, an inlet orifice, an outlet orifice, and a valve base. At the same time the fabricated components have to meet all the processing parameters associated with the demanda described in the sections that follow.

1. Single wafer fabrication

This is the most difficult part of the microvalve fabrication process. As discussed in the literature review in chapter 1, most microvalves, whether they are electromagnetically, electrostatically, or piezoelectrically driven, have fabrication processes that require using two or more silicon wafers. Capanu et. al. [56] developed a

bistable electromagnetically driven microvalve, which was fabricated using two silicon wafers. One wafer was used to define the inlet hole and the Au microcoil. Another wafer was used to define the beam-actuator. Finally, for the bistable mechanism, the microvalve had an external permanent magnet that was glued onto the beam actuator.

Rich and Wise [66] have developed a high-flow thermopneumatic microvalve for which they use three substrates during its fabrication. One glass substrate is used to define the inlet for the gas, a silicon substrate is used to define the membrane actuator, and another glass substrate is used to define the micro heaters and gas outlet.

For the fabrication process developed in this research, all of the components parts of the microvalve: Au microcoil, membrane actuator, valve base, inlet orifice, outlet orifice, and permanent magnet have to be built on top of a silicon single wafer.

2. All components have to be fabricated entirely by surface micromachining in a batch process.

The words “surface micromachining” and “bath process” mean that there are no external parts can be incorporated into the foundry process to define the valve structure. This is obviously a difficult challenge to overcome. The fabrication of the microvalve would be much easier if an external electromagnetic coil and an external permanent magnet were incorporated in the valve mechanism.

Capanu et. al. [56], his latching electromagnetic microvalve, adopted an external 46-μm-thick Arnokrome#3 rolled magnetic foil (Arnold Engineering Company, Marengo, IL) made of Cr/Co/Fe rolled alloy. Cho and Ahn [54] developed a bidirectional

magnetic actuator and incorporated a commercially available surface mountable planar inductor (Coilcraft, LPO2506OB-105, 1000 μH).

3. CMOS compatible

Judy and Myung [109] mention that the most successful MEMS product exploits one or more of the following characteristics: (1) batch fabrication to reduce size and hopefully cost, and (2) circuit integration to improve performance, increase capability, and thereby reduce barriers to incorporation into larger systems. In order for MEMS devices to be integrated with electric circuits that are often complementary metal-oxide-semiconductor (CMOS) based, the fabrication process for the MEMS device has to be adaptable to the limitation of the electrical components or CMOS compatible. One of the critical parameters is temperature limitation; the metallization part of the circuits start to deteriorate at a temperature of 400 °C. Thus the maximum fabrication temperature of the microvalve has to be less than this temperature. This limitation produces a major problem for the permanent magnet that is a main component for the bistable mechanism of the microvalve. In order to achieve anisotropy for the permanent magnet, heat treatment has been commonly used in conventional permanent magnets such as Nd-Fe-B permanent magnets [112, 113]. Although this method is a very effective way to align the magnetic moment into a hard magnetic film through crystallization, the device should be heated up to a temperature of 600°C, which, however, is not compatible with the electronics device and MEMS structure.

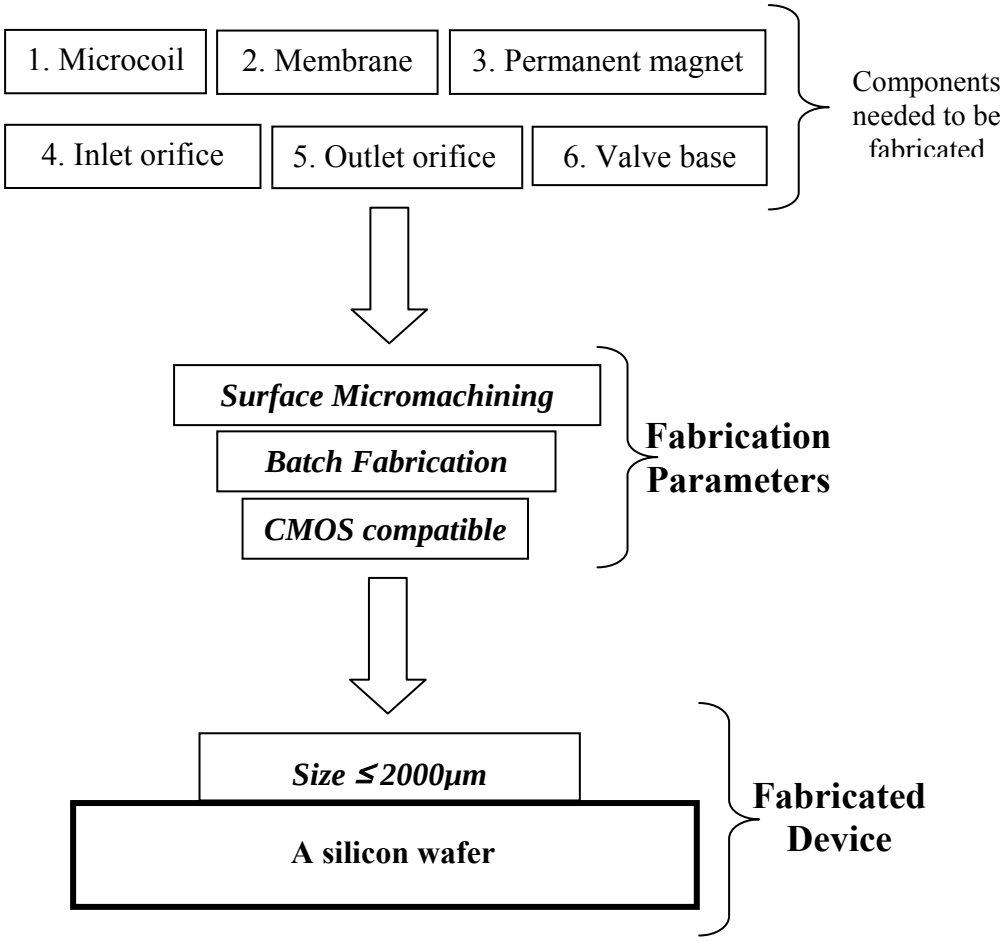

Figure 5.1. The fabrication challenges of the microvalve

5.2 The Microvalve Structure

The proposed fully assembled microvalve is shown in Figure 5.2. As shown in the figure, the surface micromachined microvalve structure, labeled C, consists of eight components. The parts labeled A, B, D, and E in Figure 5.2 are external. Their function is to package the microvalve (C) so that it can be incorporated into external fluidic devices. Details concerning the fabrication of parts A, B, D, and E are described in Chapter 6. This chapter discusses in detail the fabrication of the microvalve structure.

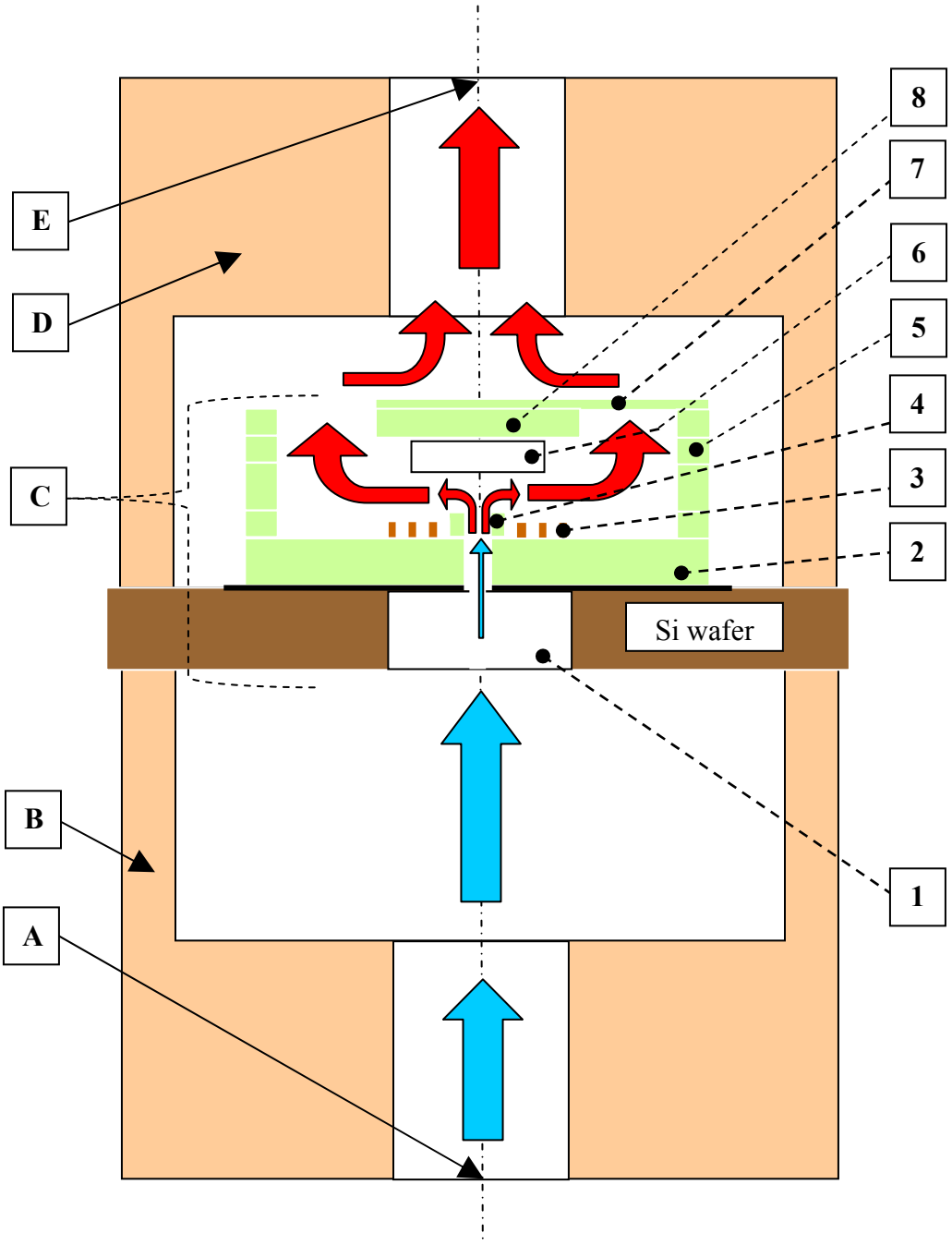

Figure 5.2. The full assembled structure of the microvalve. Where: A = Inlet connector for fluidic flow; B = Inlet flow channel; C = Surface-micromachined microvalve; D = Outlet flow channel; E = Outlet connector for fluidic flow

The microvalve structure these eight components:

[1] Inlet orifice; this is a hole through the silicon wafer where the fluid passes through. The diameter of the circular hole is D_S = 250 μm. To drill a hole through the wafer, deep reactive ion etching (ICP) is used. The process is done by machine, namely the Plasma Therm Inc. model Dual ICP SLR. The etching process called Bosch process has been very effective in etching the silicon and producing high anisotropy with a good quality of side wall. Each cycle of the Bosch process consists of 3 steps: polymerization, polymers etch, and silicon etch. In order to etch through a (100) silicon wafer with the thickness of 500 – 550 μm, the required number of cycles are 1,000 – 1,200. The recipe for the Bosch process is shown in Table 5.1 below.

Table 5.1. Pertinent process parameters for the silicon etch (Bosch Process)

Step	**C_2F_6**	**SF_6**	**Ar**	**Pressure**	**Power**	**Time**
	Sccm	**sccm**	**Sccm**	**mTorr**	**W**	**s**
Polymerization	70	0.5	40	16	825	4
Polymer Etch	0.5	50	40	16	825	2
Silicon Etch	0.5	100	40	16	825	6

[2] The base of the microvalve, it is made of orthonol (50% Ni and 50 %Fe).It is fabricated by thick film electrodeposition or electroplating. The details of the electroplating process are presented in section 5.4.2. The diameter of the base defines the overall diameter ($D_{overall}$) of the microvalve, that is 1,600 μm. The base has a small hole on its center for fluidic flow; the majority of the design has D_b = 60 μm.

[3] The microcoil, which is made of Au (Gold). It is fabricated by electroplating. The detail of the electroplating process is shown in section 5.4.3. The design's important points are these dimensions: the width (W) of the coil is 14 μm, the space (S) between each coil is 10 μm, and the height/thickness (H) of the microcoil varies between 8 – 10 μm.

[4] Outlet orifice, which is the opening for the liquid after passes through the silicon wafer. It is defined by the center of the Au microcoil. It has an inner diameter that is the same as D_b = 60 μm and an outer diameter of 200 μm.

[5] Circular support, which is the solid structure to which the membrane leg is attached. It is made of permalloy (80% Ni and 20% Fe). It is fabricated by thin film electrodeposition or electroplating. The details of the electroplating process are presented in section 5.4.1.

[6] Permanent magnet. This part is required only for a bistable microvalve with a latching mechanism. The permanent magnet is fabricated by electroplating. The details are discussed in sections 5.4.4 and 5.4.5. The diameter of the permanent magnet is D_M = 500 μm.

[7] Centered soft magnetic dome. This is made of permalloy (80% Ni and 20% Fe). It is fabricated by thin film electrodeposition or electroplating. The details of the electroplating process are covered in section 5.4.1.

[8] Membrane supported legs. These are made of orthonol (80% Ni and 20% Fe). They are fabricated by thin film electrodeposition or electroplating. The details of the electroplating process are presented in section 5.4.2.

5.3 Multi Layers Structure

The complex structure of the microvalve includes an actuator with a released membrane that requires multi layer fabrication processes. This means that each layer is fabricated on top of another layer. This fabrication method is very challenging and demands a lot of patience. In each layer, the photoresist is patterned and then the subsequent layer of photoresist is built on top of it. The number of layers the photoresist requires depends on the complexity of the built structure. For example, to define an electromagnetic actuator, only 2 (two) layers are needed. The photoresist is also used as the sacrificial layer to define the gap between the membrane and the microcoil. For the on/off microvalve, the required number of layers are 3 (three). One layer to define the microcoil, another layer to define the soft magnetic centered dome, and the last layer to define the membrane supported legs. The details of the fabrication sequence of the on/off microvalve are discussed in section 5.5. For the bistable microvalve with latching mechanism, one more layer is required to define the permanent magnet. During the fabrication process, the photoresist layers are not removed until the end of the process. Thus the wafer can only be cleaned by D.I. water; there is no solvent and methanol can be used to clean the wafer.

The positive photoresist used for the fabrication process is AZ 4620 (Shipley Inc.). Figure 5.3 shows the approximated thickness of the AZ4620 that is the spin on the top of a clean silicon wafer. The ramping speed is 1,000 rpm/s. The spinning duration is 30 s. The fabrication process become, more challenging as it gets into thicker layers because the photoresist may experience cracking. The cracks may be caused by overheating during soft baking.

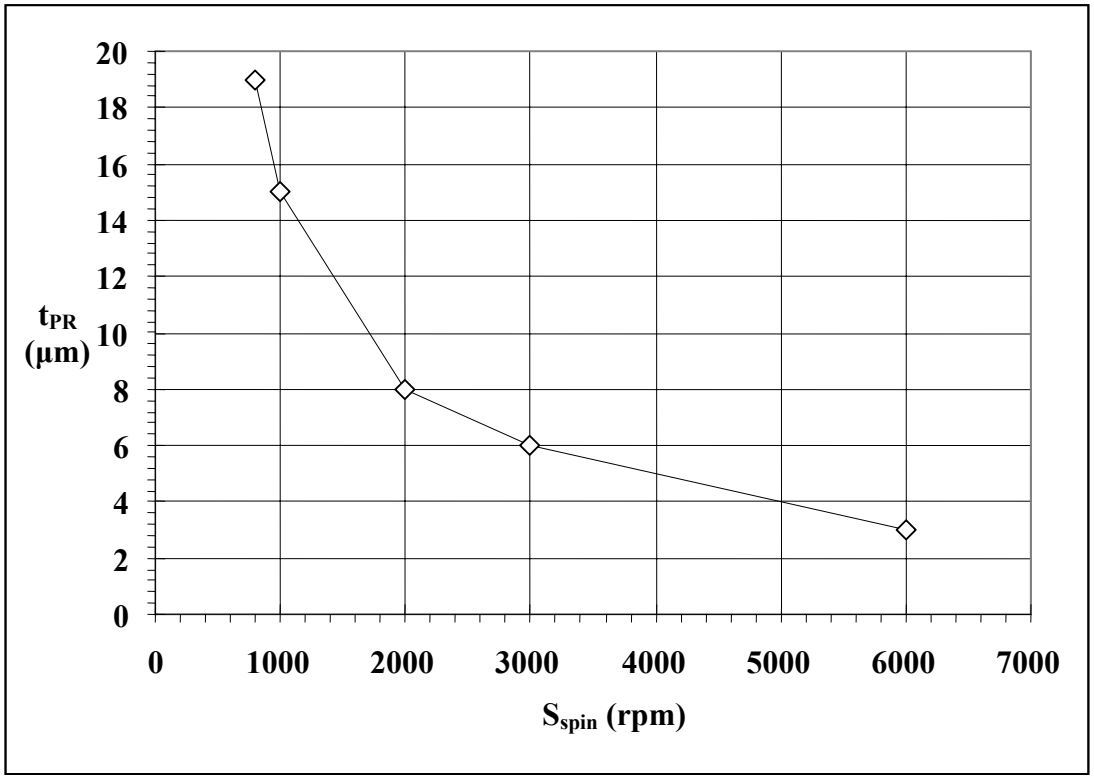

Figure 5.3. Thickness (t_{PR}) of photoresist AZ4620 at different spinning speed (S_{spin}) for duration of 30 s, on top of a clean surface silicon wafer (4" diameter). The ramping speed is 1,000 rpm/s.

For multilayer fabrication processing with AZ 4620, the soft baking temperature has to be reduced as more layers are built up. To compensate for the reduction in the temperature, the required soft baking time has to be increased. Figure 5.4 shows the required soft baking temperature and the required time for different numbers of AZ4620 layers. The soft baking is done inside a convection oven.

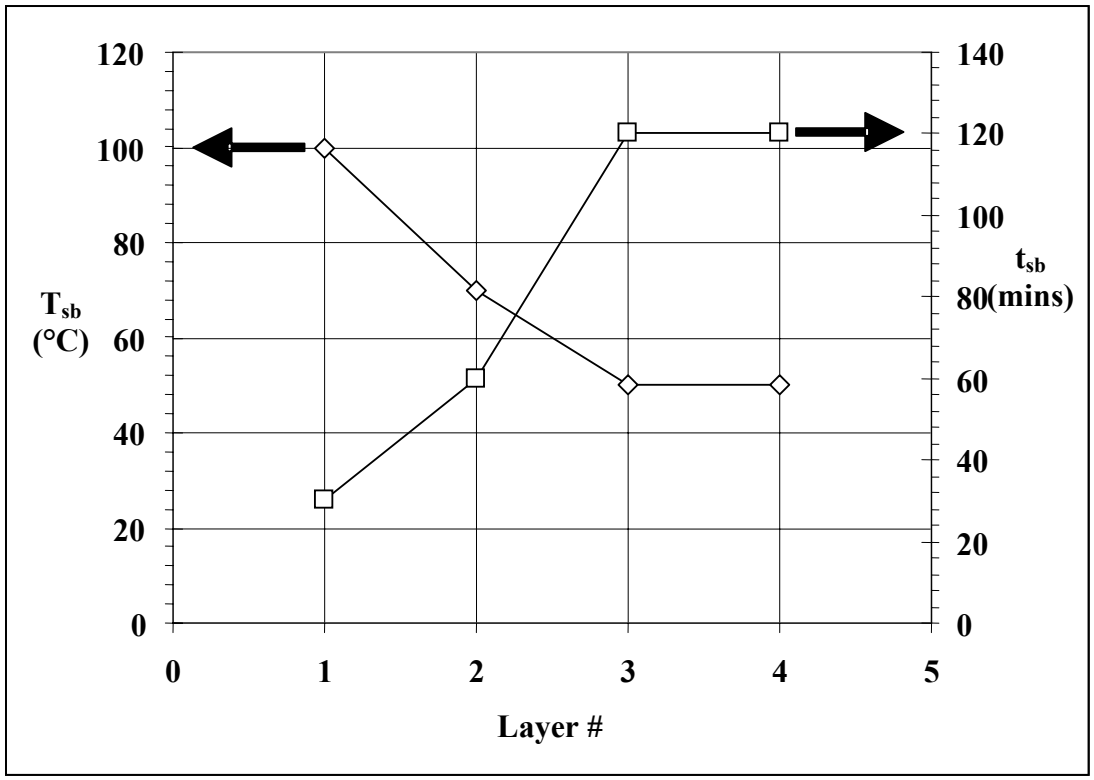

Figure 5.4. The required soft baking temperature and duration inside a convection oven for different number of photoresist AZ4620 layers

5.4 Electroplating

Electroplating has been selected to build the valve structure. The process is relatively simple and inexpensive. The deposition rate is much faster than other metal deposition process such as DC Sputter, RF Sputter, and Chemical Vapor Deposition. There are four different electroplating solutions that have been used to build the valve structure: Permalloy (80% Ni, 20% Fe), Orthonol (50% Ni, 50% Fe), Au (Gold), and permanent magnet.

5.4.1 Permalloy Electroplating

Permalloy is a soft magnetic material. It is used to build the circular supports (label no. 5) and centered soft magnetic dome (label no. 8) as shown in Figure 5.2. The recipe of the electrolyte is shown in Table 5.2 below:

Table 5.2. Chemical composition of electroplating bath for permalloy

Chemical Name	Chemical Compound	gr/L
Nickel Sulfate Hexahydrate	$NiSO_4$. $6H_2O$	200
Ferrous Sulfate Heptahydrate	$FeSO_4$. $7H_2O$	8
Nickel Chloride Hexahydrate	$NiCl_2$. $6H_2O$	5
Boric Acid	H_3BO_3	25
Saccharine		3
Ascorbic Acid		1

Ni foil is used as an anode to maintain a constant metal (Ni) ion composition in the bath. The pH level of the bath is maintained at 2 – 3. The temperature of the bath is maintained at room temperature 22 °C. The electroplating bath composition is adapted from [86] and modified for our purpose as described in Table 5.2. The electroplating of permalloy was done using pulsed current. The parameters of pulsed electroplating include: current density (J), duty ratio (DR), and bias, which are determined by the following Equation 5.1:

$$J = \frac{I_H}{A_{plating}}; \quad DR = \frac{t_{on}}{t_{period}}.100\%; \quad bias = \frac{I_L}{I_H}.100\% \tag{5.1}$$

Where: $A_{plating}$ is the total electroplated area, I_H is the maximum current of pulsed plating, t_{on} is the time duration for I_H, and t_{period} is the total time for both I_H and I_L. Figure 5.5 below shows the samples of pulsed current for electroplating:

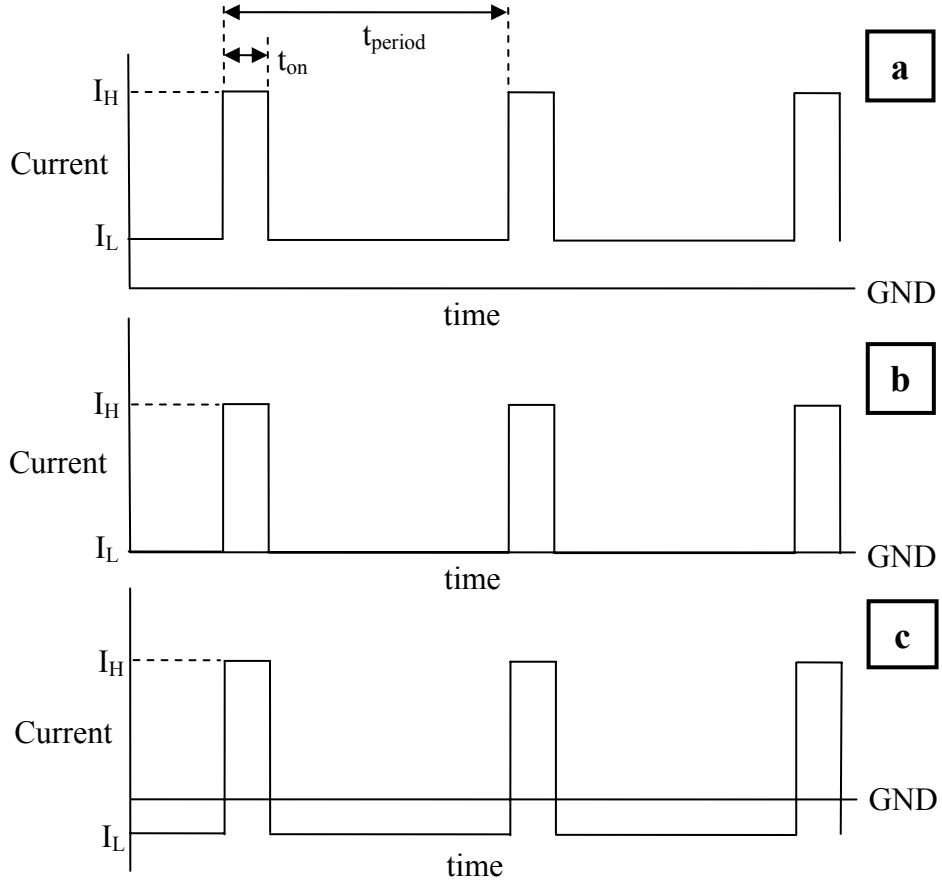

Figure 5.5. (a) Positive DC-biased pulse current; (b) Standard square-wave pulse current; (c) negative DC-biased pulse current

A Solartron SI 1287 electrochemical interface is used to control the pulsed current flowing through the electrodeposition cell. The 1.4 lt. electrolyte with the recipe shown in Table 5.2 is placed into 1.5 lt. beaker. A continuous magnetic stirrer is provided to ensure

that a uniform bath composition is attained. The permalloy electroplating was done at the J = 30 mA/cm^2, DR = 40 %, and Bias = -10 %. The deposition rate is varied with the surface condition; it is approximately 0.15 – 0.16 μm/min.

Prior to electrodeposition, a seed layer must be deposited on the wafer. The seed layer conducts the current over the wafer surface and under the photoresist mold to areas that are to be electrodeposited. The seed layer consists of a 300 Å layer of titanium (Ti) and a 3000 Å layer of copper (Cu). The titanium readily adheres to the silicon and photoresist AZ4620; the copper readily adheres to the titanium; and the permalloy readily adheres to the copper. The titanium and copper seed layers are deposited with the use of DC sputtering. The sputtering process is carried out in the machine manufactured by CVC Products Inc., model: CVC-601. The metal composition of the permalloy is measured by using EDS. The machine is a Hitachi S800 FEG scanning electron microscope (SEM). It shows that the composition of the Ni and Fe are pretty much in agreement with the reported literatures [86], which are 80 % and 20 % respectively.

5.4.2 Orthonol Electroplating

Orthonol is a soft magnetic material. It is used to build the base of the microvalve (label no. 1) and the membrane supported legs (label no. 7) as shown in Figure 5.2. The recipe for the electrolyte is shown in Table 5.3.

Ni foil is used as an anode to maintain the constant metal (Ni) ion composition in the bath. The pH level of the bath is maintained at 2 – 3. The temperature of the bath is maintained at the temperature of 50 °C. The electroplating bath composition is adapted

from [86] and modified for our purpose as described in Table 5.2. The 1.4 lt. electrolyte with the recipe shown in Table 5.2 is placed into 1.5 lt. beaker. A continuous magnetic stirrer is provided to ensure that a uniform bath composition is attained. The orthonol electroplating was done at the J = 30 mA/cm^2, DR = 40 %, and Bias = -10 %. The deposition rate is approximately 0.18 – 0.19 μm/min.

Table 5.3. Chemical composition of electroplating bath for orthonol

Chemical Name	**Chemical Compound**	**gr/L**
Nickel Sulfate Hexahydrate	$NiSO_4.\ 6H_2O$	168
Ferrous Sulfate Heptahydrate	$FeSO_4.\ 7H_2O$	81
Nickel Chloride Hexahydrate	$NiCl_2.\ 6H_2O$	135
Boric Acid	H_3BO_3	50
Saccharine		3
Ascorbic Acid		1

The metal composition of the orthonol is measured by EDS. The compositions are 48 % Ni, 51 % Fe, and about 1 % of impurities: Ti and Cu. Figure 5.6 below shows the result from EDS.

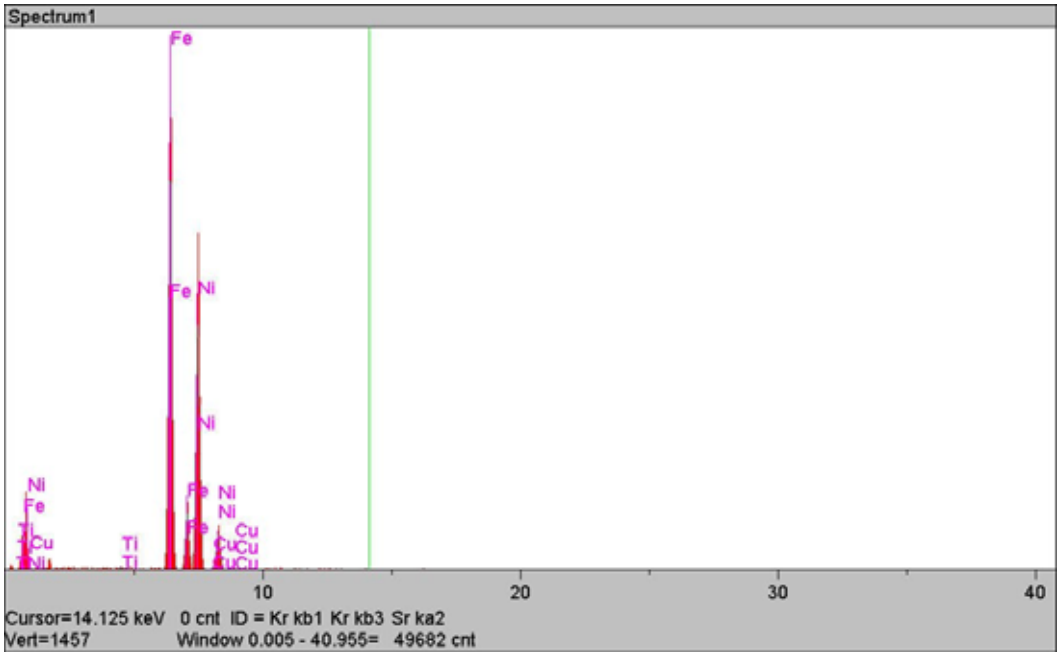

Figure 5.6. Metal composition of the orthonol deposited on top of silicon wafer with 300 Å of Ti and 3000 Å of Cu seed layers. It shows the compositions of: 48% Ni, 51% Fe, and 1 % of Ti and Cu.

5.4.3 Gold Electroplating

Gold is used as the material for the microcoil (label no. 3) as shown in Figure 5.2. The gold is deposited by electroplating in a non phosphate-gold cyanide solution produced by Technique Inc. (Cranston, Rhode Island). This solution is ready to use, the part no: 434 HS solution with 0.25 tr.oz of gold/qt. solution. The gold plating solution is maintained at room temperature with the pH level: 5 – 7. Platinized aluminum is used as the anode. The gold electroplating is done by direct current at the J = 2 - 3 mA/cm^2. The deposition rate is about 0.15 – 0.17 μm/min. The metal composition of the electroplated gold is measured by EDS and the result is shown in Figure 5.7 below. The compositions are: 95 % Au, 3 % Pt, and 2% impurities of Ti and Cu.

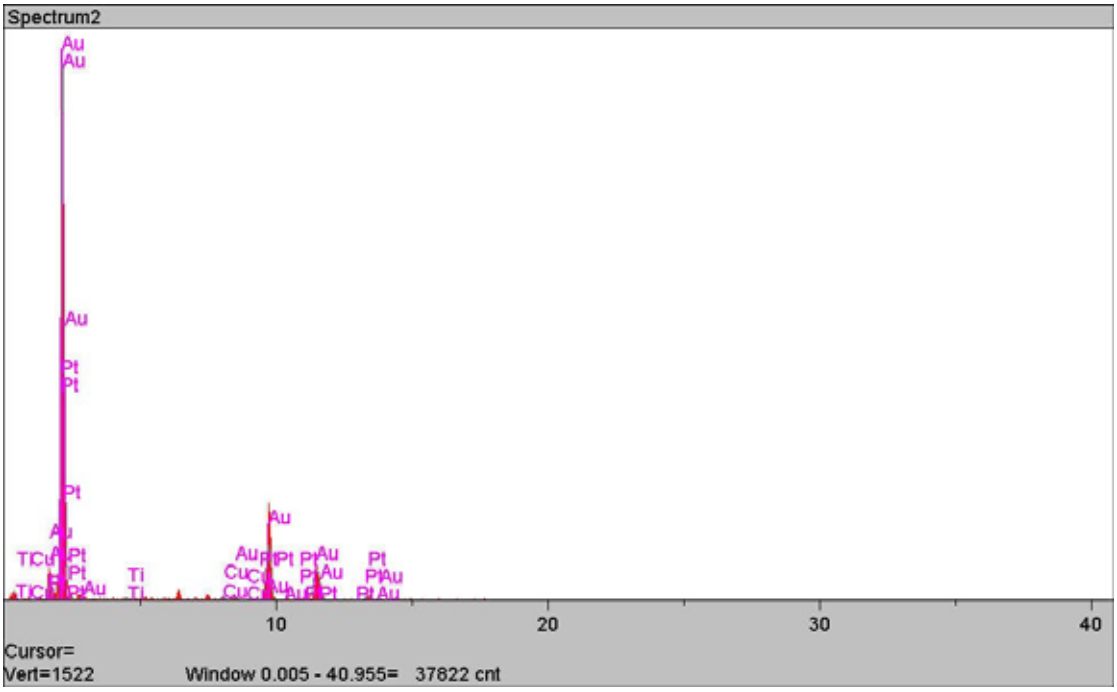

Figure 5.7. The metal composition of the gold (Au) deposited on top of silicon wafer with 300 Å of Ti and 3000 Å of Cu seed layers. It shows the compositions of: 95% Au, 3% Pt, and 2 % of Ti and Cu.

5.4.4 Co-Pt Electroplating

Co-Pt is one of the alloys that are selected to fabricate the permanent magnet (label no. 6) for the bistable microvalve as shown in Figure 5.2. The recipe of the electrolyte is adapted from [114] and modified for our purpose as shown in Table 5.3 below. Co foil is used as the anode to maintain the constant metal ion composition in the bath. The solution is very corrosive, so extra handling is required during the fabrication process. The pH level of the solution is maintained around 8.

The 1.4 lt. electrolyte with the recipe shown in Table 5.2 is placed into a 1.5 lt. beaker. A continuous magnetic stirrer is provided to ensure that a uniform bath composition is attained. There are several difficulties encountered during the deposition

of thick film Co-Pt permanent magnet, especially when thickness is greater than 5 μm. The two major difficulties are: bubble production and surface cracking. H_2 gas bubble is the non-preventable product from electroplating process. The gas bubbles produced a rough/non-uniform plating surface, bubbling, and cracking of the photoresist. The bubble production became more pronounced for thicker deposition, $t_M > 10$ μm. In order to minimize the bubble production, the wafer was taken out from the electrolyte bath every 10 minutes to remove the bubbles to the air.

Table 5.4. Chemical composition of electroplating bath for Co-Pt permanent magnet

Chemical Name	**Chemical Compound**	**gr/L**
Diammine Platinum (II) Nitrate	$Pt(NO_2)_2(NH_3)_2$	3.21
Cobalt (II) Sulfamate	$Co(NH_2SO_3)_2$	25.11
Ammonium Citrate	$(NH_4)_2C_6H_6O_7$	22.62
Glycine	NH_2CH_2COOH	7.51
Saccharin		2
Sodium Hypophosphite Monohydrate	$NaH_2PO_2.H_2O$	10.6

Co-Pt deposition produces a tension stress, with a value that depends on the Co composition, for example, for 80% Co, the stress is about 250 MPa [109]. In order to reduce the stress from Co-Pt deposition to 100 MPa [109], 2 gr/L of saccharin is added to the electrolyte and the electrolyte temperature is increased from room temperature to 40 – 50 °C. The increase of the electrolyte temperature may soften and taper the sidewall of AZ4620 photoresist mould.

Very serious cracking and large grain size (D_h > 10 μm) were experienced for the Co-Pt deposition at room temperature, 20 – 25 °C. Figure 5.8a shows the SEM picture for Co-Pt film plated at room temperature on top of Si(100) and Ti/Cu seed layer with direct current of J = 20 mA/cm^2 .

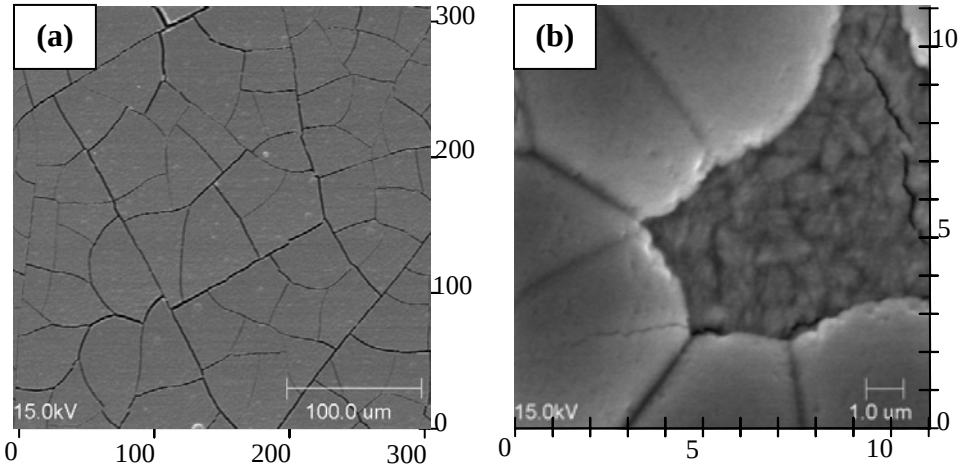

Figure 5.8. The Co-Pt film deposited on top of Si (100) and Ti/Cu seed layer (dimensions are in μm). (a) J = 20 mA/cm^2 deposited at room temperature, 20 °C ; (b) J = 25 mA/cm^2, deposited at temperature of 50 °C

Deposition of Co-Pt at higher temperature increases the mass transfer, reduces the grain size, and minimizes the surface cracking. Figure 5.8b shows the SEM (Scanning Electron Microscopy) structure of Co-Pt that is plated on top of the Si(100) and Ti/Cu seed layers with the direct current of J = 25 mA/cm^2 at the electrolyte temperature of 50° C. Figure 5.8b shows a 7000 x magnification of the film. It shows that the grain can be divided into two main types according to the size: major grain size and minor grain size (D_h < 0.5 μm). Some minor cracking occurred in the minor grain size with a size of roughly 100 nm. The figure shows that the film consists of 70 % major grain size; this

indicates that the surface is not very smooth. Another approach to slightly improve the bubble production and increase the surface quality is to electroplate the Co-Pt magnet by pulsed current at J = 20 – 30 mA/cm^2, duty ratio = 40 %, and bias = -10 %. However the deposition rate becomes very slow and it takes much longer to electroplate. Thus direct current electroplating at J = 25 – 30 mA/cm^2 was used for fabricating the Co-Pt magnet with the deposition rate of 0.2 – 0.22 μm/min.

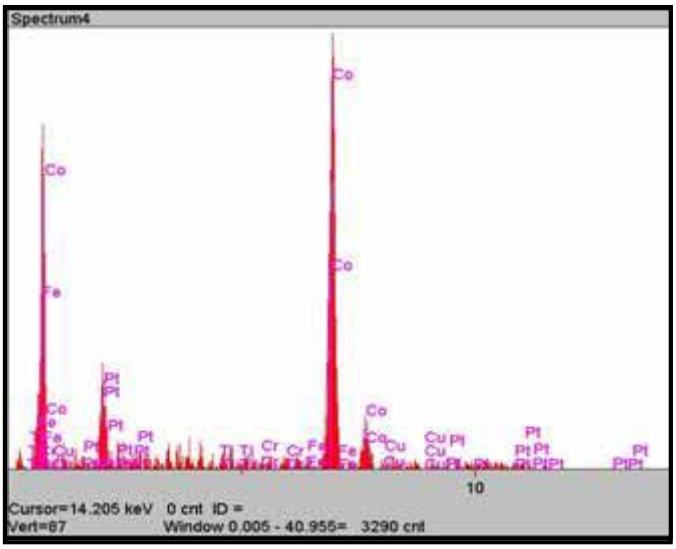

Figure 5.9. Composition of the Co-Pt permanent magnet measured by EDX; the percentages of weight are: Co = 84.5 %; Pt = 12.5 %; Cu = 1.35 %; and Fe = 0.79 %.

Figure 5.9 shows the composition of the deposited Co-Pt measured on a separate sample by EDS. The deposition was done on top of Si (100) and Ti/Cu seed layer with a direct current of J = 30 mA/cm^2 and an electrolyte temperature of 50 °C with no magnetic stirring. It shows that the major contents are Co and Pt, with the weight composition of

84.5 % and 12.5 %. Other minor compositions are Cu and Fe. This is consistent with the reported literature [114, 115], where the Co-Pt composition is about 80% and 20% respectively. The experiment showed that with the addition of magnetic stirring, an increase in the Co composition to 90% and a decrease in the Pt composition to 7 % were observed.

5.4.5 CoNiMnP Electroplating

CoNiMnP is one of the alloys selected to fabricate the permanent magnet (label no. 6) for the bistable microvalve as shown in Figure 5.2. The recipe for the electrolyte is adapted from [54] and modified for our purpose as shown in Table 5.5 below. The electroplating process for the CoNiMnP is a little different than for CoPt. In order to improve the vertical anisotropy of the permanent magnet, CoNiMnP is plated inside a constant magnetic field. The electroplating bath is located in between ceramic magnets (Ferrimag 8A, Adams Magnetic Products, 3900 G). The produced constant magnetic field between the ceramic magnets is measured by magnetometer and is about 800 G. In order to remove the gas bubbles produced on the electroplated CoNiMnP magnet and to ensure uniform concentration of solution inside the bath, nitrogen (N_2) gas is constantly supplied to the solution. Figure 5.10 below shows the schematic of CoNiMnP electroplating. Co foil is used as an anode to maintain the constant metal ion composition in the bath. The electroplating is performed with a pulsed current at J = 5 – 10 mA/cm^2, DR = 40%, and bias of -10 %. The electrolyte is maintained at room temperature with the pH level of 3 – 4.

Table 5.5. Chemical composition of electroplating bath for CoNiMnP permanent magnet

Chemical Name	Chemical Compound	gr/L
Cobalt Chloride Heptahydrate	$CoCl_2 . 6H_2O$	24
Nickel Chloride Hexahydrate	$NiCl_2 . 6H_2O$	24
Manganese Sulfate Monohydrate	$MnSO_4 . H_2O$	3.6
Sodium Hypophosphite	$NH_2PO_2 – xH_2O$	4.6
Boric Acid	H_3BO_3	22
Sodium Lauryl Sulfate	$CH_3(CH_2)_{11}OSO_3Na$	0.2
Saccharin		2
Sodium Chloride	NaCl	22

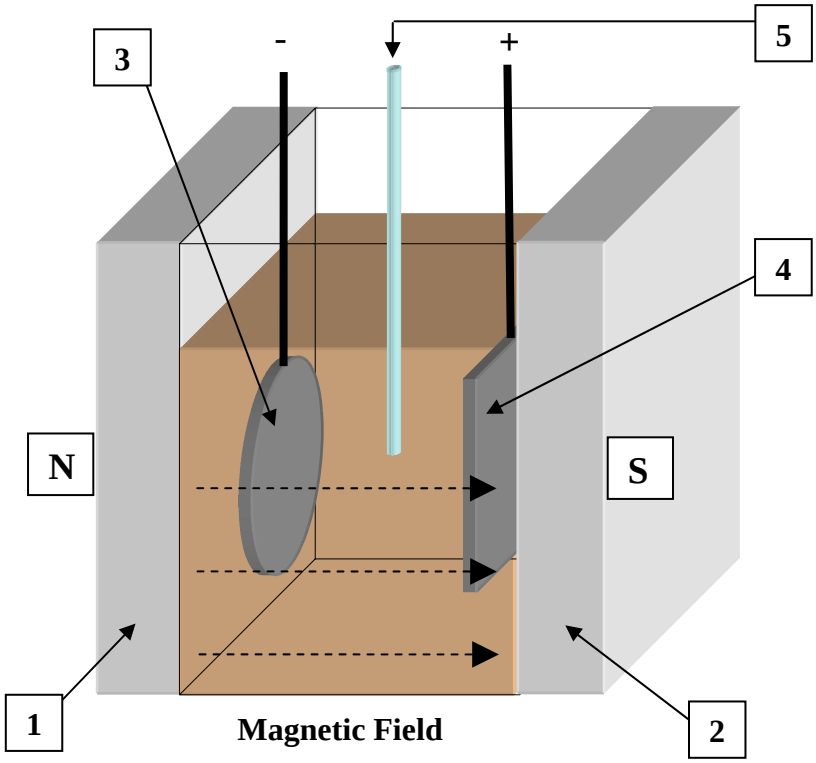

Figure 5.10. Schematic illustration of electroplating setup for CoNiMnP; where: 1, 2 = ceramic magnets, 3 = 4” Si-wafer, 4 = Anode, 4” Co plate, 5 = N_2 gas supply.

5.5 SiO_2 Deposition

A thin film of SiO_2 is deposited on top of the valve base to act as an insulator between the Au microcoil and the NiFe base. The SiO_2 is deposited by plasma enhanced chemical vapor deposition (PECVD). Because of the CMOS limitation, PECVD is chosen to deposit the SiO_2 to avoid damaging any electrical circuits that may be built at the same substrate as the microvalve that is below 400 °C. Another problem with high temperature fabrication is thermal stress that can cause delamination to the electroplated NiFe. PECVD process is performed in the machine Uniaxis PECVD Inc, model Uniaxis 78324, for 20 – 25 minutes at the temperature of 250 – 300 °C. The deposited thickness is about 1 μm. The recipe of the SiO_2 deposition is shown in Table 5.6 below:

Table 5.6. The process parameters for SiO_2 deposition by PECVD

Gas	**Rate**
SiH_4	400 sccm
N_2O	900 sccm
Pressure	**900 mtorr**
Power	30 W
Temperature	300 °C

5.6 RIE Etching

In order to open a contact window to the SiO_2 insulator, some regions of the SiO_2 have to be etched. The SiO_2 is removed by reactive ion etching (RIE), where the AZ4620 photoresist is used as the mask. The process is performed in a Plasma Therm Inc., model 790 at room temperature for 110 minutes to removes about 1 μm SiO_2. The recipe of the

RIE etching for SiO_2 is shown in Table 5.7 below, with the etching rate of about 100 Å/min.

Table 5.7. The process parameters for SiO_2 etching by RIE

Gas	**Rate**
CHF_3	45 sccm
O_2	5 sccm
Pressure	**40 mtorr**
Power	200 W
DC-bias	440 V

5.7 The Fabrication Processes for On/Off Microvalve

5.7.1 Fabrication Sequence

The microvalve fabrication process is summarized in this section. The cross sectional diagrams of the on/off valve during each stage of the fabrication process are shown in Figure 5.11. The details are as follows:

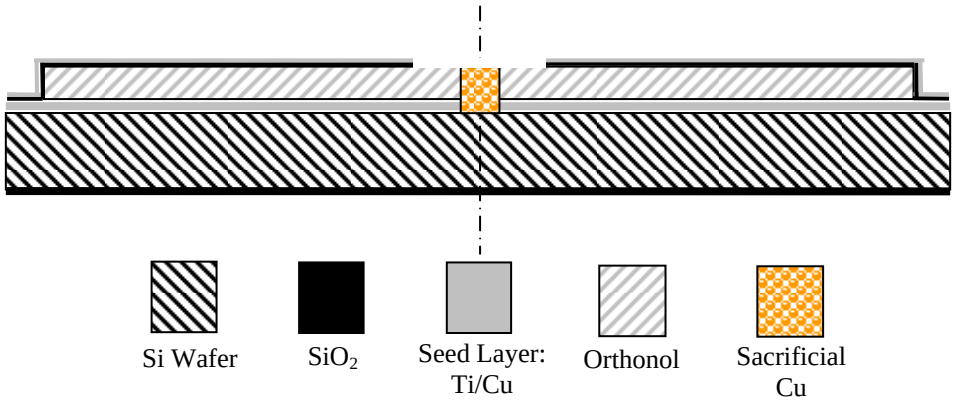

Figure 5.11a. The first fabrication steps of on/off microvalve

Figure 5.11a: First of all, a 0.5 μm SiO_2 is thermally grown on the wafer at the temperature of 1100 ºC for 3 hours inside the furnace manufactured by Lindberg, model 55667. Ti/Cu/Ti seed layers are deposited on the top side of the wafer by DC sputtering. The thickness of Ti/Cu/Ti seed layers are 300 Å, 3000 Å, and 300 Å respectively. The process is carried out in the machine CVC Products Inc., model CVC-601. **Photolithography #1**, using positive photoresist AZ4620 by Shipley Inc., creates the mould for electroplating the valve base. Electroplating of orthonol (50% Ni, 50% Fe) is done by pulsed plating at J = 30 mA/cm^2, bias of -10%, and duty ratio of 40% to a thickness of 10-12 μm. It takes approximately 50 minutes. The next process is to remove the photoresist mould with acetone and AZ 400 T (Shipley Inc.), etch the Ti seed layer by 3 % buffered HF, and etch Cu seed layer with NH_4OH, $CuSO_4$. $5H_20$ saturated solution at room temperature. **Photolithography #2** creates the mould to fill up the inlet hole in the base center with electroplated Cu at direct current of 10 mA/cm^2. PECVD 0.8 μm of SiO_2 at the temperature of 300 ºC creates an insulation layer between the base and the coil; this is performed inside the Uniaxis PECVD chamber for 15 minutes. **Photolithography #3** creates the contact window for etching SiO_2 insulating layer. The etching of the SiO_2 is done by reactive ion etching (RIE) in Plasma Therm. Inc., model 790. The recipe is shown in section 5.6.

Figure 5.11b: Photolithography #4 creates the mould for microcoil electroplating. The gold electroplating is done by direct current at the J = 2 - 3 mA/cm^2 in a none phosphate-gold cyanide solution produced by Technique Inc. (Cranston, Rhode Island). The thickness of the electroplated gold is 10 μm, which takes about 55 minutes.

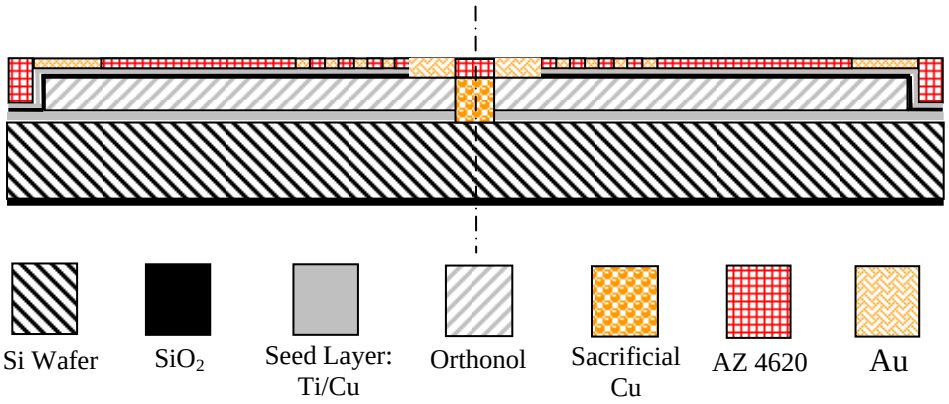

Figure 5.11b. The second fabrication steps of on/off microvalve

Figure 5.11c: Photolithography #5 creates the mould for valve circular support made by electroplated permalloy (20 % Fe and 80 % Ni) by pulsed current electroplating at J = 30 mA/cm^2, bias of -10%, and the duty ratio of 40%. The thickness of the electroplated NiFe defines the gap movement of the valve. Different designs were fabricated in the range of 12 to 40 μm.

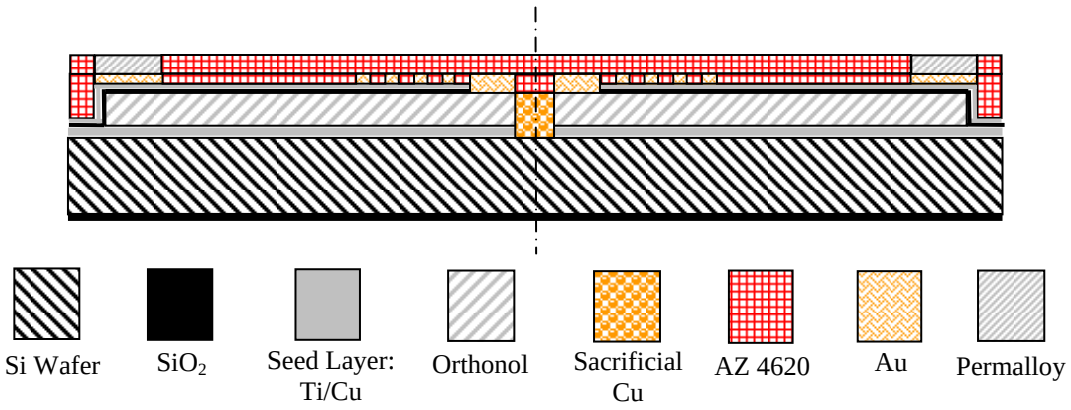

Figure 5.11c. The third fabrication steps of on/off microvalve

Figure 5.11d: Photolithography #6 creates the mould for the center dome soft magnetic membrane. It is made by electroplated Permalloy at pulsed current, J = 30

mA/cm^2, bias of -10%, and the duty ratio of 40%. Different designs were fabricated with a film thickness in the range of 8 to 16 μm.

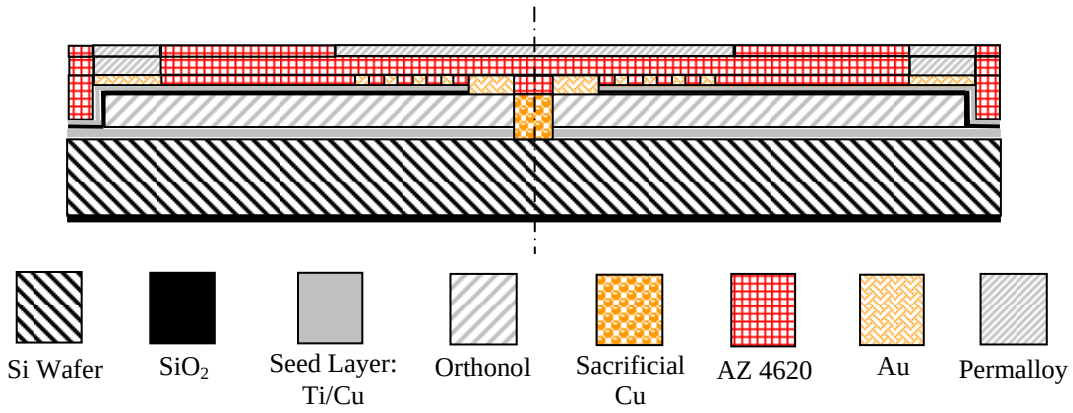

Figure 5.11d. The fourth fabrication steps of on/off microvalve

Figure 5.11e: Photolithography #7 creates the mould for the membrane and cantilever legs, made by electroplated orthonol to a thickness of 3 μm by pulsed plating at J = 30 mA/cm^2, bias of -10%, and duty ratio of 40%. It takes about 20 minutes.

The next step is to do back side photolithography. Mask #8 defines the etching pattern for the inlet hole. AZ 4620 (Shipley Inc.) is used as the photoresist. Once the backside photolithography has been done, the SiO_2 in the windows is etched first by deep RIE (ICP) for 15 minutes. And then the Si is etched though the wafer by Bosch process in ICP for 12 – 14 hours, the etching is stopped on the SiO_2 that was previously thermally grown. The SiO_2 is then etched by RIE (Plasma Therm Inc.) for 50 minutes.

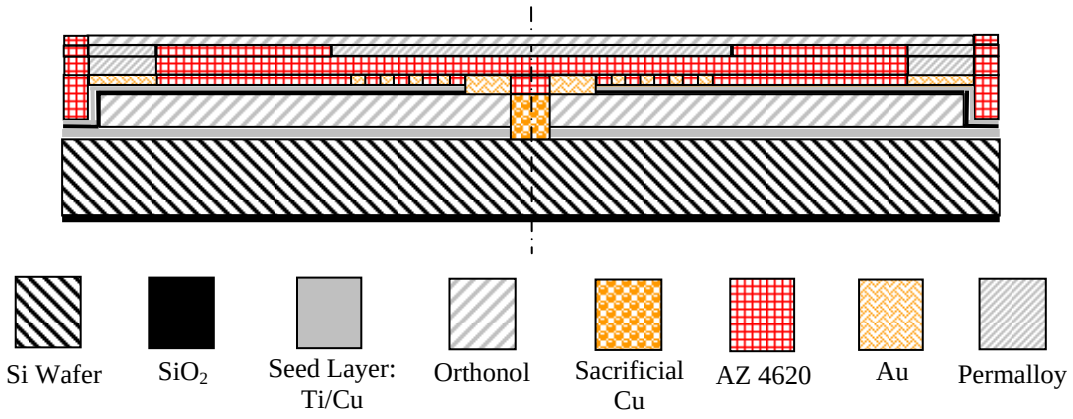

Figure 5.11e. The fifth fabrication steps of on/off microvalve

Figure 5.11f: The sacrificial copper seed layer is etched by the solution NH_4OH, $CuSO_4.5H_2O$ saturated. The Ti seed layer is etched by using 3% buffered HF solution. The photoresist was stripped by acetone and AZ 400 T with mild ultrasonic agitation. The release membrane was inspected under the microscope.

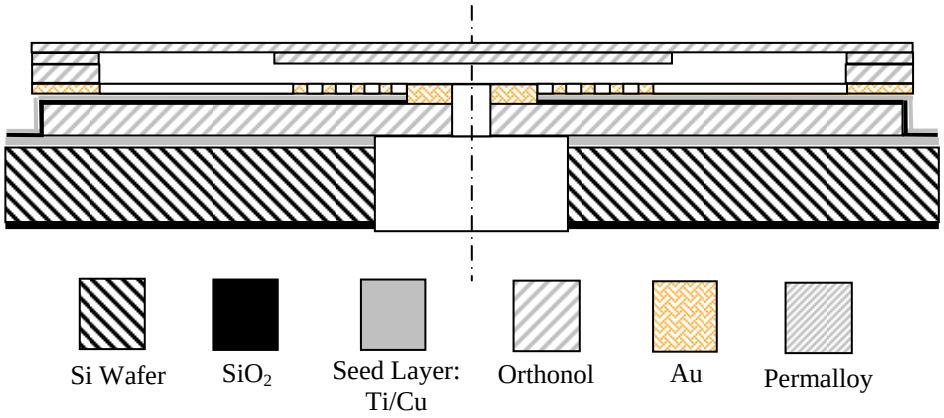

Figure 5.11f. The final fabrication steps of the on/off microvalve

5.7.2 The Picture of the Fabricated On/Off Microvalve

Figure 5.12 and 5.13 shows SEM pictures of the on/off microvalves that have been fabricated. There are two type of microvalve generations have been fabricated. The first generation microvalve is shown in Figure 5.12. The overall size of the microvalve is 1,000 μm; this includes a membrane with centered dome of 300 μm and a microcoil underneath with the width (W) of 8 μm and height (H) of 10 μm. There is a gap of 12 μm between the centered soft magnetic dome and the microcoil surface. There are two types of membrane supported legs that are built for the first generation microvalve, a flat/plain support and a bending support (as shown in Figure 5.12). The folded/bending support is developed to overcome the possible tension stress happened during the membrane electroplating.

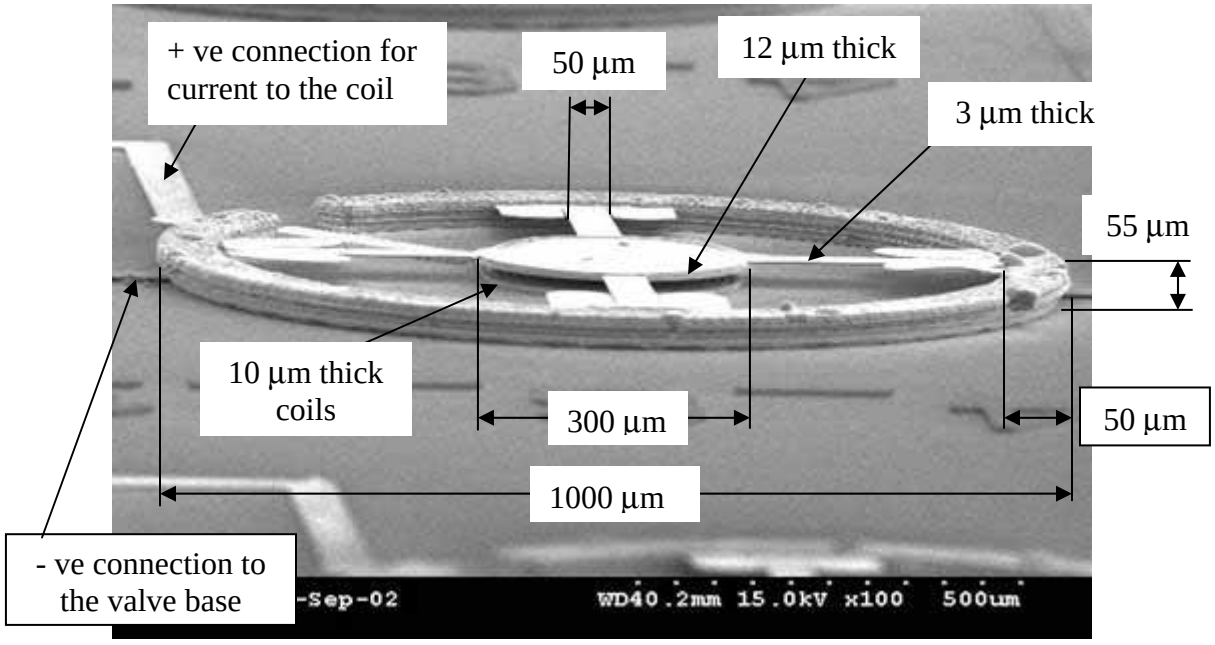

Figure 5.12. Close up picture of the first generation of on/off microvalve with four bending supported legs

As shown in Figure 5.12, the microvalve structure has two electrical connections for the microcoil, the positive and the negative connections. The negative connection is basically connected to the base of the microvalve with SiO_2 as the insulation layer. In the first generation of microvalve, several fabrication issues have been experienced, including the difficulty of etching the microcoil seed layer. As shown in Figure 5.12, there is only a 12 μm gap available for the etchant to etch the seed layer in between the microcoil turns. This introduces a significant difficulty into the etching process; furthermore, a longer time in the etchant solution (NH_4OH with $CuSO_4.5H_2O$ (Saturated)) results in over-etching that lifts the microcoil off.

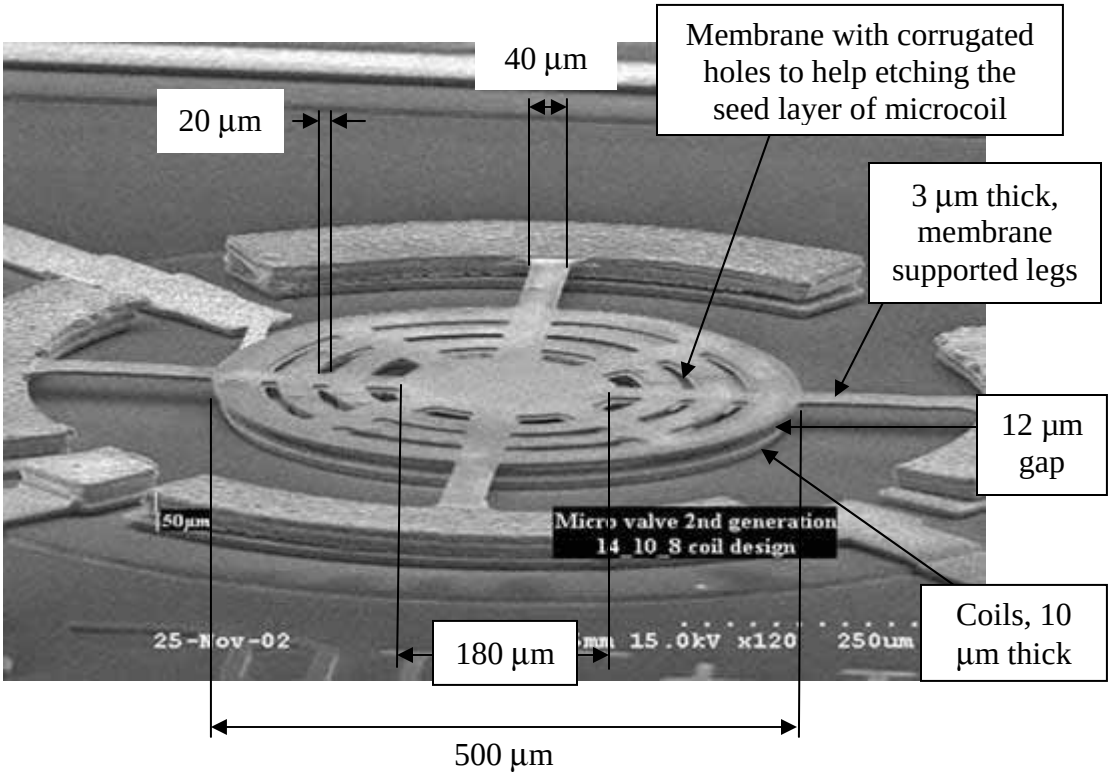

Figure 5.13. Close up picture of the second generation on/off microvalve

Figure 5.13 shows the complete microvalve structure of the second generation of on/off microvalve. In this valve, a membrane design with the corrugated hole has been introduced to the microvalve structure in order to facilitate the flow of etchant for etching the seed layer in between microcoil turns.

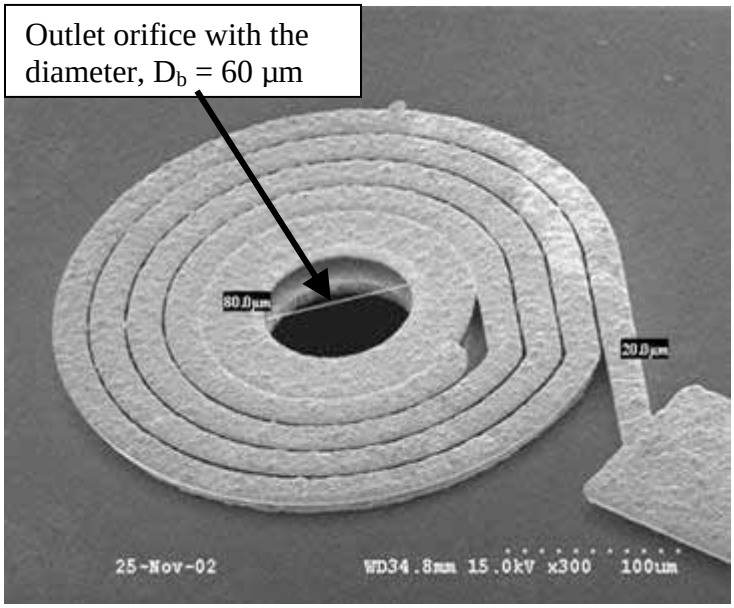

Figure 5.14. The close up pictures of the hole, which is the outlet orifice, when the membrane is lifted off

Figure 5.14 shows the close up picture of the hole, which is the outlet orifice with diameter of 60 μm, when the membrane is lifted off. There are three different overall sizes of 2nd generation microvalve that have been fabricated, 1,000 μm, 1,500 μm, and 2,000 μm. Figure 5.13 shows the microvalve with the overall sizes of 1,000 μm. It shows that the centered dome, with the diameter of 500 μm, has a corrugated hole with the size of 20 μm. Its center has a solid part with a diameter of 180 μm. An outlet orifice with the

diameter of 60 μm is located beneath this membrane. There are four different designs of membrane: a membrane with 2 supported legs separated by 90º: with 2 supported legs separated by 180º; one with 3 supported legs separated by 120º; and one with four supported legs separated by 90º.

In addition, there are three different types for the supported legs: the plain type as shown in Figure 5.13, the bending type as shown in Figure 5.12, and the torsional type.

Figure 5.15 shows an array of microvalves with plain supported legs; it shows a membrane with 2 supported legs separated by 180º and with 3 supported legs separated by 120º. Figure 5.12 illustrates an on/off microvalve with four bending supported legs.

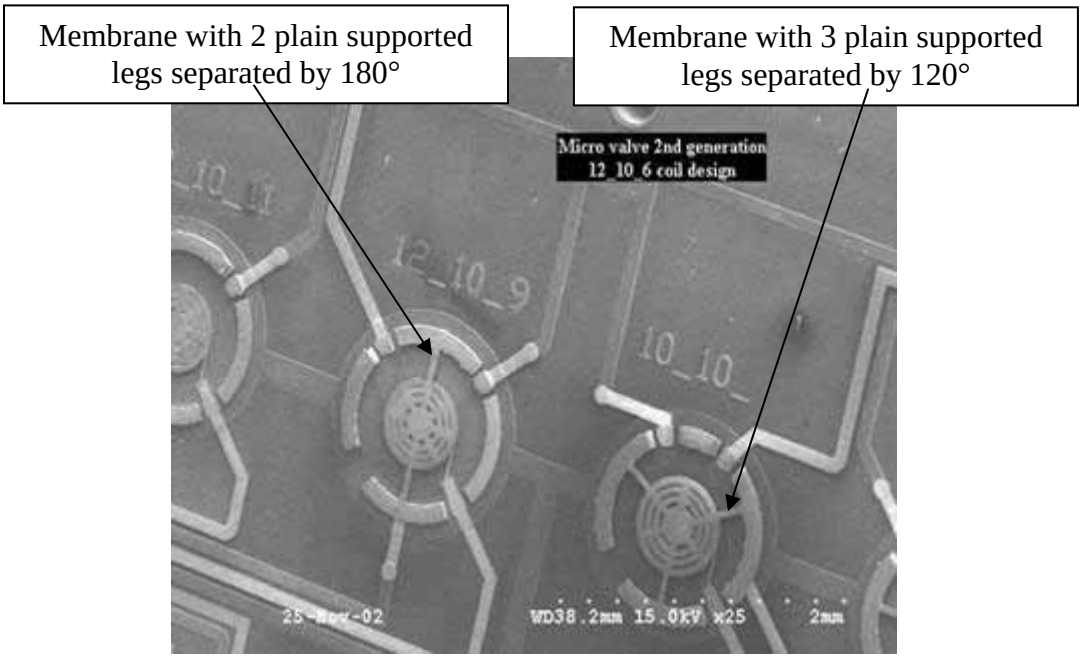

Figure 5.15. Array of microvalves

5.8 Fabrication Processes of Bistable Microvalve

5.8.1 Fabrication Steps

The fabrication of the bistable microvalve is summarized in this section. The cross sectional diagrams of the bistable microvalve during each stage of fabrication process are shown in Figure 5.16. The details are as follows:

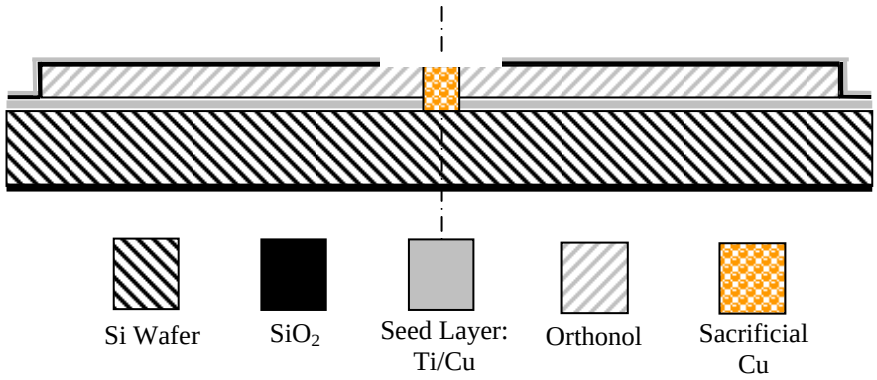

Figure 5.16a. The first fabrication step of bistable microvalve with latching mechanism

Figure 5.16a: First of all, SiO_2 is thermally grown on both sides of the wafer in the furnace at the temperature of 1,100 °C for 3 hours. The top side of the wafer is then DC sputtered with Ti/Cu/Ti at the thickness of 500 Å, 3000 Å, and 500 Å respectively. The sputtering process is carried out in the machine manufactured by CVC Products Inc., model CVC-601. **Photolithography #1**, using positive photoresist AZ4620 by Shipley Inc., creates the mold for electroplating the valve base. Electroplating of NiFe (50% Ni, 50% Fe) is accomplished by pulsed plating at J = 30 mA/cm^2, bias of -10%, and duty ratio of 40% to a thickness of 30 - 35 µm. It takes approximately 3 hours. The photoresist is removed with acetone and AZ 400 T (Shipley Inc.). The Ti seed layer is etched by 3 %

buffered HF, and the Cu seed layer is etched with NH_4OH, $CuSO_4$. $5H_20$ saturated solution at room temperature. **Photolithography #2**, using positive photoresist AZ4620, creates the mould to fill up the inlet hole in the base center with electroplated Cu at the current density of 10 mA/cm^2. A low stress SiO_2 is deposited on top of the wafer by PECVD, with the thickness of 0.8 µm at the temperature of 200 ºC to create an insulation layer between the base and the coil. The process is done inside the Uniaxis PECVD chamber for 45 minutes. **Photolithography #3**, using positive photoresist AZ4620 by Shipley Inc., creates the contact window for etching SiO_2 insulating layer. The etching of the SiO_2 is done by reactive ion etcher (RIE) (Plasma Therm, Inc., model 790). The photoresist is then stripped by using acetone. A Ti/Cu/Ti seed layer is then deposited on top of the wafer.

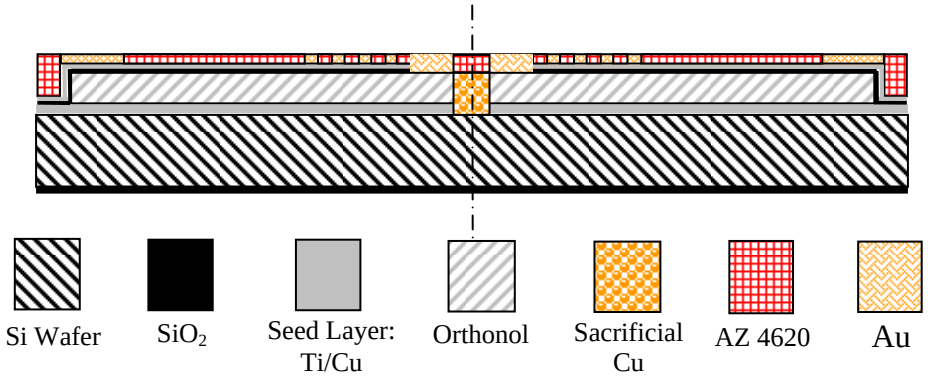

Figure 5.16b. The second fabrication step of bistable microvalve with latching mechanism

Figure 5.16b: Photolithography #4 creates the mold for electroplating the microcoil. The gold electroplating is accomplished by direct current at the J = 5 mA/cm^2

in non-phosphate-gold cyanide solution produced by Technique Inc. (Cranston, Rhode Island). The solution is ready to use with the part no. 434 HS solution with 0.25 tr.oz of gold/qt. solution. The gold plating solution is maintained at room temperature with the pH level: 5 – 7. The thickness of the electroplated gold is 8 µm. It takes about 55 minutes to achieve this thickness.

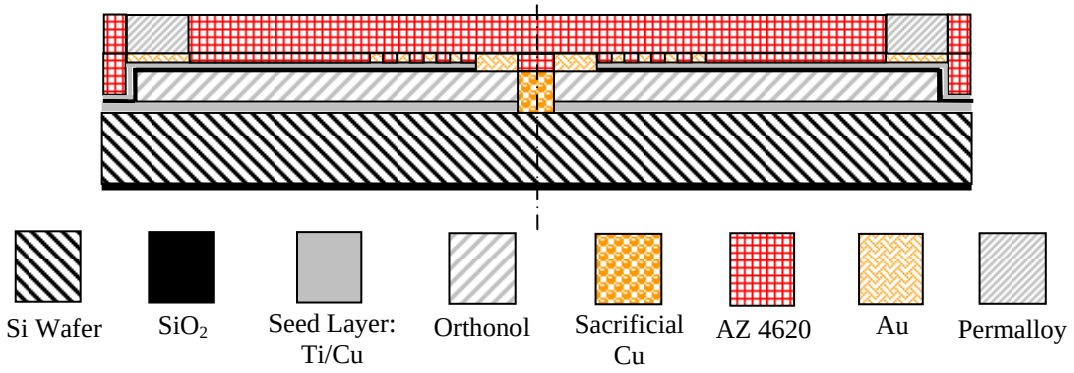

Figure 5.16c. The third fabrication step of bistable microvalve with latching mechanism

Figure 5.16c: Photolithography #5 creates the mould for a valve circular support made by electroplated NiFe alloy (20 % Fe and 80 % Ni) with the recipe available in [27] by pulsed current electroplating at J = 30 mA/cm^2, bias of -10%, and the duty ratio of 40%. The thickness of the electroplated NiFe defines the gap movement of the valve. A Ti/Cu/Ti seed layer is then deposited on top of the wafer.

Figure 5.16d: Photolithography #6 creates the mould for the centered CoNiMnP permanent magnet, using the recipe for the electrolyte shown in [66]. The plating was accomplished by pulsed current at the J = 5 - 10 mA/cm^2, bias of -10%, and a duty ratio of 80%. The process is then continued by re-exposure (photolithography #6) of the existing photoresist layer to define the circular support mold. Another NiFe (80% Ni,

20% Fe) layer is then electroplated in the mold by pulsed plating at J = 30 mA/cm^2, bias of -10%, and duty ratio of 40%. A Ti/Cu/Ti seed layer is then deposited on top of the wafer.

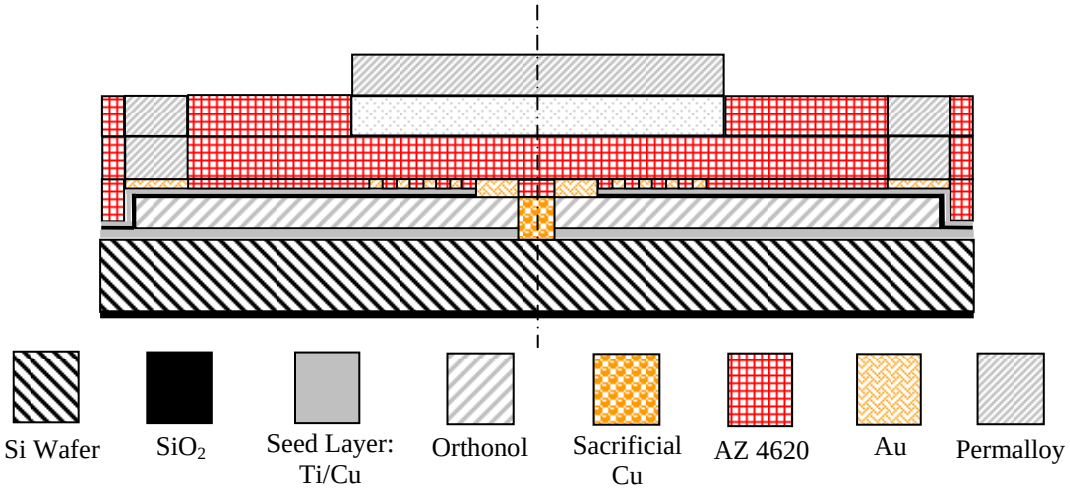

Figure 5.16d. The fourth fabrication step of the bistable microvalve with latching mechanism

Figure 5.16e: Photolithography #7 creates the mold for center dome NiFe (80% Ni, 20% Fe) electroplated with pulsed current J = 30 mA/cm^2, with a bias of -10%, and a duty ratio of 40%. A Ti/Cu/Ti seed layer is then deposited on top of the wafer.

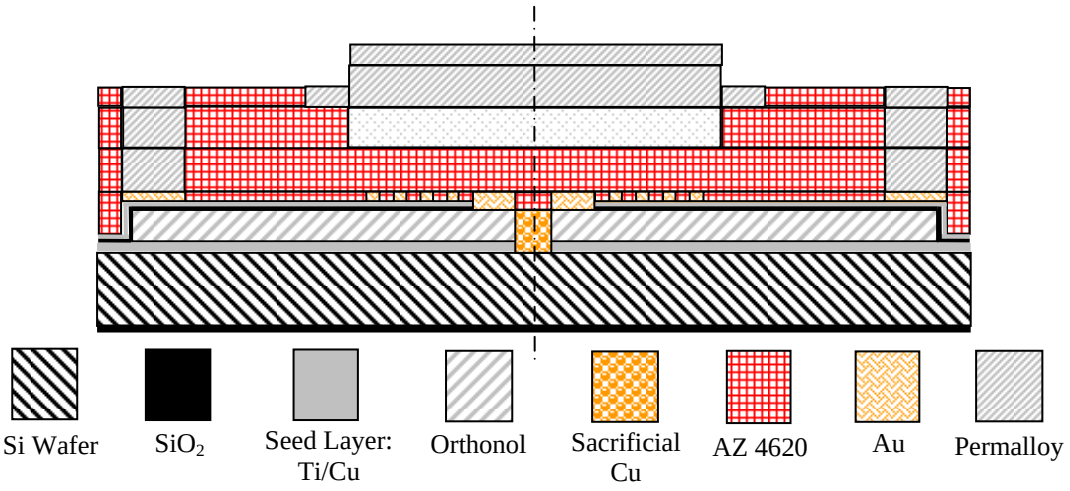

Figure 5.16e. The fifth fabrication step of the bistable microvalve with latching mechanism

Figure 5.16f: Photolithography #8 creates the mold for the membrane and cantilever legs, made by electroplated NiFe under same conditions. The desired thickness of the membrane is 4 μm. It takes about 15 minutes of electroplating.

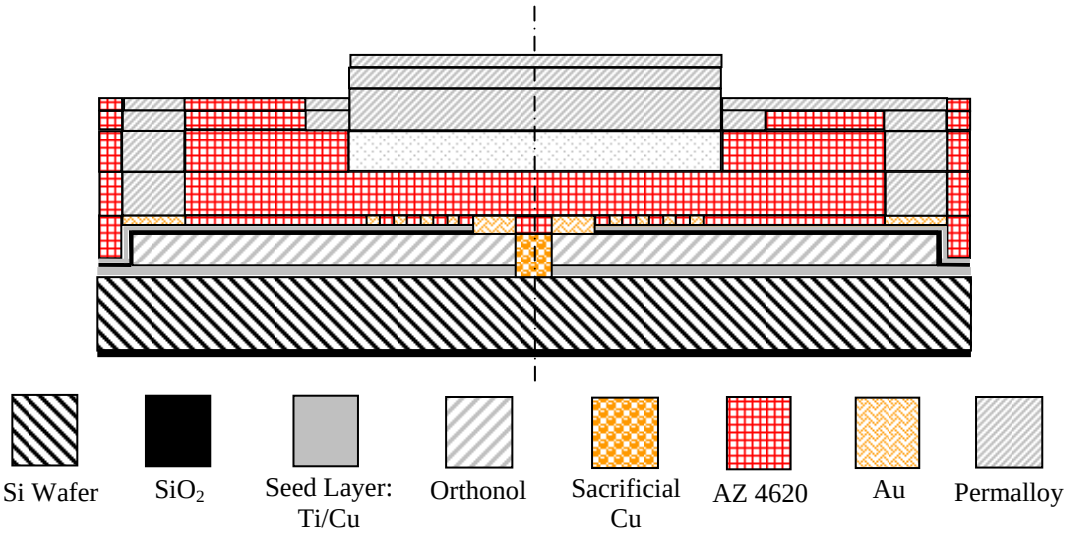

Figure 5.16f. The sixth fabrication step of the bistable microvalve with latching mechanism

Figure 5.16g: The next step is to do the backside alignment that define the hole-patterns for etching through the back of wafer (photolithography #9). For this step, the back side of the wafer is spin coated with a positive photoresist, AZ 4620. The SiO_2 film on the back of the wafer is first etched by deep RIE/ICP by Plasma Therm Inc, model Dual ICP SLR. for 15 minutes. The Si then is etched though the wafer by Bosch process for 12 – 14 hours for the wafer thickness of 500 - 550 μm; the etching is stopped when it reaches the SiO_2 film that was previously grown on top of the wafer. The SiO_2 layer is then etched by RIE (Plasma Therm Inc.) for 50 minutes. The Si etching through the wafer

at the end of the fabrication process is more robust than etching at the start or in the middle of the process, which causes the wafer to become fragile.

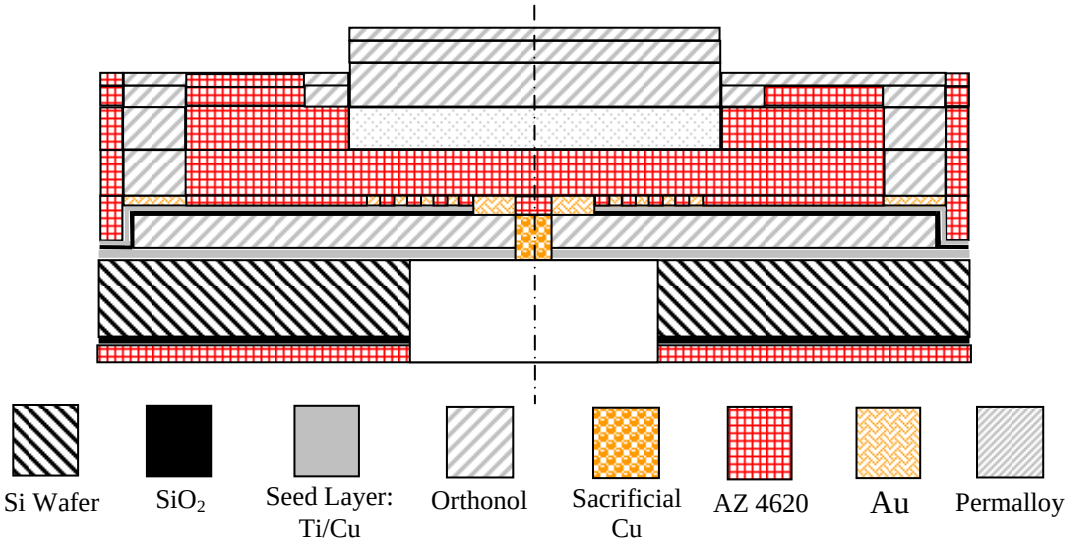

Figure 5.16g. The seventh fabrication steps of bistable microvalve with latching mechanism

The next step is to magnetize the electroplated CoNiMnP permanent magnet that is plated on the membrane. To magnetize a fully dense magnet to its saturation, an external field of 3 – 5 times of its intrinsic coercivity (H_{ci}) must be applied. According to the literature [54], H_{ci} of the electroplated CoNiMnP is in the order of 1100 Oe as shown in the table 1. So an external field in the order of 3.3 – 5.5 kOe is required to fully magnetize the magnet. The sample was magnetized by Arnold Engineering under the kind help of Mr. Jim Roozee and Dr. Neil Manning. A capacitor discharge magnetizer that consists of a solenoid coil fixture is used to generate this high magnetic field (H_s > 10 kOe) for magnet magnetization. The sample after wafer dicing in the size of 12 mm x 12 mm is basically placed in the bore of the coil 50.8 mm in diameter.

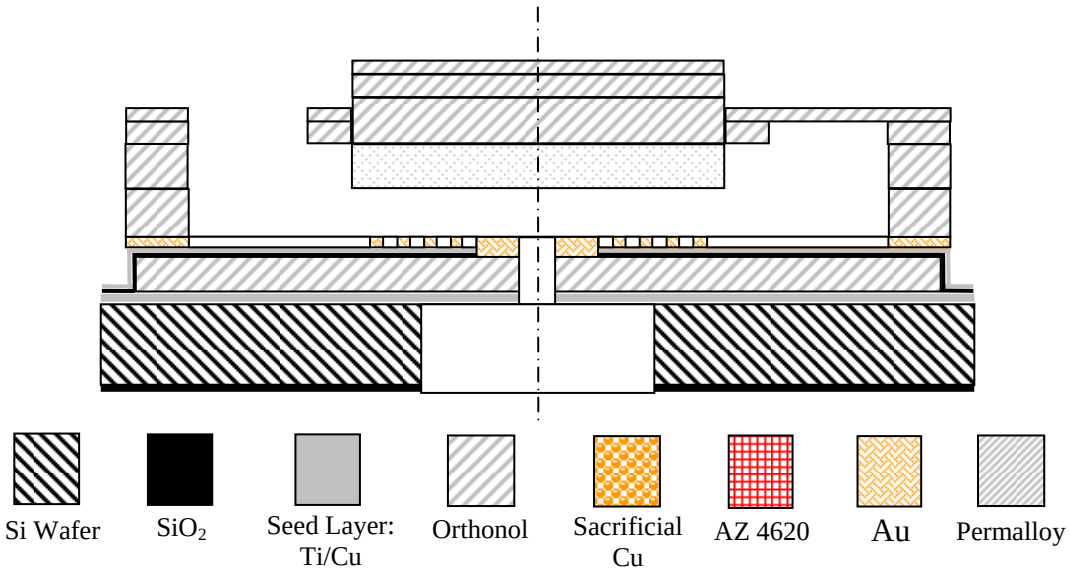

Figure 5.16h. The eight fabrication steps of bistable microvalve with latching mechanism

Figure 5.16h: The photoresist was stripped by acetone and/or AZ 400T with mild ultrasonic agitation. The release membrane was inspected under the microscope. The sacrificial copper seed layer is etched by the solution NH_4OH, $CuSO_4.5H_2O$ saturated. The Ti seed layer is etched by using 3% buffered HF solution.

At the end of the process, a thin film of parylene-C is deposited on the whole structure of bidirectional actuator. The deposition was done at room temperature by vapor phase in a Parylene Deposition System type 2010 (SCS, Indianapolis, Indiana, 46241). The function of the parylene is to protect the actuator structure from oxidation since it is made from metal (NiFe).

5.8.2 The Fabrication Results

5.8.2.1 Bidirectional Microactuator

The fabrication of the bistable microvalve is far more difficult than that of the on/off valve. The addition of an electroplated permanent magnet integrated on the bottom of the centered soft magnetic membrane proves more difficult than might be first imagined. The fabrication needs extremely great patience. The surface roughness of the permanent magnet is not as suitable as soft magnetic material (NiFe). As mentioned before that the surface is mainly caused by the bubble generation during electroplating. The rough surface profile is patterned to the next electroplated layer, which is the soft magnetic membrane.

As mentioned before, there are two different permanent magnets electroplated on the membrane of the microvalve to produce the bistable mechanism. These are CoPt and CoMnNiP permanent magnets. Unfortunately, the CoPt magnet does not give a satisfying result in producing bistable mechanism. The wafer condition after the fabrication process as shown in Figure 5.16f is very unsatisfactory and makes it impossible to carry on the backside alignment and etch a hole through the back of the wafer. Meanwhile, the integration of the CoPt magnet on the soft magnetic membrane produces a bidirectional microactuator with a large membrane's displacement in both vertical directions. The experimental static and dynamic responses of the microactuator are presented in chapter 7.

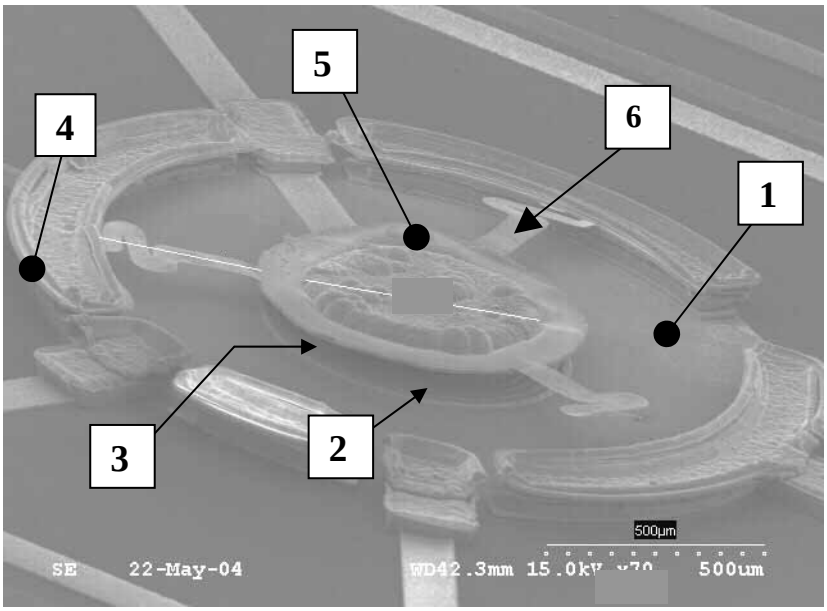

Figure 5.17. SEM micrograph of bidirectional actuator with double-legs design; 1 = Orthonol base; 2 = microcoil; 3 = Co-Pt permanent magnet plated on the bottom of membrane; 4 = circular supports; 5 = Soft magnetic centered membrane; and 6 = membrane's supported legs

The fabrication results of the bidirectional microactuator are shown in Figures 5.17 and 5.18 for double-leg design and single-leg design respectively. As shown in Figure 5.17, the membrane (label no. 5) is supported by two spring-designed legs (label no. 6) that are anchored to the circular support (label no. 4), the other leg is free. All legs are separated by a 120° angle. The distance between the center of the membrane and the top surface of the microcoil is about 70 µm. The measured dimensions of the bidirectional actuators are shown in Table 5.7.

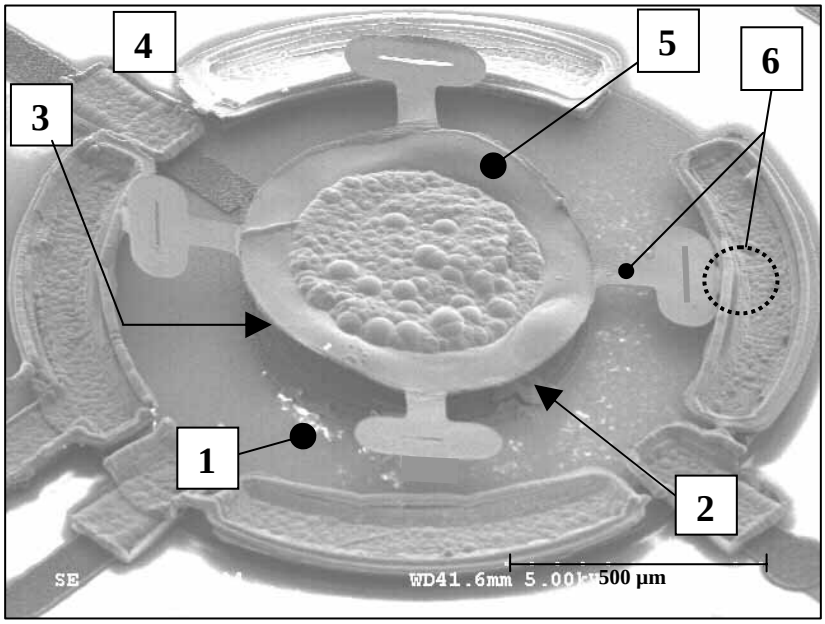

Figure 5.18. SEM Picture of bidirectional actuator with single-leg design; 1 = Soft magnetic base; 2 = microcoil; 3 = Co-Pt permanent magnet plated on the bottom of membrane; 4 = circular supports; 5 = Soft magnetic centered membrane; and 6 = membrane's supported leg

Figure 5.18 shows the figure of bidirectional actuator with single-leg design that is anchored to the circular support. The other three legs connected to the soft magnetic membrane are free. Due to the stress in the permalloy electroplating, the membrane is deflected upward with the angle rotation of 4.1°. The distance between the center of the membrane and the microcoil is about 105 µm. The measured dimensions of the bidirectional actuators are shown in Table 5.8.

Table 5.8. Measured geometry of the bidirectional actuator

Structural		
Overall diameter ($D_{overall}$)	1,600	µm
Base thickness (t_{base})	10	µm
Gap/Actuation displacement (g)	70 or 105	µm
Magnet thickness (t_M)	25	µm
Magnet diameter (D_M)	500	µm
Membrane diameter (D_1)	700	µm
Thickness of centered membrane (t_1)	21	µm
Number of legs	2 and 1	
Thickness of legs (t_2)	2	µm
Legs width (w_2)	60	µm

Electrical		
Number of coils	12	
Width of the coil	14	µm
Thickness of the coils	8	µm

Coating		
Thickness of parylene	1	µm

5.8.2.2 Bistable Microvalve

The integration of CoMnNiP magnet onto the membrane has been able to successfully create a bistable mechanism for the microvalve. The bistable and bidirectional tests for the membrane actuator in the medium of air are discussed in Chapter 7. The results for the liquid tests of the microvalve in the flow rate of water are discussed in Chapter 8. Figure 5.19 shows the fabrication results for the bistable microvalve. It illustrates clearly the main components of the microvalve. The microvalve has a membrane with 2 legs-design. The CoMnNiP magnet is electroplated on the soft magnetic membrane per the close up picture in Figure 5.20.

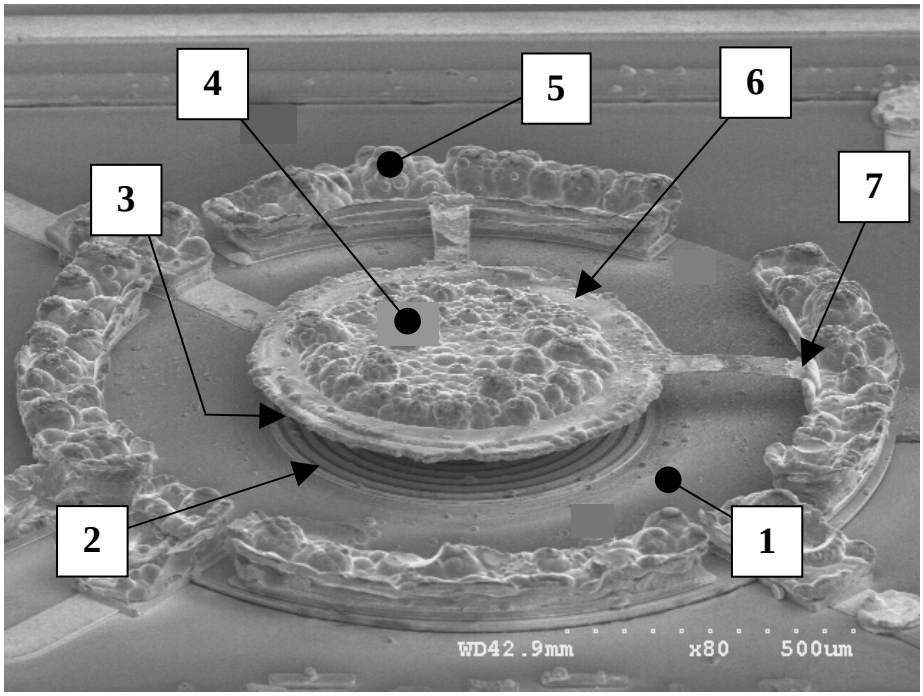

Figure 5.19. SEM micrograph picture of the bistable microvalve, Where: 1 = Orthonol base; 2 = Au microcoil; 3 = CoMnNiP magnet; 4 =Membrane; 5 = Soft magnetic (Permalloy) centered membrane; and 6 = Membrane's supported legs

Figure 5.20 shows a close up picture of the CoMnNiP magnet. It shows that the thickness of the magnet is about 39.2 μm. The thickness of the soft magnetic membrane is 23.2 μm. The gap distance between magnet and the bottom coil is measured to be 28 μm by SEM as shown in Figure 5.20. The experimental measurement on the deflection of the membrane's center by Laser Doppler Vibrometer indicates, a maximum deflection of 30 μm. The measured dimensions of the bistable microvalve as shown in Figures 5.19 and 5.20 are tabulated in Table 5.8.

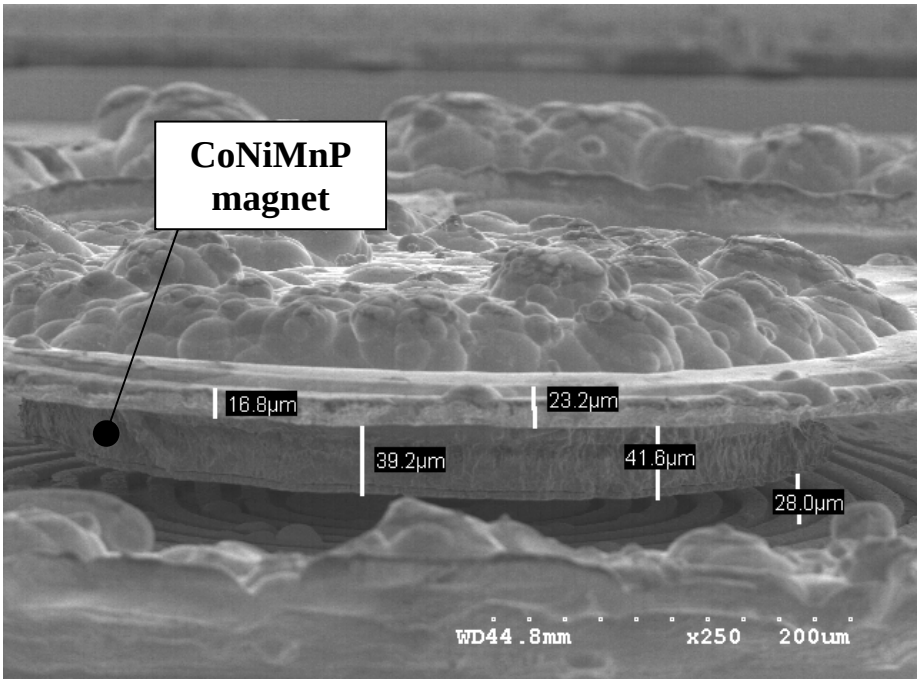

Figure 5.20. Close up SEM picture of the integrated CoNiMnP permanent magnet on the bottom of the membrane

Table 5.9. The details geometries of the bistable microvalve with latching mechanism

Structural		
Overall size ($D_{overall}$)	1,600	µm
Base thickness (t_{base})	25	µm
Actuation displacement	28 - 30	µm
Hole size in the base (D_b)	60	µm
Magnet diameter (D_M)	500	µm
Membrane diameter (w_1)	700	µm
Number of legs	2	
Thickness of legs (t_2)	4	µm
Type of legs design	Plain	
Legs width (w_2)	60	µm

Electrical		
Number of coils	12	
Width of the coil	14	µm
Thickness of the coils	8	µm

Dielectric Coating		
Thickness of parylene	1	µm

CHAPTER 6

PACKAGING

6.1 Introduction

This chapter discusses the packaging of the fabricated microvalve. Packaging is a very challenging issue for MEMS devices. For a MEMS device to be successful in commercialization, its packaging should be robust, suitable for the intended application, and proportional with the device's size. Therefore packaging tends to be application specific. Packaging bridges the connection between the MEMS fabricated devices and the external/outside environment, which may not necessarily be fabricated by silicon surface micromachining. For example, in the robotic applications, the MEMS device can be force, position, contact, and chemical sensors placed on robot fingers that are fabricated by traditional machining processes. The robot fingers can be several magnitudes larger than the actual MEMS devices themselves. Thus the packaging provides the bridge-connection between two different dimensions. The packaging size is not only dependent on the MEMS size, but also on the external devices it must connect to.

The same challenge is also faced in the packaging of the fabricated microvalve for testing in the flow of liquid. The size of the silicon chip, with 12 microvalves fabricated on it, is 12 mm x 12 mm. There are 12 inlet orifices in the wafer, each with a diameter of 250 μm. The packaging of the microvalve is designed so that it can be used for fluidic

testing for all 12 microvalves in one time. The packaging has to be able to connect the microvalve with the commercial syringe pump for testing. Obviously there are several magnitudes difference in size between the microvalve and the syringe pump. Because the package is not a final product, it should be easy to install from one chip to another. The packaging of the microvalve is provided by the combined SLA and PDMS structures, which provide great flexibility in the design and fabrication.

6.2 SLA and PDMS Structure

SLA (Stereo Lithography Apparatus) is an easy and quick means for developing a prototype of a product. The parts are designed in the software called Pro-Engineer, and the designs are saved in the *.stl file, which is compatible for SLA. The design parts are then converted to the file that is compatible to the SLA machine, Viper 5010. The conversion software is called Light Year 3.1. The resin used to make the SLA product is called SPA 1234. Inside the Viper 5010 machine, the uncured photo sensitive resin is placed in a bath and a beam of UV light partly cures the resin to the designed pattern of the parts. After that, the UV light has the pattern of the designed parts. The parts need to be cleaned to remove the residue of uncured resin. The chemical used for cleaning is TPA and ethanol with light ultrasonic agitation. At this stage the parts are still not fully cured. In order to fully cure the parts, they are placed inside a UV oven for 90 minutes.

The schematic of the packaging for the microvalve is shown in Figure 6.1. Each microvalve is placed in a bowl-cavity as shown in Figure 6.1. The cavity is large enough to provide free bidirectional movements for the microvalve membrane.

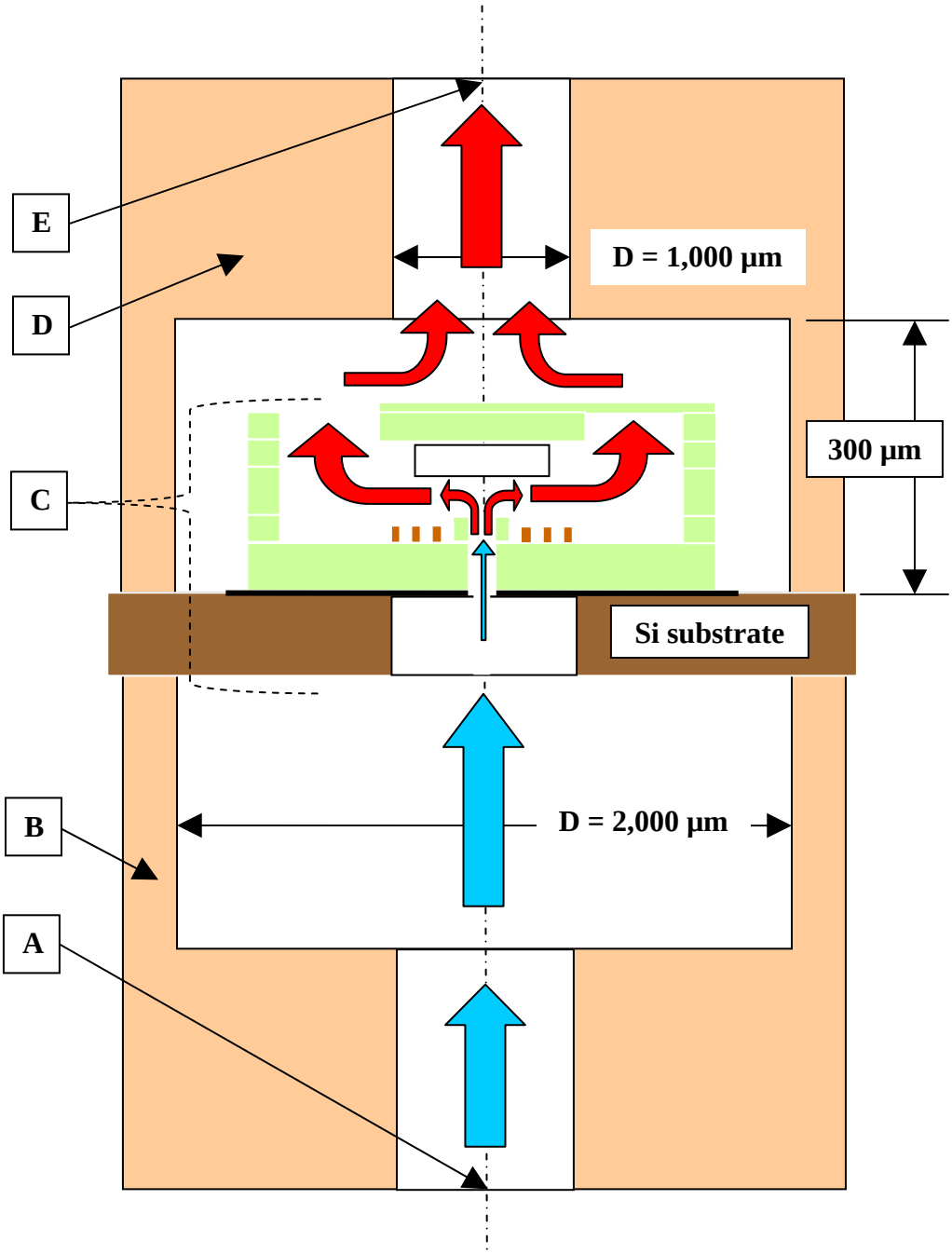

Figure 6.1. Schematic diagram cross-sectional view of the cavity made by the combination between the mould made by SLA and the SLA housing filled by PDMS; A = access to the inlet fluidic connectors; B = PDMS filled; C = Microvalve structure; D = PDMS filled; E = access to the outlet fluidic connectors

The diameter of the cavity is 2,000 μm and the height of 300 μm. There are two cavities that are placed on the top and bottom sides of the silicon substrate. There is a connection hole with the diameter of 1,000 μm between the cavities to the inlet/outlet fluidic connectors. The fluidic cavities are made by PDMS (Poly Di-Methyl Siloxane) that is filled into the mould made by SLA products.

There are 7 main parts that are built by SLA: an inlet fluidic housing, a base mould for inlet fluidic housing, an outlet fluidic housing, a base mould for outlet fluidic housing, poles, fluidic connectors, and packaging covers. The "inlet/outlet fluidic housings" are attached to the "base mould for inlet/outlet fluidic housing" respectively. Twelve poles are then attached to the base mould as shown in Figure 6.2.

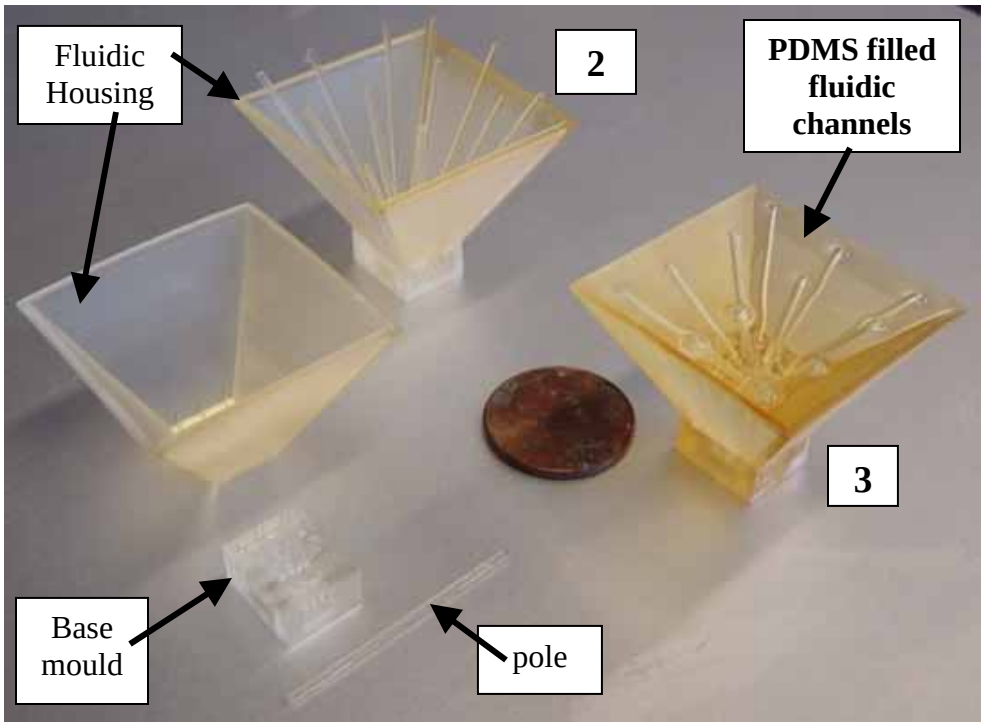

Figure 6.2. The assembly of the fluidic housing, base mould, and poles to make "PDMS filled fluidic channels"; Where: 1 = before the assembly, 2 = after the assembly, and 3 = after pouring the PDMS into the fluidic housing and it solidify

The mixing of 1 hardener to 10 PDMS is then prepared. The air bubbles trapped inside the PDMS is released by continuous vacuuming with vacuum pump. The free-bubble PDMS is then poured into the SLA assembly as shown in Figure 6.2. The assembly is then placed into an oven at 60 °C to solidify the PDMS for 24 hours. The poles are taken off and they left with holes. The base mould is also removed from the assembly and left with the SLA housing with PDMS-filled fluidic channels, as shown in Figure 6.3 labels no. 3 and 4.

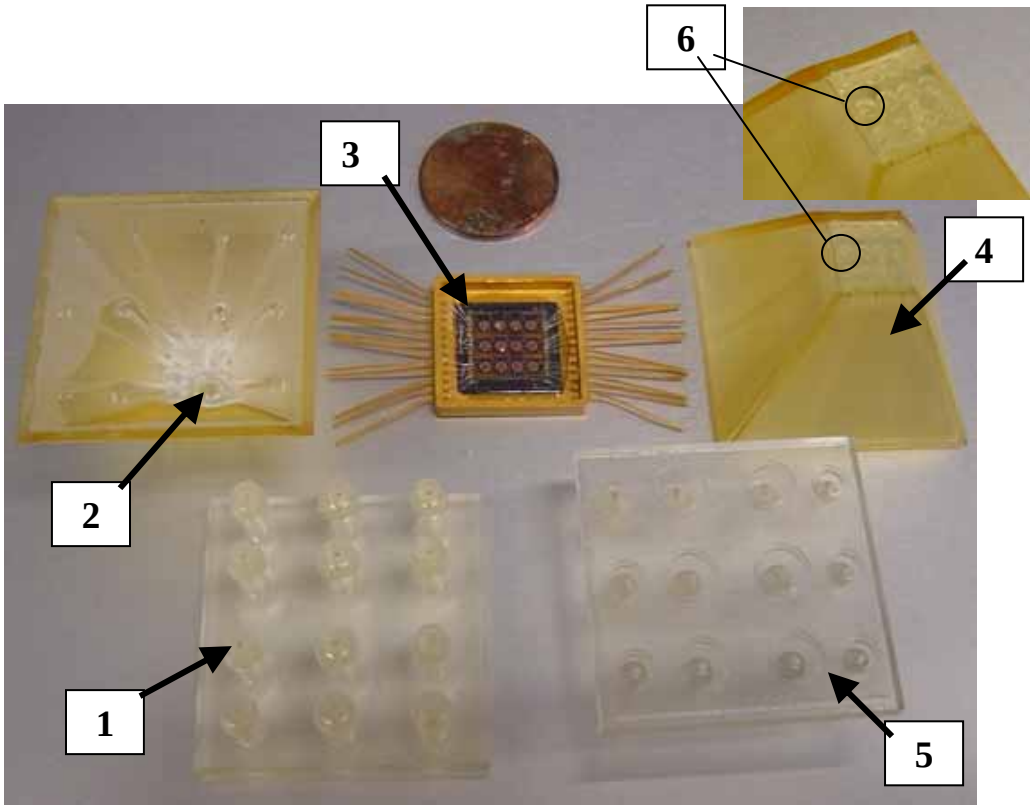

Figure 6.3. The parts required for packaging the microvalve: 1 = inlet hose connector; 2 = PDMS filled inlet fluidic channels, the top face is attached to the hose connector; 3 = 12 mm x 12 mm silicon ship consists of 12 fabricated microvalves, mounted on a gold plated package; 4 = PDMS filled fluidic channels, the top face is attached to the top surface of silicon chip; 5 = outlet hose connector; 6 = 12 x “bowl cavity” with the size of 2,000 µm in diameter and 300 µm depth, for the room of the microvalve structure”

6.3 Gold Plated Package and Parylene Deposition

The microvalve is tested in the flow rate of DI (deionized) water and 50 % diluted methanol at room temperature (approximately 22 °C). The tested chip has the dimensions of 12 mm x 12 mm square that consists of 12 microvalves. The chip is mounted on the gold plated package with epoxy glue and then wire bonded to pins on the package as shown in Figure 6.4. Aluminum is used as the wire. After wire bonding, a thin parylene-C film is deposited on top of the chip and Au package by vapor phase deposition. The deposition is at room temperature in a Parylene Deposition System type: 2010 (SCS, Indianapolis, Indiana, 46241).

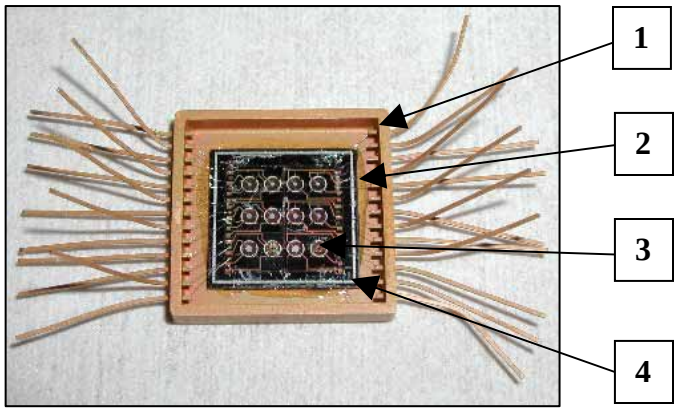

Figure 6.4. The mounted silicon chip on gold plated package. 1 = Gold plated package; 2 = Aluminum (Al) wire bonding; 3 = 12 microvalves fabricated on the substrate; 4 = 12 mm x 12mm silicon chip.

The thickness of the deposited parylene is between 1 – 2 μm. The parylene film has several functions: to protect the microvalve structure from corrosion as the entire valve structures are made of metal (NiFe); to provide a gasket between the top coil and

bottom surface of the magnet; and to prevent the possibility of electrolysis on the microcoil surface.

6.4 Final Assembly

The parts as shown in Figure 6.3 are then assembled to the silicon chip mounted on the gold plated package. Figure 6.5 shows the carton and the actual pictures of the assembled fluidic package of the microvalve. The inlet and outlet PDMS-filled fluidic channels is attached to the back and top of the silicon substrate. Proper alignments are required to ensure that all the cavities are placed over the microvalves.

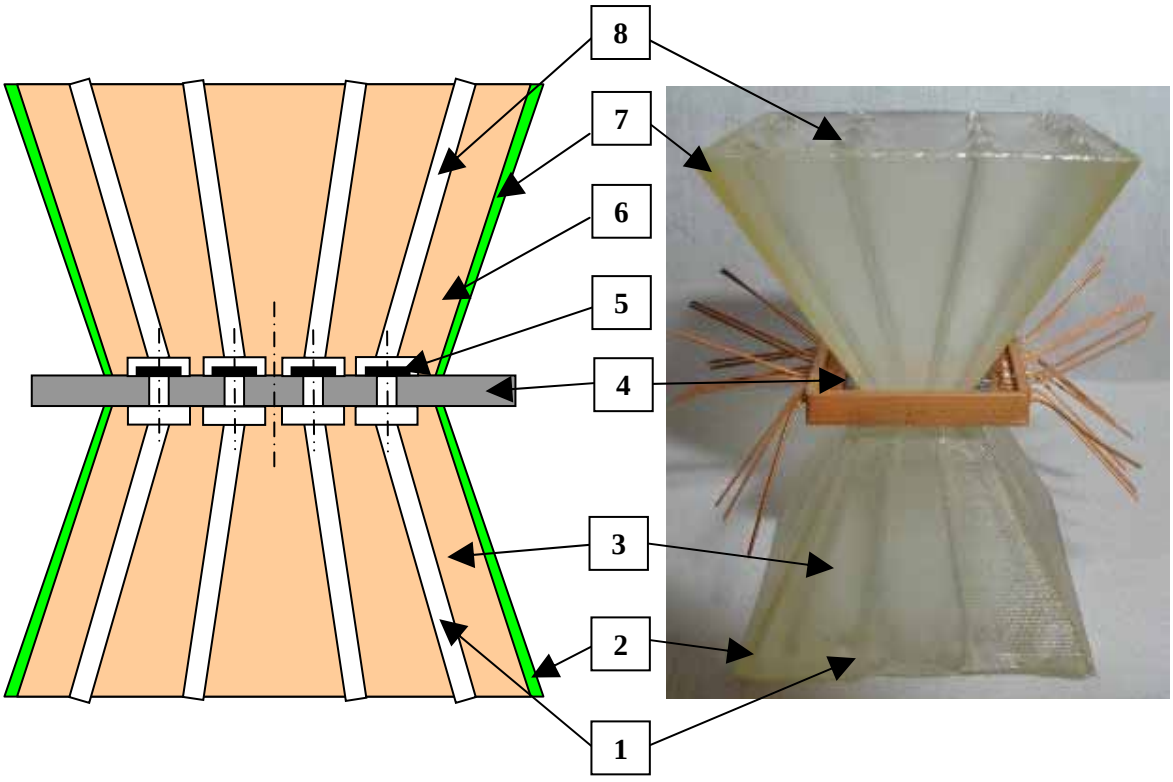

Figure 6.5. The assembled fluidic package for the microvalves. Where: 1 = Inlet fluidic channels; 2 = Inlet fluidic housing made by SLA; 3 = PDMS filled; 4 = Silicon substrate; 5 = microvalves; 6 = PDMS filled; 7 = Outlet fluidic housing; 8 = Outlet fluidic channels

Once the assembly depicted in Figure 6.5 is complete, the top and bottom fluidic connectors are connected and the packaging covers are tighten with bolts and nuts as shown in Figure 6.6. The microvalves package is then ready for fluidic testing. Silicone hoses are attached to the fluidic connectors, which are then connected to the pressure sensors. The details fluidic testing is discussed in Chapter 8.

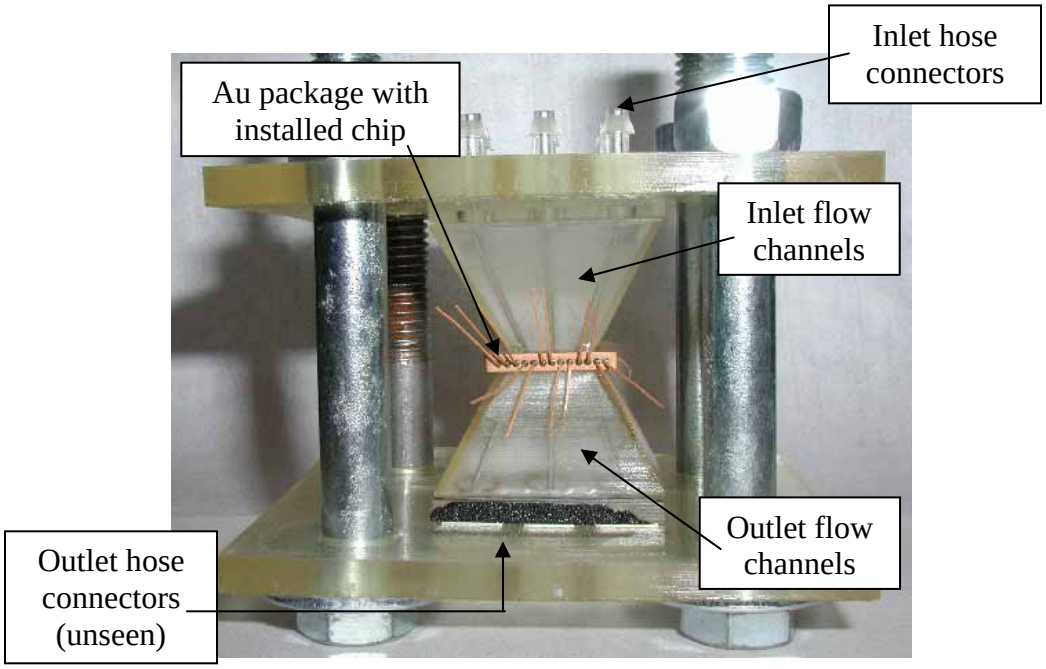

Figure 6.6. Complete assembly of the microvalve ready for fluidic testing

CHAPTER 7

TESTING OF THE MICROACTUATOR

7.1 Introduction

This chapter discusses the work that has been done to test the microvalve actuators: on/off, bidirectional, and bistable-bidirectional mechanisms. The majority of the tests were carried out in the medium of air for the bidirectional actuators. The tests were carried out in the mediums of air and water for the bistable-bidirectional actuators. Tests in different mediums: water, 50% diluted methanol, air, and pressurized air, were carried out for the on/off microvalve actuator. The results of these tests describe the membrane displacement (d_m), static, and dynamic responses of the actuator at different input currents (I_{coil}), burst time (t_b), and energies (E_{coil}). Even though the actuator is used for the microvalve operation, characteristics of the actuator are useful when utilized as an RF relay, applied to optical switches, for nano printing, or nano indenter studies.

7.2 Schematic of the Testing Setup

In order to measure the membrane displacement (d_m) of the microvalve actuator, an instrument called a Polytec OFV 3001 Laser Doppler Vibrometer was used. The device focuses a He-Ne laser spot, with the minimum size of 20 μm on the membrane

center. As the membrane moves, the device continuously monitors the phase/Doppler shift of the light reflected from the membrane. This data is converted into instantaneous velocity (V_m) by data acquisition software, which gives very precise (Å/s) velocity data at time intervals as small as 1.95 μs. The integration of velocity over time gives the instantaneous position of the membrane.

In order to produce the displacement and the dynamic response of the membrane with an applied electromagnetic force, a pulse of current is applied through the microcoil. A square wave burst input was generated with a signal generator, Stanford research center (SRC), model DS 345. The signal was sent 180° out of phase, so that only the positive portion of the waveform was transmitted. A Hewlett Packard oscilloscope, model 54616B is attached to the signal generator to continuously monitor the waveform. The burst time (t_b), which is the length of time during which a pulse of current is passed through the coil, is determined by Equation 7.1 below:

$$\frac{1}{2}\left(\frac{1}{f_b}\right) = t_b \qquad (7.1)$$

Where: f_b is the input burst frequency (Hz). This signal was passed through an amplifier built in-house and then delivered to the microcoil. The amplifier is powered by DC power supply, Tektronix, model PS2520. The laser was then focused on the center of the membrane. Measurements were recorded for various drive voltages/currents and burst frequencies ranging from 2 kHz to 50 Hz; these correspond to the range of t_b= 0.25 ms to 10 ms. Figure 7.1 shows the pulses of current that pass through the microcoil at a certain t_b. The pulses are separated from one another by a trigger time ($t_{trigger}$). The $t_{trigger}$ is set to be $\geqslant$ 2 s, long enough to insure that the membrane displacement and vibration from one

pulse does not interfere with the next one. Three different measurements are taken for each set of settings to check their repeatability.

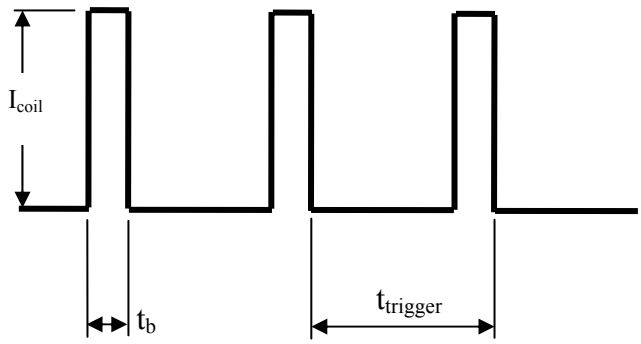

Figure 7.1. Pulses of current (I_{coil}) input to the microcoil at a certain burst time (t_s). The pulses are separated by a trigger time ($t_{trigger}$).

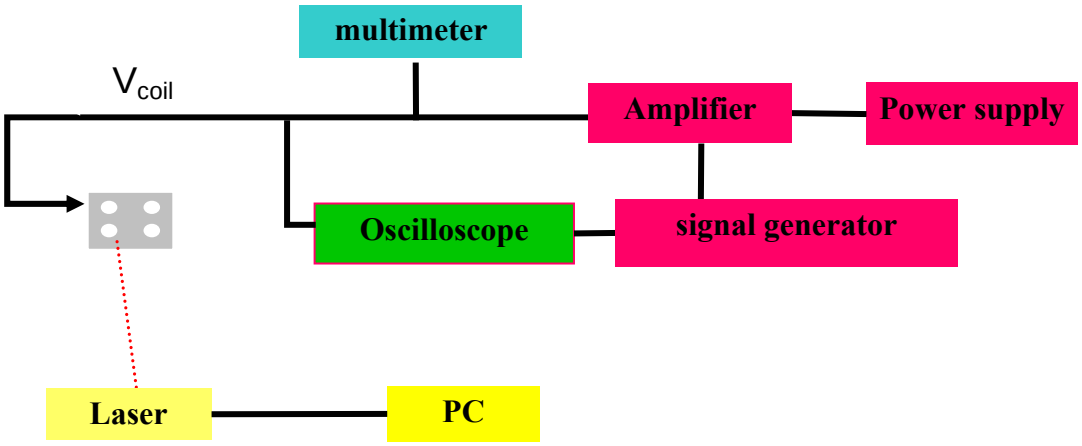

Figure 7.2. The schematic of the experimental setup for measuring the membrane displacement and its dynamic characteristic by using Laser Doppler Vibrometer

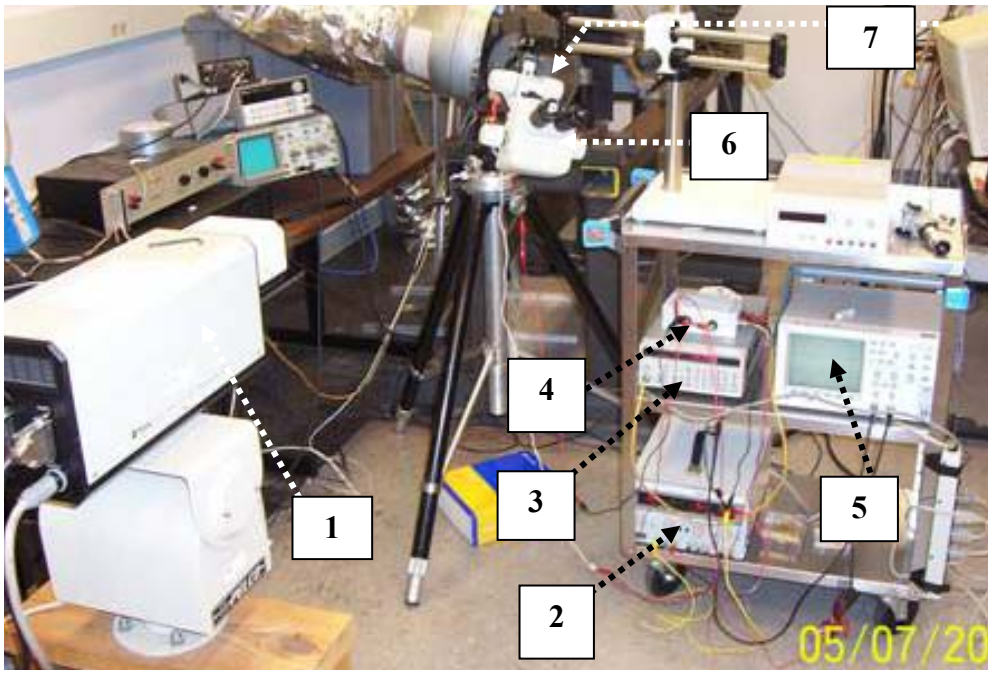

Figure 7.3. Picture shows the setup for the membrane displacement measurement by Laser Doppler Vibrometer. Where: 1 = Polytec OFV 3001 Lazer Doppler vibrometer; 2 = DC power supply; 3 = Signal generator (SRC); 4 = Amplifier built in house; 5 = Oscilloscope; 6 = Microscope; 7 = the tested microactuator behind the microscope.

The energy supplied to the bidirectional microactuator for each pulse of current is determined by Equation 7.2 below:

$$E_{coil} = P_{coil}.t_b = I_{coil}^2.R_{coil}.t_b \qquad (7.2)$$

Where: P_{coil}, E_{coil}, and R_{coil} are the input power, energy, and resistance of the micro coil respectively. Figures 7.2 and 7.3 below show the schematic and the photograph of the experimental setup for measuring the membrane displacement and its static and dynamic characteristic using a Laser Doppler Vibrometer.

Measurement Correction

Because the He-Ne laser is focused vertically onto the membrane surface, some correction is required as the membrane moves. A schematic indicating the geometry for this correction is shown in Figure 7.4 below:

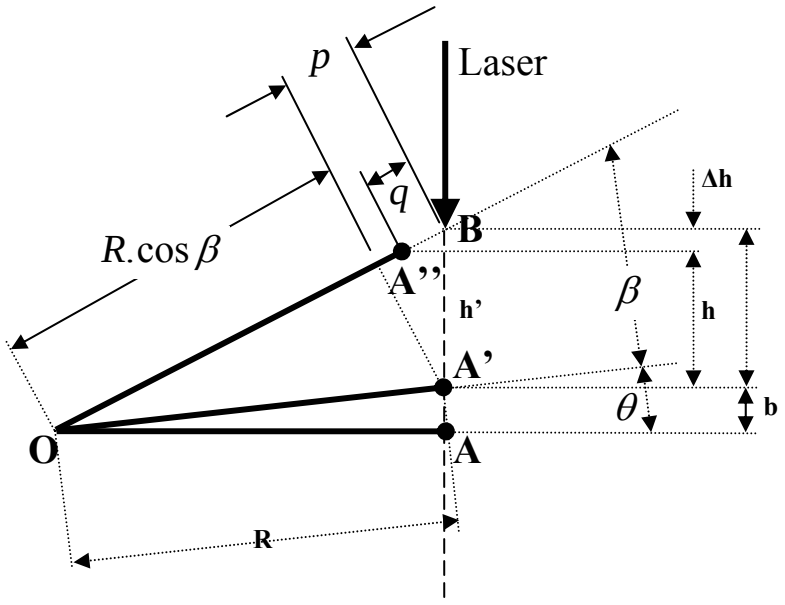

Figure 7.4. Correction for the Laser Doppler Vibrometer measurement

As shown in Figure 7.4 above, the membrane is anchored at point O. Ideally the membrane should be flat as shown by line OA, where A is the center of the membrane and R is the length of OA. Due to the film stress, the membrane may slightly deflect upward at a distance "b" and an angle of θ, where $\theta < 5°$. The center of the membrane is marked A' as shown in Figure 7.4. A current is applied to the microcoil and causes the center of the membrane to move upwards from A' to A'' with a vertical distance h.

Because the laser from the vibrometer is impinged vertically and the membrane rotates at an angle β, the laser recognizes point B instead of point A''. Thus the vibrometer gives a displacement result of h'. In order to correct the measurement data, the value of Δh has to be found. Some mathematical equations are developed to find Δh as shown in Equations 7.3 and 7.7 below:

$$\tan(\theta) = \frac{b}{R} \quad \text{and} \quad \tan(\theta + \beta) = \frac{(h'+b)}{R} \tag{7.3}$$

As θ and β are obtained, the value of Δh is determined as follows:

$$\begin{aligned} q &= h'.\sin(\theta + \beta) - R(1 - \cos\beta) \\ \Delta h &= q.\sin(\theta + \beta) \end{aligned} \tag{7.4}$$

As shown in Equation 7.4 above that the value of Δh increases with the increase of h' and β.Thus the larger the displacement the larger the correction value. It is found that the maximum correction value is less than 8 %.

7.3 Data Processing

7.3.1 Membrane Displacement (d_m)

The computer connected to the laser vibrometer gives output text files containing 16,384 velocity and time pairs. Since the time interval is short and continuous, the displacement of the membrane is determined by the integration of the instantaneous velocity, as shown by the following Equation 7.5.

$$x_n = \sum_{n=1}^{N} \left(h \times v_n + \frac{h \times (v_{n+1} - v_n)}{2} + x_{n-1} \right) \tag{7.5}$$

In this case, x, v, and h represent the membrane displacement, membrane velocity, and the time interval respectively.

Figure 7.5 provides an example of graphs showing the instantaneous velocity (V_m) and displacement (d_m) of a microvalve membrane. The figure shows that the membrane displaces downward with the minimum displacement of -50 μm. The time required for the membrane to achieve this displacement is about 0.625 ms; this is called the actuation time (t_a). Then the membrane sits on top of the micro coils for about 1.875 ms, which is a closed condition for the microvalve actuator, and the elapsed time is the called sitting time (t_s). The total actuation and sitting time, as shown in the graph, is 2.5 ms; this value is equal to the burst time, t_b, which is the length of time the impulse current is applied to the micro coil. Once the current is off, the membrane is moved upward by the stiffness of the spring. In this condition, the valve opens. When there is no current input, the membrane experiences a damped vibration in the medium, which is in this case water. Finally it returns to its original position. The rest of time is called damped vibration time (t_{dv})

7.3.2 Damped Vibration

As shown in Figure 7.5, damped vibration is a part of the membrane displacement in the medium. Time of damped vibration (t_{dv}) gives information about how often the membrane can be actuated at a given frequency without carrying this vibration wave to the next displacement. The natural frequency (f_n) of the vibration can be determined experimentally from the damped vibration in air. Since $\zeta << 1$, $\omega_d \cong \omega_n$, where ω_d and

ω_n are the damped and natural frequency (rad/s) respectively. The damping coefficient (ζ) is defined as Equation 7.6.

$$\zeta = \sqrt{1 - \left[\frac{\omega_d}{\omega_n}\right]^2} \tag{7.6}$$

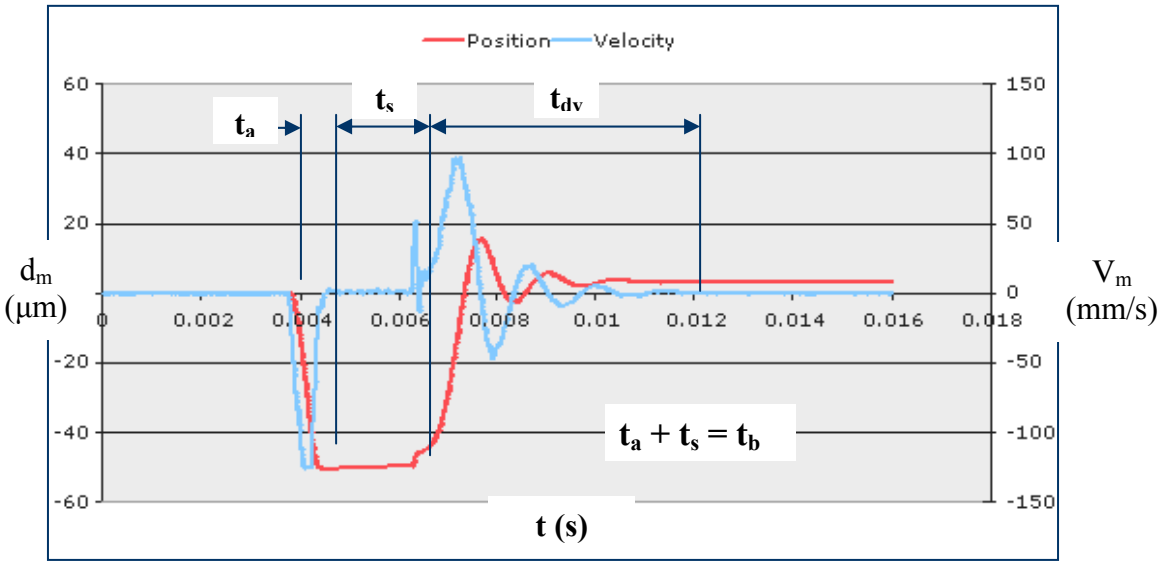

Figure 7.5. Sample of the combined velocity (V_m) and the displacement (d_m) graphs of the membrane at instantaneous time (t). The burst time (t_b) is 2.5 ms in the medium of water

7.4 On/Off Microvalve Actuator

7.4.1 Introduction

This section discusses the testing of the on/off microvalve actuator. There are two different on/off microvalve actuators discussed; Actuator A, tested in the mediums of water, 50 % diluted methanol, and air; and Actuator B, which was tested in the medium of air.

7.4.2 Packaging

The microvalve chip packaging for this experiment includes the mounting of a 12 x 12 mm silicon chip with 12 fabricated microvalves in an SLA mini box. The chip has 12 x 250 μm-diameters through holes etched through to the base of the valves. The chip is mounted on the Au-plated package for wire bonding. There are 14 Al wires needed for bonding to the package. After wire bonding, the whole device is coated by 0.5 – 1.5 μm parylene C to prevent the metal corrosion to the valve structure and to prevent the bubble production by electrolysis in water or 50% diluted methanol. Once the package is coated by parylene, the front side of the package is covered by a thin transparent glass slide and the SLA mini box is attached to the back as shown in Figure 7.6. Figure 7.7 also shows a close up of the tested microvalve actuator. The detail dimensions of the on/off microvalve are given in Table 7.1.

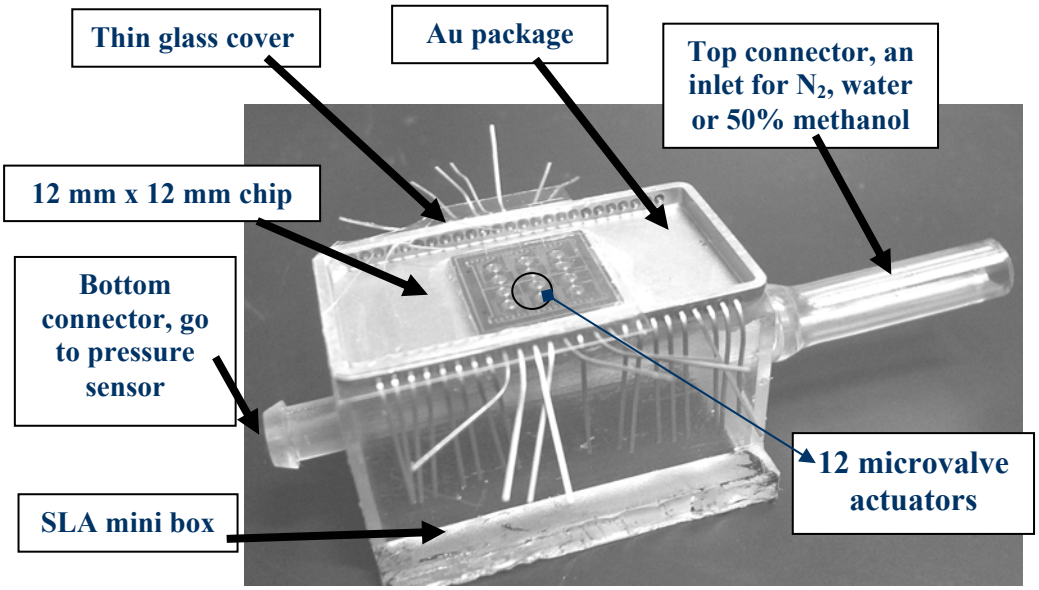

Figure 7.6. The installed package for the on/off microvalve ready for actuator testing in the medium of air, pressurized air, water, or diluted methanol

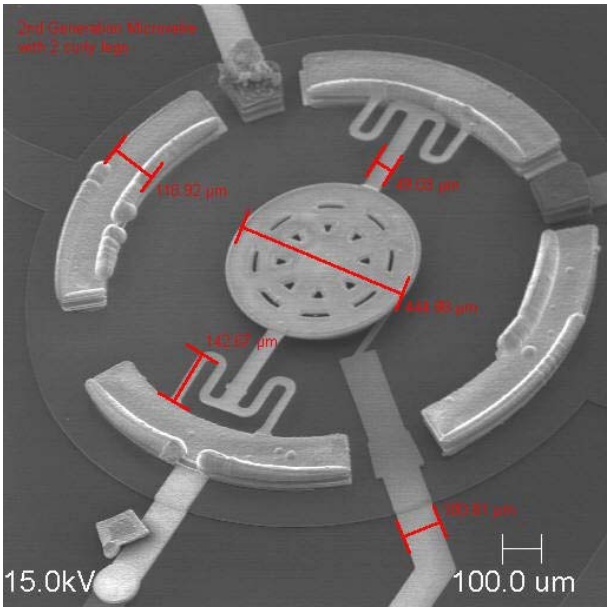

Figure 7.7. The SEM picture of the on/off microvalve (actuator B) that is tested in the medium of air and pressurized air

There are two tube connections on the SLA mini box. For the experiment in air, a pressurized N_2 gas is supplied to the back of the wafer through the top tube connection. Meanwhile a pressure gauge is connected to the bottom connector to continuously measure the applied N_2 gas pressure. For an experiment with water or 50% diluted methanol, the liquid is filled through the top connector and the bottom connector is closed. The liquid also fills the cavity covered by the thin glass. And there is no pressure applied to the fluid.

Table 7.1. The geometries of the tested on/off microvalve that are tested for their actuation

Structural		
Overall diameter	1,400	μm
Base thickness (t_{base})	10	μm
Gap/Actuation displacement (g)	55* and 38**	μm
Membrane diameter (D_1)	400	μm
Thickness of centered membrane (t_1)	15	μm
Number of legs	2	
Thickness of legs (t_2)	2	μm
Legs width (w_2)	50	μm
Electrical		
Number of coils	10	μm
Width of the coil	12	μm
Thickness of the coils	9	μm
Coating		
Thickness of parylene	1	μm

Where: * = actuator A, # of legs = 2 separated by 90°; tested in the medium of air, water, and 50% diluted methanol/water

** = actuator B, # of legs = 2 separated by 180°; tested in the medium of air and pressurized air. The picture is shown in Figure 7.7.

7.4.4 Testing in Liquid: Water and 50% diluted Methanol

A. Displacement versus Current

Figure 7.8 shows the membrane displacement (d_m) in the medium of water at different input currents to the microcoil (I_{coil}). The results are plotted for 0.5 ms $\leqslant t_b \leqslant$ 5 ms. The results shows that d_m are independent of t_b when $t_b \geqslant$ 1.25 ms. At these t_b, the graphs collide together; the membrane touches the bottom coil at I_{coil} = 0.28 A.

As mentioned before, when the membrane touches the bottom coil, the on/off microvalve is at the closed position. Figure 7.8 shows that when $t_b \leq 1.25$ ms, d_m becomes dependent of both I_{coil} and t_b, and it requires more I_{coil} and more power (P_{coil}) for the membrane to touch the bottom coil.

Figure 7.9 shows the variation of d_m in 50% diluted methanol with the applied I_{coil}. The results are plotted for t_b = 0.5, 0.67, 1, 2, 5 ms. In this medium, the membrane is slightly deflected upward, which results in a minimum d_m of -55 μm instead of -51 μm in water as shown in Figure 7.8.

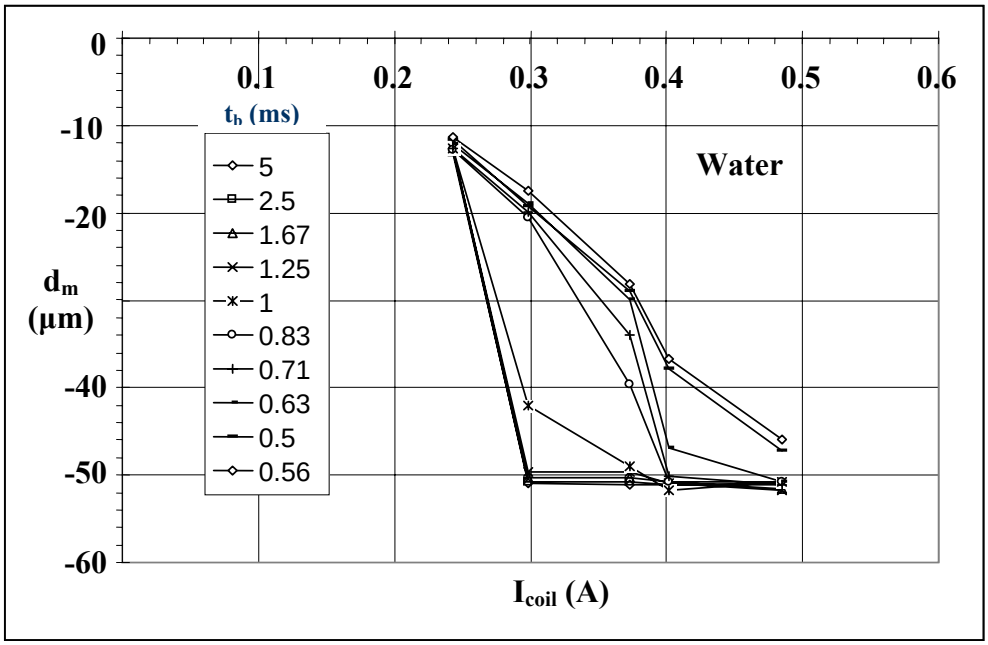

Figure 7.8. The membrane displacement (d_m) in the medium of water at different current to the microcoil (I_{coil}). The results are plotted at different burst times (t_b). The membrane touches the bottom coil at d_m = -51 μm.

Figure 7.9 shows that the required I_{coil} to close the valve at d_m = -55 μm is 0.35 A for t_b = 2 and 5 ms. The amount of current required is larger than that required to close the microvalve in water. When t_b < 2 ms, much more current (I_{coil}) and more power (P_{coil}) is required to close the valve in 50% diluted methanol. Figure 7.10 shows a comparison in d_m for actuation in the medium of water and 50% diluted methanol. It shows d_m at various t_b = 2.5, 5, and 10 ms. It also shows that the results are pretty much independent of t_b as supported in Figures 7.8 and 7.9. Figure 7.10 shows that when I_{coil} < 0.25 A, it requires more I_{coil} in 50% diluted methanol to produce the same amount of d_m. When I_{coil} > 0.25 A, d_m does not seem to differ that much in both mediums. However it still indicates that d_m is larger in water than 50% diluted methanol at the same I_{coil}.

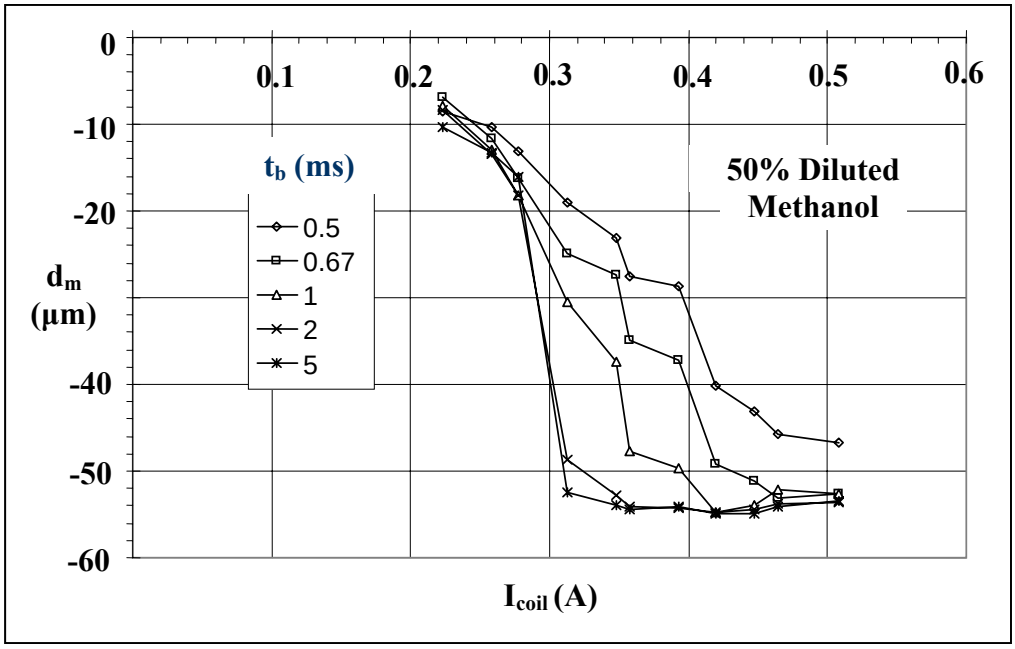

Figure 7.9. The membrane displacement (d_m) in the medium of 50% diluted methanol at different current to the microcoil (I_{coil}). The results are plotted at different burst times (t_b). The membrane touches the bottom coil at d_m = -55 μm.

Figure 7.11 shows d_m for both mediums at smaller t_b, t_b = 0.5 ms, and 1 ms. It shows clearly that the membrane displaces more in water than in 50% diluted methanol at the same I_{coil} and t_b. It shows that at large I_{coil}, $I_{coil} \geqslant 0.4$ A, the difference in d_m between both mediums becomes smaller. This is mostly because the membrane approaches the bottom coil and experiences a large electromagnetic force (F_{EM}). Figure 7.11 also shows that the difference in d_m for both mediums gets smaller as t_b gets smaller.

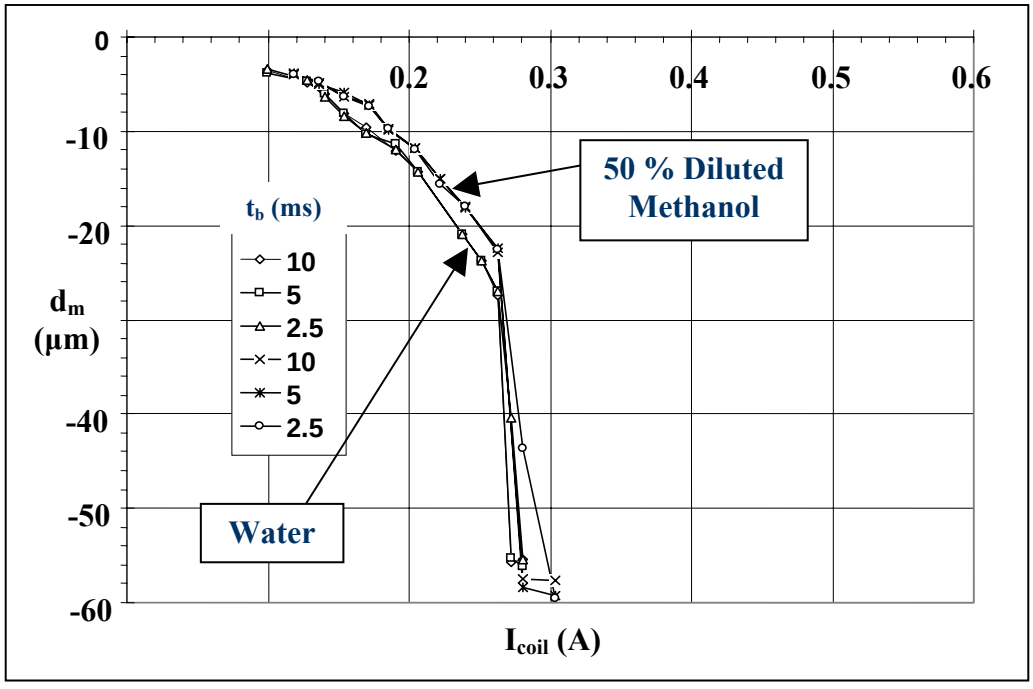

Figure 7.10. The comparison on the membrane displacement (d_m) at two different mediums: water and 50% diluted methanol plotted at the burst time (t_b), 2.5, 5, 10 ms.

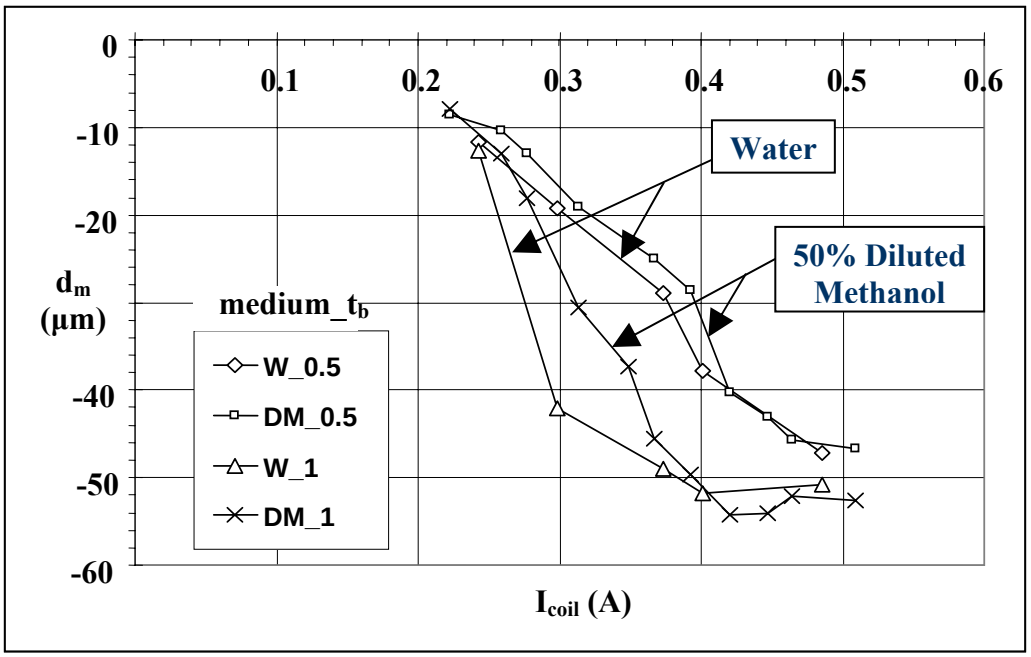

Figure 7.11. The comparison on the membrane displacement (d_m) at two different mediums: water and 50% diluted methanol. The results are plotted at the burst time (t_b) = 0.5 and 1 ms. The results shows very strong dependent on the burst time (t_b).

B. Displacement versus Energy

Figure 7.12 shows the membrane displacement at different input energies to the microcoil (E_{coil}), and the results are plotted at various burst times (t_b), t_b = 1, 1.25, 1.67, 2.5, and 5 ms. The graph shows that the minimum displacement is about -51 µm. At this condition, the membrane touches the bottom microcoil, which resembles the condition where the on/off microvalve is closed.

There is a large difference in the energy consumption at t_b = 5 ms and 2.5 ms, with the energy of 3 mJ and 1.4 mJ respectively, required to close the microvalve. This indicates that most of the energy has been consumed to maintain the membrane in the sitting/closed (t_S) position as described in Figure 7.5. Up to the point that the microvalve

closes, a small change in the energy yields a large change in the displacement; this gradient seems to be larger as t_b decreases. Further more, as the t_b decreases, the graphs in Figure 7.12 move toward to the left. This seems to indicate that the required energy is decreasing with the decrease in t_b. However, in order to fully close the microvalve, E_{coil} in the range of 0.8 to 1.3 mJ is required at $t_b \leqslant 2.5$ ms for this particular microvalve design.

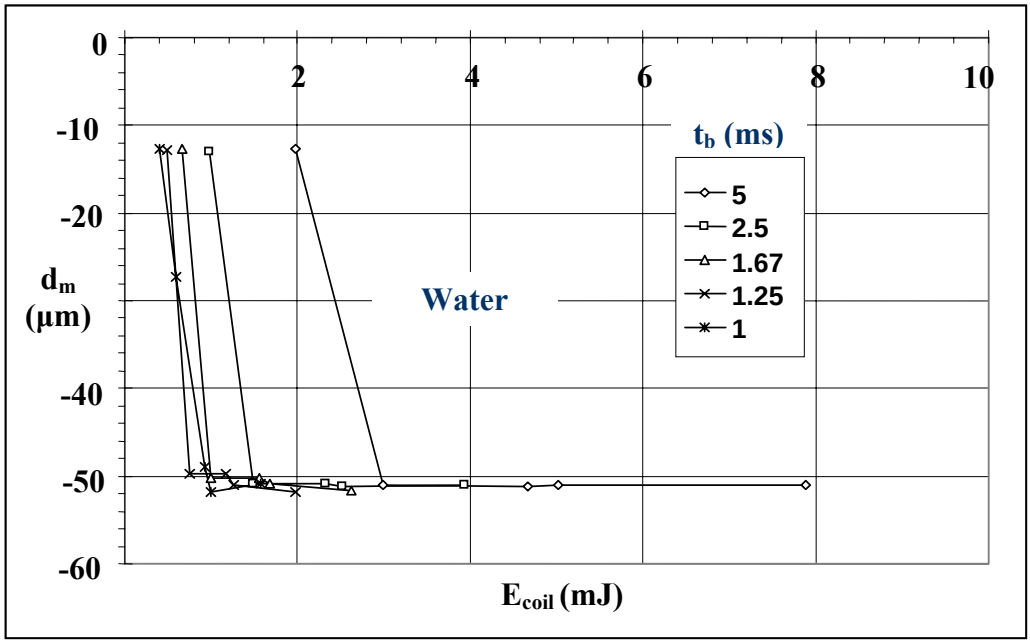

Figure 7.12. The membrane displacement (d_m) in the medium of water, plotted as a function of energy to the microcoil (E_{coil}) and the burst time (t_b), 1 ms < t_b< 5 ms.

Figure 7.13 shows d_m at lower E_{coil} when 0.5 ms $\leqslant t_b \leqslant$ 1 ms. At $E_{coil} \leqslant$ 0.5 mJ, the graphs show the same trend as in Figure 7.12, where the energy decreases with t_b. However, it shows that the minimum E_{coil} to close the valve is 0.7 mJ and it is achieved at t_b = 0.71 ms instead of 0.5 ms, which is the lowest t_b.

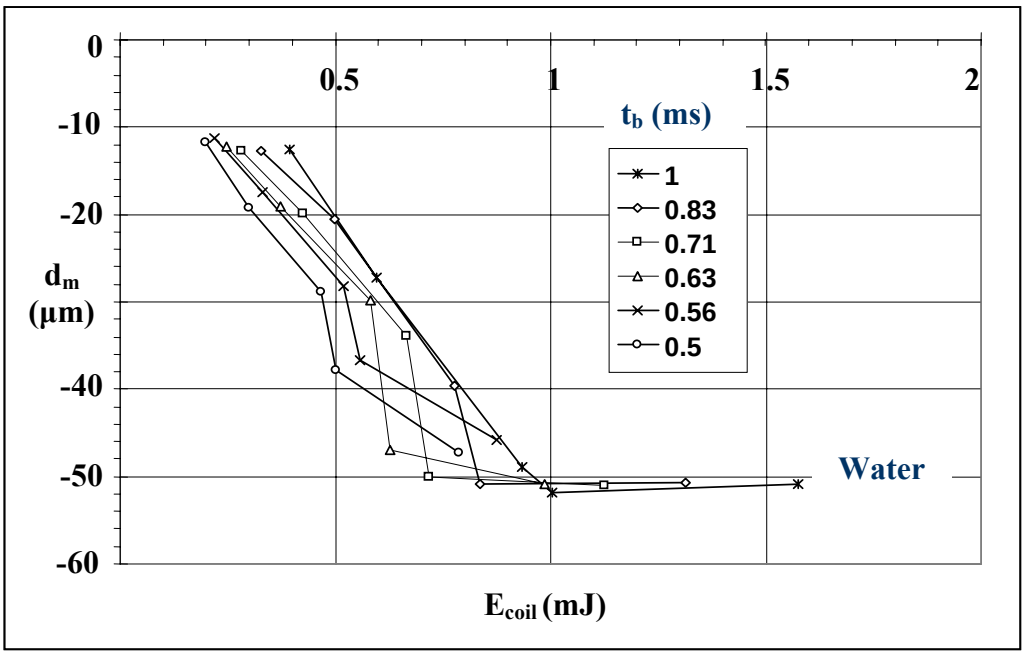

Figure 7.13. The membrane displacement (d_m) in the medium of water, plotted as a function of energy to the microcoil (E_{coil}) and the burst time (t_b), 0.5 ms < t_b< 1 ms.

Figure 7.14 shows d_m at different E_{coil}, for the actuation in 50% diluted methanol at various t_b, 0.5 ms $\leqslant$ t_b $\leqslant$ 5 ms. It shows the same trend as in water where d_m decreases with t_b. This indicates that d_m has a strong dependence on I_{coil}; as shown in Equation 7.2, the decreases in t_b at the same E_{coil} results in increases in I_{coil}, which increases the electromagnetic force (F_{EM}) that deflects the membrane downward. The membrane touches the bottom coil at E_{coil} = 0.8 mJ and t_b = 0.5 ms.

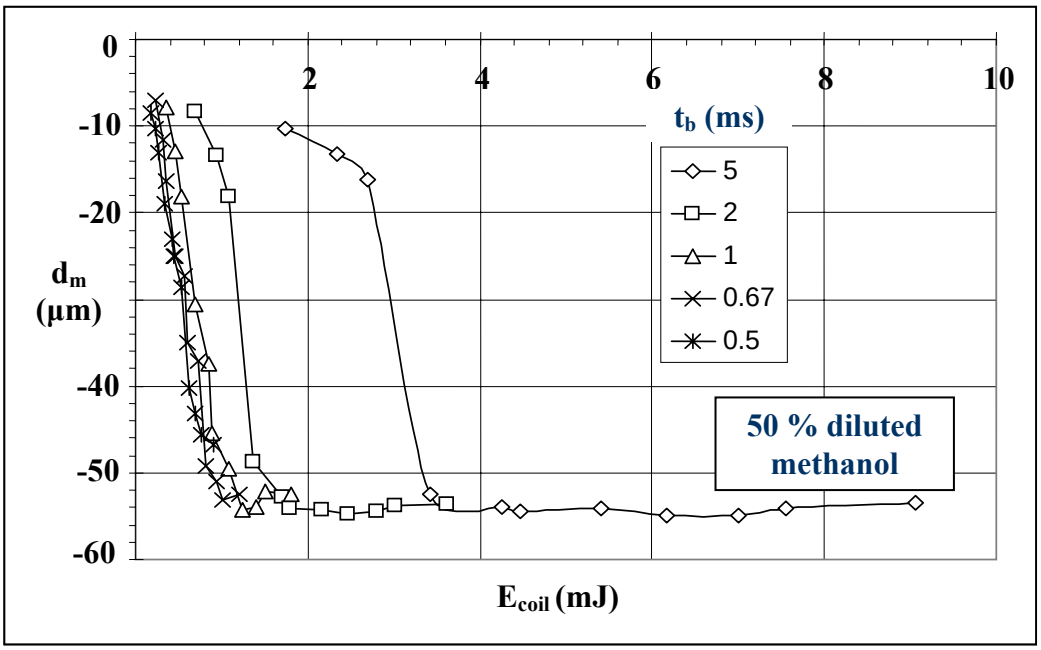

Figure 7.14. The membrane displacement (d_m) in the medium of 50% diluted methanol, plotted as a function of energy to the microcoil (E_{coil}) and the burst time (t_b) at 0.5 ms < t_b< 5 ms.

C. Results of Damped Vibration

Table 7.2 shows the analysis in the damped vibration of the microvalve actuator. It illustrates that the natural frequency (f_n) of the valve vibration is 1,392 Hz; this number is an averaging over a number of experiments. It has the standard deviation, σ=5.25. The damped frequency (f_d) of water is about 730 Hz, and 680 Hz for 50% diluted methanol. This corresponds to the damping coefficient (ζ) of 0.85 for water and 0.87 for 50% methanol.

Table 7.2. The vibration properties of the on/off microvalve actuator in three different mediums: air, water, and 50% diluted methanol

Medium	I_{coil}	f (Hz)	ζ
Air (f_n)	0.324	1,392	-
Water (f_d)	0.456	727	0.85
Water (f_d)	0.232	736	0.85
50% Methanol (f_d)	0.493	679	0.88
50 % Methanol (f_d)	0.31	686	0.88

f_n = Natural Frequency (Hz); f_d = Damped Frequency (Hz);
ζ =Damping Coefficient

D. Actuation Time (t_a) at Different I_{coil}

Figure 7.15 shows the membrane displacement (d_m) versus time (t) when a current (I_{coil}) = 0.5 A is applied at different t_b. While, Figures 7.8 to 7.14 do not contain the information about the time required for the valve to fully close, Figure 7.15 clearly indicates the actuation time (t_a) and the sitting time (t_s) of the membrane at different t_b values. Figure 7.15 shows that the graphs collide together during their actuation time (t_a). It indicates that t_a is independent of t_b; it is only a function of I_{coil}. Figure 7.16 shows the variation of t_a at different I_{coil} for the membrane actuation in 50% diluted methanol at t_b = 5 ms.

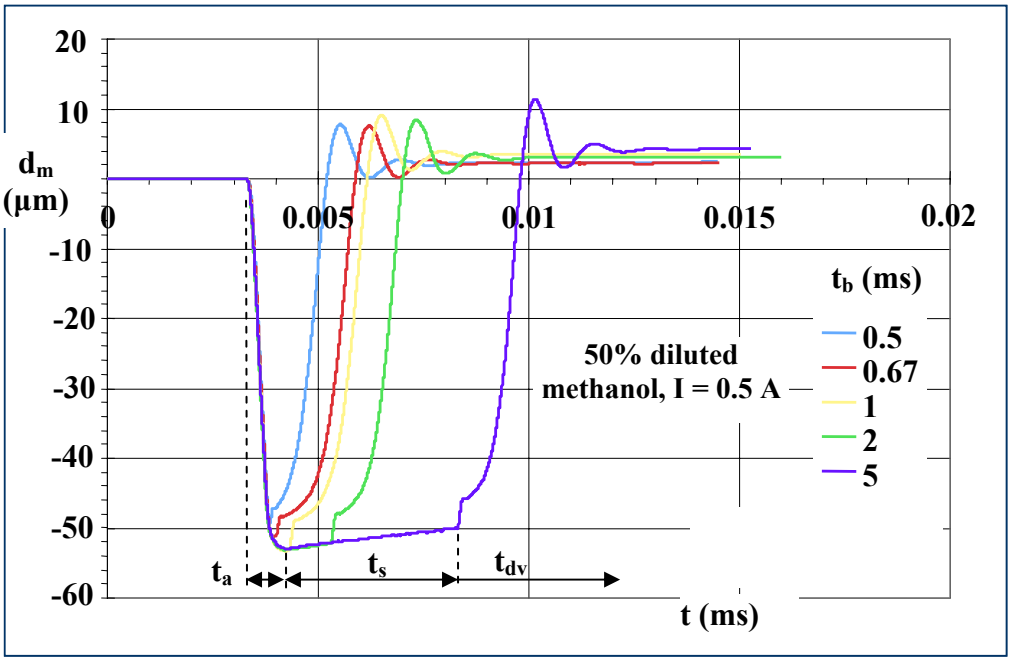

Figure 7.15. The membrane displacement profiles at the instantaneous time (t) in the medium of 50% diluted methanol, plotted at different burst time (t_b). It shows that the actuation time (t_a) is independent of burst time (t_b)

Since the gradient of d_m versus time is the same during t_a as shown in Figure 7.15, the membrane should have the same average velocity before it touches the bottom microcoil. The results in Figures 7.15 and 7.16 conclude that the I_{coil} determines how fast the actuator should move. It is in agreement with Equation 7.7 where the generated electromagnetic force (F_{EM}) is proportional to the number coil (N_{coil}) and the current (I_{coil}). The F_{EM} creates the momentum for the membrane to move at a certain velocity (V_m).

$$F_{EM} \propto N_{coil}.I_{coil}$$
$$F = F_{EM} - F_d - F_s \qquad (7.7)$$
$$F = m_e.V_m = (m_m + m_f).V_m$$

Where: F_d is the squeeze film damping force in the fluid and F_S is the spring force of the membrane, and m_e is the equivalent mass of the membrane that consists of the static mass of the membrane (m_m) and the mass of the fluid (m_f) surrounding the membrane.

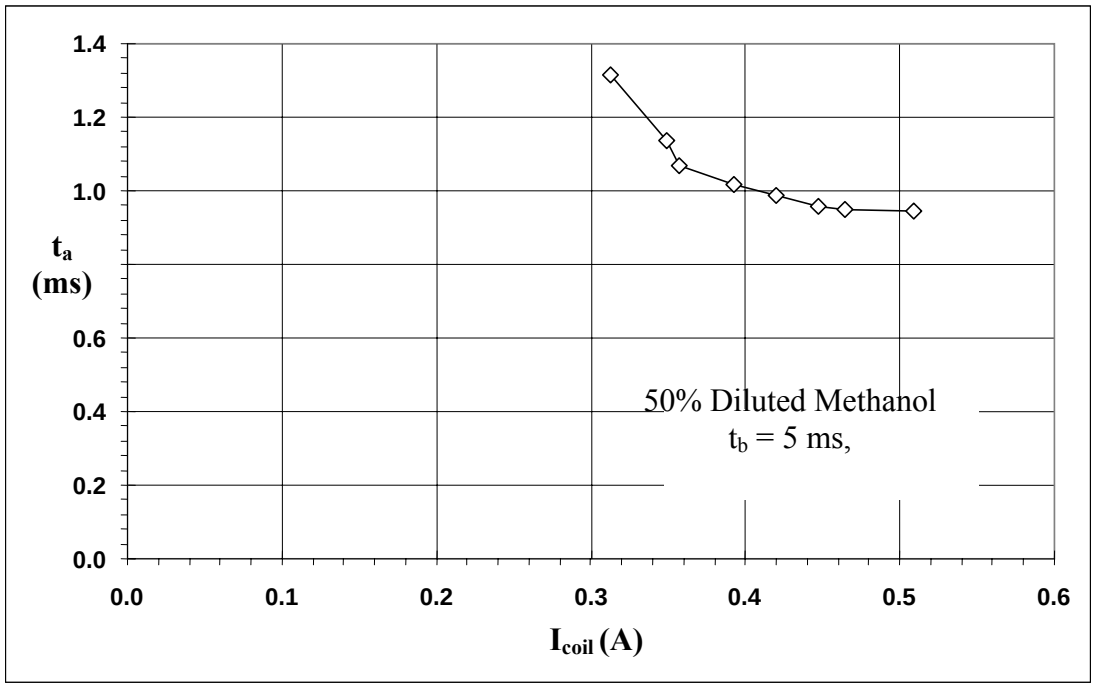

Figure 7.16. The variation of the actuation time (t_a) with input current to the microcoil (I_{coil}). The graph is plotted for the medium of 50% diluted methanol with the burst time (t_b) = 5 ms

7.4.5 Testing in the Medium of Air and Pressurized Air

The tests in the medium of air and pressurized air are carried out for the actuator B with the detail geometries as tabulated in Table 7.1 and the SEM picture in Figure 7.7. Figure 7.17 shows the gap distance between the membrane and the bottom coil at

different air input pressure (P_{input}). It shows that the membrane's upward deflection, with the increases in P_{input}, is indicated by a larger value of the gap. It seems that the gap increases linearly with P_{input}, when $P_{input} = 0$, g = 38 μm.

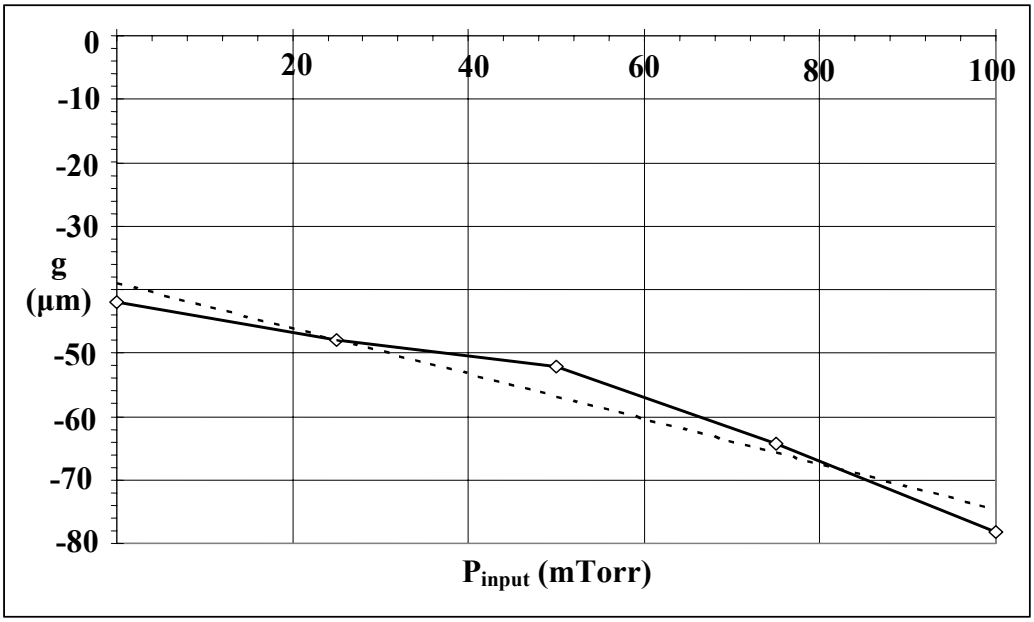

Figure 7.17. The gap distance (g) between the membrane and the microcoil at different air input pressure (P_{input})

Figure 7.18 shows that the membrane touches the bottom coil when $I_{coil} = 0.47$ A. This amount of current is sufficient to close the membrane at different input pressure (P_{input}). The results in Figure 7.18 is for $t_b = 5$ ms.

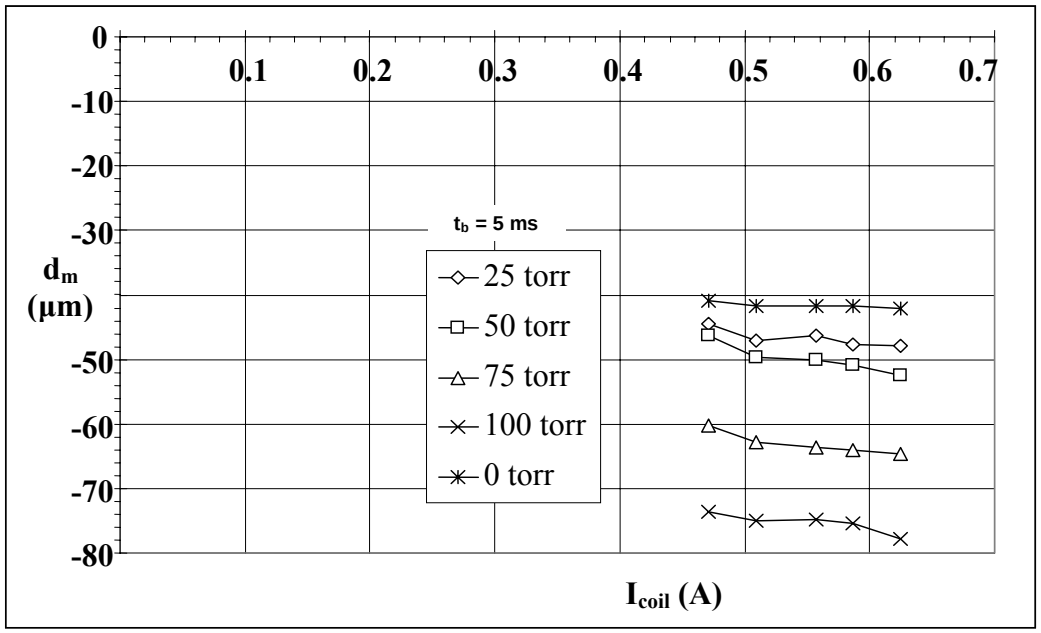

Figure 7.18. The membrane displacement (d_m) at different input current (I_{coil}). The results are plotted at different air pressure (P_{input}) and the burst time (t_b) of 5 ms.

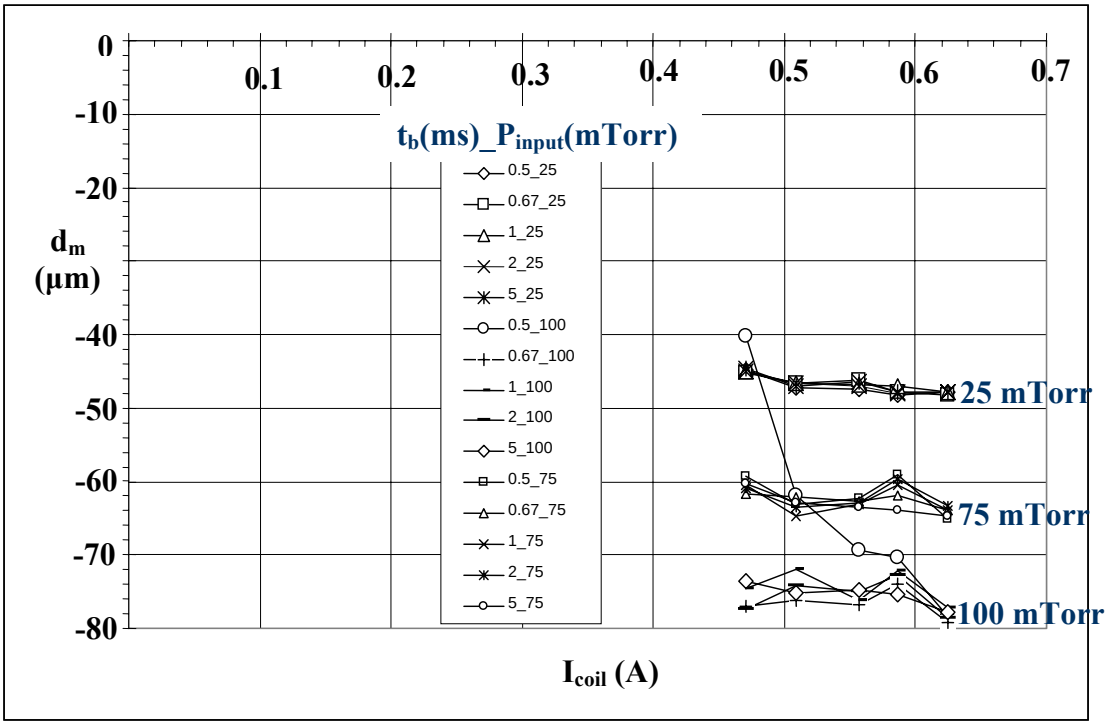

Figure 7.19. The variation of the membrane displacement (d_m) with the burst time (t_b) and the input air pressure (P_{input}).

Figure 7.19 shows the variation of d_m with I_{coil} and P_{input}. The results are plotted at various t_b, t_b = 0.5, 0.67, 1, 2, 5 ms. The results show that the d_m becomes more dependent on t_b as the pressure increases. Figure 7.19 shows that the d_m does not seem to vary with t_b when P_{input} = 25 mTorr. When P_{input} = 100 mTorr, it shows a strong variation in d_m with t_b.

7.5 Bidirectional Actuator

7.5.1 Introduction

This section discusses about the actuation of the bidirectional actuator in the medium of air. There are two bidirectional actuators tested: double-legs and single-leg designs.

7.5.2 Results

7.5.2.1 Double-legs Bidirectional Actuator

A. Displacement versus Current

The displacement results of the membrane (d_m) at different input currents (I_{coil}) to the microcoil are shown in Figure 7.20. The schematic of the bidirectional actuator is shown in Figure 3.5, except that there is no inlet hole through the substrate. Figure 7.20 shows the combined finite element analysis (FEA) and experimental results at various burst times (t_b), t_b = 1.67, 2.5, 5, and 10 ms. The top and bottom portion of Figure 7.20 shows the upward d_m and downward d_m respectively. The two displacements are not

symmetrical, so the slope of downward d_m increases more rapidly than upward d_m at the increase of I_{coil}. This is caused by the change of $\frac{dB_Z}{dz}$ as the membrane moves. As shown in Equation 3.4, the repulsive or attraction force is proportional to $\frac{dB_Z}{dz}$. The increase in the gap (g) distance between the membrane and the microcoil as the upward d_m becomes larger reduces $\frac{dB_Z}{dz}$. It reduces the repelling force that moves the membrane upward. The opposite situation happens for a downward d_m where $\frac{dB_Z}{dz}$ increases as d_m gets smaller. The results show that the minimum displacement (d_{min}) is 71 μm, which is achieved at I_{coil} = -0.25 A. Smaller current than -0.25 A produces the same amount of d_m. The FEA results nearly agree with experiment; though FEA slightly overestimates the performance of the microactuator to produce both downward and upward d_m. FEA shows that less I_{coil} is required to produce the same magnitude of d_m. The experimental results show that the upward d_m saturates at its maximum value, d_{max} = 28.3 μm when I_{coil} > 0.25 A. The saturation of upward d_m occurs because the air reluctance between membrane and the microcoil exceeds the strength of electromagnetic field generated by the microcoil. FEA results show that the slope of upward d_m decreases as I_{coil} gets larger but it does not show any saturation up to I = 0.35A.

If we look closely at the downward d_m, it shows that the slope of d_m increases as I_{coil} decreases. However up to the point labeled "X", when d_m = -60 μm, the slope decreases and then the membrane touches the bottom coils at d_m = -71 μm. This change of slope is not observed by FEA but it explains the behavior of membrane rotation as described in Figure 3.12d.

Figure 7.20 shows that d_m are independent of t_b. The graphs of d_m versus I_{coil} coincide with one another when t_b = 1.67, 2.5, 5, and 10 ms. It indicates that when t_b > 1.67 ms, d_m is independent of t_b or f_b. Figure 7.21 shows the membrane deflection (d_m) at lower burst time (t_b), where t_b = 1.67, 1.25, 1, 0.67, 0.5, 0.4, 0.33, 0.29, and 0.25 ms. The results shows that d_m is strongly dependent on t_b. Smaller t_b correspond to smaller magnitude of d_m. When t_b is reduced from 1.67 ms to 1.25 ms, we observe that d_m does not reach its minimum (d_{min}) value of -71 μm with I = -0.25 A; a larger magnitude of I = -0.3 A is required. When t_b < 0.67 ms, an even greater magnitude of current than -0.3 A is required for the membrane to achieve d_{min}.

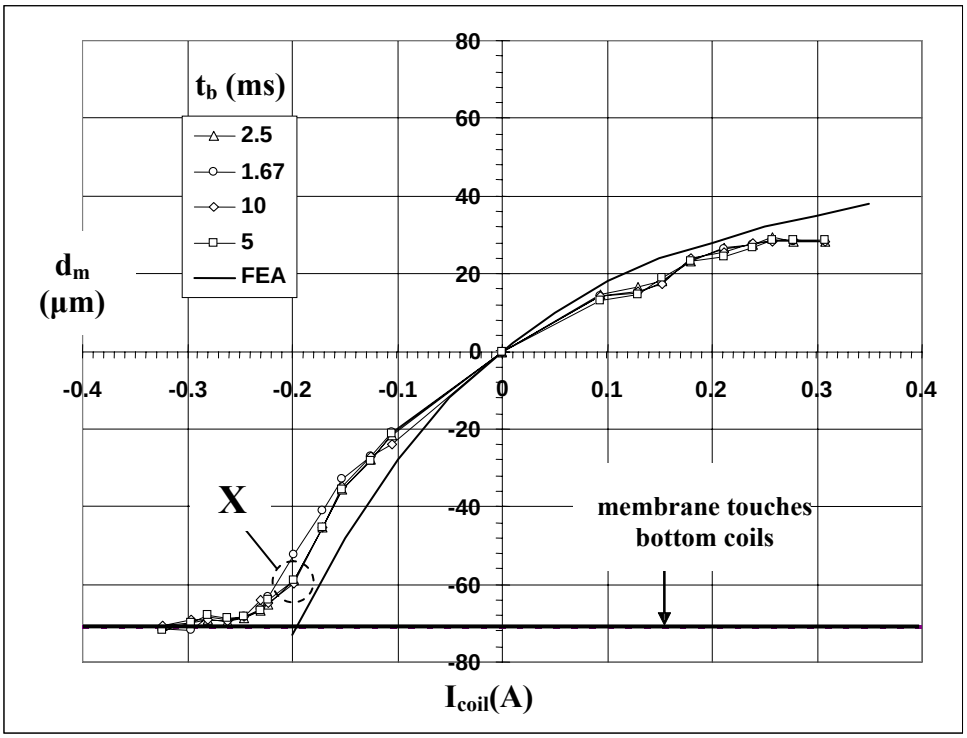

Figure 7.20. Combined experimental and FEA results on the membrane bidirectional displacements (d_m) for double-legs design at different input current (I_{coil}). The results are plotted at the burst time (t_b) ≥ 1.67 ms.

Figure 7.21 shows that the slope of d_m decreases as t_b gets smaller. It is also shown that d_{max} reduced as t_b gets smaller. This means that the response of the microactuator to displace the membrane becomes weaker at shorter impulse (t_b), and eventually the response would diminish as t_b goes to zero. Figure 7.22 shows the variation of d_{max} with t_b. Figure 7.22 shows that the maximum d_{max} is 28.3 μm, and it is achieved at $t_b > 1.67$ ms. The magnitude of d_{max} decreases linearly with t_b as t_b gets smaller than 1.67 ms. Figures 7.21 and 7.22 give important results; they show that the membrane displacement (d_m) can be varied not only by I_{coil} but also by t_b. These dynamic characterizations are useful when the bidirectional actuator is utilized for optical switching, nano indenter, or nano writing.

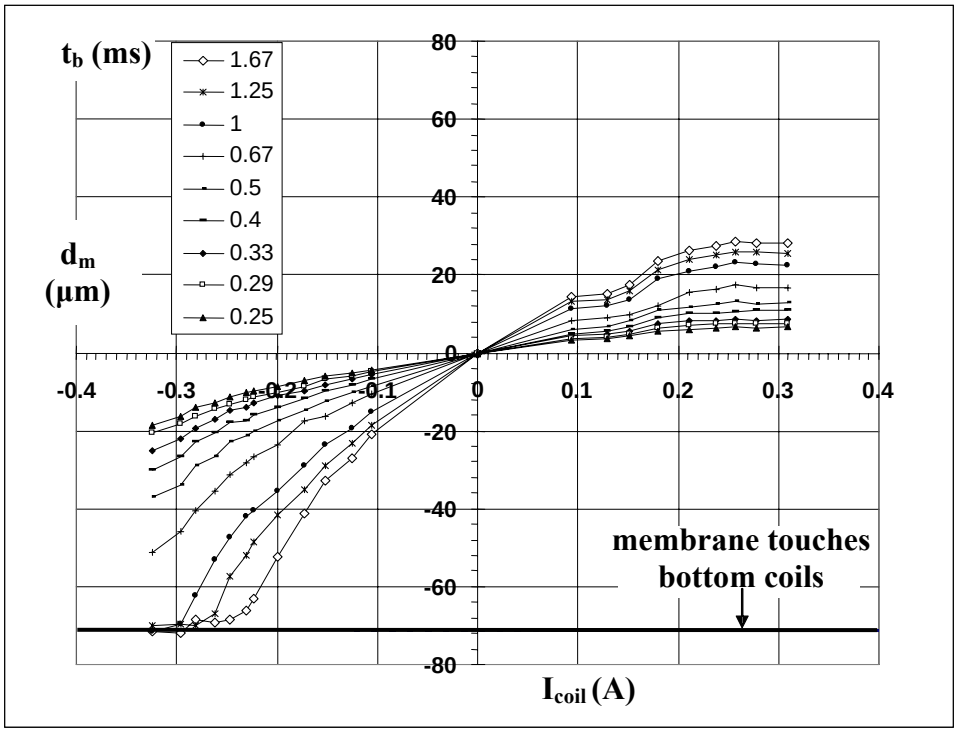

Figure 7.21. The membrane deflection (d_m) for double-legs design at different input current (I_{coil}). The results are plotted at various burst time (t_b), $t_b \leq 1.67$ ms.

Figure 7.21 shows that when $t_b \leq 1.67$ ms, the displacement results have strong dependency on t_b. We can also say that 1.67 ms is the limit of t_b beyond which the displacement is no longer a function of t_b. The natural frequency (f_n) of the actuator for double-legs design was found to be 287 Hz. The corresponding burst frequency (f_b) for t_b = 1.67 ms is 300 Hz. Hence, we observe that when $f_b \approx f_n$ of the membrane structure, the optimal d_m is achieved. This result is very surprising because the current pulses that are sent to the microcoil are separated by $t_{trigger}$ = 2s from one another as shown in Figure 7.1. This time is long enough to ensure that the membrane displacement and vibration from one pulse do not effect to the next one.

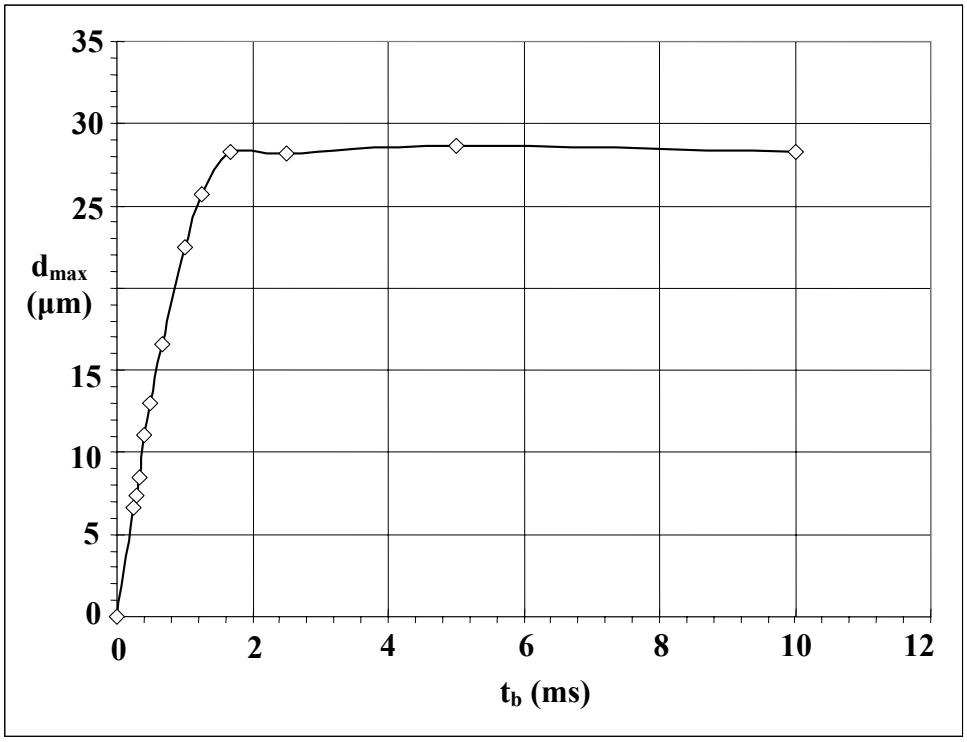

Figure 7.22. Maximum upward displacement (d_{max}) for double-legs design plotted at various burst time (t_b).

Figure 7.23 shows a sample of the instantaneous velocity (V_m) profile of the membrane captured by Laser Doppler Vibrometer when an impulse of current, I_{coil} = 0.32 at t_b = 10 ms, is applied. Figure 7.23 shows that once the current is turned off, the membrane oscillates upward and downward with decaying velocity amplitude as indicated by the exponential equation as shown in Figure 7.23.

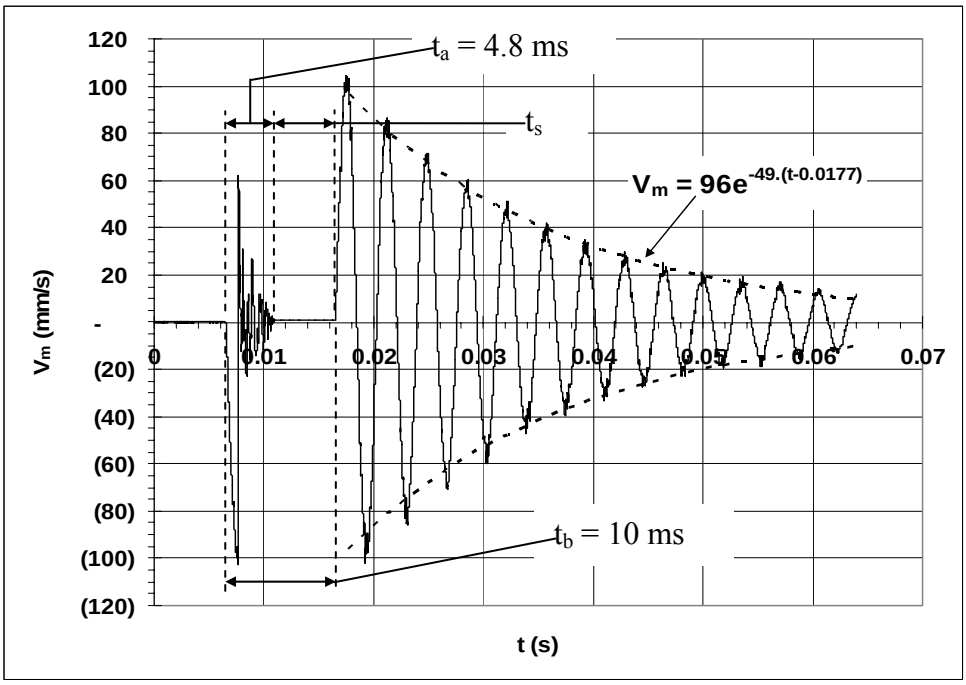

Figure 7.23. The velocity profile of the membrane captured by Laser Doppler Vibrometer for the bidirectional actuator that moves downward because of the impulse current of I_{coil} at -0.32A and at the burst time (t_b) 10 ms.

Based on this equation, the velocity amplitude has decayed to 0.01 % of its peak value when t = 0.2 s. Figure 7.24 shows the condition when the membrane moves upward because of the impulse current of I_{coil} = 0.32 A at t_b = 50 ms. Based on the Equation shown in Figure 7.24, the velocity amplitude has decayed to 0.04 % of its maximum

value when t = 0.2 s. Thus when the two impulses of current are separated by $t_{trigger}$ = 2s, it ensures that the two velocity profiles do not interfere to each other. This raises a question regarding the relationship of membrane displacement (d_m) with the input energy to microcoil (E_{coil}), because t_b is a component in defining E_{coil}, as shown in Equation 7.2.

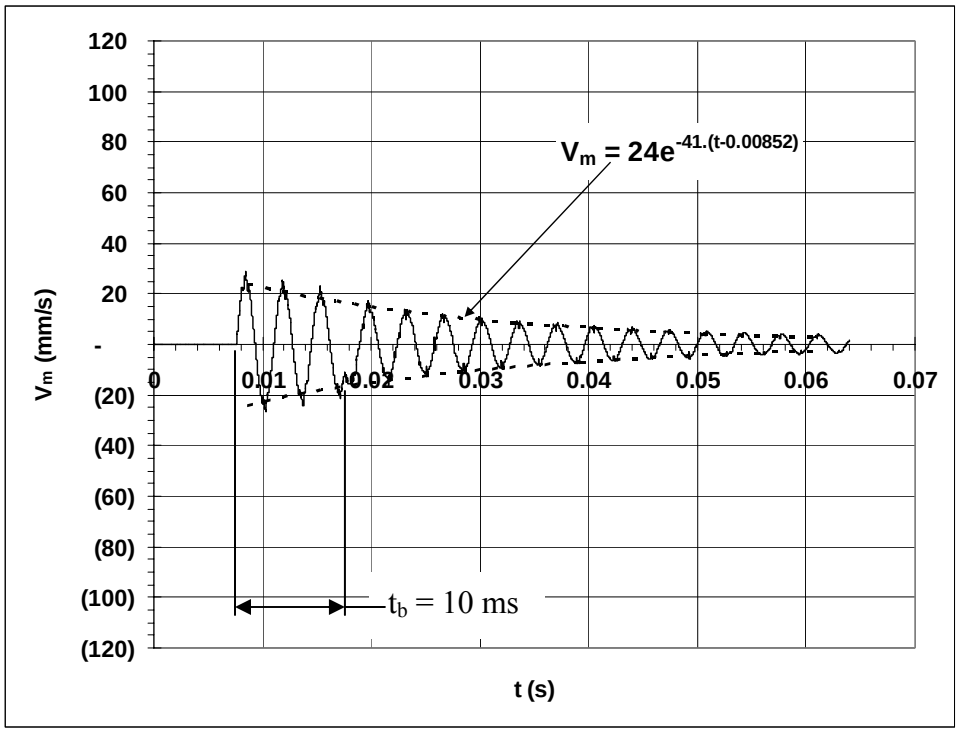

Figure 7.24. The velocity profile of the membrane captured by Laser Doppler Vibrometer for the bidirectional actuator that moves upward because of an impulse current of I_{coil} at 0.32A and at the burst time (t_b) = 10 ms.

B. Displacement versus Energy

Figure 7.25 shows the membrane displacement at different energies (E_{coil}) when $t_b \geq 1.6$ ms, e.g. t_b = 10, 5, 2.5, and 1.67 ms. It shows that the same E_{coil} does not give the same d_m when t_b is altered. Reducing t_b results in a higher magnitude of d_m, and the slope

of d_m increases as t_b decreases. Figure 7.25 indirectly indicates the dependence of d_m on I_{coil}. Equation 7.2 shows that when E_{coil} is kept constant, the decrease in t_b leads to the increase in I_{coil}. This supports the results shown in Figure 7.20; that d_m is independent of t_b when $t_b > 1.67$ ms but that it does depend on I_{coil}. This is in agreement with the Equation 3.4 because the dynamic equation for the motion of the actuator is $F_m = m_e \,.\, A_m$, where F_m, m_e, and A_m are the force, equivalent mass, and acceleration respectively experienced by the membrane. When the squeeze film damping in the fluid is negligible, $F_m = F_Z$, which is the electromagnetic force (F_{EM}) as indicated in Equation 3.4. The increase in I_{coil} causes an increases in $\frac{dB_Z}{dz}$ and F_{EM}.

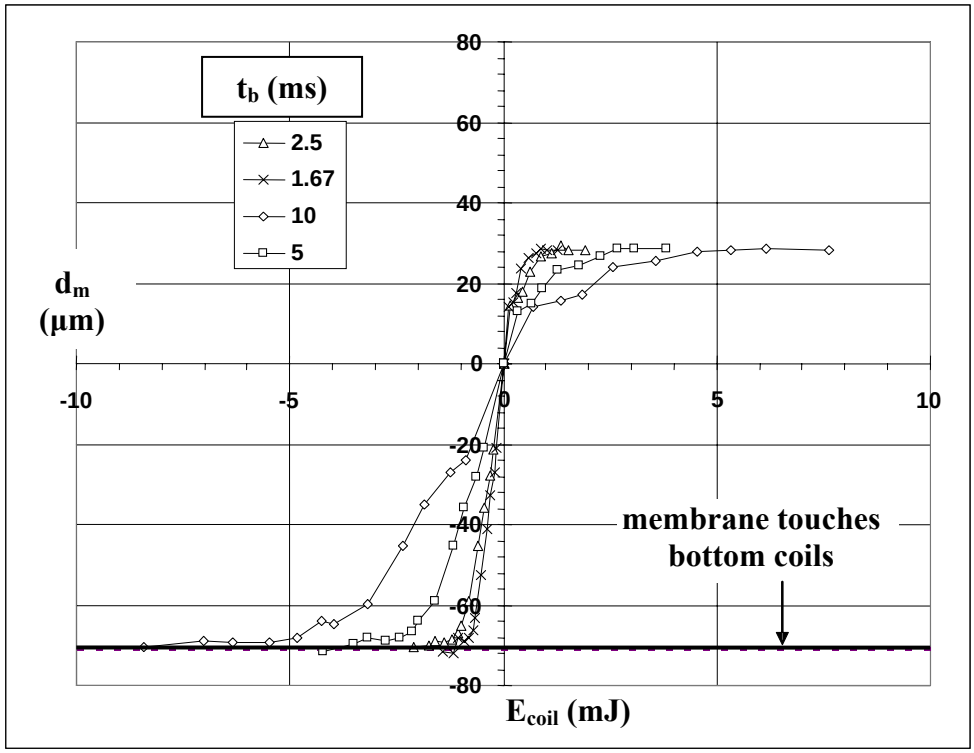

Figure 7.25. Membrane deflection (d_m) for double-legs design at different input energy (E_{coil}); The results are plotted at different burst time (t_b), 10 ms $\leq t_b \leq$ 1.67 ms, and indicates very strong dependence on the burst time (t_b).

Figure 7.26 shows d_m at different E_{coil} when $t_b \leq 1.67$ ms. It shows that at the same E_{coil}, the magnitude of d_m decreases at lower t_b. The results are more distinguished for upward d_m. This is the opposite of the results shown in Figure 7.25, where $t_b \geq 1.67$ ms. As mentioned before, the decrease in t_b increases values for I_{coil}, and it also increases F_{EM}. This physically shows the limitation of the membrane/actuator to provide the reaction force against the applied F_{EM}. The upward and downward d_m are the reaction of the membrane against the applied F_{EM}.

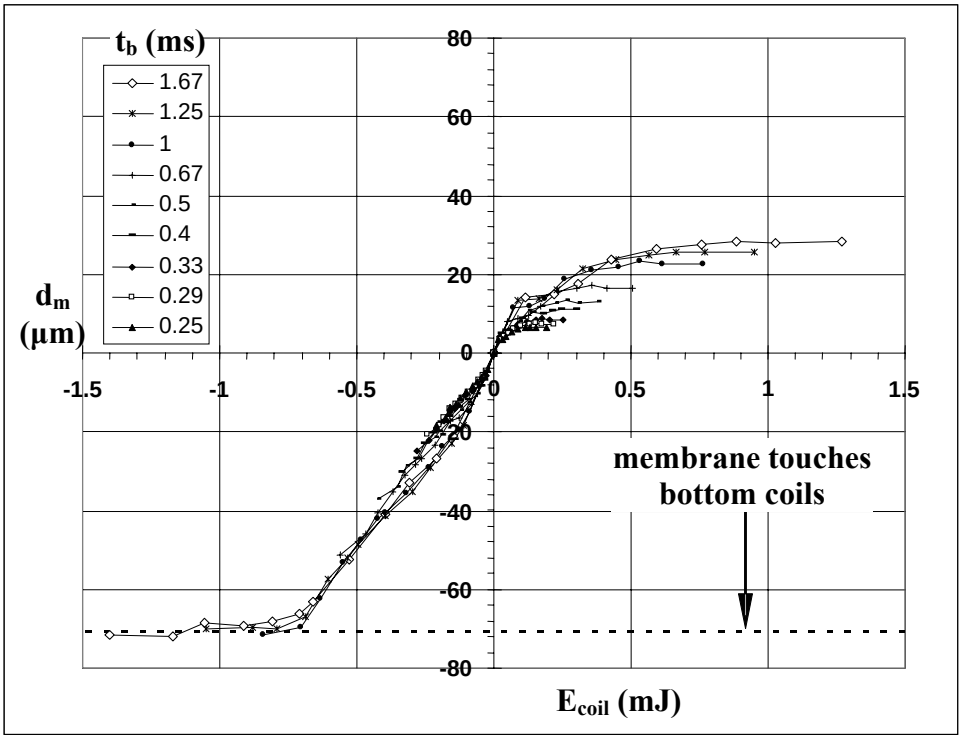

Figure 7.26. Membrane displacement (d_m) for double-legs design at different input energy (E_{coil}). The results are plotted at various different burst times (t_b), 1.67 ms $\leq t_b \leq$ 0.25 ms

At t_b < 1.67 ms, even though the same amount of energy (E_{coil}) and larger I_{coil} are applied, a shorter impulse time or smaller (t_b) will produce a smaller displacement. From a thermodynamics point of view, the membrane has a rapid acceleration (A_m) and the applied F_{EM} has a high irreversibility that produces a lot of losses in the fluid. A_m increases rapidly as t_b gets smaller. A lot of energy may be lost to the environment in the form of sound waves or when transferred to the fluid motion.

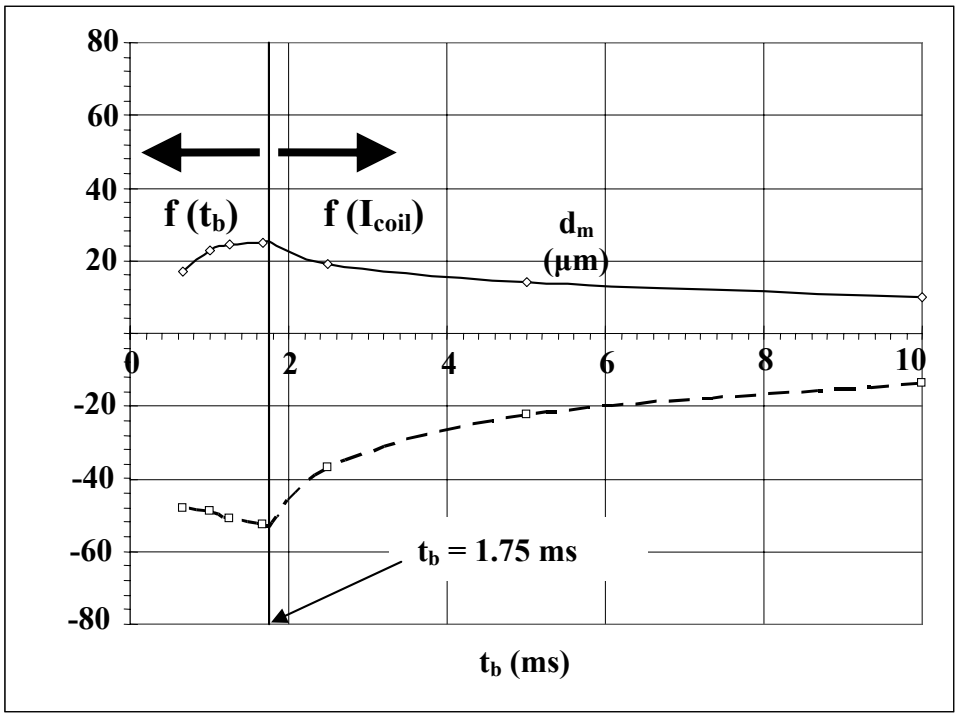

Figure 7.27. Membrane displacement (d_m) for double-legs design at different burst time (t_b) when the input energy (E_{coil}) is kept at +/- 0.5 mJ for the upward/downward d_m.

Figure 7.27 shows d_m at various t_b, when a constant E_{coil} = 0.5 mJ is applied for the upward d_m and E_{coil} = -0.5 mJ for downward d_m. The results show clearly that d_{min} and

d_{max} are achieved when t_b = 1.75 ms, where the corresponding f_b is the natural frequency (f_n) of the membrane. This confirms the previous statement in which the optimal displacement is achieved at t_b = 1.75 ms. Figure 7.27 distinguishes clearly the area when d_m is strongly dependent on I_{coil}, i.e. $f(I_{coil})$, and when it is strongly dependent on t_b, i.e. $f(t_b)$. Thus t_b = 1.75 ms is the boundary between these two cases.

As mentioned before, there is great motivation to achieve a low energy consumption microactuator. One way to reduce the energy is to reduce the duration of applied current (t_b). However, it is important to understand that reducing t_b to a certain limit will shift the behavior of the actuator from I_{coil} dependence to both I_{coil} and t_b dependence. The results in Figures 25, 26, and 27 give a clear explanation of this limitation. These results are important, particularly when the membrane actuation is utilized for relay/optical applications. It means that d_m can be varied not only by I_{coil} or P_{coil} but also by E_{coil} and t_b.

C. Actuation Time (t_a)

When an impulse of current (I_{coil}) at a certain duration t_b is input to the microcoil, an electromagnetic force is generated. This force can be either repulsive, which moves the membrane upward, or attractive, which moves the membrane down. Once the generated electromagnetic force is balanced by the spring force (F_S), the membrane stops. The parameter actuation time (t_a) is the time that is required for the membrane to move from its initial position to its final destination, at a given impulse of current (I_{coil}), at a certain duration of t_b. The possible remaining time, which is $t_b - t_a$, is no longer useful

toward further membrane displacement; thus the remaining time is called t_s, or sitting time. Figure 7.23 shows a sample of a velocity profile that indicates clearly the t_a, t_s, and t_b. For a certain input current (I_{coil}), in order to achieve its full displacement (d_m), the burst time (t_b) should be more than the required actuation time (t_a). This bidirectional actuator, when $t_b \geq t_a$, d_m depends only on I_{coil}, e.g. f (I_{coil}). When $t_b = t_a$, t_b is called the optimum burst time (t_{b_opt}) and $t_s = 0$ ms. When $t_b < t_{b\_opt}$, the value of t_a is the same as t_b and d_m depends on both I_{coil} and t_b, e.g. f (I_{coil}, t_a).

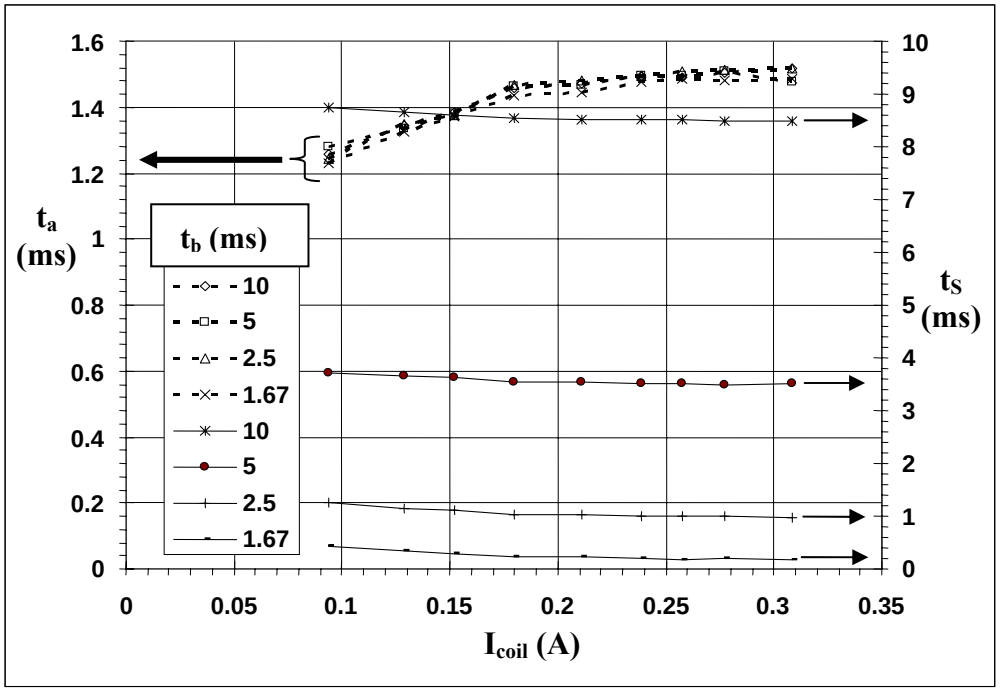

Figure 7.28. Actuation time (t_a) and sitting time (t_s) versus the membrane upward displacement for double-legs design plotted at various burst time (t_b).

Figure 7.28 shows the variation of t_a (ms) and t_s (ms) at different I_{coil} (A) for $t_b \geqslant$ 1.67 ms. As shown in Figure 7.20, d_m is independent of t_b when $t_b > 1.67$; e.g. d_m = f

(I_{coil}). Figure 7.28 shows that for all t_b = 10, 5, 2.5, and 1.67 ms, t_a are about the same. The variance is less than 0.2 ms, which small enough to be accounted for by an error in data processing. It shows that t_a increases with the increase of I_{coil}. The slope of t_a decreases as with I_{coil}, and t_a seems to saturate at the value of 1.55 ms. Thus t_{b_opt} when I_{coil}>0.3 is 1.55 ms. This value is very close to the natural t_b, which is 1.75 ms. This difference also should be due to some experimental error or data processing. Thus, it confirms our previous statement that the natural t_d can be used to estimate t_{b_opt}.

Figure 7.28 also shows the variation of sitting time (t_s) with I_{coil}. It shows that t_s increases with the increase in t_b, and it decreases with the increase in I_{coil}. The amount of t_s shows the excess time for the membrane to settle at its full deflection. It corresponds to the amount energy (E_{coil}) that is not useful in displacing the membrane. It shows that when t_b = 1.67 ms, t_s is almost zero, e.g. t_s < 0.3 ms; it supports the results shown in Figure 7.27, where t_b = 1.67 ms gives the maximum d_m. Figure 7.28 is descriptive when the bidirectional actuator is used for the application and where low power/energy consumption is important. It shows the optimum amount of pulse time (t_{b_opt}) to produce a certain membrane displacement (d_m).

7.5.2.2 Single-leg Bidirectional Actuator

A. Displacement versus Current

Figure 7.29 shows the membrane displacement (d_m) for a single-leg design at various t_b = 10, 5, 2.5 ms. It shows that the membrane touches the bottom coils at d_{min} = -108 μm. It shows that the slope of d_m is much larger than the double-legs design as

shown in Figure 7.20. This is due to the fact that the membrane for single-leg design is less stiff than the double-legs design. As shown in Figure 4.22, the experimental F_S for double-legs design is 1,700 μN when d_m = 70 μm. Compare this to F_S for single-leg design, which is only 720 μN at d_m = 100 μm, as shown in Figure 4.23. Figure 7.29 shows that d_m is independent of t_b when $t_b \geq 0.5$ ms, e.g. t_b is a function of I_{coil} only. It shows that the plot of d_m for t_b = 10 ms and for 5 ms intersect with each other. When $t_b <$ 5 ms, e.g. t_b = 2.5 ms, the magnitude and slope of d_m decreases significantly. More results at $t_b \leq 5$ ms are shown in Figure 7.30.

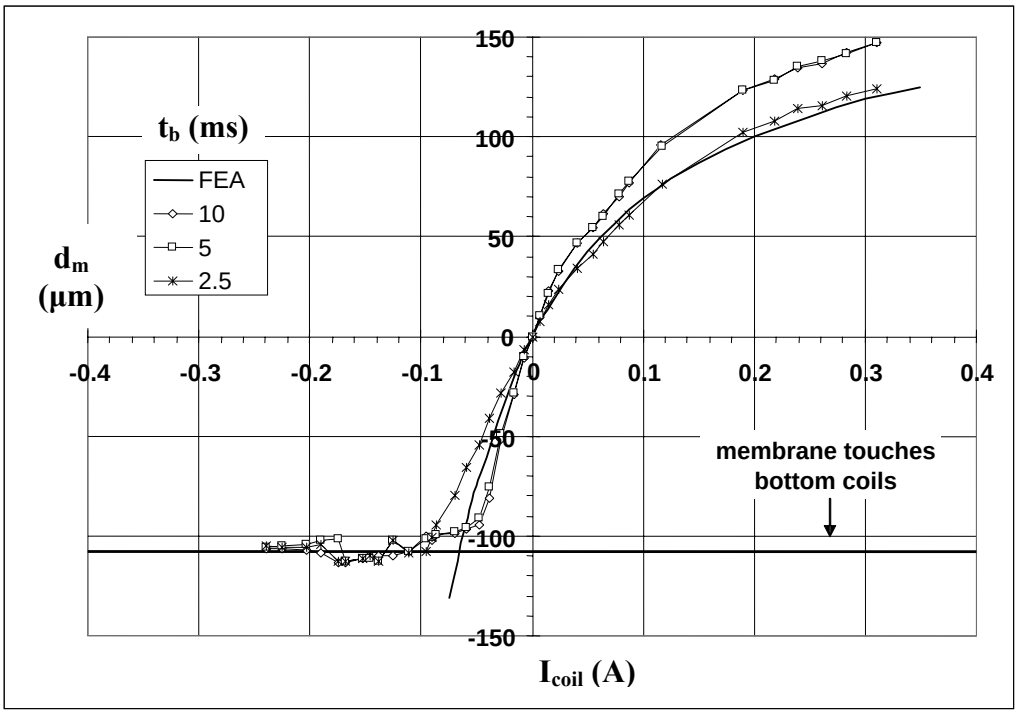

Figure 7.29. Combined experimental and FEA results on the membrane deflection (d_m) for single-leg design at different input current (I_{coil}) to the microcoil.

Figure 7.30 shows that when $t_b \leq 5$ ms, d_m has a strong dependence on both t_b and I_{coil}, e.g. $d_m = f(I_{coil}, t_b)$. The upward d_m starts to saturate at $I_{coil} = 0.3$ A when $t_b \leq 0.5$ ms. These details raise the question: what is the significance of $t_b = 5$ ms or $f_b = 100$ Hz in term of the membrane structure? It was found that the natural frequency (f_n) of the membrane with a single-leg design is 90.5 Hz. The corresponding t_b at this frequency is 5.53 ms, which is very close to 5 ms. This confirms our previous statement in the double-legs design that the optimal displacement (d_m) is achieved when the burst frequency (f_b) = f_n of the membrane.

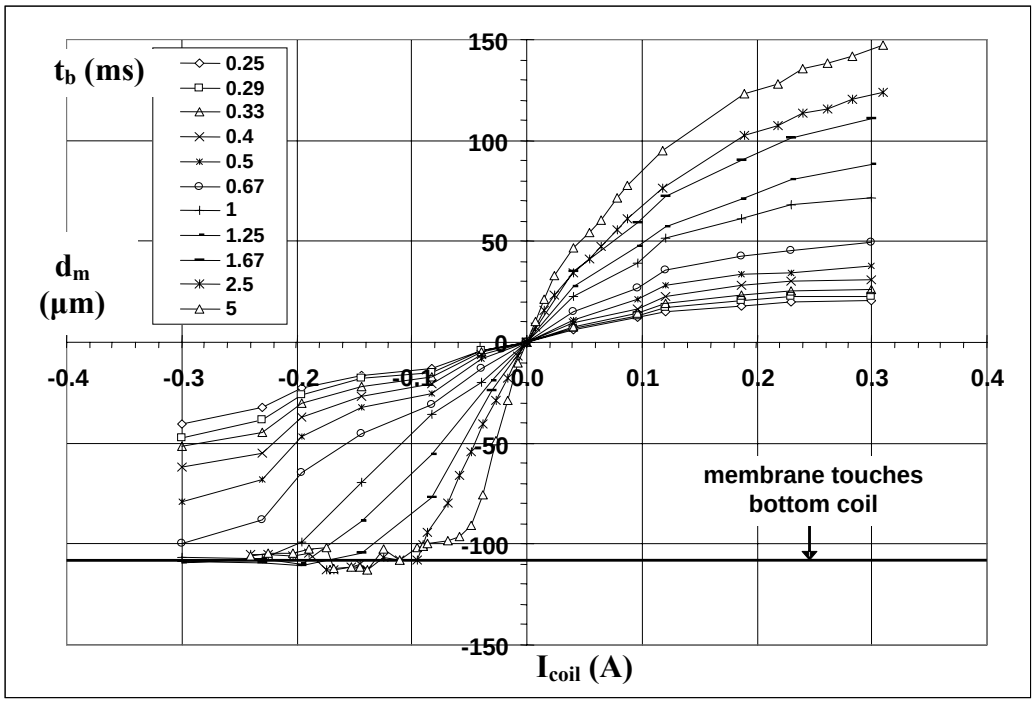

Figure 7.30. Membrane deflection (d_m) for single-leg design at different input current to the microcoil (I_{coil}) when $t_b \leq 0.5$ ms.

B. Displacement versus Energy

Figure 7.31 shows the membrane displacement (d_m) at different input energy (E_{coil}) to the microcoil. The results are plotted at t_b = 10, 5, and 2.5 ms. It shows that the energy required for the membrane to achieve d_{min} is very small compared to what is needed with the double-legs design: it is less than 0.5 mJ. The results show that d_m increases with energy; however in Figure 7.31 the dependency is unclear, especially for downward d_m. It shows that upward d_m varies with t_b as E_{coil} becomes larger.

Figure 7.32 shows repeat results as in Figure 7.31 focusing to low energies, from -0.15 mJ to 0.15 mJ. Figure 7.32 shows that the energy required to produce a large d_m is very low, this is mostly due to the low stiffness of the membrane. It shows that a certain E_{coil}, when $t_b \geq 5$ ms, any increase in t_b causes a decrease in d_m; this supports the results shown for double-legs design in Figure 7.25.

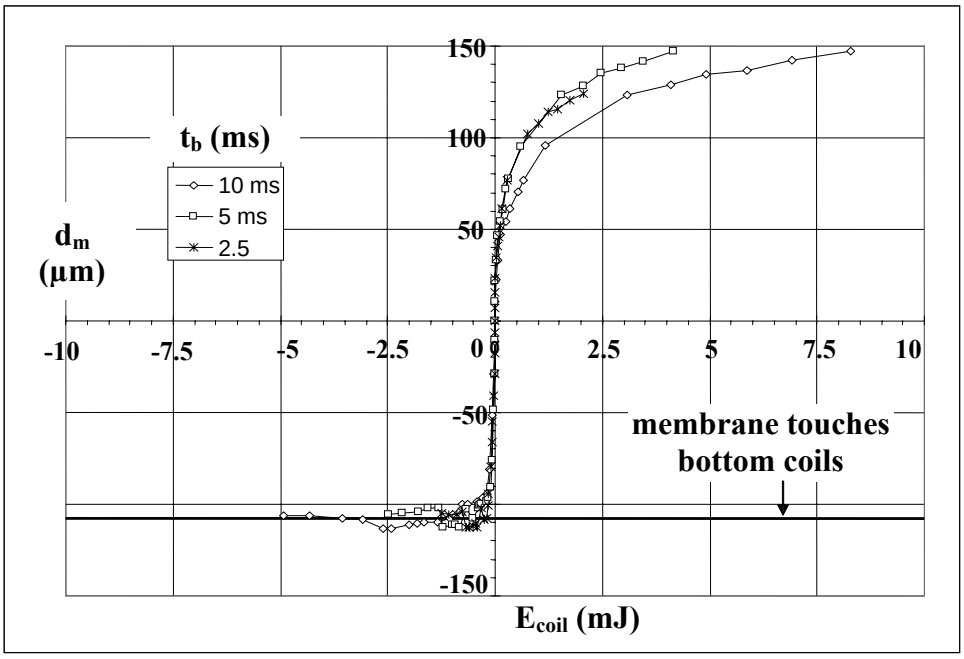

Figure 7.31. Membrane displacement (d_m) for single-leg design at different input energy (E_{coil}) plotted at different burst time (t_b), 2.5 ms $\leqslant t_b \leqslant$10 ms

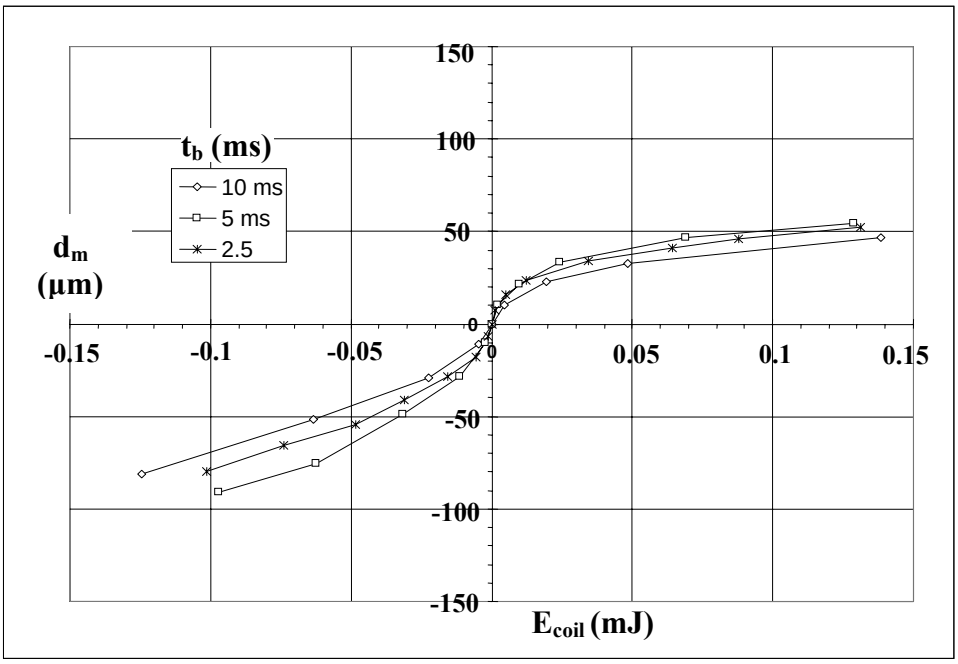

Figure 7.32. Membrane displacement (d_m) for single-leg design at different input energy (E_{coil}). A close look to low E_{coil}, -0.15 mJ < E_{coil} < 0.15 mJ.

Figure 7.33 shows the variation of d_m with E_{coil} at lower t_b, e.g. $t_b \leq 5$ ms. It shows clearly that d_m is not only a function of E_{coil} but also of t_b. The decrease in t_b causes a decrease in d_m. This confirms our previous results for double-legs design, as shown in Figure 7.26, when $t_b < 1/(2.f_n)$. Figure 7.34 shows d_m at various t_b, when a constant E_{coil} = 0.1 mJ is applied for upward d_m and E_{coil} = -0.1 mJ for downward d_m. The results shows clearly that d_{min} and d_{max} are achieved when t_b = 5.5 ms, where the corresponding f_b is the natural frequency (f_n) of the membrane for the single-leg design. Figure 7.34 clearly distinguishes the area when d_m is strongly dependent on I_{coil}, e.g. f(I_{coil}), and when it is strongly dependent on t_b, e.g. f(t_b). Thus t_b = 5.5 ms is the boundary between these two cases.

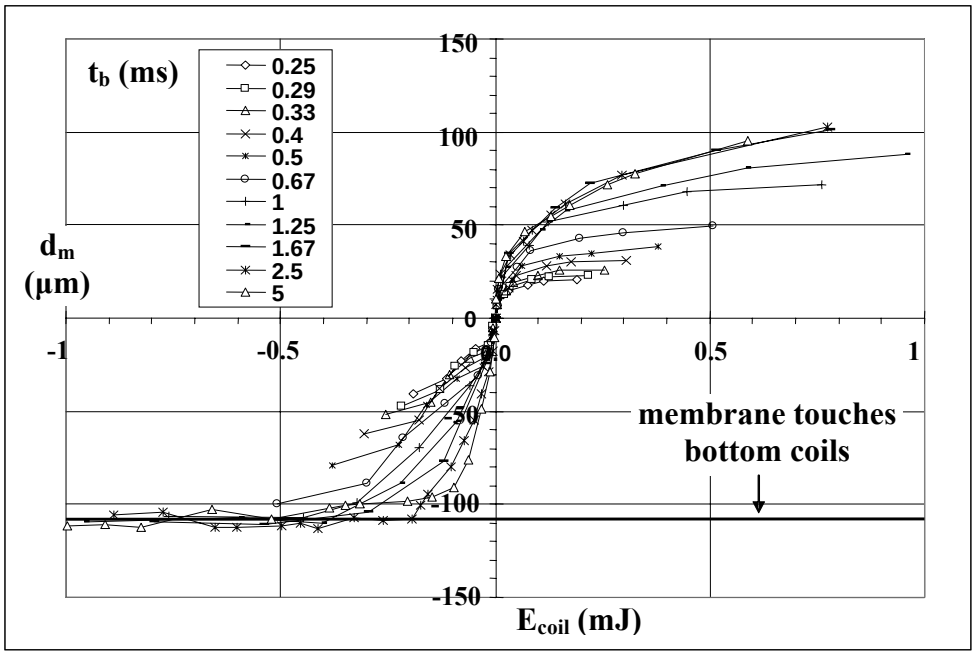

Figure 7.33. Membrane displacement (d_m) for single-leg design at different input energy (E_{coil}), plotted at various different burst times (t_b), 0.25 ms $\leqslant t_b \leqslant$ 5 ms.

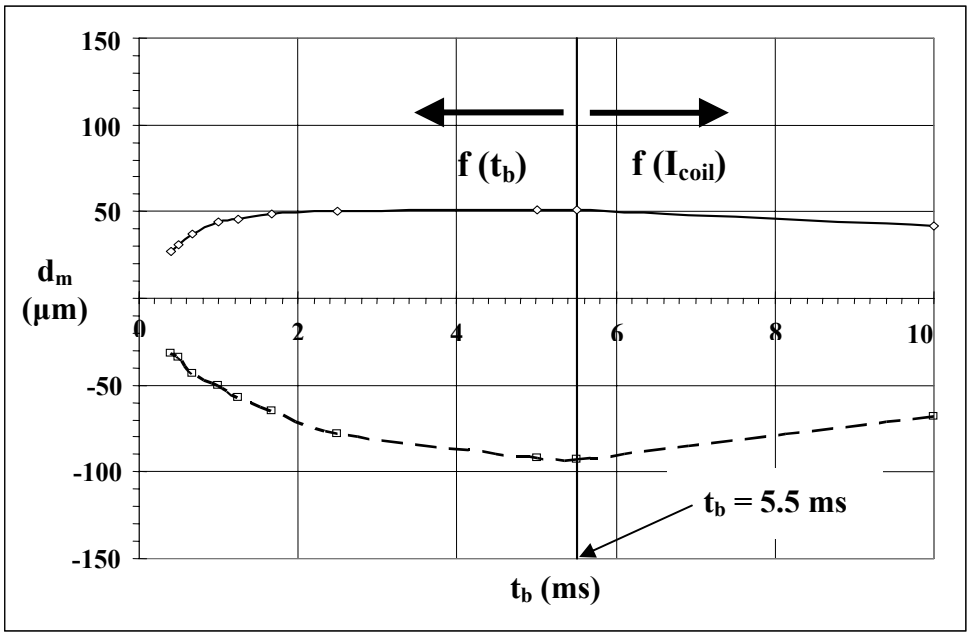

Figure 7.34. Membrane displacement (d_m) for single-leg design at different burst time (t_b) when the input energy (E_{coil}) is kept at +/-0.1 mJ for the upward/downward d_m

7.6 Bistable-Bidirectional Microactuator with Latching Mechanism

7.6.1 Introduction

This section describes the testing results for the microvalve actuator with a bistable-bidirectional latching mechanism. Both static and dynamic tests were carried out with three different microvalve actuators: a double-legs design with g = 30 μm, a single-leg design with g = 21 μm, and a single-leg design with g = 32 μm. These three valves are named actuator C, D, and E respectively. The geometry details of the microvalve are listed in Table 5.8. In all actuators, a permanent magnet is integrated into the membrane.

7.6.2 Double-legs design

Figure 7.35 delineates the static results for the membrane displacement (d_m) for actuator C at different input currents to the microcoil (I_{coil}). Here, the combined results for both the experiments and those results predicted by FEA are plotted for the medium air. A detailed discussion of the FEA is provided in section 4.2.4, and the results are shown in Figure 4.19. Figure 7.35 shows the bidirectional movement of the membrane produced by reversing the input current to the microcoil (I_{coil}). The positive current means that the electromagnetic field produced by the microcoil is at the opposite direction to the permanent magnet alignment, resulting in the upward movement of the membrane. The results show that the membrane is latched at an input current (I_{coil}) of -0.1 A. This is in agreement with the predicted value from the FEA at I_{coil} = 0.094 A, as shown in Figure 4.19, for a permanent magnet with the thickness, t_M = 40 μm. In order to unlatch the

membrane, the experiment shows that a reversed current of a magnitude that is equal to or greater than I_{coil} = 0.1 A is required.

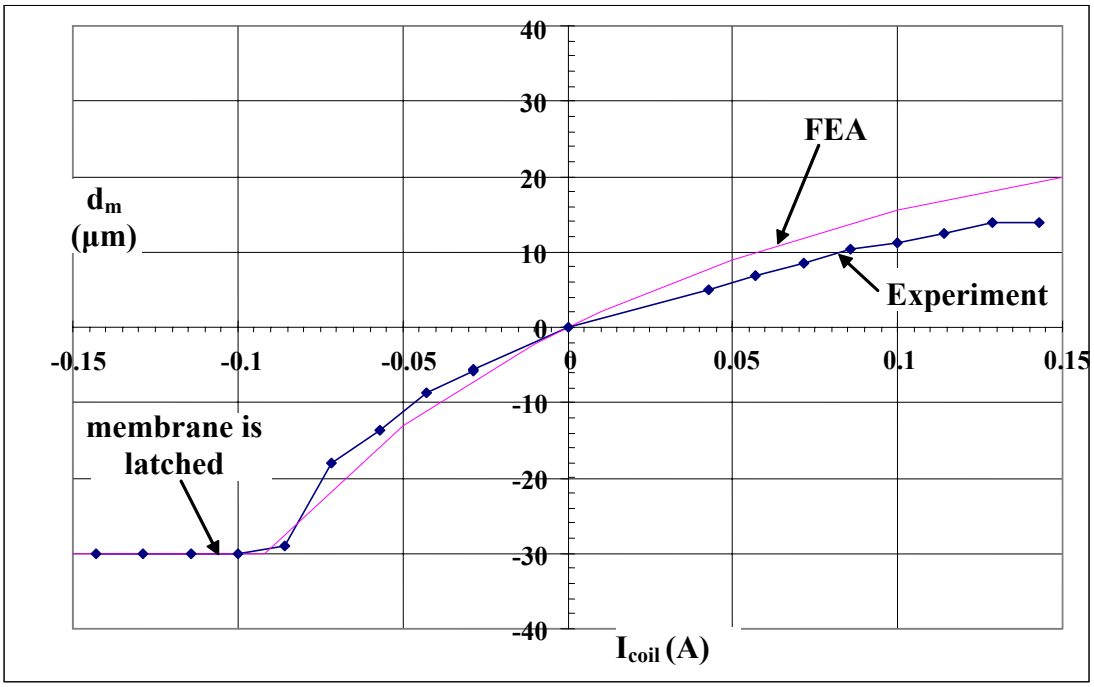

Figure 7.35. The membrane displacement (d_m) for double-legs design (actuator C) at different input current to the microcoil (I_{coil}) tested in the medium of air. It shows the combined results for both FEM and experiment. The details geometries of microvalve actuator are shown in Table 5.8.

Figure 7.35 shows that the bidirectional results of both the experiment and FEA are pretty much in a good agreement. Some differences are shown in the upward displacements (d_m), where the FEA overestimated the results. The experimental results clearly show that the slope of the upward d_m decreases with increases in current (I_{coil}). It finally saturates at the value of approximately 14 µm.

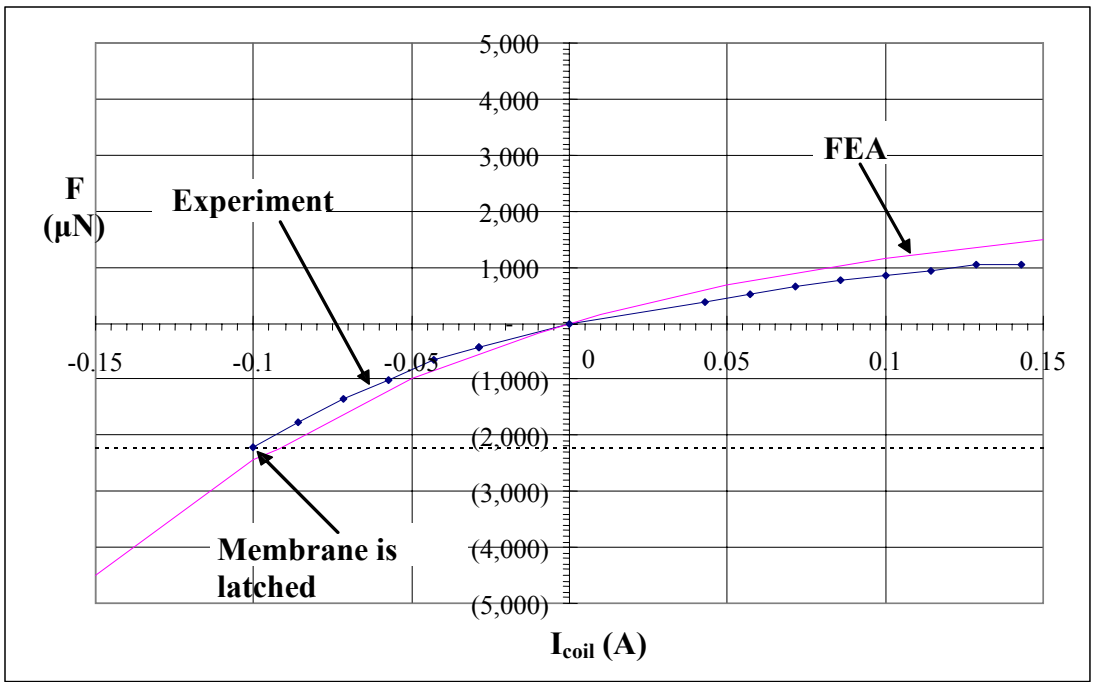

Figure 7.36. The bidirectional force (F) produced for double-legs design (actuator C) at different input current to the microcoil (I_{coil}), tested in the medium of air.

Figure 7.36 shows the bidirectional forces produced by the interaction between the permanent magnet and the electromagnetic field produced by the microcoil. In order to plot the forces, the experimentally determined membrane spring force (F_S) (as shown in Figure 4.16) is used. The combined results for both experiments and FEA show that the produced electromagnetic force, when the membrane is latched, is approximately 2,300 µN.

7.6.3 Single-leg design (actuator D)

7.6.3.1 Static Response in Air

The static response of actuator D at different input currents (I_{coil}) is shown in Figure 7.37. The membrane displacement (d_m) is plotted for both experiments and FEA estimates.

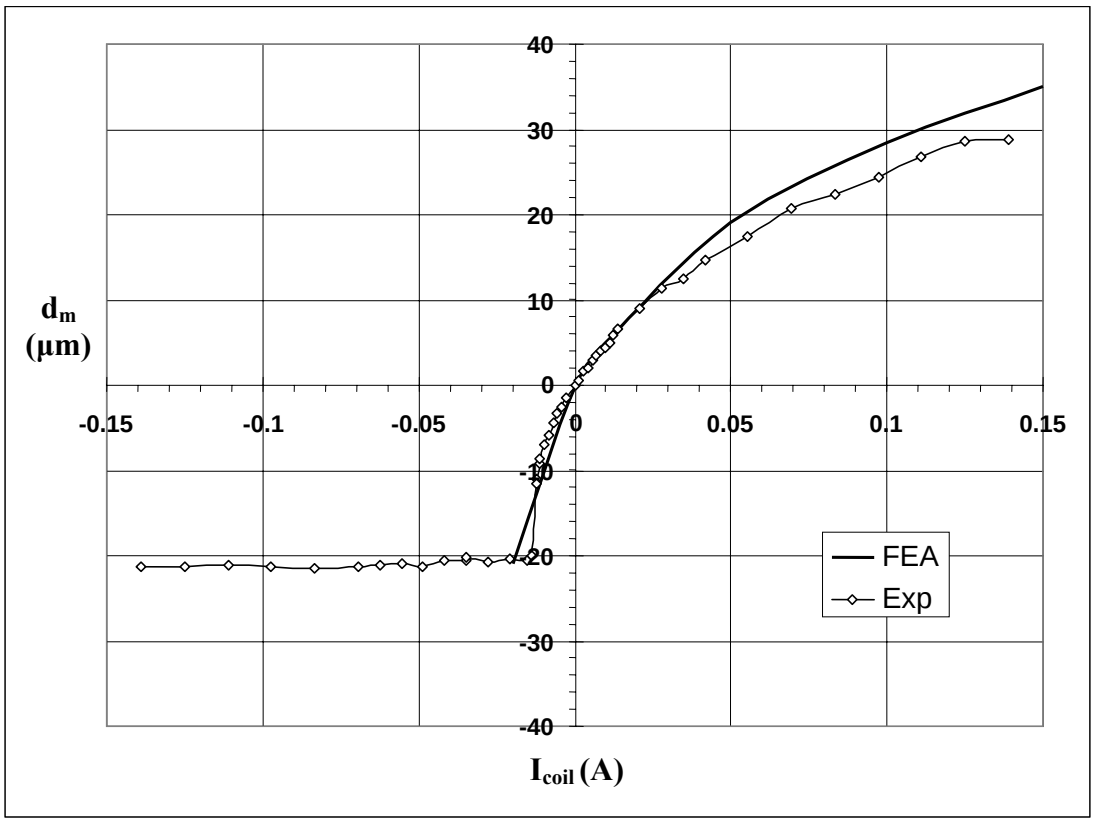

Figure 7.37. Membrane displacement (d_m) for bistable-bidirectional microvalve actuator with single-leg design (actuator D) at different input current (I_{coil}) tested in medium of air.

Details about the geometries of the microvalve are tabulated in Table 5.8, except that the number of legs is 1 and the initial gap distance (g) is 20.5 μm. The membrane has to move downward at this distance before it is latched. Figure 7.37 shows that, in order to

latch the membranes, the minimum input current (I_{coil}) required is in the magnitude of 0.0139 A. This result is smaller than the prediction from FEA that is 0.02 A. To unlatch the membrane in the medium of air, the experiments show that a reversed current with a magnitude that is equal or greater than I_{coil} = 0.0139 A is required.

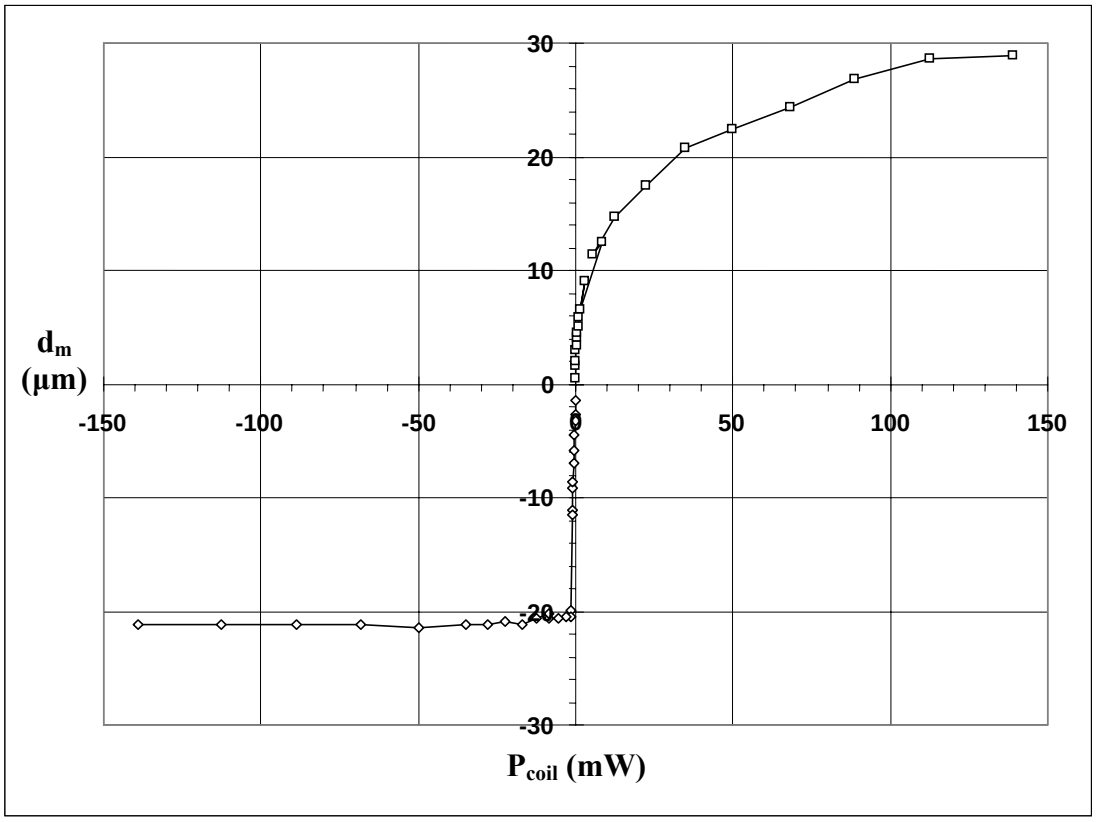

Figure 7.38. The membrane displacement (d_m) for actuator D at different input power to the microcoil (P_{coil}), tested in the medium of air.

Figure 7.38 shows the membrane displacement (d_m) at various input powers to the microcoil (I_{coil}). It shows that the minimum input power (P_{coil}) required to latch and unlatch the membrane is 1.39 mW. Figure 7.39 and 7.40 shows the instantaneous velocity

of the membrane (V_m) and the membrane displacement during its latching and unlatching mechanism respectively.

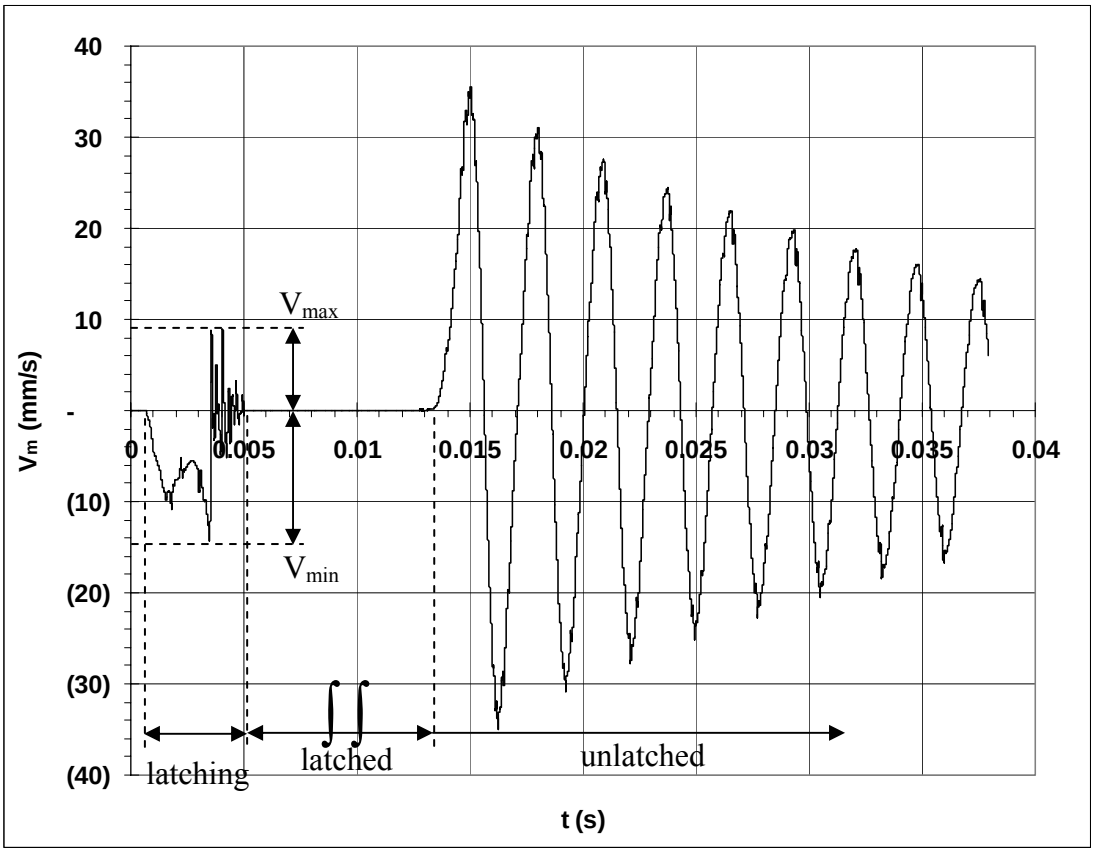

Figure 7.39. The instantaneous membrane velocity (V_m) for single-leg design bistable-bidirectional microvalve actuator (actuator D). It shows the static response for latching and unlatching mechanism at I_{coil} = 0.0139 A and P_{coil} = 1.39 mW. (Note: the symbol ∫∫ means that the actual "latched time" is longer than the one displayed in the figure)

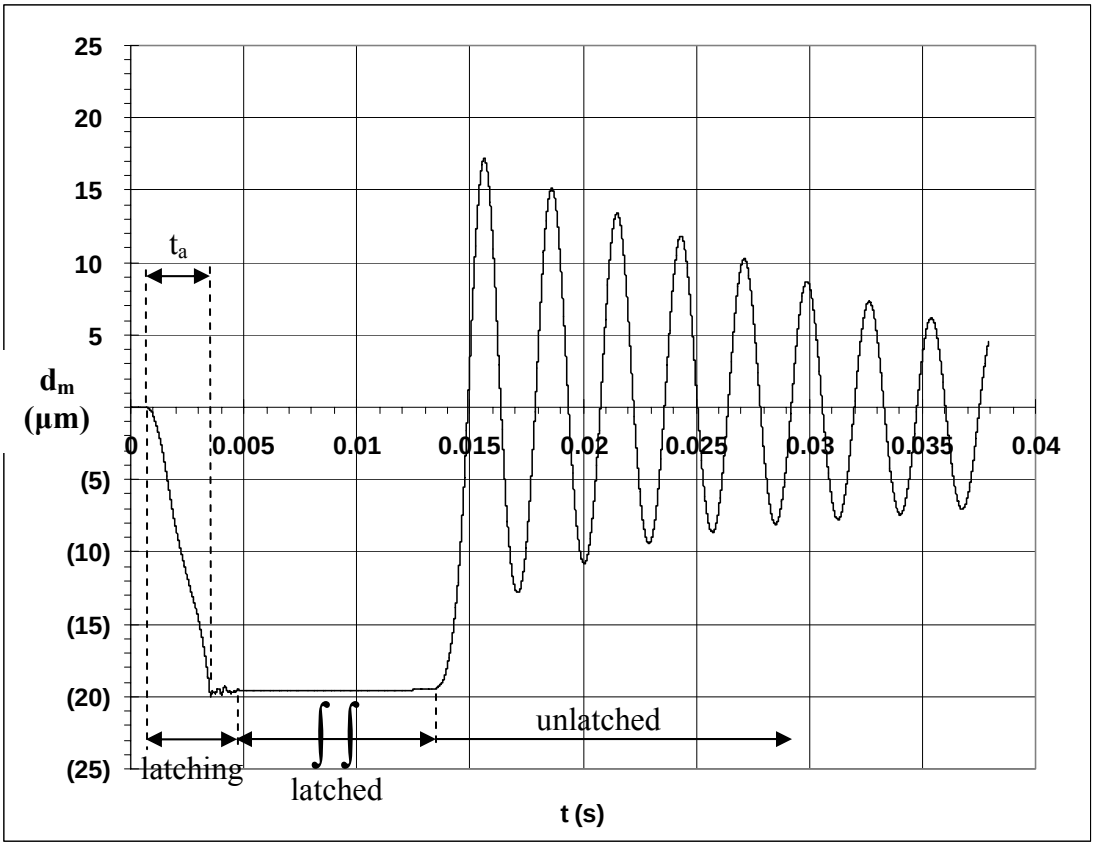

Figure 7.40. The instantaneous membrane displacement (d_m) for single-leg design bistable-bidirectional microvalve actuator (actuator D). It shows the static response for latching and unlatching mechanism at I_{coil} = 0.0139 A and P_{coil} = 1.39 mW. (Note: the symbol ∫∫ means that the actual "latched time" is longer than the one displayed in the figure)

Figure 7.41 shows the instantaneous membrane displacement (d_m) during the latching mechanism at different input currents (I_{coil}). It shows that a higher current requires less time for the membrane to touch the bottom coil and latch. These results are for the most part expected because an increase in current increases the electromagnetic force (F_{EM}) that moves and accelerates the membrane downward more rapidly. Figure 7.42 shows the minimum membrane velocity (V_{min}) during its latching mechanism

plotted at various I_{coil}. As shown in Figure 7.39 that V_{min} happens just before the membrane touches the bottom coil.

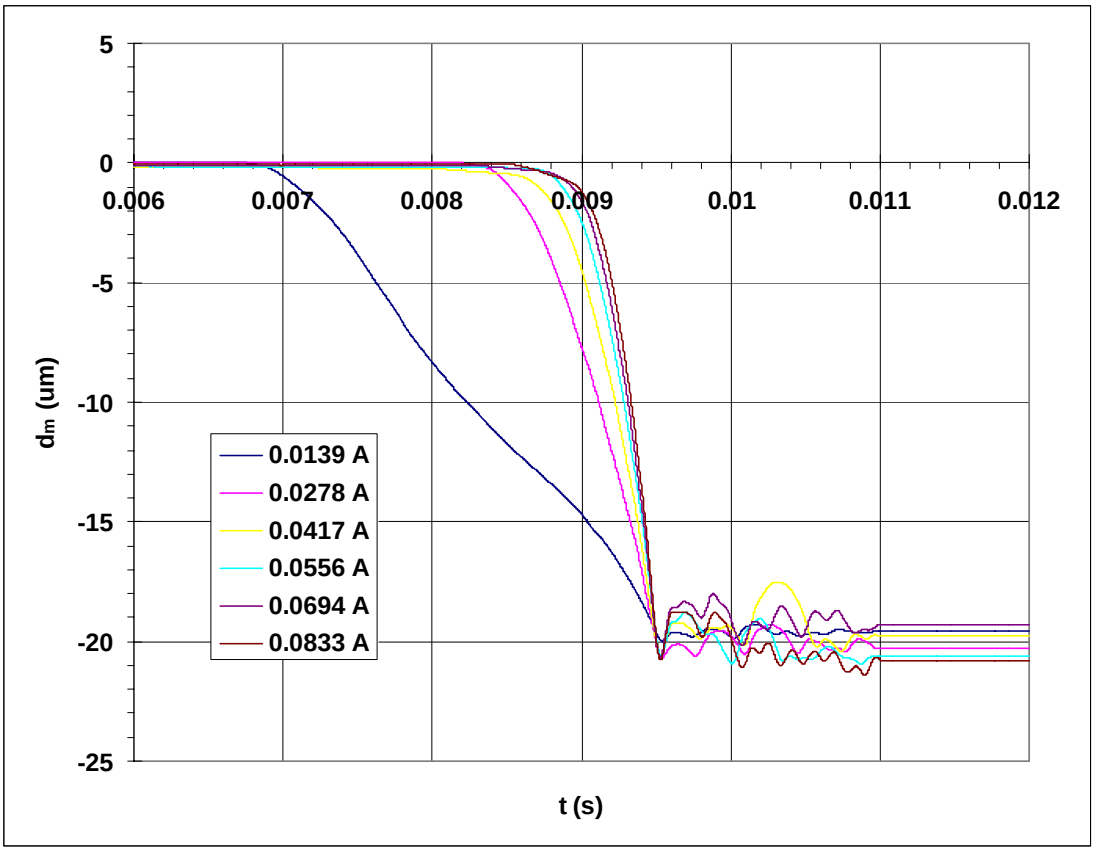

Figure 7.41. The instantaneous membrane displacement (d_m) during the latching mechanism for single-leg design bistable-bidirectional microvalve actuator (actuator D). The results are plotted at various input current (I_{coil}).

Figure 7.42 shows that the magnitude of V_{min} increases with I_{coil}. The slope of V_{min} decreases with the increase in I_{coil}. The parabolic equation as shown in Figure 7.42 can be used to estimate the V_{min} within the range of I_{coil}. The increase in velocity with current (I_{coil}) reduces the required time for the membrane to touch the bottom coil and latch. This time is called the actuation time (t_a).

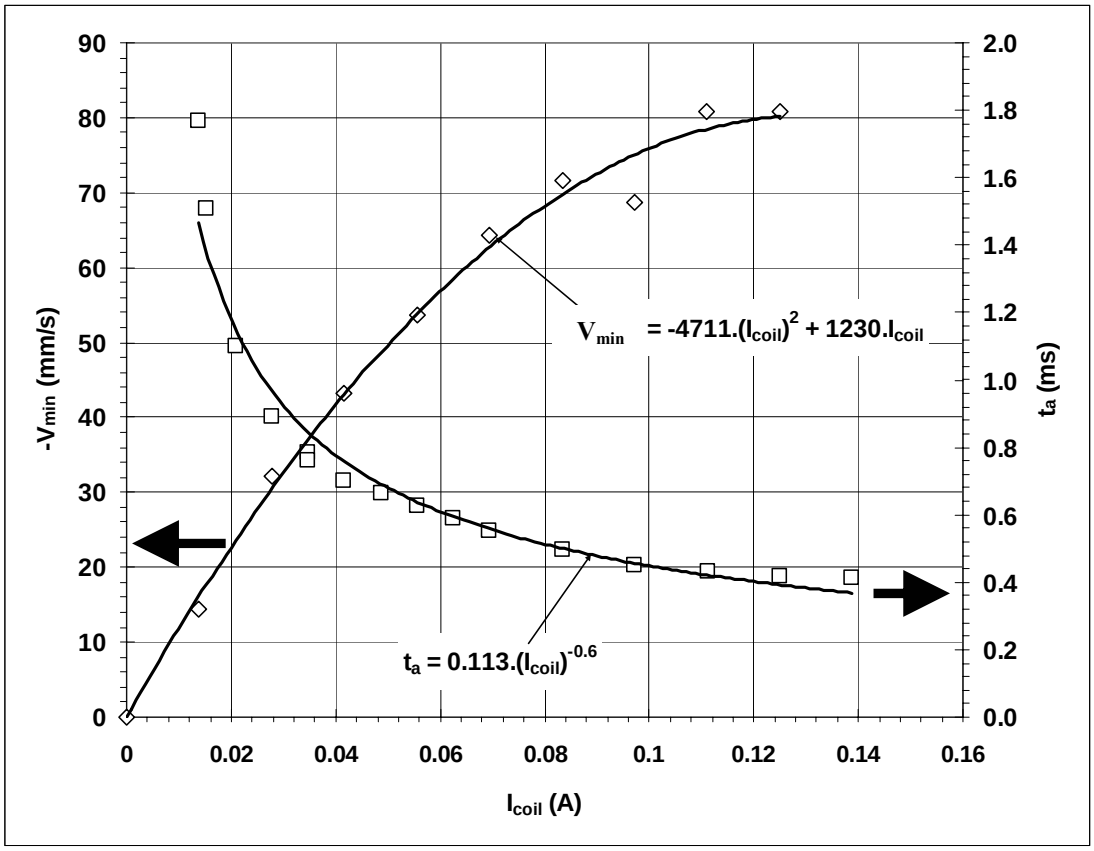

Figure 7.42. The minimum membrane velocity (V_{min}) during the latching mechanism and the actuation time (t_a) plotted at various input current (I_{coil})

Figure 7.42 also shows the variation of t_a in I_{coil}. It shows that t_a decreases with the increase of I_{coil}. A sharp decrease in t_a is indicated at low input current, $I_{coil} \leqslant 0.03$ A. The slope of t_a decreases with the increase of I_{coil}. The actuation time (t_a) seems to saturate at $t_a \approx 0.4$ ms when $I_{coil} \geqslant 0.14$ A. These values suggest a question: will the membrane be latched when a pulse of current with the duration of 0.4 ms at 0.14 A is applied to the microcoil? This is answered in the next section, Dynamic Response in Air.

7.6.3.2 Dynamic Response in Air

This section discusses the dynamic response of the microvalve actuator (actuator D) in the medium of air when a pulse of current of duration (t_b) is applied to the microcoil.

A. Displacement versus Current

Figure 7.43 shows the membrane displacement (d_m) at different input current (I_{coil}) and at 1 ms $\leqslant t_b \leqslant$ 10 ms. The static responses of the membrane are also shown in Figure 7.37 and indicated by INF (infinity) on the figure. The results show that d_m are independent of t_b, and, for $t_b \geqslant$ 1 ms, d_m is only a function of I_{coil}.

Even though the displacement results are much the same for 1 ms $\leqslant t_b \leqslant$ 10 ms, the experiments show that the membrane only latched when t_b = 2.5, 5, and 10 ms. Thus it requires a burst time (t_b) of at least 2.5 ms to latch the membrane in air. This is called the static latching time for the microvalve actuator. When t_b = 2.5 ms, there is enough time for the membrane to sit on the bottom coil to align the permanent magnet and achieve latching. The time is enough for the force produced by the permanent magnet to recover the momentum experienced by the membrane as it touches the bottom coil. As shown in Figure 7.39, this momentum bounces the membrane upward and may unlatch the membrane if there is not sufficient force and time. When t_b = 1, 1.25 and 1.67 ms, the membrane does touch the bottom coil; but the membrane unlatched when the current is off because of the impact and the momentum change.

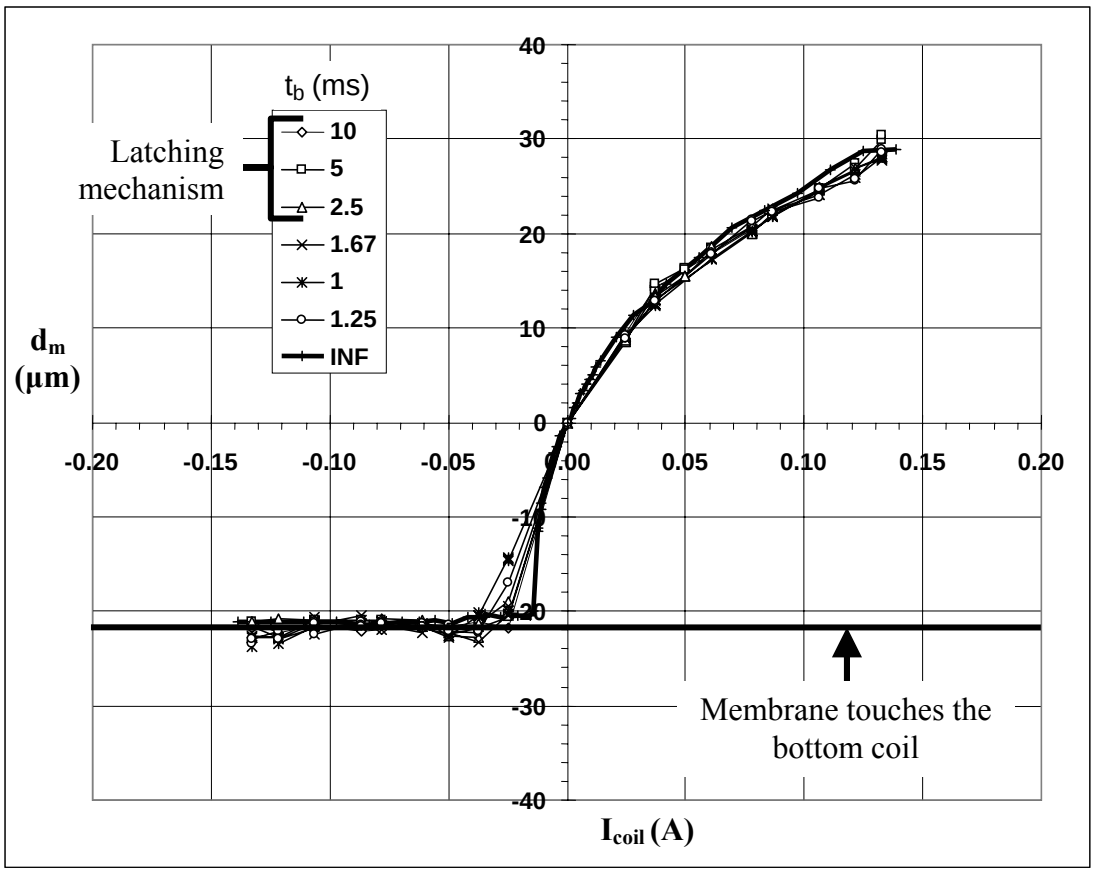

Figure 7.43. The membrane displacement (d_m) for single-leg design bidirectional microvalve actuator (actuator D) at different input current (I_{coil}), tested in the medium of air. The graphs are plotted at various burst times (t_b), $1 \leq t_b \leq 10$ ms. The static response is indicated as INF

The membrane displacements (d_m) are shown in Figure 7.44 when 0.25 ms $\leqslant t_b \leqslant$ 1 ms. The results shows that d_m does depend on t_b. Thus d_m is a function of I_{coil} and t_b. It shows that d_m decreases with t_b. For the membrane bidirectional movement, t_b = 1 ms is a boundary when d_m starts to be dependent on t_b.

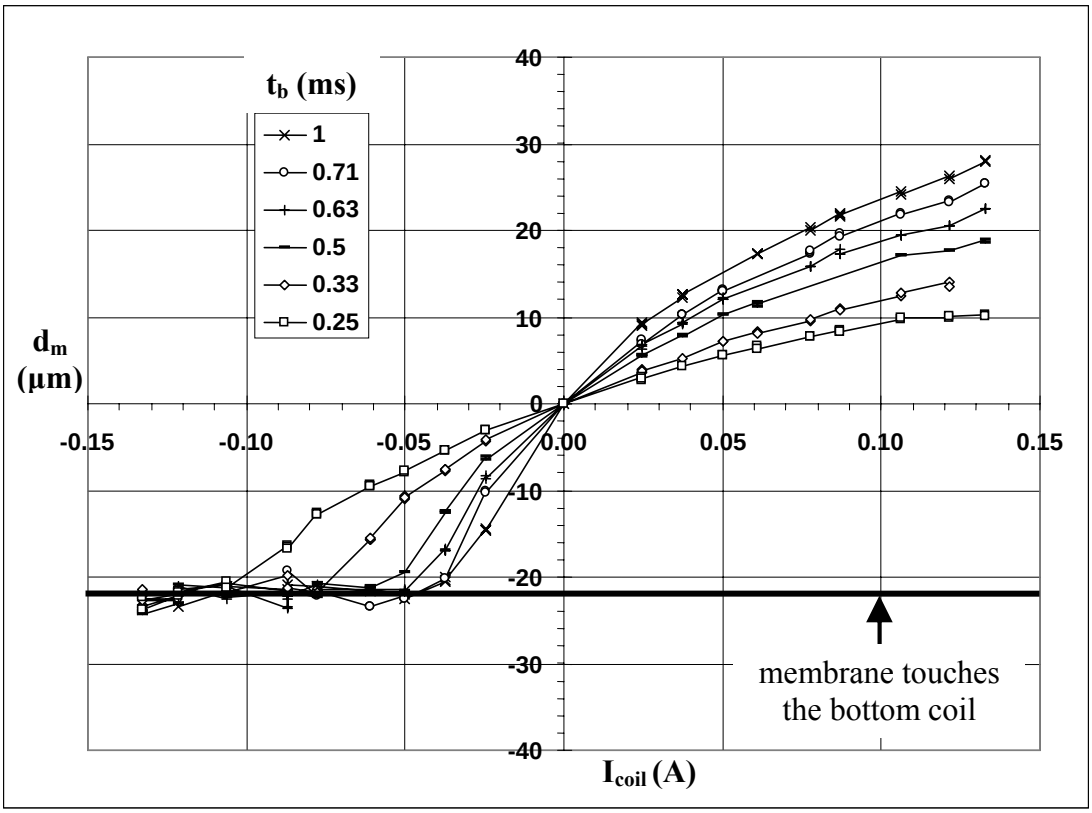

Figure 7.44. The membrane displacement (d_m) for single-leg design bidirectional microvalve actuator (actuator D) at different input current (I_{coil}) tested in the medium of air. The graphs are plotted at various burst times (t_b), $0.25 \leq t_b \leq 1$ ms.

B. Displacement versus Energy

Figure 7.45 shows the membrane displacement (d_m) at different input energies to the microcoil (E_{coil}). The results are plotted when 1 ms $\leqslant t_b \leqslant$ 10 ms. It shows that the same amount of energy does not result in the same amount of deflection as the t_b is altered. It also shows that d_m is more variable to t_b for the upward displacement than the downward one. This is because the electromagnetic field reduces as the membrane moves upward farther from the microcoil. On the other hand, the remanence field from the permanent magnet increases as the membrane moves downward closer to the microcoil.

Figure 7.45 shows that d_m increases with the decrease in t_b. These results are expected because the decrease in t_b increases I_{coil} when E_{coil} is kept constant, as shown in Equation 7.2. The increase in I_{coil} increases the electromagnetic force, as shown by Equation 3.4. This leads to the increases in the membrane acceleration (A_m) and displacement (d_m).

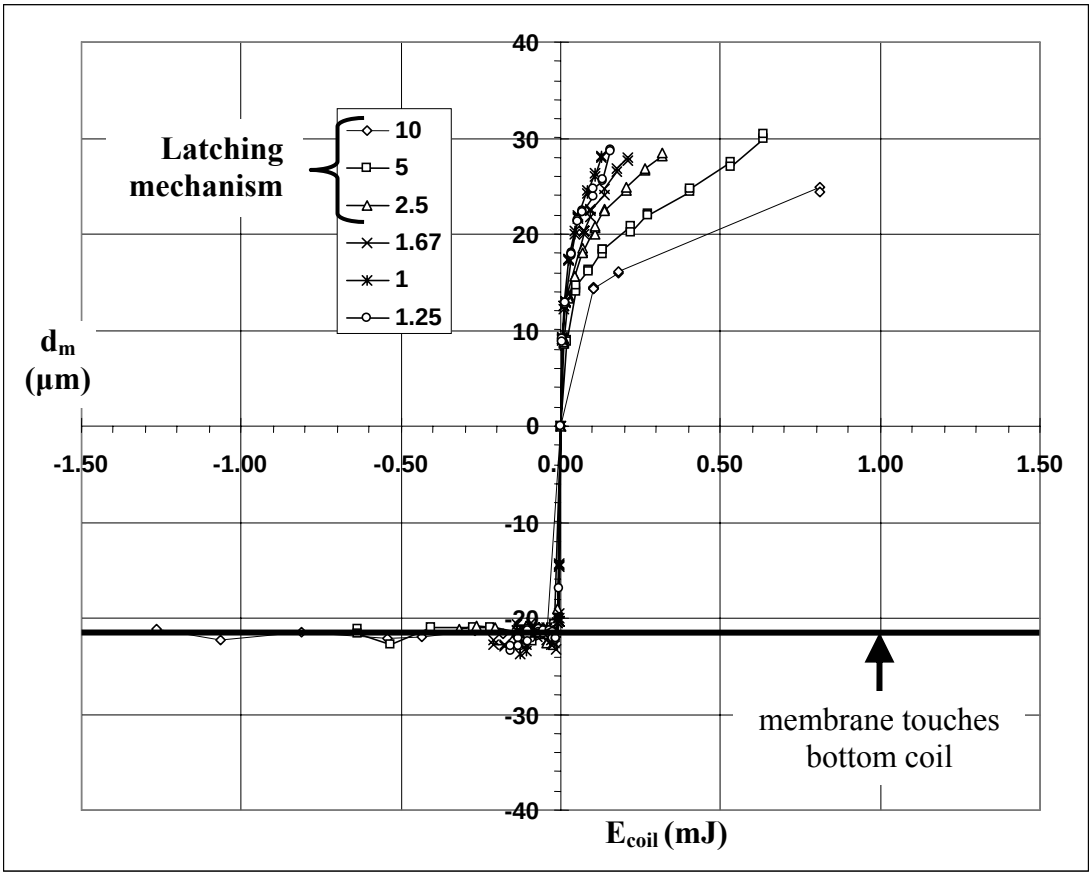

Figure 7.45. The membrane displacement (d_m) for single-leg design bidirectional microvalve actuator (actuator D) at different input energy (E_{coil}), tested in the medium of air. The graphs are plotted at various burst times (t_b), $1 \leq t_b \leq 10$ ms.

Figure 7.45 shows that the maximum d_m is obtained when $t_b = 1$ ms. Thus in terms of membrane bidirectional movement, $t_b = 1$ ms produces the optimum results. The

time in excess of 1 ms allows the membrane to sit on the coil and does not produce displacement. However, the latching mechanism is not observed at t_b = 1ms. It is observed at $t_b \geqslant 2.5$ ms.

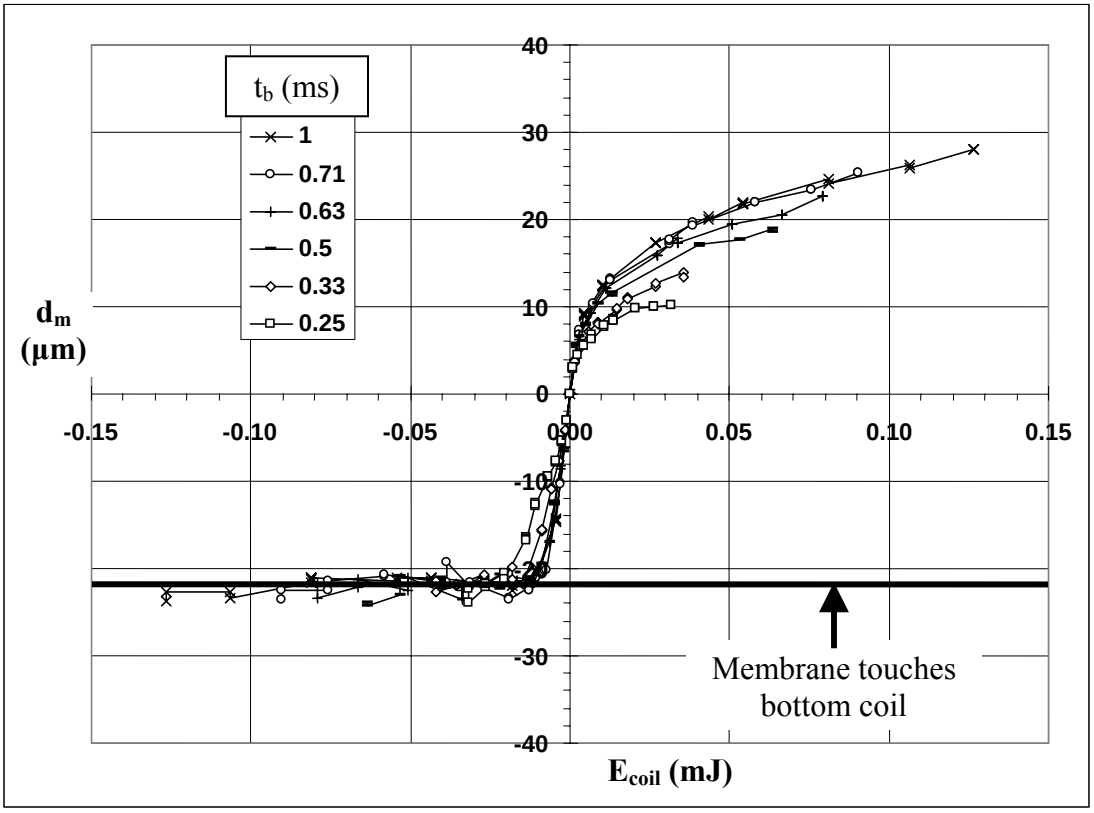

Figure 7.46. The membrane displacement (d_m) for single-leg design bidirectional microvalve actuator (actuator D) at different input energy (E_{coil}), tested in the medium of air. The graphs are plotted at various burst times (t_b), $0.25 \leq t_b \leq 1$ ms.

Figure 7.46 shows the membrane displacement (d_m) when 0.25 ms $\leqslant t_b \leqslant$ 1 ms. It shows that d_m decreases with t_b. This is opposite to the results shown in Figure 7.45. Figure 7.46 shows that the optimum d_m is obtained at t_b = 1 ms.

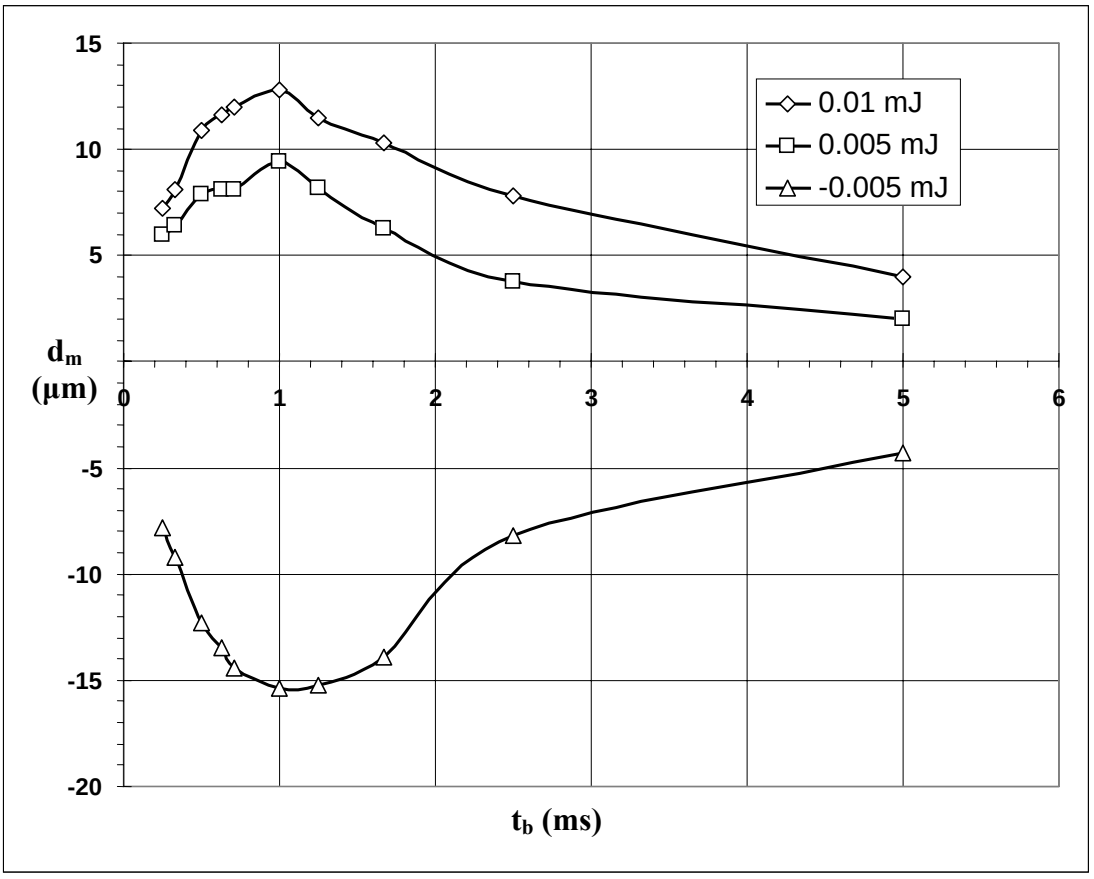

Figure 7.47. The membrane displacement (d_m) at various burst time (t_b) when the energy input to the microcoil (E_{coil}) is fixed at E_{coil} = 0.01 or 0.005 mJ.

Figure 7.47 shows d_m at different t_b while keeping E_{coil} constant. The results show that the best performance of d_m is achieved when t_b = 1 ms. This is in agreement with the results shown in Figures 7.43 to 7.46. The t_b = 1 ms is then termed optimum t_b or t_{b_opt}. The question this discussion raises is what is the significance of t = 1 ms to the membrane structure? The bidirectional results, described in section 7.4, indicate that the optimum d_m is achieved when $t_b = t_{b\_opt} = 1/(2.f_n)$, where f_n is the natural frequency of the membrane. For the single-leg design bistable and bidirectional microvalve actuator (actuator D), the

f_n of the membrane is approximately 300 Hz, which corresponds to t_b = 1.67 ms. At this t_b, the optimum results are not achieved, as shown in Figures 7.43 to 7.46. Meanwhile t_b = 1 ms is closer to $1/(3.f_n)$ which is equal to 1.11 ms. Thus the strong influence of the permanent magnet in the latching mechanism reduces the value of t_{b_opt} from $1/(2.f_n)$ to $1/(3.f_n)$. This result is desirable because it reduces the amount of E_{coil} required to achieve the optimum result.

C. Dynamic Latching Mechanism

The results in Figure 7.43 indicates that the latching mechanism is only achieved when $t_b \geqslant 2.5$ ms. This time is called static latching time (t_{latch_st}). This provides sufficient time for the permanent magnet force to overcome the large impulse in momentum experienced by the membrane as it touches the bottom coil as shown in Figure 7.39. The source of this momentum change is the excess amount of energy supplied by the microcoil to the membrane kinetic energy. Some of this energy is transferred to the kinetic energy that bounces the membrane upward. One way to measure this upward momentum is shown by Equation 7.8 below:

$$e = \frac{V_{max}}{V_{min}} \qquad (7.8)$$

Where: "e" is identical to the coefficient of restitution in physics, which is the ratio of speed of separation to the speed of approach in a collision for a single moving body [115]. For example: A basketball has e ≈ 0.6 and a baseball has e ≈ 0.55 [115]. In this PhD dissertation, e is also called the coefficient of restitution, where: V_{max} = the upward maximum velocity experienced by the membrane once it touches the bottom coil;

V_{min} = the downward minimum velocity experienced by the membrane just before it touches the bottom coil.

One idea is to provide just a sufficient amount of energy to bring the membrane close to the bottom coil. The remanence force (F_R) produced by the permanent magnet then pulls the membrane further and brings it into contact with the bottom coil and finally it is latched. In order to obtain this optimum energy, experiments were carried out by setting I_{coil} at a certain value and varied the values of t_b. It is found that for a particular I_{coil}, there is a new t_b that is smaller than the static t_b, 2.5 ms, at which the membrane experienced a latching mechanism. This t_b is called dynamic latching time (t_{latch_dy}). Figure 7.48 shows the variation t_{latch_dy} and t_{a_static} with I_{coil}, where t_{a_static} is the actuation time of the membrane obtained from the static latching experiments as shown in Figure 7.42.

Figure 7.48 shows that both t_{latch_dy} and t_{a_static} decreases with I_{coil} and then saturates. It is also shown that as $I_{coil} \geqslant 0.036$ A, t_{latch_dy} gets smaller than t_{a_static}. As mentioned before, t_{a_static} is the time required by the electromagnetic force (F_{EM}) to move the membrane downward until it touches the bottom coil. The fact $t_{latch\_dy} < t_{a\_static}$ means that within the time of t_{latch_dy}, F_{EM} has not yet brought the membrane to touch the bottom coil. When I_{coil} is turned off at $t = t_{latch\_dy}$, the only remaining force is the remanence force (F_R) from the permanent magnet that is large enough to latch the membrane.

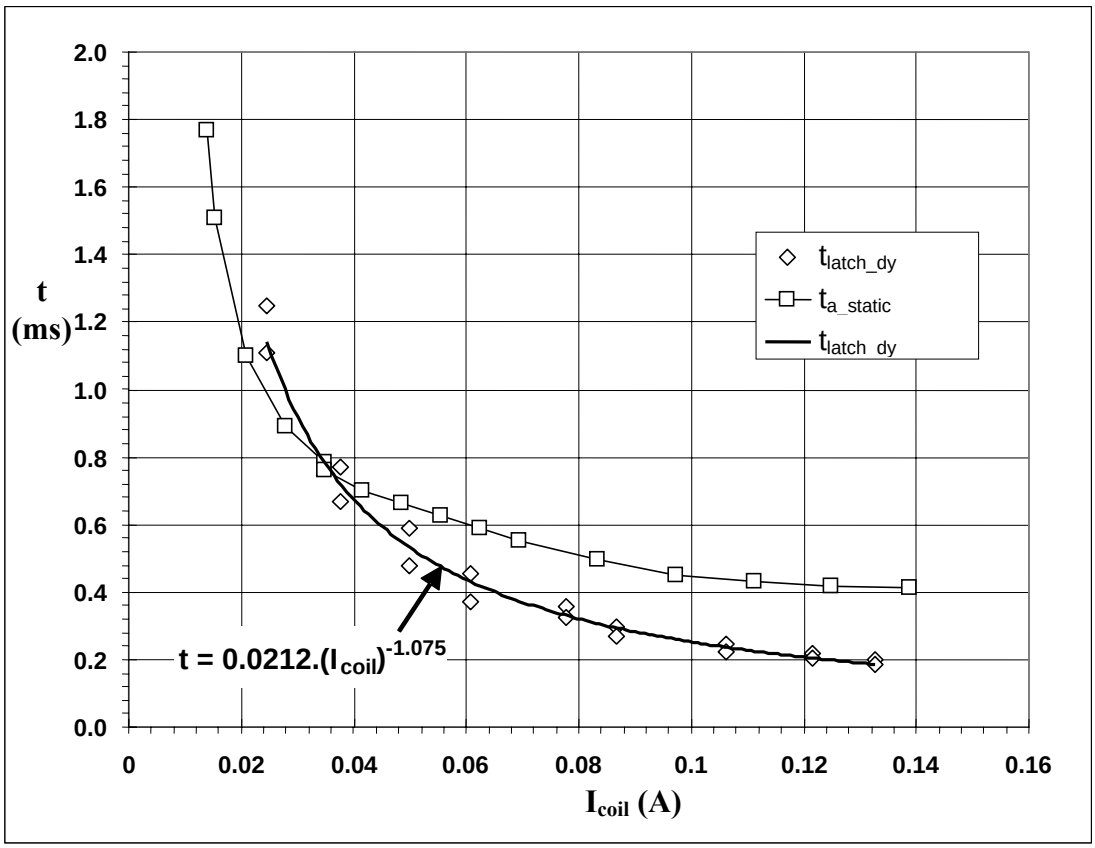

Figure 7.48. Variation of dynamic latching time (t_{latch_dy}) with input current to the microcoil (I_{coil}). It also shows the variation of actuation time from the static analysis (t_{a_static}) with I_{coil}.

Figure 7.49 shows the maximum upward velocity (V_{max}) experienced by the membrane once it touches the bottom coil. It shows that for the static latching mechanism, the membrane experiences much larger repelling momentum than the dynamic one. It shows that $V_{max\_dynamic}$ is increasing with I_{coil} and then saturates; but V_{max_static} seems to be steady and does not increase that much.

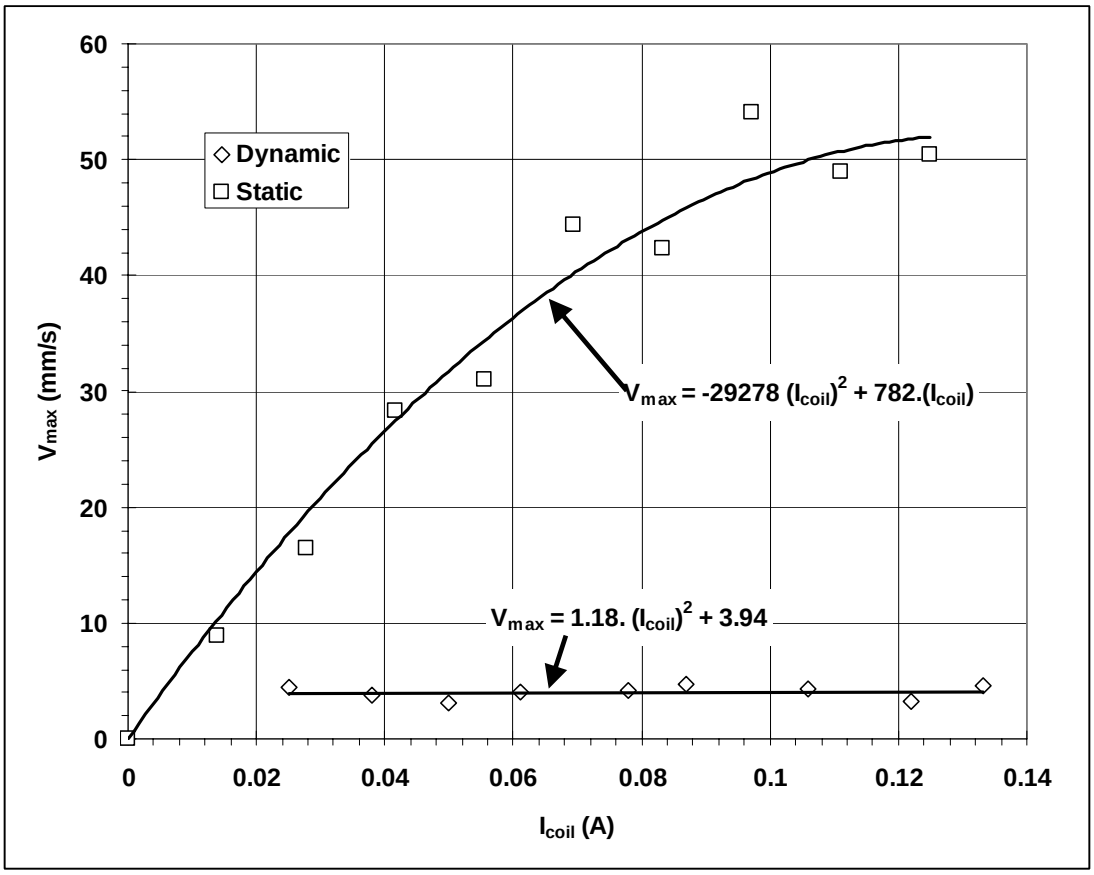

Figure 7.49. The maximum upward velocity (V_{max}) experienced by the membrane as it touches the bottom coil. It shows both cases, the static and dynamic latching mechanisms at different input current to the microcoil (I_{coil}).

Figure 7.50 shows the coefficient of restitution (e) of the membrane just after it touches the bottom coil. It shows that e increases with I_{coil} for the static latching mechanism. However the coefficient of restitution (e) decreases with I_{coil} for the dynamic one. It means that in the dynamic latching mechanism, the repelling momentum decreases as I_{coil} and t_{latch_dy} increases and decreases, respectively, and the membrane moves slower after the impact.

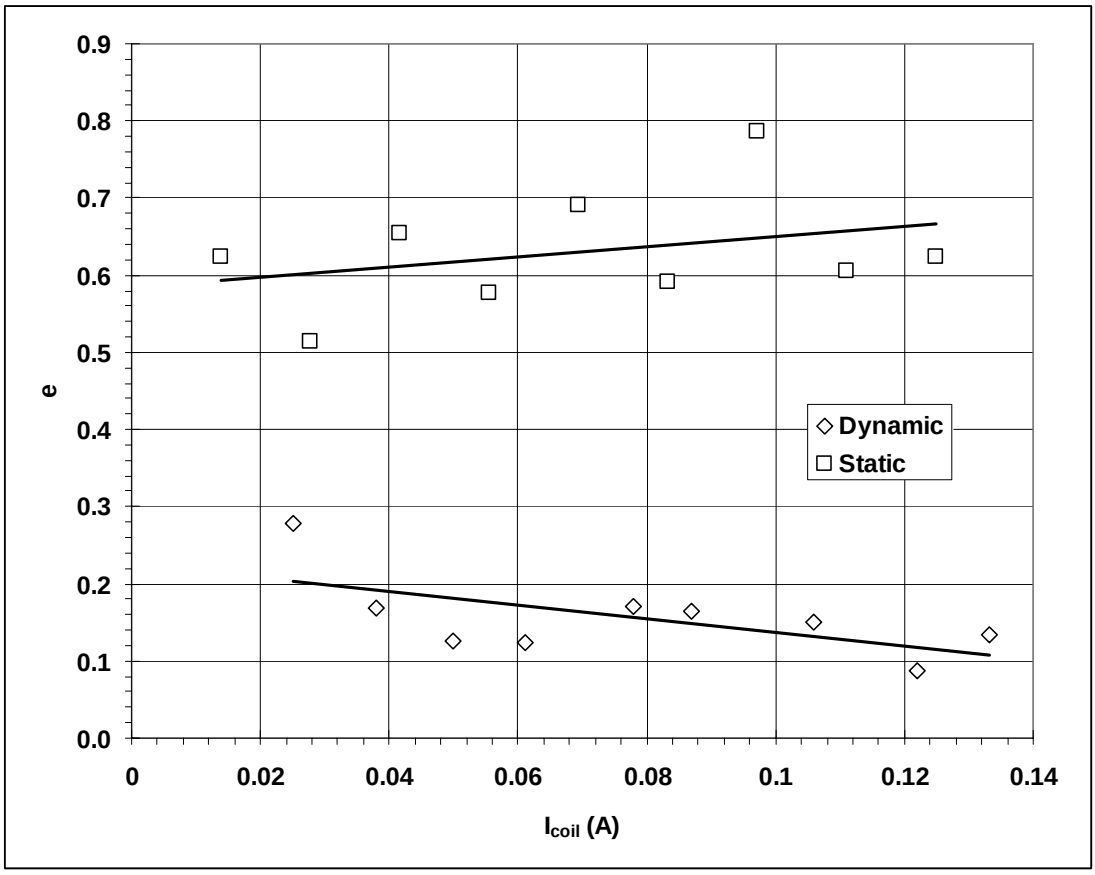

Figure 7.50. The coefficient of restitution (e) of the membrane at different input current to the microcoil (I_{coil}). It shows both cases, the dynamic and static mechanisms.

Figure 7.51 shows the energy consumptions required to carry the static (E_{latch_st}) and dynamic (E_{latch_dv}) latching mechanisms. It shows that at any I_{coil}, (E_{latch_st}) > (E_{latch_dv}). It shows that E_{latch_st} increases parabolically with I_{coil}, while E_{latch_dv} increases linearly with I_{coil}. This shows that the dynamic latching mechanism has reduced the energy consumption significantly. According to our literature search, it is the first time that an electromagnetic bistable-bidirectional microactuator with latching mechanism has been reported having such a very small energy consumption, in the order of μJ.

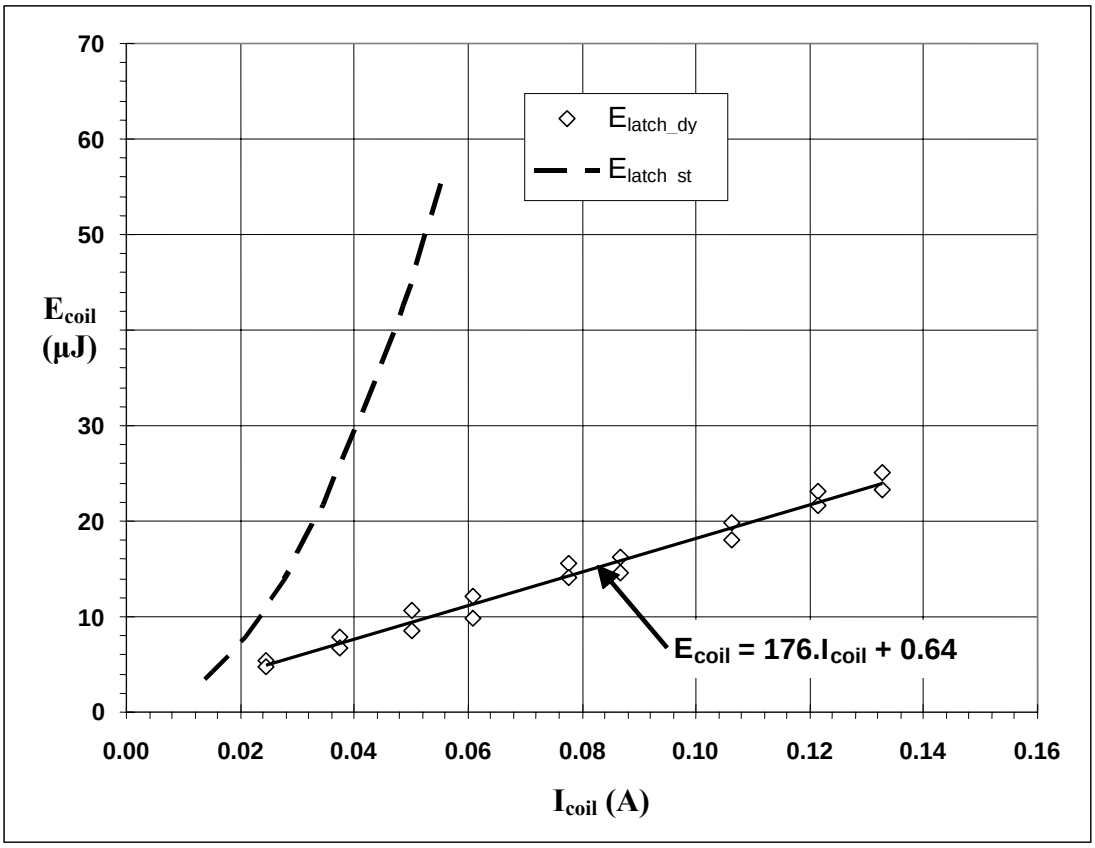

Figure 7.51. The energy consumption to carry out the static (E_{latch_st}) and dynamic (E_{latch_dy}) latching mechanisms

D. Up, Close, and Latched Mechanism

This new mechanism was observed during our testing for the upward displacements of the membrane at different I_{coil} and t_b. The experiments show that when a current of I_{coil} with a certain t_b is applied to the microcoil, the membrane moves upward, then downward due to the large spring force of the membrane, and then latched. Another pulse of I_{coil} at the same direction and the same t_b causes the membrane to move upward and unlatched. As the processes are repeated, two consecutive mechanisms are noticed: up-down- latched and up-unlatched mechanisms. The details are shown in Figure 7.52.

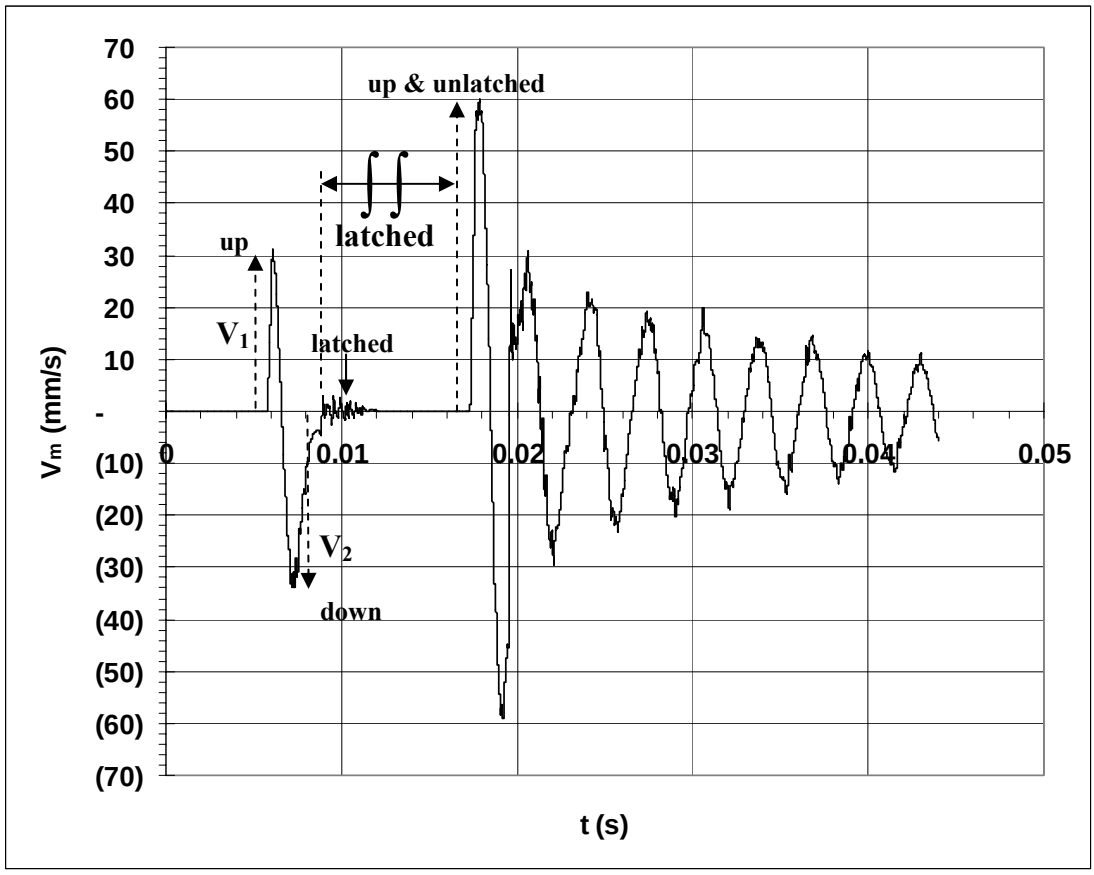

Figure 7.52. The instantaneous velocity of the membrane (V_m) for actuator D, showing two consecutive mechanisms: "up-down-latched" and "up-unlatched" mechanisms at the input current, I_{coil} = 0.133 A and the burst time, t_b = 0.313 ms. (Note: the symbol ∫∫ means that the actual "latched time" is longer than the one displayed in the figure)

Figure 7.52 shows the instantaneous velocity of the membrane when two pulses of current at I_{coil} = 0.133 A and t_b = 0.313 ms are applied to the microcoil. The produced current provides electromagnetic fields at the opposite direction to the permanent magnet alignment, which causes the membrane to move upward. It shows that $V_2 > V_1$, which means that the membrane touches the bottom coil not only because of the spring force, but also because of the remanence force (F_R). Figure 7.53 shows the instantaneous acceleration (A_m) of the membrane.

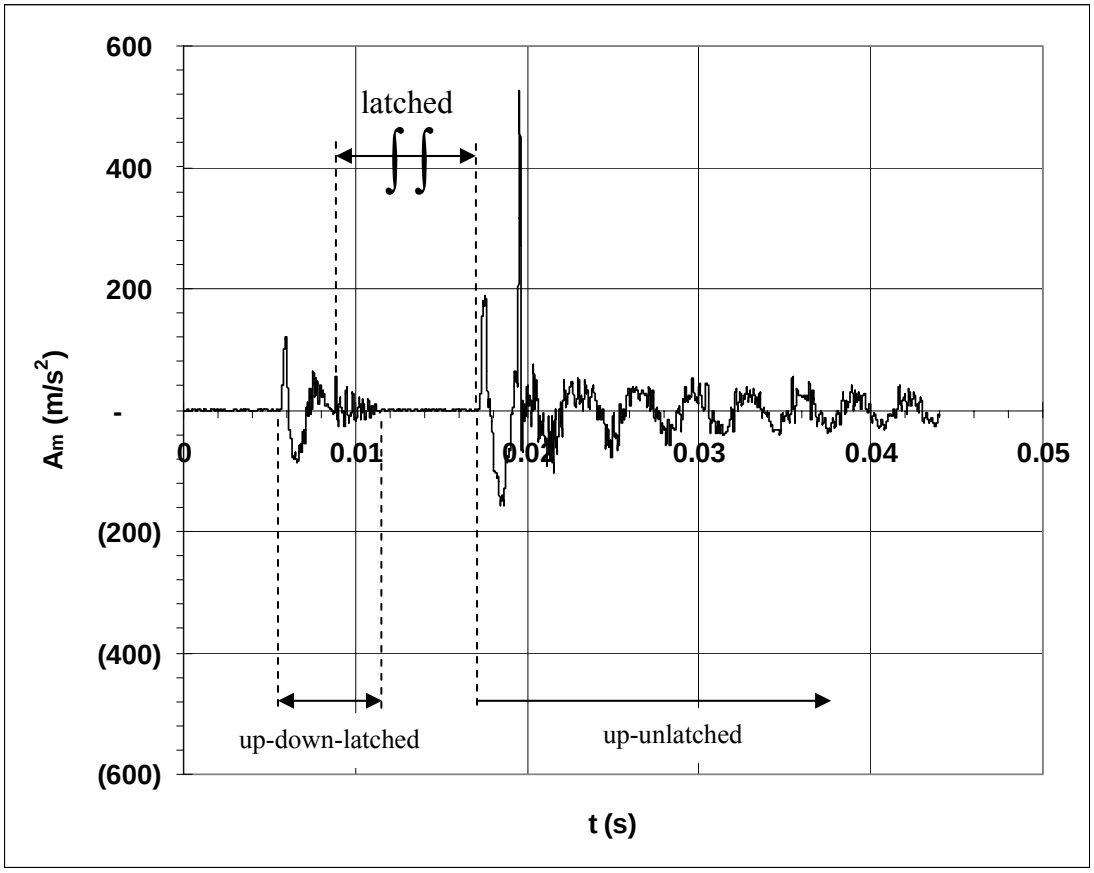

Figure 7.53. The instantaneous acceleration of the membrane (A_m) for actuator D, showing two consecutive mechanisms: "up-down-latched" and "up-unlatched" mechanisms at the input current, I_{coil} = 0.133 A and the burst time, t_b = 0.313 ms. (Note: the symbol $\int\int$ means that the actual "latched time" is longer than the one displayed in the figure)

Figure 7.53 shows that during the up and unlatched mechanism, the membrane experienced a rapid acceleration of $A_m \approx 520$ m/s^2. This acceleration is expected because the membrane moves up unlatched, then moves downward, and bounces up again with an extremely high acceleration rate. The instantaneous displacement (d_m) of the membrane is shown in Figure 7.54 below.

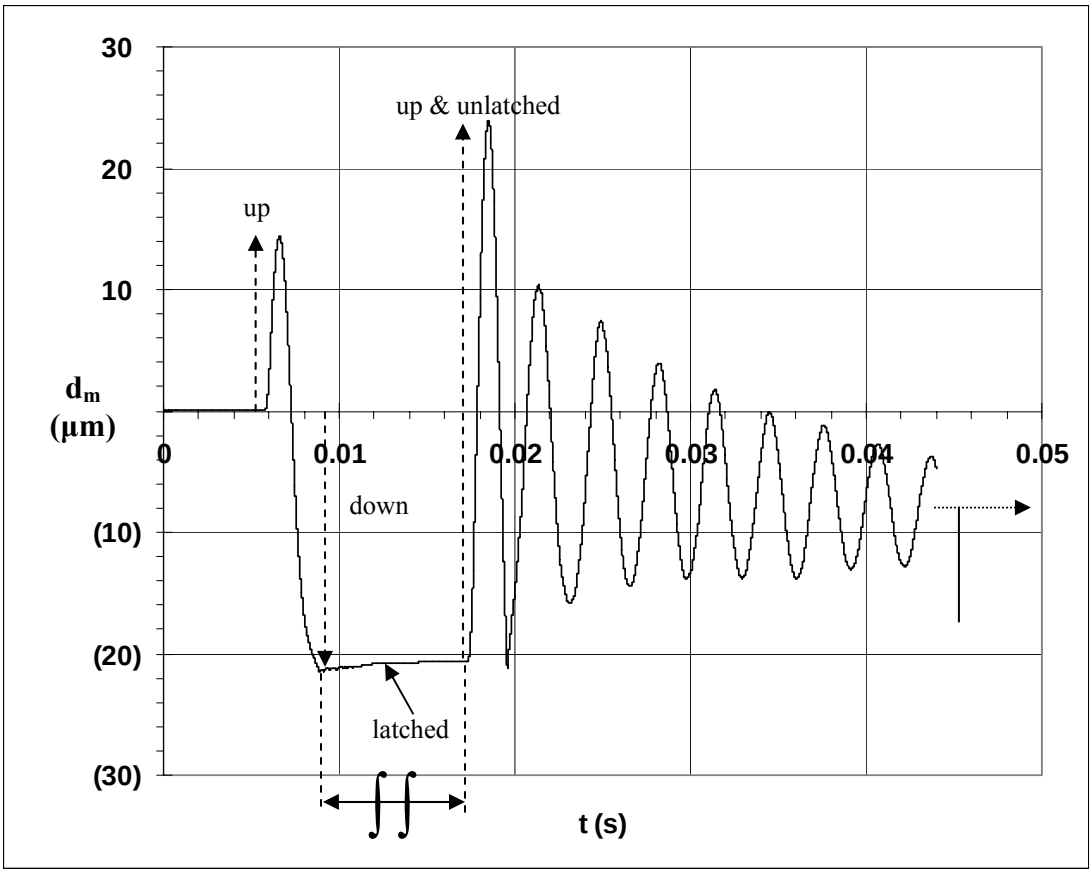

Figure 7.54. The instantaneous displacement of the membrane (A_m) for actuator D, showing two consecutive mechanisms: "up-down-latched" and "up-unlatched" mechanisms at the input current, I_{coil} = 0.133 A and the burst time, t_b = 0.313 ms. (Note: the symbol ∫∫ means that the actual "latched time" is longer than the one displayed in the figure)

The up-down-unlatched mechanism can possibly be used for an optical application. A second approach might be to create latching mechanism at a slightly longer pulse time (t_b) than the dynamic latching mechanism. This behavior could be utilized for a high frequency inkjet printer and/or high frequency pump.

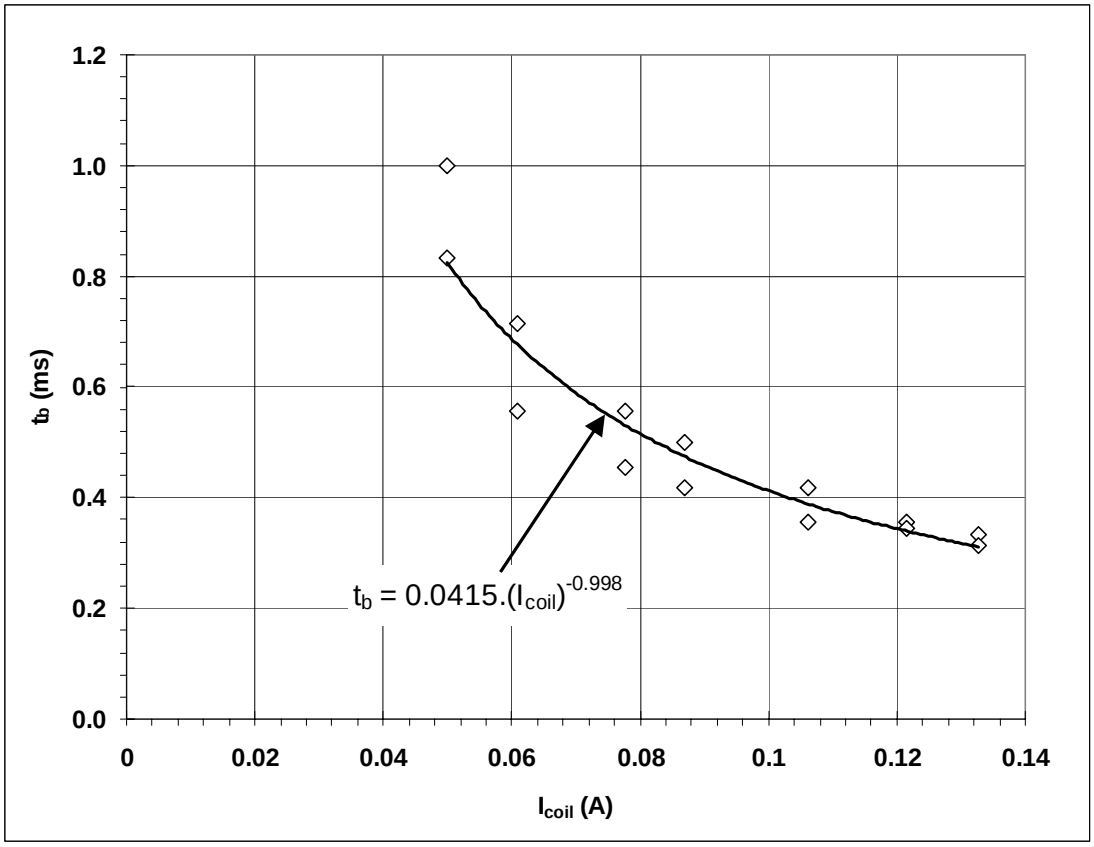

Figure 7.55. The required pulse time (t_b) at different input currents to the microcoil (I_{coil}) to perform up-down-latch mechanism

Figures 7.55 and 7.56 shows the burst time (t_b) and input energy (E_{coil}) required to perform the up-down-latched mechanism at different input currents. It shows that the required time (t_b) decreases with input current (I_{coil}). Obviously it is desirable to have t_b to be a small as possible for minimum energy consumption. However, Figure 7.55 shows that the slope of t_b decreases with I_{coil}, and t_b seems to saturate at a certain value. This indicates the limitation of the up-down-latched mechanism. Figure 7.56 shows that the required energy to carry out the up-down-latched mechanism increases linearly with I_{coil}.

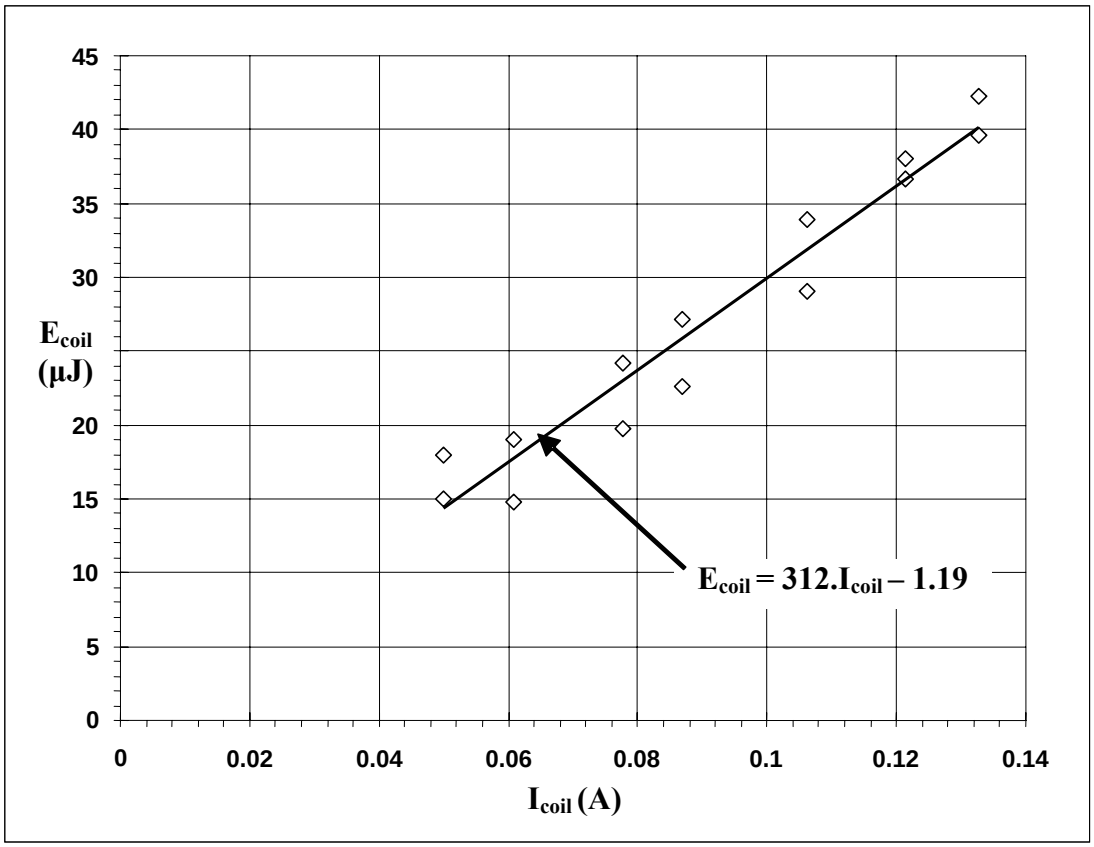

Figure 7.56. The required energy (E_{coil}) at different input currents to the microcoil (I_{coil}) to perform up-down-latch mechanism

7.6.4 Single-leg Design (Actuator E)

7.6.4.1 Latching Mechanism in Air and Water

Figure 7.57 below shows the membrane downward displacement of actuator E tested in the mediums of air and water. The tests were carried out at t_b = 10 ms. It shows that the initial gap in the medium of air is 32.2 μm compared to 45.9 μm in the medium of water. Thus water has initially displaced the membrane upward by 13.7 μm.

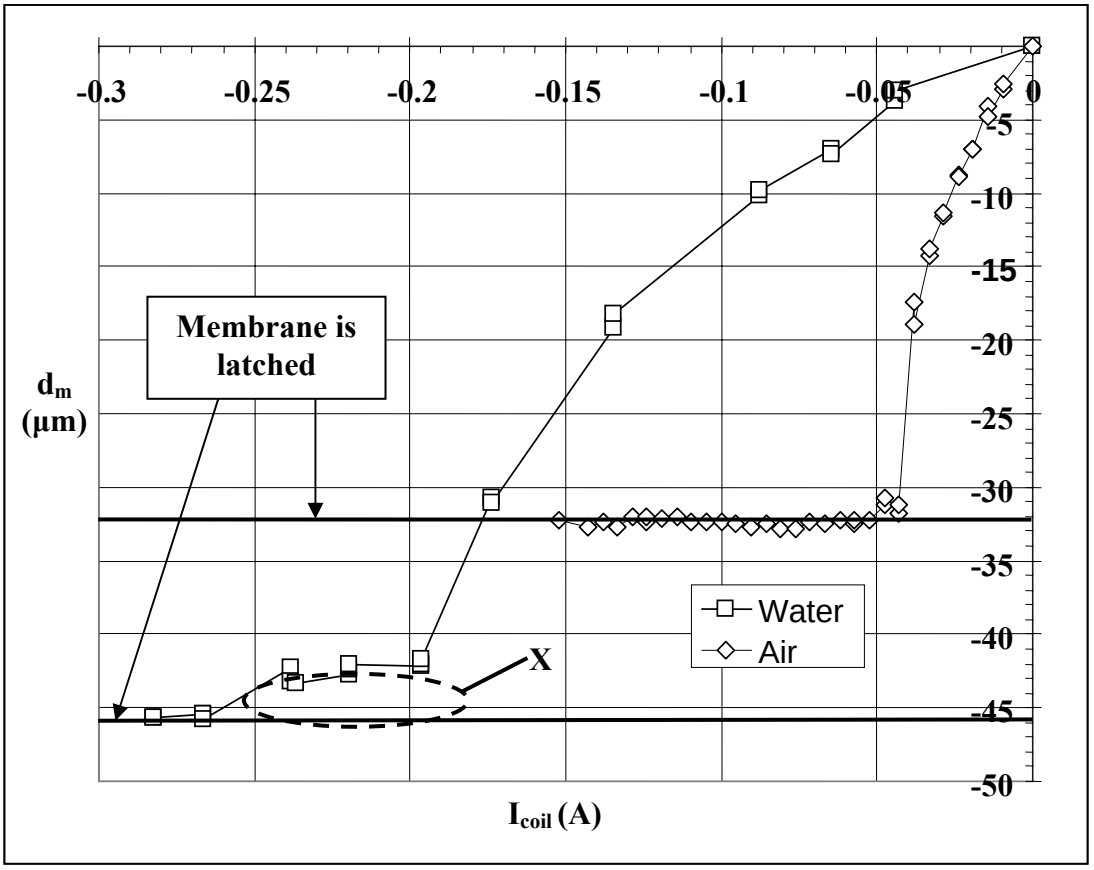

Figure 7.57. The membrane displacement (d_m) for single-leg design bistable-bidirectional microvalve actuator (actuator E) at different input currents (I_{coil}) tested in the medium of air and water at t_b = 10 ms.

Figure 7.57 shows that it requires a much larger I_{coil} to displace the membrane in water as compared to in air. This is obviously because water has a larger squeeze film damping effect, larger viscosity, and higher density than air. It shows that the required I_{coil} for latching in air is only 0.04 A compared to 0.265 A in water. The membrane downward displacement (d_m) in water shows an interesting behavior. The downward displacement continues to increase with I_{coil}, up to I_{coil} = 0.195 A. But when I_{coil} > 0.195 A, there is only a small increase in d_m, as shown in Figure 7.57. The slope of d_m with I_{coil} decreases substantially. As I_{coil} increases to 0.245 A, the slope starts to increase again and the membrane is latched at 0.265 A. This behavior is marked as circle-X in Figure 7.57. It

indicates that when the membrane approaches the bottom coil, there is still some remaining fluid beneath the membrane that provides substantial surface forces that prevent further displacement of the membrane. In order to latch the membrane, a substantial amount of magnetic force and energy are requiredto push the remaining liquid aside. This is the reason that the required latching time in water is much larger than in air. Figure 7.57 shows that the latching is performed at t_b = 10 ms. In air, the membrane has a static latching time at t_{latch_st} = 2.5 ms and the dynamic latching time can be as low as 0.5 ms.

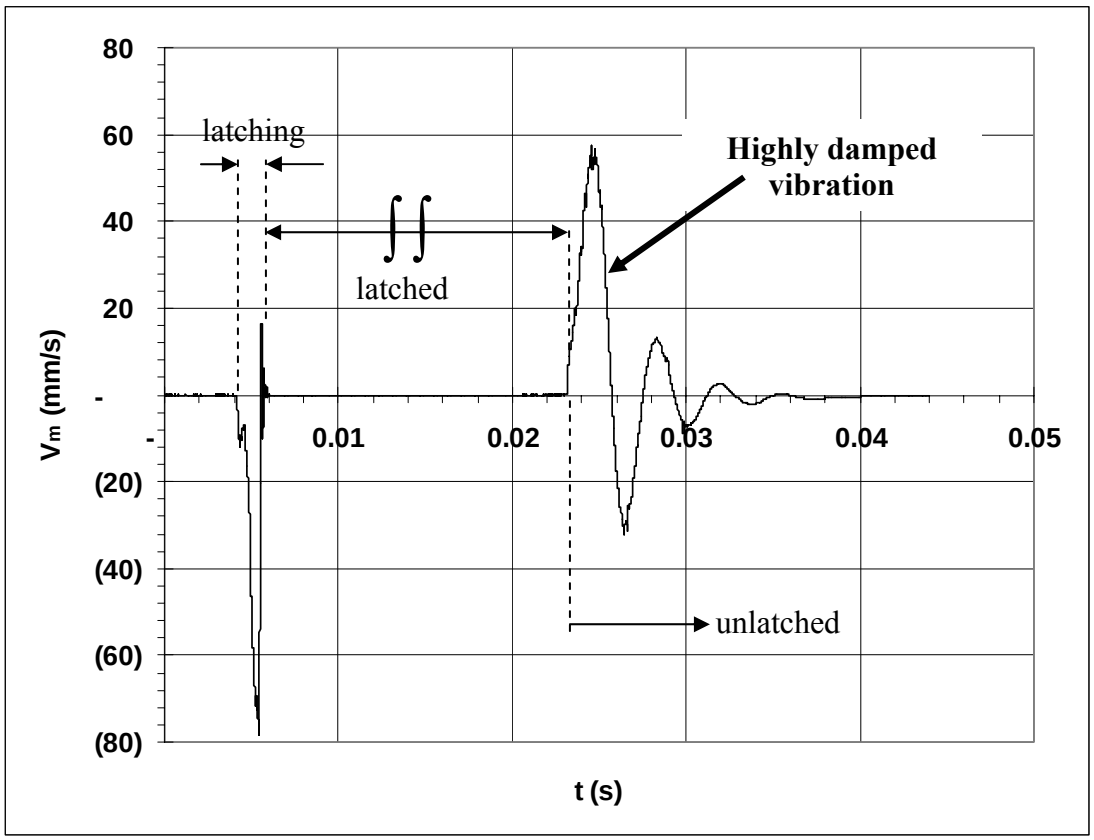

Figure 7.58. The instantaneous velocity of the membrane (V_m) for single-leg design (actuator E) during its latching and unlatching mechanism in the medium of water. The input current (I_{coil}) is 0.25 A at t_b = 10 ms. (Note: the symbol ∫∫ means that the actual "latched time" is longer than the one displayed in the figure)

During the experiments in the medium of water, we did not observe any dynamic latching behavior. In fact, there was only a minor repelling momentum observed in water during latching, because most of the momentum has been damped by the water medium. As is indicated by Figure 7.58, the membrane experiences a highly damped vibration in water. Thus the latching mechanism in water is more dependent on the fluid's properties. Meanwhile, in air, the latching mechanism is more dependent on the momentum effect.

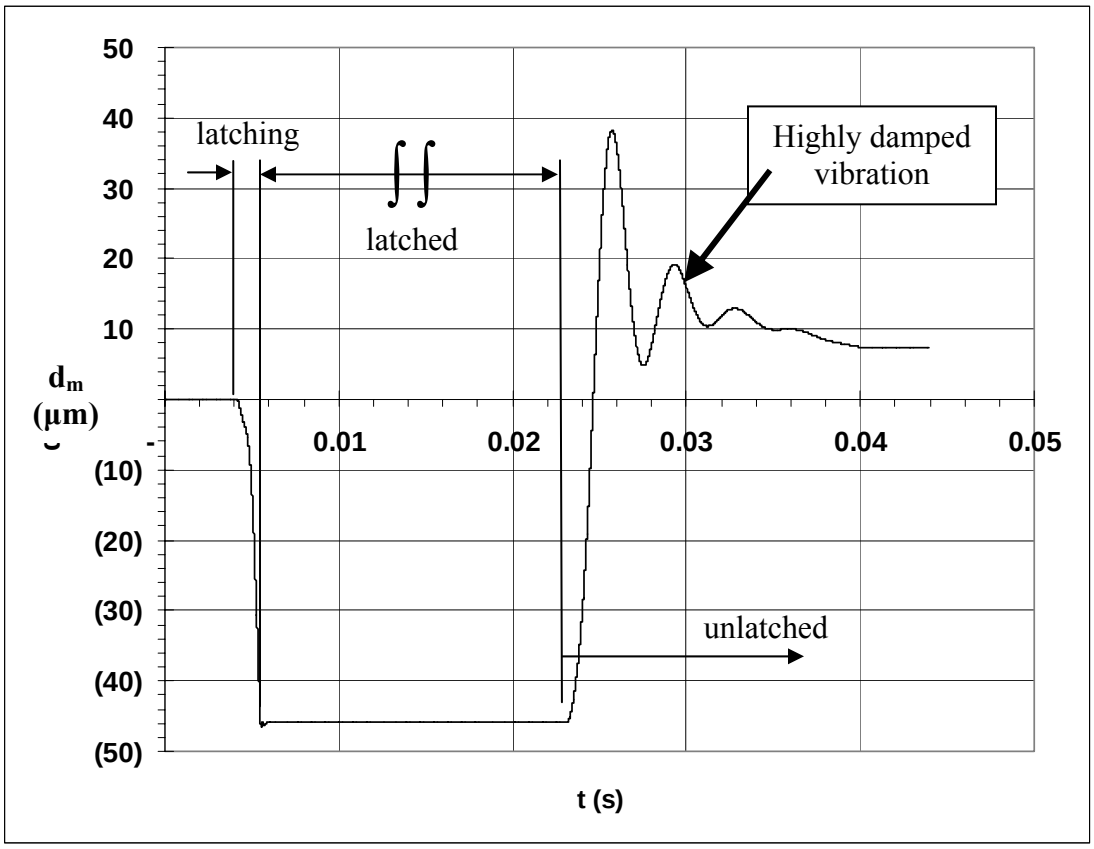

Figure 7.59. The instantaneous displacement of the membrane (d_m) for single-leg design (actuator E) during its latching and unlatching mechanism in the medium of water. The input current (I_{coil}) is 0.25 A at t_b = 10 ms. (Note: the symbol ∫∫ means that the actual "latched time" is longer than the one displayed in the figure)

Figure 7.58, 7.59, and 7.60 show the instantaneous velocity (V_m), displacement (d_m), and acceleration (A_m) of the membrane during its latching and unlatching mechanism in the medium of water when $I_{coil} = 0.25$ A is applied to the microcoil at the pulse time of 10 ms. The results show that the membrane experienced a highly damped vibration. The repelling momentum, once the membrane touches the bottom coil, is quickly absorbed by water. Figure 7.60 shows that the membrane experiences a very large upward acceleration (A_m) once it touches the bottom coil, with $A_{max} \approx 580$ m/s^2.

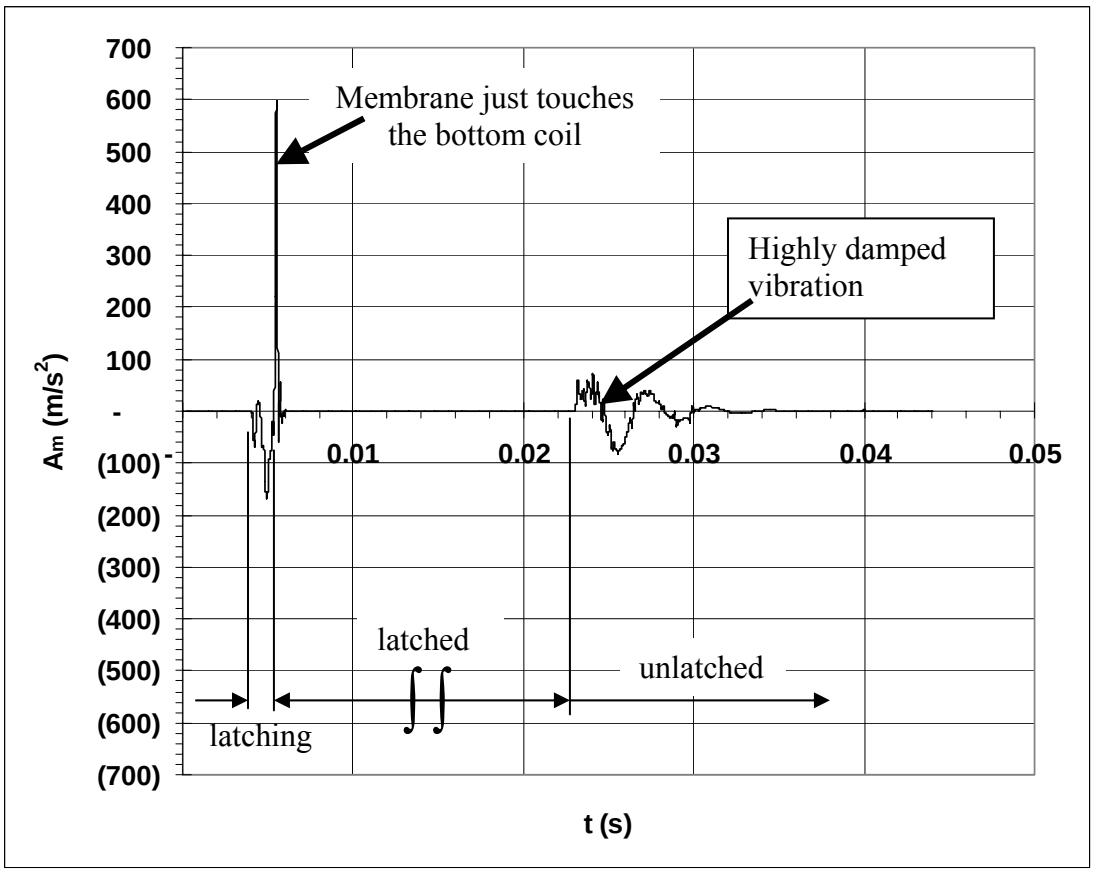

Figure 7.60. The instantaneous acceleration of the membrane (A_m) for single-leg design (actuator E) during its latching and unlatching mechanism in the medium of water. The input current (I_{coil}) is 0.25 A at t_b = 10 ms. (Note: the symbol ∫∫ means that the actual "latched time" is longer than the one displayed in the figure)

CHAPTER 8

LIQUID TESTING OF THE MICROVALVES

8.1 Introduction

This chapter discusses the liquid testing results that have been obtained for the microvalves. The liquid testing determines the free flow rate of the microvalve ($\dot{V}_{free}$) at different pressure heads (dP_{free}), the required input current (I_{coil}) for the operation, the power consumption (P_{coil}), the leaking rate ($\dot{V}_{leak}$), and the burst pressure (dP_{burst}) of the microvalves. The experimental setup and the theoretical equations to determine the pressure drop across the microvalve are also discussed in this chapter. There are two types of microvalves that were tested: the on/off microvalve and the bistable microvalve with latching mechanism.

8.2 Experimental Setup

8.2.1 Schematic of the Setup

The schematic and picture of the liquid testing setup for the microvalves are shown in Figures 8.1and 8.2 respectively. The testing setup is designed such that it is convenient to connect and disconnect the hoses between different microvalves. The complete assembly of the microvalve packaging is shown in Figure 6.6 and the detailed

descriptions of the microvalve packaging for liquid testing are discussed in Chapter 6. The microvalve testing package consists of 12 microvalves, and each package has 12 inlets and 12 outlets for hose connections. The testing was carried out at room temperature and the temperature of the fluid was estimated at room temperature (T ≈ 22 °C)

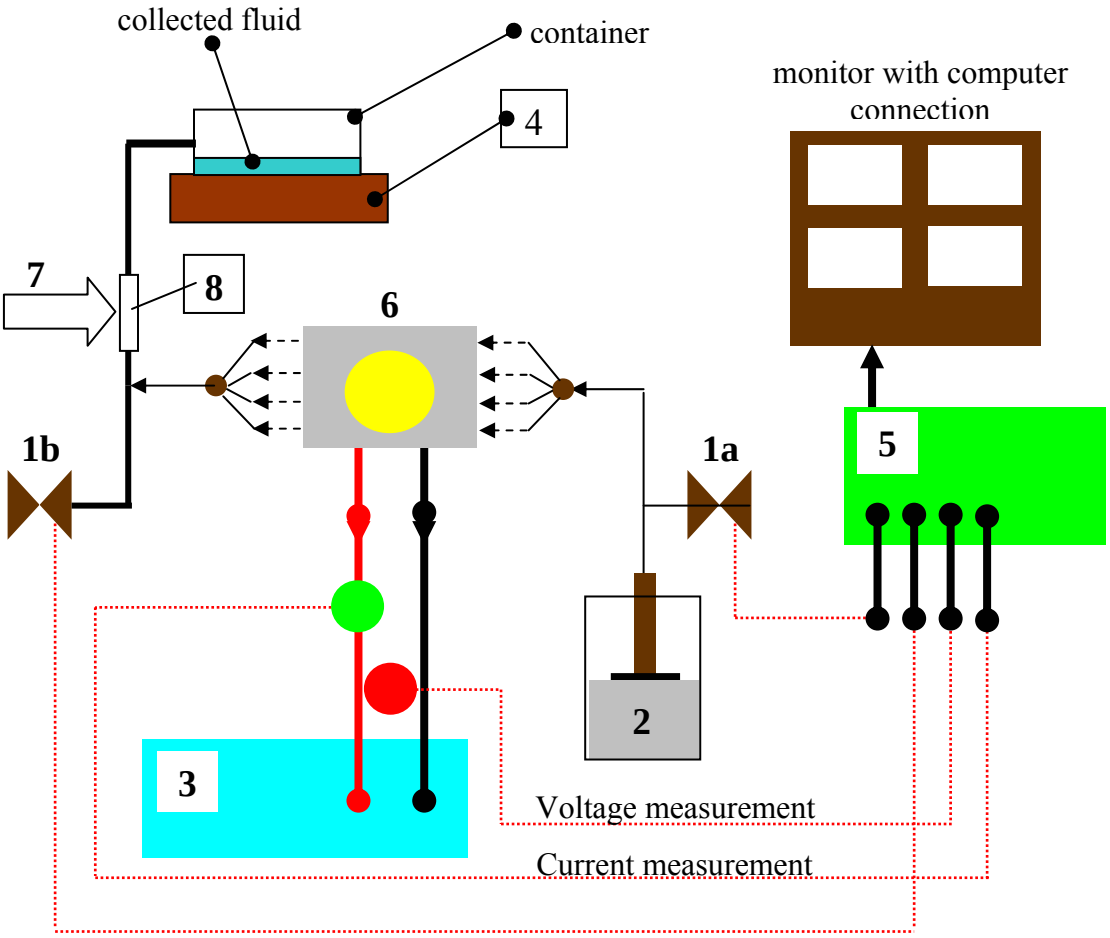

Figure 8.1. The schematic of the liquid testing for the microvalve, where: 1a = inlet pressure sensor, 1b = outlet pressure sensor, 2 = syringe pump, 3 = potential step generator, 4 = electronic weight scale, 5 = data acquisition system, 6 = microvalve testing package, 7 = microscope, 8 = 100 μm diameter clear tube.

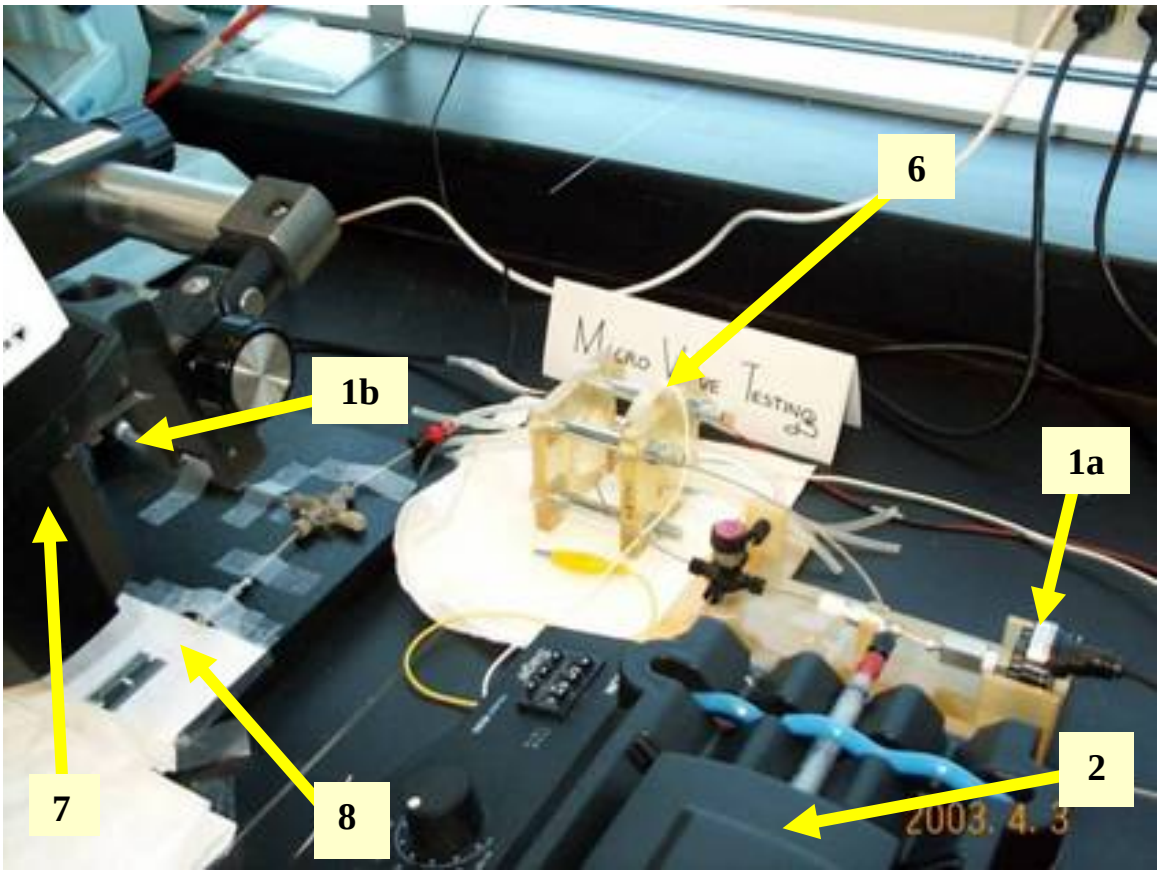

Figure 8.2. The picture of the liquid testing for the microvalve, where: 1a = inlet pressure sensor, 1b = outlet pressure sensor, 2 = syringe pump, 6 = microvalve testing package, 7 = microscope, 8 = 100 μm diameter clear tube. Note: the potential step, electronic weight scale, and data acquisition system are not shown.

The main parts for the liquid testing are:

[1] Pressure sensors

The pressure sensors used were manufactured by Omega Engineering Inc., model PX180-015GV. The pressure sensors give the voltage output signal that is converted to the pressure (kPa) by the calibration provided by the manufacturer. 2 (two) pressure sensors were used: one to measure the inlet pressure to the microvalve (labeled 1a in Figures 8.1 and 8.2), and the other one to measure the outlet pressure of the microvalve

(labeled 1b in Figures 8.1 and 8.2). The difference in pressures between these pressure sensors provides the pressure head (dP) across the microvalve.

[2] Constant flow controller (syringe pump)

This device controls the volume flow rate of the liquids - water or diluted methanol - entering the microvalve at a constant rate. It is manufactured by Orien, model Sage M362. The device has an electric motor with a gear mechanism that produces an axial movement to push the syringe at a constant volume flow rate ($\dot{V}$). Thus this device is also called a "syringe pump". The minimum flow rate produced by the device is 1 μL/hr or 0.0167 μL/min. Before use, the device is calibrated by the scale to ensure its accuracy. The flow of liquid coming out from the microvalve when it is fully open is collected in a container and is continuously weighed by a scale (labeled No. 4 in Figure 8.1). The weight change over a certain time provides the mass flow rate ($\dot{m}$) of the liquid. The mass flow rate is then divided by the density to yield the volume flow rate ($\dot{V}$). This volume flow rate is then compared with the setting rate of the syringe pump. The results show that the syringe pump has an accuracy in the range of 2 – 15 %. The fluid properties are taken at the temperature of 20 °C.

[3] Potential step generator

The function of this device is to supply the electrical power to the microvalve (P_{coil}) to close/open or to latch/unlatch the microvalves. The device can produce a pulse of current or voltage, which is used for the bistable microvalve operation with latching mechanism. This device is manufactured by Solartron, model 1207.

[4] Electronic weight scale

This device is manufactured by Mettler Toledo, model AG245. It continuously measures the weight of the liquid collected in the container. This device has the display accuracy of 0.01 mg. If the density of the liquid, such as water, is ρ_{water} =1,000 kg/m^3 = 1 kg/L, the corresponding volume accuracy is 0.01 μL. However, the device is extremely sensitive to a small vibration in the testing room, which can cause the measured weight to fluctuate on the order of +/- 1 mg, which corresponds to +/-1 μL. Thus this device is not suitable for measuring the leaking rate of the microvalve, which is estimated to be in the order of less than 1 μL/min. This device is then used to calibrate the volume flow rate of the syringe pump. It was found that the syringe pump has an accuracy in the range of 2–15%.

[5] Data acquisition system

The data acquisition system by Hewlett Packard is the model 34970 A. It was used to store data produced by the equipment and to display the instantaneous measurements for monitoring during an experiment. The data was transferred to the computer by IEEE interface and stored into the hard drive for further data processing with Excel after the experiments were completed. The program HP BenchLink Data Logger V. 1.3 was used to display the output from the data acquisition system.

[6] Microvalve testing package

The details are discussed in Chapter 6.

[7] Microscope

A microscope is installed in the experiment to examine the liquid flow through the clear tube (100 μm in diameter, label no 8 in Figures 8.1 and 8.2) installed on the outlet of the microvalve. In the experiment, it is necessary to ensure that there is no air bubble in the liquid flow as it could cause clogging of the microvalve.

8.2.2 Leaking Rate Measurement

There were two different microvalves tested in the experiments: the on/off microvalve and the bistable microvalve. The on/off microvalve was tested for the flow of diluted methanol at the free flow ($\dot{V}_{free}$) from 1 to 50 μL/min. The bistable microvalve was tested for the flow of DI water at the free flow ($\dot{V}_{free}$) from 10 to 50 μL/min. It was anticipated that $\dot{V}_{leak}$ of the microvalves was on the order of 0.01 – 1 μL/min. Based on our research, there is no commercially available flow meter that is able to measure $\dot{V}$ at this small a level.

Thus, in order to measure the leaking of the microvalve with this experimental setup, the flow rate controller (syringe pump) was utilized. By adjusting the volume flow rate to very low level, while the microvalve is closed, or latched for the bistable microvalves, the pressure change was monitored with time. The procedures were as follows:

1. Adjust the knob in the syringe pump to the desired free volume flow rate ($\dot{V}_{free}$), ranging from 1 – 50 μL/min for the experiment.

2. Close or latch the microvalve by applying sufficient current to the microcoil. The closing/latching of the microvalve is indicated by the continuous increase in pressure head across the microvalve, observed on the monitor.
3. Once the pressure head (dP) across the microvalve has increased to a desired value, the volume flow rate is decreased to a level so that there was no further increase in the pressure head, as seen on the monitor. This step required the patience to continuously adjust the volume flow rate until the pressure head was maintained at a reasonably constant level. The flow rate of the syringe pump was adjusted to the level in the range of 0.016 to 1 μL/min. Once this step was done, the pressure was called the closing ($dP_{closing}$) or latching pressure head (dP_{latch}) for the on/off or the bistable microvalve, respectively. The volume flow rate is then called the leaking rate ($\dot{V}_{leak}$).
4. Steps no 2 and 3 were repeated to find the value of $\dot{V}_{leak}$ at different $dP_{closing}$ or dP_{latch} .

These procedures proved an effective method for measuring the leaking of the microvalves ($\dot{V}_{leak}$) with the lowest measured $\dot{V}_{leak}$ of 0.016 μL/min, which is the same as the lowest volume flow rate of the syringe pump. This method can measure $\dot{V}_{leak}$ in increments of 0.016 μL/min, with the optimum accuracy of +/- 0.008 μL/min. When $\dot{V}_{leak}$ of the microvalve is within this increment, such as when 0.016 μL/min < $\dot{V}_{leak}$ < 0.032 μL/min. Some interpolation is required to determine more accurate $\dot{V}_{leak}$ values. More details are provided in Appendix 1.

8.3 Theoretical Equation

The schematic of the liquid flow across the microvalve at the fully open position is shown in Figure 8.3 below.

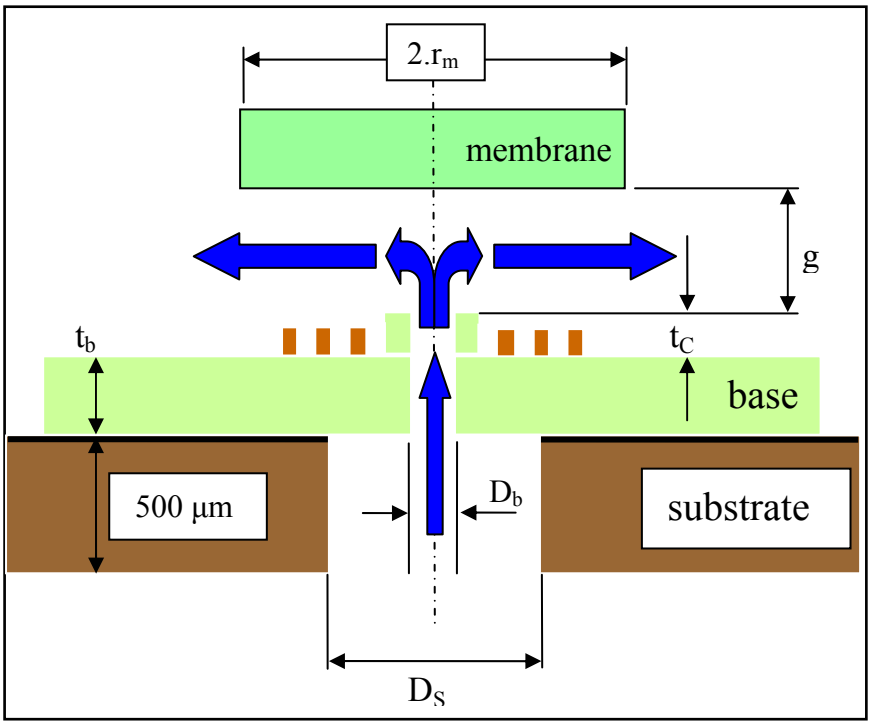

Figure 8.3. Schematic of the liquid flow across the microvalve when it is fully open. Where: t_b, t_C, g, and r_m are the thickness of the base, the thickness of the microcoil, the gap between the membrane and the coil, and the radius of the soft magnetic membrane or the permanent magnet for the on/off or bistable microvalve respectively.

Initially the liquid enters the large hole (D_S = 250 µm) through the back of the wafer, then emerges into the small hole in the microvalve base (D_b = 60 µm). The flow then bends 90° and flows across the space/gap between the membrane and the micro coil. As shown in Figure 8.3, a number of pressure drops occur across the microvalve. The

pressure drop across the inlet holes (bigger and smaller holes) with the liquid flow rate ($\dot{Q}$) can be described by Equation 8.1 below for a fluid flow through a straight circular tube whose radius is r_0 [116, p.34], where L_{hole} is the length of the hole.

$$dP_{inlet} = \frac{8.\dot{Q}.\mu.L_{hole}}{\pi.r_0^4} \tag{8.1}$$

The pressure head due to the 90° bend/change of flow direction at the outlet of the orifice can be described by Equation 8.2 below [117], where ξ = 1.3.

$$dP_{bend} = \frac{\rho}{2}.\frac{\dot{Q}^2}{A_g{}^2}.\xi \tag{8.2}$$

The pressure head across the space between the membrane and micro coil can be approximated as the flow between two fixed parallel plates, with Equation 8.3 below:

$$dP_{space} = \frac{\dot{Q}}{w_m}.\frac{3.\mu.(2.r_m)}{2.(0.5.g)^3} \tag{8.3}$$

Where: "w_m" and "r_m" are the equivalent width and the radius of the soft magnetic membrane or the permanent magnet for the on/off or the bistable microvalves respectively, and $w_m = \sqrt{\pi.r_m^2}$ for a circular shape membrane.

The pressure head due to the contraction from D_S to D_b and enlargement from D_b to ($2.r_m$) are determined by Equation 8.4 below (116, p.46):

$$\begin{aligned} dP_{contract} &= \frac{\rho.K_1}{2}.\left(\frac{Q}{A}\right)^2; K_1 = \frac{1}{2}(1 - D_b / D_S) \\ dP_{enlarge} &= \frac{\rho.K_2}{2}.\left(\frac{Q}{A}\right)^2; K_2 = \left(1 - \left(D_b /(2.r_m)\right)^2\right)^2 \end{aligned} \tag{8.4}$$

The sudden change from D_S to D_b can be classified as a laminar flow through an orifice and it gives an additional pressure head as shown in Equation 8 below [116, p. 44].

$$dP_{orifice} = \frac{\mu.\dot{Q}}{2.\delta^2.D_b.A_b} \qquad (8.5)$$

Where: the coefficient (δ) depends of the geometry and Reynolds (Re) number, it is tabulated in Reference [116, p44].

The sum of pressure drops described above give the theoretical estimation of the pressure drop across the valve (dP_{free_theo}) when it is fully open as described by Equation 8.6 below:

$$dP_{free\_theo} = dP_{inlet} + dP_{outlet} + dP_{bend} + dP_{space} + dP_{contract} + dP_{enlarge} + dP_{orifice} \qquad (8.6)$$

It should be noted that the theoretical equations described in Equations 8.1 to 8.6 above are for case when the liquid flow is laminar and fully developed, which is not always the case particularly for small channels.

8.4 Results for On/Off Microvalve

8.4.1 Free Flow Results

The on/off microvalve was tested with 50% diluted methanol flow over a range of free flow rate ($\dot{V}_{free}$) from 1 to 50 μL/min. Free flow occurs when the microvalve is in the open position, with results that are shown in Figures 8.4 and 8.5 for the microvalve with D_b = 45 μm and D_b = 60 μm respectively.

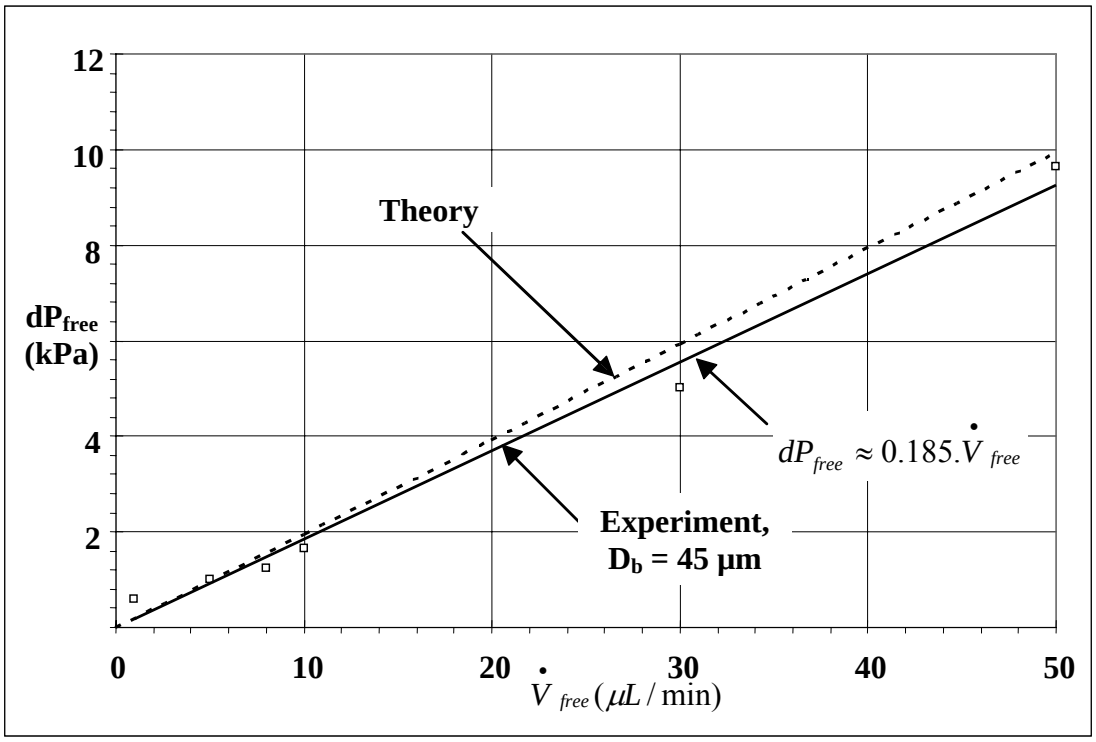

Figure 8.4. The combined results, experiment and theory, for the pressure drop (dP_{free}) across the on/off microvalve with the diameter (D_b), 45 µm, for various free flow rate ($\dot{V}_{free}$) of 50% diluted methanol (no parylene coating is applied).

The experimental results as shown in Figures 8.4 and 8.5 are pretty much in agreement with the theoretical estimation as indicated by Equation 8.6, where the properties of the fluids are taken at 20°C. Some differences between the experimental and theoretical results were experienced at low $\dot{V}_{free}$, 1 – 10 µL/min. Figure 8.5 shows that the theoretical results underestimate the pressure drop (dP_{free}) across the microvalve for $\dot{V}_{free} > 10$ µL/min. This could be due to the fact that the theoretical estimation assumed that the liquid flow is laminar and completely developed which is not always the case for small orifice and for a very low volume flow rate and small Reynolds number.

The equations in Figures 8.4 and 8.5 give an approximation of the experimental dP_{free} across the microvalve at different $\dot{V}_{free}$. The experimental volumetric flow rate measured is expected to have an accuracy similar to the syringe pump, which is approximately 15 %.

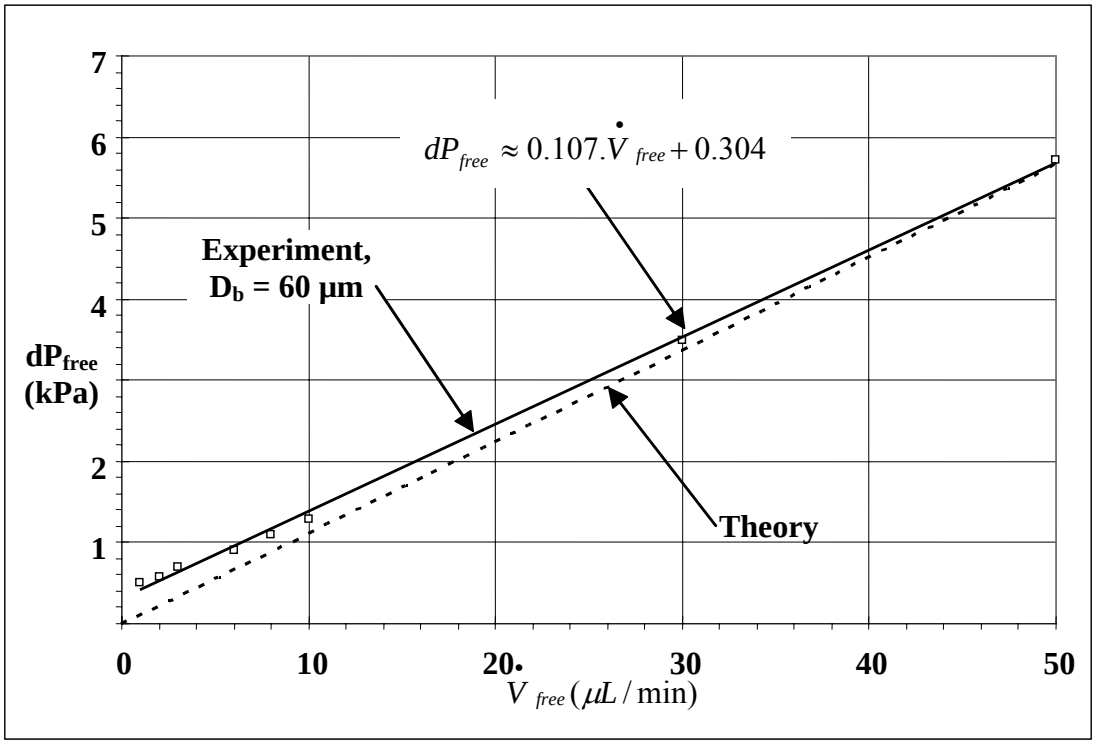

Figure 8.5. The combined results, experiment and theory, for the pressure drop across the on/off microvalve (dP_{free}) with the diameter, D_b = 60 μm, for various free flow rate ($\dot{V}_{free}$) of 50% diluted methanol. (no parylene coating is applied).

8.4.2 On/Off Testing of the Microvalve

8.4.2.1 On/Off Microvalve without Parylene Coating

After the whole microvalve structure has been fabricated, mounted on the gold plated package, and wire bonded, the whole microvalve structure, as shown in Figure 6.4, is coated with a thin parylene-C. The purpose of this coating is to prevent corrosion of the microvalve structure as it is entirely made of electroplated metal, to prevent the possibility of electrolysis on the microcoil surface, and to act as a gasket between the gold microcoil and the membrane. Figures 8.6 to 8.7 and Figures 8.8 to 8.9 shows the liquid testing results for the on/off microvalves without and with parylene coating respectively. The on/off microvalves were tested with the flow of 50% diluted methanol (weight by volume) at the free flow rate of 1 μL/min. Figure 8.6 shows the liquid testing of the microvalve with corrugated membrane with 4(four) bending supported legs. The sample SEM picture of the fabricated on/off microvalve with corrugated membrane is shown in Figure 5.13.

Figure 8.6 shows that the microvalve is closed or opened by turning on/off the input power (P_{coil}) at 1.1 W. The resistance of the microcoil (R_{coil}) is 3.1 Ω and the required operating current (I_{coil}) is 0.6 A. When the microvalve is closed, the membrane touches the bottom microcoil; the flow of liquid is hindered as indicated by the increase of pressure drop across the microvalve (dP).

Figure 8.6 shows that a continuous P_{coil} is required to keep the microvalve closed. It also shows that the microvalve experiences substantial leaking, as indicated by label no. 1. The continuous input current to the microcoil (I_{coil}) may generate some air bubbles on its surface that have enough force to slightly open the membrane and cause leaking.

As indicated by label no.1 in the figure, dP suddenly decreases while P_{coil} is continuously applied to the microcoil. The leaking is also indicated by no further increases in dP as P_{coil} is applied.

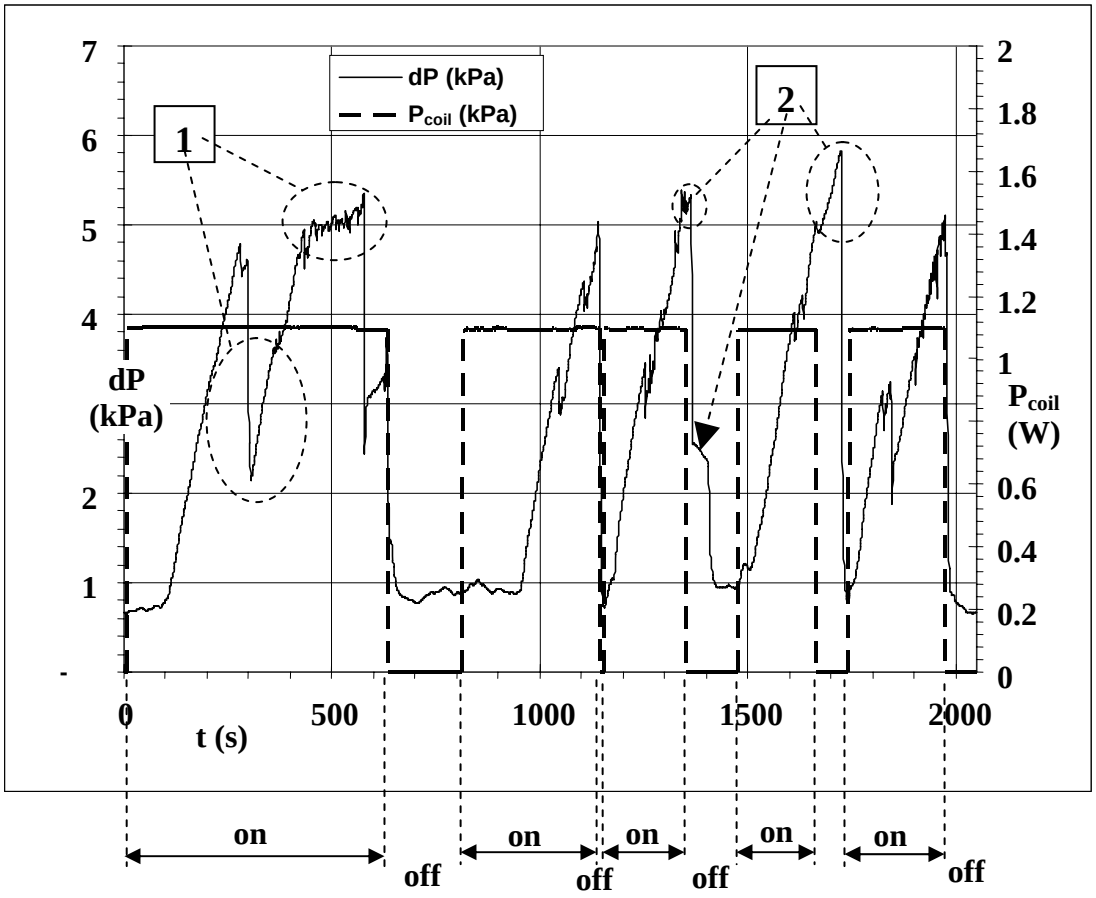

Figure 8.6. The pressure head (dP) across the microvalve with the applied input power to the microcoil (P_{coil}). It shows the on/off performance of the microvalve without parylene coating at the free flow rate ($\dot{V}_{free}$) of 1 μL/min of 50% diluted methanol. The microvalve has a corrugated membrane with 4 (four) bending supported-legs, D_b = 60 μm and R_{coil} = 3.1 Ω.

Figure 8.6 shows another problem, which is called sticking, as indicated by label no. 2. Once P_{coil} is turned off, the membrane should come back to its initial open position by the spring force (F_S), and this is indicated experimentally by the sudden decrease in dP. When the microvalve experiences the sticking problem, the membrane does not immediately come back to its open position even though P_{coil} is turned off. This is indicated experimentally by the continuous increase in dP. Since the microcoil is made of gold (Au), which is a relatively soft metal, and the membrane is made of NiFe, a continuously applied current (I_{coil}) for a sufficient length of time might temporarily weld two touching surfaces together. The membrane then sticks on the microcoil when I_{coil} is turned off. Sticking problems are definitely undesirable in the microvalve operation.

The tested sample shown in Figure 8.6 was removed from the package, indicating that the structure has experienced enormous corrosions. This was expected to occur when the microvalve is in direct contact with the liquid during the tests. Another test was carried out for the same on/off microvalve of the same design. The results are shown in Figure 8.7. However, this time the microvalve was heated in the oven at 120 °C for 24 hours after it was soaked in acetone, methanol, and water. It is expected that a thin layer of metal oxide forms on the microvalve structure during the heating process that will help minimize the corrosion, sticking, and leaking problems.

Figure 8.7 shows that the technique has provided a little bit of help in minimizing the leaking and the sticking problems. It shows that the graph is smoother than the one in Figure 8.6, and the fluctuation in dP is relatively unseen. However, the experimental results still indicated a measurable leak and sticking problems during microvalve operation as indicated by labels no 1 and 2 in Figure 8.7. The sample was removed from

the package and the condition visually inspected to reveal that some corrosion was present on the structure. Further testing on this microvalve causes the corrosion to get worse. Thus there is a need for a dielectric coating on the microvalve structure to prevent the problems shown in Figures 8.6 and 8.7.

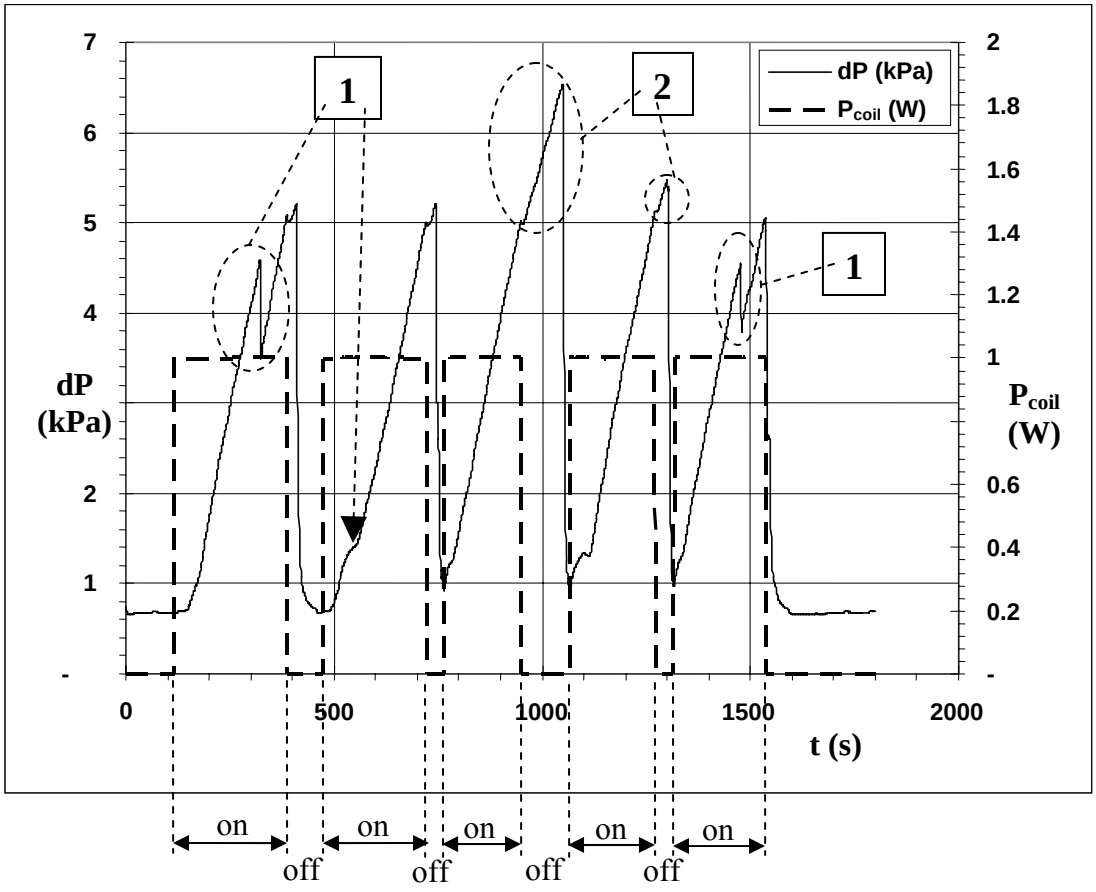

Figure 8.7. The pressure head (dP) across the microvalve with the applied input power to the microcoil (P_{coil}). It shows the on/off performance of the microvalve without parylene coating at the free flow rate ($\dot{V}_{free}$) of 1 μL/min of 50% diluted methanol. The microvalve has a corrugated membrane with 4 (four) bending supported legs, D_b = 60 μm and R_{coil} = 3.1 Ω. Extra heat treatment at 100°C inside a convective oven is given to the microvalve structure to minimize corrosion

8.4.2.2 On/Off Microvalve with an Additional Parylene Coating

The testing results for the on/off microvalve with 1 μm parylene-C coating are shown in Figure 8.8. A tremendous improvement in the opening and closing operations of the microvalve were observed. There is no leaking or sticking occurring during the operation. Thus, the parylene has created a good coating that prevents the electrolysis on the microcoil surface. Parylene-C has also acted as a gasket between the membrane and the microcoil, as it shows the microvalve has been able to close at a flow rate of 50% methanol at a much higher pressure, 26.5 kPa, than is the case without parylene coating, only 5 kPa, as shown in Figures 8.6 and 8.7. The burst pressure (dP_{burst}) of this on/off microvalve, for which the microvalve is always open, is found to be more than 57 kPa, which is the maximum pressure of the microvalve package. The on/off microvalve is operated at P_{coil} = 1.22 W. The R_{coil} is 3.74 Ω and operating I_{coil} is 0.57 A.

Figure 8.8 shows that there is slight leaking during the closing stage of the valve operation, as indicated by a minor fluctuation in the pressure drop (dP) across the microvalve, label no. 1*. This fluctuation does not happen during the next closing operation. A slight sticking problem is experienced by the microvalve during its opening stage as indicated by a slight delay (< 5s) in the pressure drop (dP) when the power (P_{coil}) is turned off, label no 2*. The tested sample was removed from the package and did not shown any corrosion problem at all; thus the parylene-C has provided very good protection to the metal structure of the microvalve. The experimental results in Figure 8.8 have demonstrated a promising performance by the on/off microvalve and have highlighted the great advantages of thin layer parylene-C.

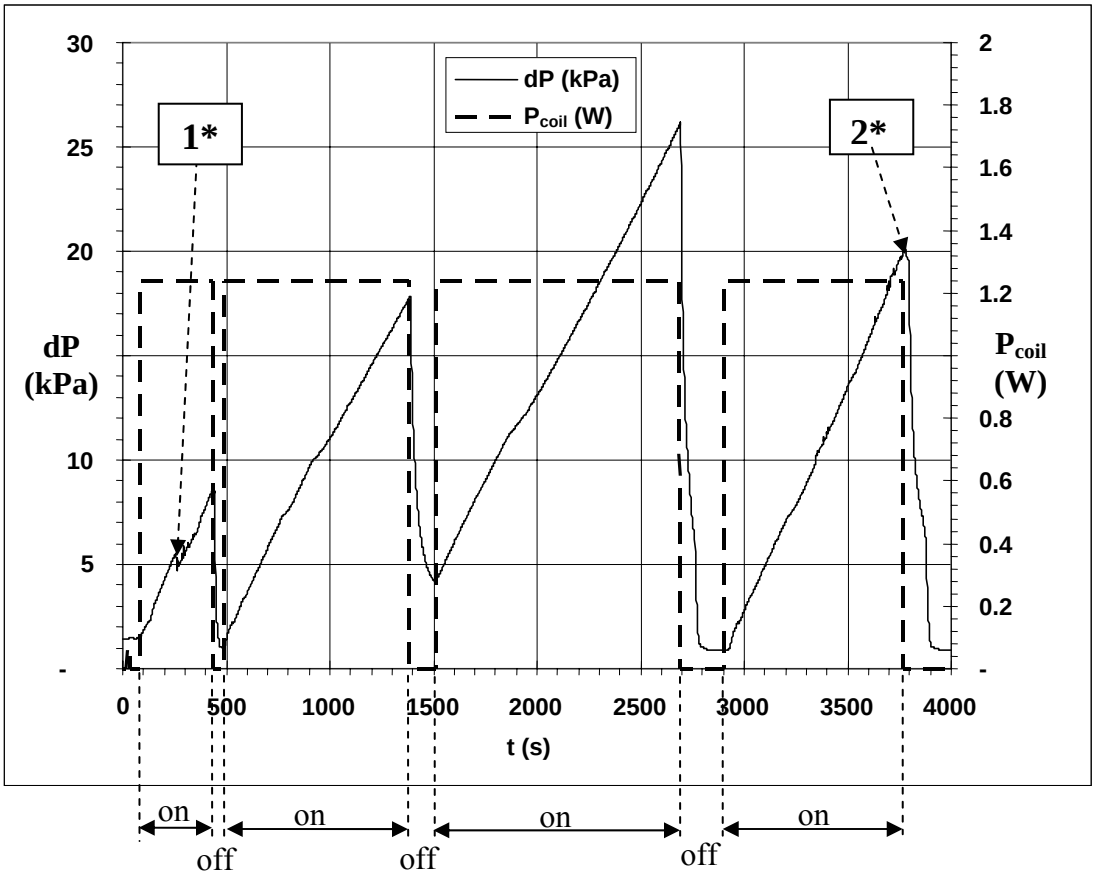

Figure 8.8. The pressure head (dP) across the microvalve with the applied input power to the microcoil (P_{coil}). It shows the on/off performance of the microvalve with 1 μm parylene coating at the free flow rate ($\dot{V}_{free}$) of 1 μL/min of 50% diluted methanol. The microvalve has a corrugated membrane with 2 (two) torsional supported legs, D_b = 60 μm and R_{coil} = 3.74 Ω.

Testing results on another on/off microvalve with 1.5 μm parylene coating and with lower power consumptions are shown in Figure 8.9. The power required for this microvalve is 0.55 W. The resistance of the microcoil (R_{coil}) = 4.24 Ω with the operating I_{coil} = 0.36 A. The testing results as shown in Figure 8.9 do not indicate any leaking or sticking problems. The microvalve has successfully performed the on/off mechanism at the closing pressure (dP_{close}) of 5.8 kPa. The burst pressure (dP_{burst}) of the microvalve for

this particular design is 10 kPa, which corresponds to the closing force of approximately 314 μN, as the radius of the gasket (r_G) is 100 μm.

Figure 8.9 shows that the microvalve can also be operated at half of its designed power, which is 0.3 W with I_{coil} = 0.27 A. It shows that it requires more time to close the microvalve and achieve the same (dP_{close}). The time is approximately 490 s to achieve 5.8 kPa pressure, compared with 370 s when P_{coil} is 0.55 W.

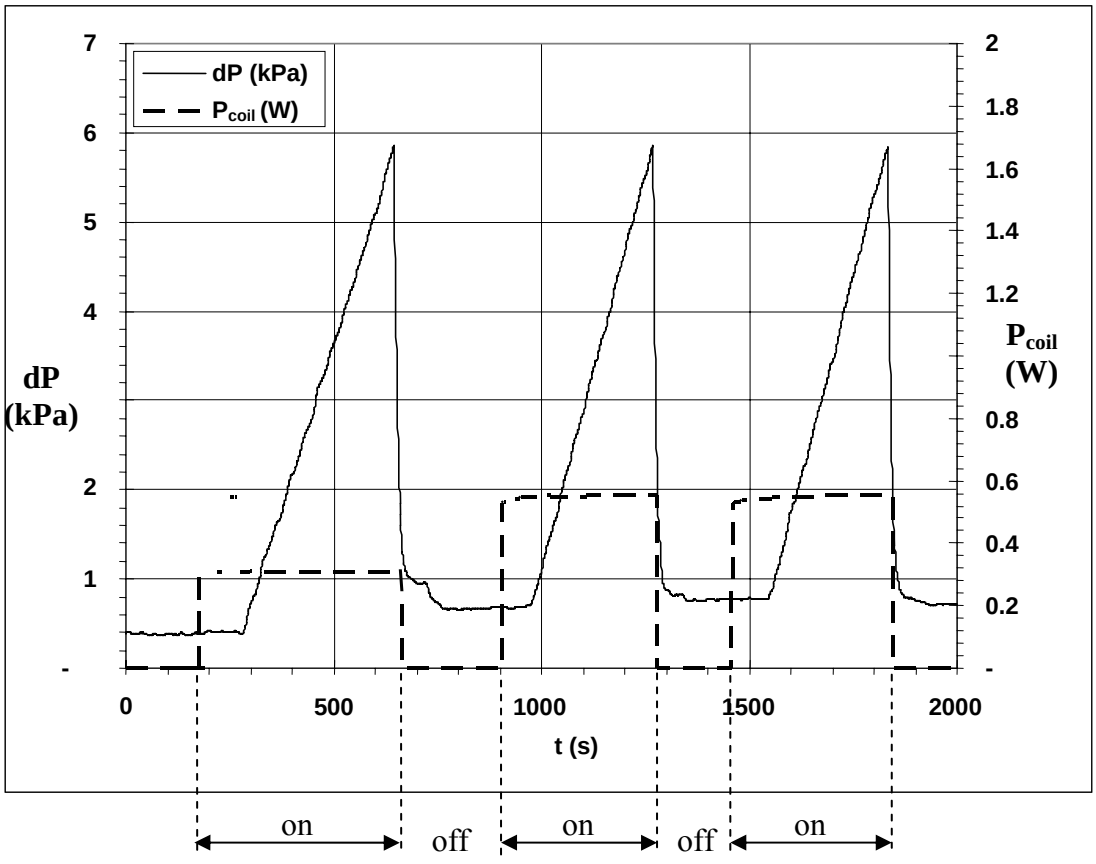

Figure 8.9. The pressure head (dP) across the microvalve with the applied input power to the microcoil (P_{coil}). It shows the on/off performance of the microvalve with 1.5 μm parylene coating at the free flow rate ($\dot{V}_{free}$) of 1 μL/min of 50% diluted methanol. The microvalve has a corrugated membrane with 4 (four) bending supported legs, D_b = 60 μm and R_{coil} = 4.24 Ω.

8.4.2.3 Leaking Rate of the On/Off Microvalve

The leaking rates of the microvalve with parylene-C coating at different closing pressures (dP_{close}) are shown in Figure 8.10. It shows the results from two different designs: the microvalve with 4 (four) bending supported legs and the microvalve with 2 (two) x 90° torsional supported legs. The liquid testing performances of these on/off microvalves are shown Figures 8.8 and 8.9 respectively.

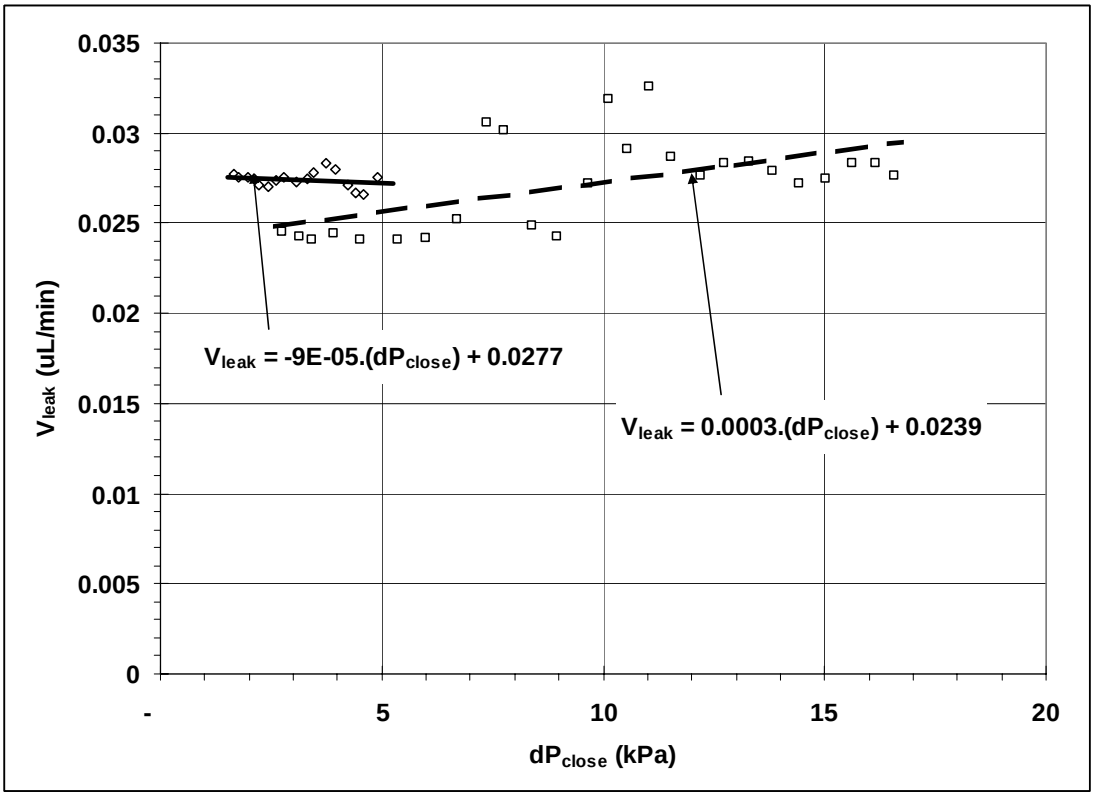

Figure 8.10. The leaking rate of the on/off microvalve with parylene coating, shows the testing results from two different designs, 4 (four) torsional supported legs (solid line) and 2 (two) x 90° torsional supported legs. The tested free flow ($\dot{V}_{free}$) is 1 μL/min.

Figure 8.10 shows that for 2 (two) x 90° torsional legs design, the trend of $\dot{V}_{leak}$ is increasing with dP_{close}. Meanwhile, for the design of 4 (four) bending supported legs, the trend of $\dot{V}_{leak}$ is mostly constant with dP_{close}. If both results are combined, Figure 8.10 shows that $\dot{V}_{leak}$ of these two microvalves are in the range of 0.024 - 0.033 μL/min over dP_{close} of 1.5 - 17 kPa. These correspond to $\Delta(\dot{V}_{leak}) / \Delta(dP_{close}) \approx 0.00581$ μL/kPa, i.e. $\dot{V}_{leak}$ is pretty much independent of dP_{close}. Since the microvalves were tested at the free flow rate ($\dot{V}_{free}$) of 1 μL/min of 50% diluted methanol, the leaking rate is approximately 2.4 to 3.3 %.

8.5 Results for Bistable Microvalve

8.5.1 Free Flow Results

The combined theoretical and experimental results for the pressure drop (dP_{free}) across the microvalve under the free flow rate ($\dot{V}_{free}$) of DI water are shown in Figure 8.11. The accuracy of the experimental results is estimated to be 15 %. The details of the tested microvalve geometry are tabulated in Table 5.9 and the SEM pictures as shown in Figures 5.19 and 5.20.

Figure 8.11 shows that the theoretical results have slightly under estimated the actual/experimental dP_{free}. This rate is mostly because the theoretical equations are for laminar flow and fully developed, which is not always the case, particularly for small

channels. The equation that is used to predict the dP_{space} may not be relevant to the geometry of the microvalve. Because the membrane is circular with a limited geometry, it is too conservative to treat the flow as between two fixed parallel plates with unlimited width. However, in general the experimental results are in reasonably close agreement with theoretical predictions. The experimental dP_{free} can be estimated by Equation as shown in Figure 8.11.

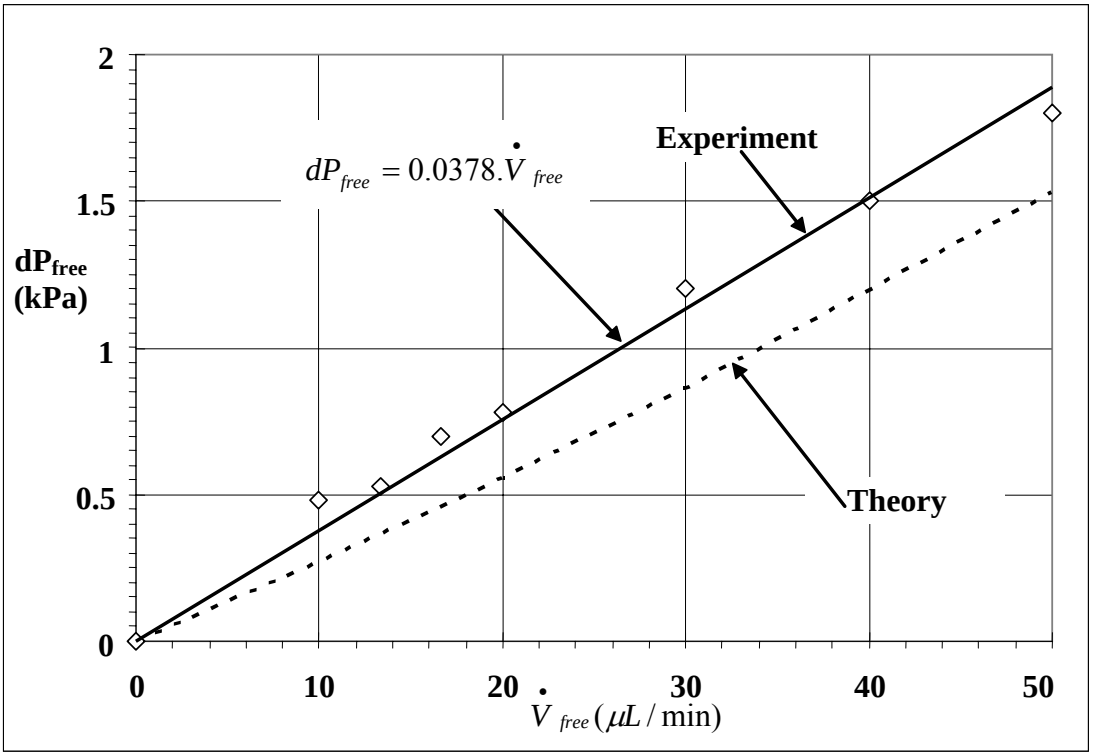

Figure 8.11. The pressure drop (dP_{free}) across the bistable microvalve at different free flow rates ($\dot{V}_{free}$) of DI water.

8.5.2 Latching and Unlatching Characteristic of the Bistable Microvalve

The test on the latching and unlatching of the bistable microvalve is performed at different free volume flow rates ($\dot{V}_{free}$) of DI water; these are 10, 16.6, 20, 30, 50 μL/min. The results for $\dot{V}_{free}$ = 20 and 30 μL/min are shown in Figures 8.12 and 8.13 respectively. In order to latch the microvalve, a positive current is applied to the micro coil. This current produces a magnetic field in the same direction as the permanent magnet alignment. The membrane then moves downward and latched. Figure 8.13 shows that the magnitude of the current required to latch the microvalve is $I_{coil} \approx 0.41$ A. This current is larger than for latching in the air medium, where the required $I_{coil} \approx 0.1$ A as shown in Figure 7.35. The latching/unlatching mechanism of this bistable microvalve actuated in the medium of air is described in Chapter 7, section 7.6.2.

The minimum pulsed time for the current (I_{coil}) to latch the valve in the flow of water is t_b = 10 ms. This result is in agreement with the bistable microvalve actuator testing in the medium of water as shown in Figure 7.58 and 7.59, which require t_b = 10 ms for latching/unlatching. The testing in the medium of air for a microvalve actuator indicates that the microvalve can be latched at the pulse of t_b = 2.5 ms for the static latching, and as low as t_b = 0.2 ms for dynamic latching. (Please refer to section 7.6.3.2 for the discussion about static/dynamic latching mechanisms.). Thus it requires more time (t_b) to latch the microvalve in the medium of water than in air. There are three possible reasons for the length of time required to latch the microvalve in the medium of water:

1. Some amount of time is required to move the membrane from the open (1st stable) to the closed (2nd stable) position. Since the medium is water with large viscosity

compared to air, it also has a large squeeze film damping effect. Thus the membrane moves at a much slower velocity than in air under the same electromagnetic force (F_{EM}).

2. Some amount of time is required to align the magnetic field produced by the permanent magnet with the magnetic domain of the soft magnetic base. As mentioned before, the latching force is regenerated by the remanence field (B_R) of the permanent magnet plated on the membrane.
3. Some amount of fluid may remain underneath the membrane as the membrane moves closer to the microcoil. This fluid has substantial surface tension that prevents further displacement of the membrane. Thus it requires an additional amount of time to push the remaining fluid (water) aside and latch the microvalve.

The resistance of the microcoil (R_{coil}) is $7.3\,\Omega$. This corresponds to the minimum input power of 1.23 W as shown in Figure 8.13and the minimum input energy of 12.3 mJ to latch the microvalve. To unlatch the membrane, a reversed pulsed current of $I \approx -0.41$ A with a pulse of $t_b = 10$ ms is required.

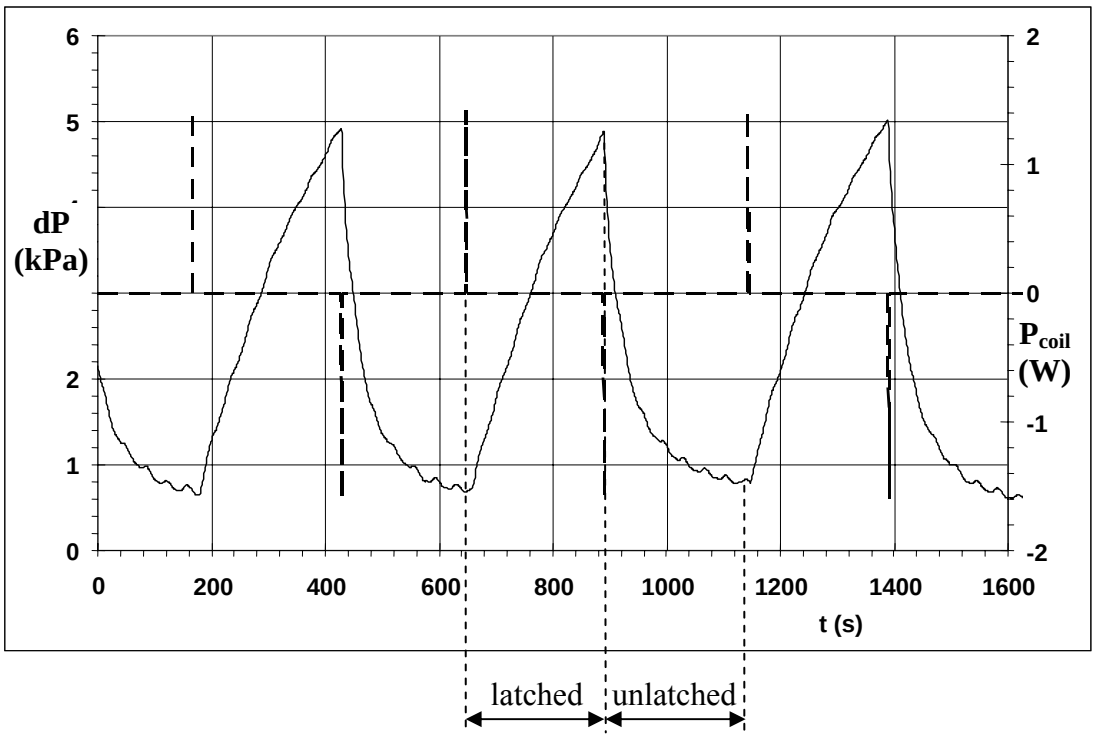

Figure 8.12. Pressure head (dP, solid line) and input power (P_{coil}, dashed line) versus time, showing the latching and unlatching characteristic of the bistable microvalve with the input power of +1.41 W and -1.6 W respectively for t_b = 10 ms. The microvalve was tested with the flow of DI water with $\dot{V}_{free}$ = 20 μL/min.

As shown in Figures 8.12 and 8.13, the latching of the microvalve is indicated by the continuous increase in the pressure head across the valve after the pulse of input power (P_{coil}) is ended. The increase in the pressure head (dP) is because there is still a continuous flow rate of water from the syringe pump while the valve is latched. The dP continues to increase until the microvalve is unlatched by applying a reversed current to the microcoil, or until dP reaches the burst pressure head (dP_{burst}); at this condition, dP is high enough to unlatch the valve without any reverse current input. The valve has dP_{burst} of 7.8 kPa; beyond this pressure the microvalve is always open and cannot

perform bistable operations. This value is 22% lower than the designed dP_{burst} of 10 kPa.[118]. Figures 8.12 and 8.13 show that the slope of dP decreases with the increases in dP. It indicates that there is a leaking in the microvalve and the rate increases with the increase of dP.

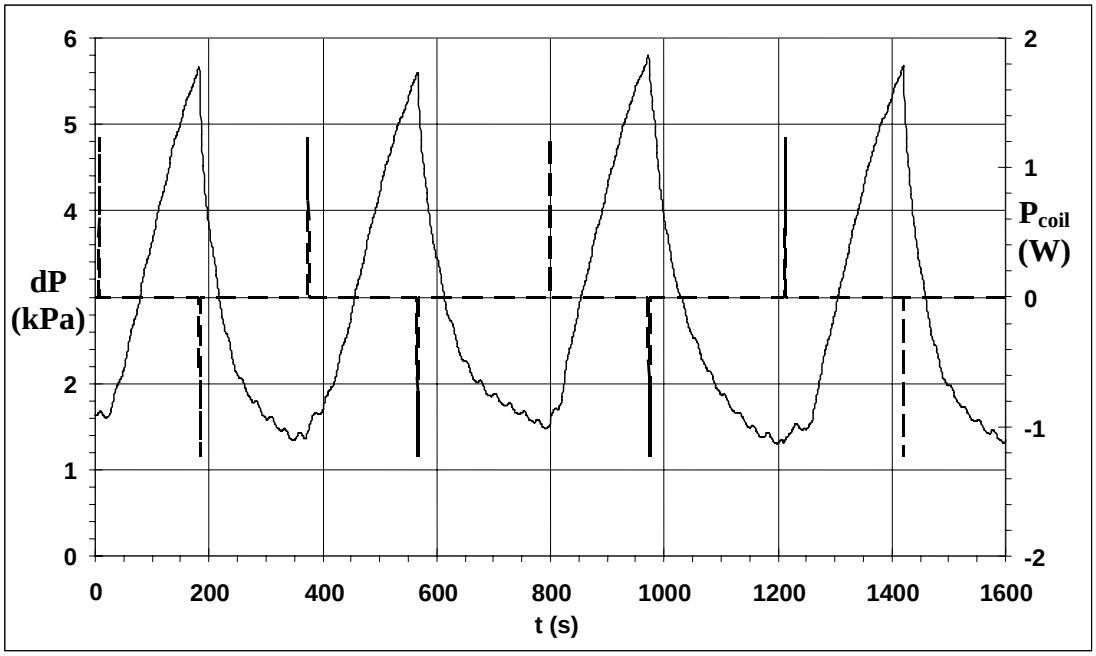

Figure 8.13. Pressure head (dP, solid line) and input power (P_{coil}, dashed line) versus time, showing the latching and unlatching characteristic of the bistable microvalve with the input power of +/- 1.23 W for t_b = 10 ms. The microvalve was tested with the flow of DI water with $\dot{V}_{free}$ = 30 μL/min.

8.5.3 Leaking Rate of the Bistable Microvalve

The leaking rate of the microvalve as a function of the latching pressure head (dP_{latch}) is shown in Figure 8.14 below. It shows that the microvalve leaking increases

linearly with dP_{latch}. This means that there is a small gap between the membrane and the microcoil when these two parts are in contact or latched. This gap occurs because of the poor surface roughness of the microcoil, nonuniform surface texture of the microvalve base, and the air bubble that occurs during the electroplating of the microvalve base.

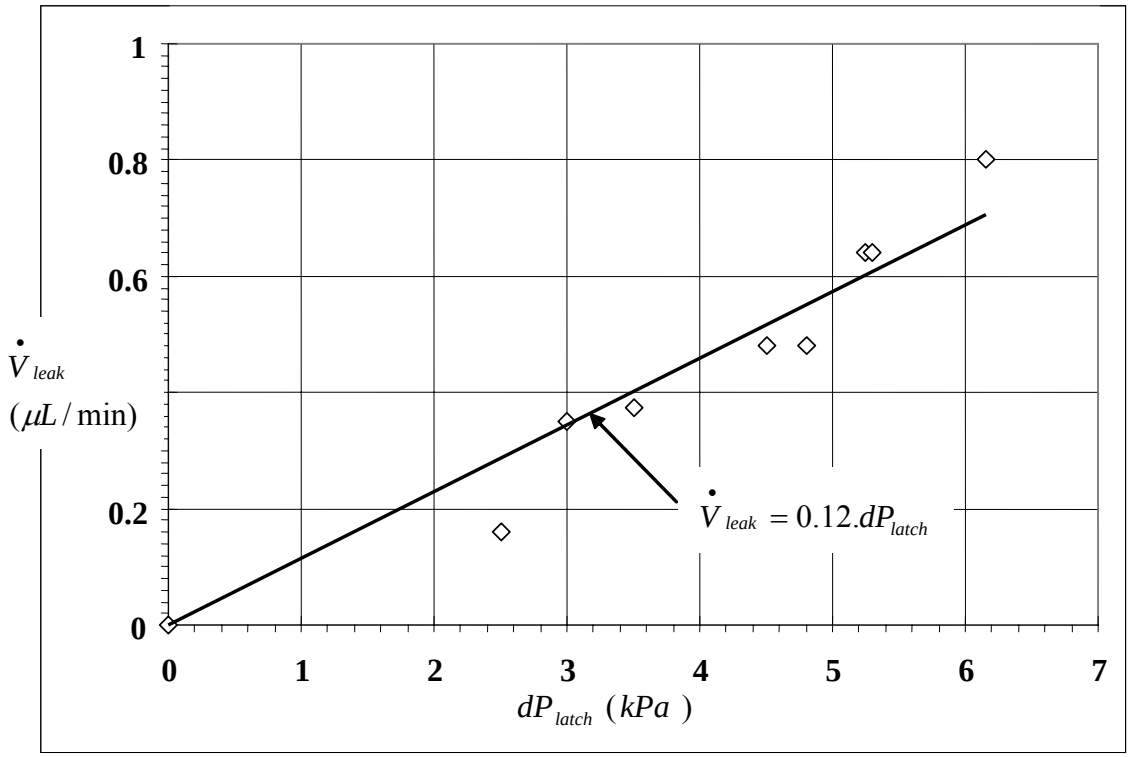

Figure 8.14. Leaking rate ($\dot{V}_{leak}$) of the bistable microvalve as a function of the latching pressure (dP_{latch}) under the flow of DI water

The microvalve leaking can be approximated by the linear equation as shown in Figure 8.14. The equation is important for the application of the microvalve in an actual micro fluidic system. It gives the approximated leakage of the microvalve at given

applied pressure provided by the micro pump, which is equivalent to dP_{latch}. It is shown in the experiment that the leaking of the microvalve ($\dot{V}_{leak}$) is 0.16 – 0.8 μL/min for the latching pressure head (dP_{latch}) of 2.5 – 6.15 kPa. If the microvalve is used to control the flow of water at $\dot{V}_{free}$ = 20 μL/min, the percentage of leaking is found to be 0.8 to 4 %.

8.5.4 Latching, Staying, and Unlatching Characteristics

As mentioned before, the microvalve operates under bistable positions, fully open (1st stable), and latching/closed (2nd stable) positions. In these two positions no electric current (I_{coil}) is required. Figure 8.15 simulates the conditions when the microvalve is initially fully open (1st stable) and the pump is on and delivering water at $\dot{V}_{free}$ of 16.6 μL/min, label no. 1. An impulse of current, t_b = 10 ms, is applied to the micro coil and the microvalve is then closed and latched (2nd stable), label no 2. Once the pressure head increases to 5.2 kPa, the flow rate of the syringe pump is switched to the corresponding leaking rate as in Figure 8.14, which is 0.6 μL/min. As shown in Figure 8.15, the pressure head (dP) remains unchanged (label no 3).This simulates the case when the micropump attached on the microvalve reaches its maximum pressure head. After a certain delay/staying time, the syringe pump is switched back to its original $\dot{V}_{free}$ of 16.6 μL/min; the pressure then increases again, label no 4. The valve is then unlatched, label no 5. The cycles were repeated and show similar responses as shown in Figure 8.15.

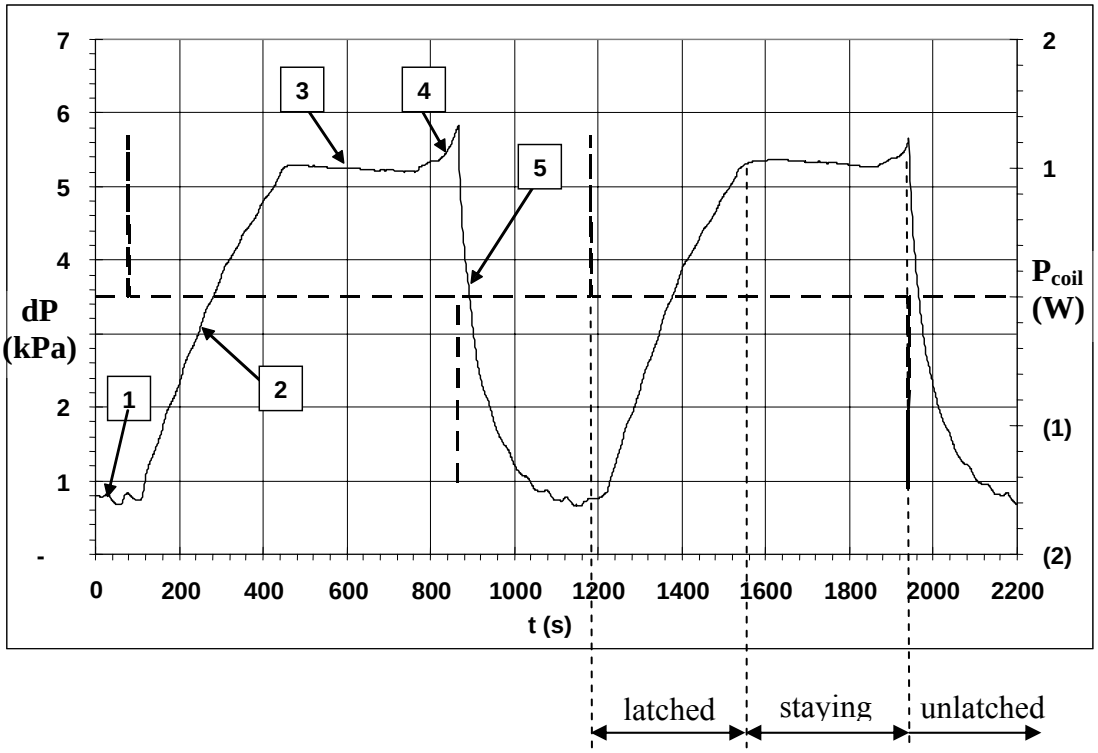

Figure 8.15. Pressure head (solid line) and input power (dashed line) versus time, showing the latching, staying, and unlatching characteristic of the microvalve

CHAPTER 9

CONCLUSIONS AND FUTURE WORKS

9.1 Introduction

This chapter summarizes the contributions that have been made in this research. The innovations in the development of fabrication processes capable of producing a microvalve integrated on a single wafer are discussed. Several devices that have been developed are described, including: an on/off microvalve, a bistable microvalve, bidirectional microactuator, and bistable-bidirectional microactuator. At the end of this chapter recommendations for future work are also discussed.

9.2 Contributions and Conclusions

9.2.1 Fabrication Process

There were two different electromagnetic actuated microvalves developed in this research: an on/off microvalve, and a bistable microvalve with latching mechanism. The overall size is less than 2,000 μm in diameter. The microvalves consists of 6 (six) components: a micro coil, a membrane, a permanent magnet (for bistable microvalve only), an inlet orifice, an outlet orifice, and a valve base. All of these are fabricated and

integrated on a single silicon (Si) wafer by surface micromachining with procedures that are potentially CMOS compatible.

Single wafer fabrication was the biggest challenge to the microvalve fabrication. Prior work on microvalves, whether they were electromagnetically, electrostatically, or piezoelectrically driven, involved the use of two or more silicon wafers during their fabrication. The words "surface micromachining" in this context means that there are no external parts incorporated into the foundry process to define the microvalve structure. Obviously, this was a very difficult challenge that this research had to face. The fabrication of the microvalve would be much easier if an external electromagnetic coil and an external permanent magnet were incorporated into the microvalve mechanism. However, incorporating external parts would introduce problems into other processes, such as the transfer, assembly, alignment, and integration of these parts into the bath fabricated microstructure.

Judy and Myung [109] mention that in order for MEMS devices to be integrated with electric circuits such as complementary metal-oxide-semiconductor (CMOS) based devices, the fabrication process for the MEMS device has to be adapted to the limitation of the electrical components or be CMOS-compatible. One of the critical parameters is the temperature limitation; the metallization part of the circuits start to deteriorate at a temperature of 400 °C. Thus the maximum fabrication temperature of the microvalve has to be less than this temperature.

In order to meet all the fabrication parameters, the complex structure of the microvalve, which includes an actuator with a released membrane, requires a multi-layer fabrication process. This means that each layer has to be fabricated on top of another

layer. In each layer, the photoresist was patterned and then the subsequent layer of photoresist was built on top of it. During the fabrication process, the photoresist layers were not removed until the end of the procedure. Thus, the wafer could only be cleaned by D.I. water, and there was no solvent or methanol rinse used to clean the wafer.

The microvalve structures were entirely built by thick metal deposition, electroplating at or close to room temperature. There were five different metal layers electroplated by pulse currents, specifically: orthonol to build the microvalve base, permalloy to build the soft magnetic membrane, gold (Au) to build the microcoil, and CoPt or CoNiMnP to build the permanent magnet on the centered membrane.

An insulation layer, SiO_2 was deposited on top of the microvalve base and the microcoil, by PECVD at the thickness of approximately 0.8 μm, with the deposition temperature of 250 – 300 °C. For the contact windows, the SiO_2 layer was etched by RIE. The Ti/Cu seed layers were deposited by DC sputter. In order to drill hole through the wafer, deep reactive ion etching (RIE), also called inductive coupled plasma (ICP), was used. The etching process called Bosch process had been very effective in etching the silicon and produced high anisotropy with a good quality of side wall.

There were several difficulties faced in the deposition of thick film Co-Pt permanent magnet, especially when thickness was greater than 5 μm. The two major difficulties were: bubble production and surface cracking. The gas bubbles produced a rough/non-uniform plating surface, bubbling, and cracking of the photoresist. In order to minimize the bubble production, the wafer was taken out from the electrolyte bath every 10 minutes to remove the bubbles into the air. Co-Pt deposition produced a tension stress, with the value depending on the Co composition. In order to reduce the stress from Co-Pt

deposition, 2 gr/L of saccharin was added to the electrolyte, and the electrolyte temperature was increased from room temperature to 40 – 50 °C.

The electroplating process for the CoNiMnP was a little different from that of the CoPt. In order to improve the vertical anisotropy of the permanent magnet, CoNiMnP was plated inside a constant magnetic field. The electroplating bath was located in between of ceramic magnets (Ferrimag 8A, Adams Magnetic Products, 3900 G). The produced constant magnetic field in between the ceramic magnets was measured by magnetometer and it was about 800 G. The multi layer fabrication processes have been successfully developed for two types of microvalves: the on/off microvalve and the bistable microvalve with latching mechanism. Both microvalves were entirely built on top of a single Si wafer.

9.2.2 On/Off Microvalve

The performances of the on/off microvalve were tested to open and close the flow of 50% diluted methanol with the free flow rate ($\dot{V}_{free}$) of 1 μL/min. The tests were carried out under two conditions, with and without parylene coating. The microvalve was closed or opened by turning on/off the input power (P_{coil}). The operational P_{coil} was in the range of 0.5 to 1.2 W and I_{coil} was in the range of 0.25 to 0.6 A, depending on the design. When the microvalve was closed, the membrane touched the bottom microcoil; the flow of liquid was then hindered. A continuous P_{coil} was required to keep the valve close.

Without parylene coating, the on/off microvalve experienced two serious problems, leaking and sticking. The leaking of the microvalve was caused by the air

bubbles generated on the microcoil surface as a continuous I_{coil} was applied; these air bubbles had enough force to slightly open the membrane. When the microvalve experienced the sticking problem, the membrane did not immediately come back to its open position once P_{coil} was turned off. Since the microcoil was made of gold (Au), a relatively soft metal, and the membrane was made of NiFe, with a continuous applied current (I_{coil}) after sufficient time, these two in contact surfaces might temporarily weld together. The membrane stuck on the microcoil when I_{coil} was off. Sticking problems are definitely undesirable in the microvalve operation. The tested on/off microvalve was removed from the package, indicating that the structure had experienced enormous corrosions. This was expected to occur when the valve was in direct contact with the liquid during the tests.

A thin film of parylene-C was deposited on the finished microvalve structures by evaporation at room temperature. Typical thickness of the deposited parylene-C were 1 – 2 μm. A tremendous improvement in the opening and closing operations of the microvalve was observed. There was no leaking or sticking that occurring during the operation. Therefore, the parylene-C had created a coating that prevented the electrolysis at the microcoil surface and associated corrosion reactions. Parylene-C had also acted as a gasket between the membrane and the microcoil, as indicated by the fact that the microvalve was able to close at much higher pressure, 26.5 kPa, than without parylene coating, only 5 kPa.

The leaking rate ($\dot{V}_{leak}$) of the on/off microvalve with parylene-C coating were mostly independent of the closing pressure (dP_{close}). The leaking rates were in the range of 0.024 - 0.033 μL/min over a dP_{close} range of 1.5 - 17 kPa. Since the microvalves were

tested at a controlled free flow rate ($\dot{V}_{free}$) of 1 μL/min for the 50% diluted methanol solution, the leaking rate observed was in the range of 2.4 to 3.3 % of the nominal flow rate.

9.2.3 Bistable Microvalve with Latching Mechanism

A bistable electromagnetically actuated microvalve has been designed and tested. The bistable mechanism was achieved by integrating CoNiMnP permanent magnet with a diameter of 500 μm and a thickness of 40 μm to the soft magnetic membrane. Proper design of the membrane spring force (F_S), electromagnetic force (F_{EM}), and the remanence force of the permanent magnet (F_R) were required in order to achieve the bistable mechanism.

The fluidic testing of the bistable microvalve was carried out with a flow of DI water. For the microvalve with a diameter (D_b) of 60 μm, when fully open, the pressure head (dP_{free}) increased linearly from 0 to 1.7 kPa for the free flow rate ($\dot{V}_{free}$) range of up to 50 μL/min. The latching and unlatching characteristic of the microvalve were performed at various $\dot{V}_{free}$, in the range of 10 – 50 μL/min.

A particular design of bistable microvalve with 2 plain supported legs required an input power (P_{coil}) of 1.23 W to latch/unlatch the microvalve at the burst time (t_b) of 10 ms. Thus, the microvalve consumed an energy of 12.3 mJ to latch/unlatch. The leaking rate of the microvalve increased linearly with a latching pressure (dP_{latch}), which indicated that there was a small gap between the membrane and the microcoil when these

two parts were in contact or latched. This gap occurred because of the poor surface roughness of the microcoil. The leaking rate ($\dot{V}_{leak}$) ranged from 0 to 0.8 μL/min for the latching pressure (dP_{latch}), in the range of 0 to 6.1 kPa. The burst pressure of microvalve (dP_{burst}) was 7.8 kPa, which was about 22% lower than the designed value, 10 kPa.

9.2.4 Bidirectional Microactuator

An electromagnetic bidirectional microactuator with a micro coil and a Co-Pt permanent magnet membrane have been developed. There are two different designs: double-legs and single-leg design.

For the double-legs design, the experimental results in the medium of air showed that a minimum membrane displacement (d_m) of, -71 μm was achieved at I_{coil} =-0.25A, and a maximum d_m of 28.3 μm was achieve at I_{coil} = +0.25 A. For the single-leg design, the minimum d_m = -105 μm was achieved at I_{coil} = -0.1A and the maximum d_m of 150 μm at I_{coil} = +0.31 A. The overall size of the microactuator was 1,600 μm. Thus, the microactuator had shown large displacement for its small size, which would make it useful for optical, fluidic, and sensors applications, micro/nano printing, and micro/nano indenter.

The dynamic characteristics of the bidirectional microactuators were also investigated. The membrane displacements (d_m) were monitored instantaneously by Laser Doppler Vibrometer. Pulses of current at a certain burst time (t_b) were passed through the microcoil. It was found that the optimum membrane displacement with the lowest energy (E_{coil}) consumption occured when $t_b \approx 1/(2.f_n)$, where f_n was the natural frequency of the

membrane structure. When $t_b > 1/(2.f_n)$, d_m depended only on I_{coil}. When $t_b < 1/(2.f_n)$, d_m depended on both I_{coil} and t_b.

For the valve actuator, it was found that d_m increased with E_{coil}. It was also found that the same amount of E_{coil} did not necessarily produce the same d_m when t_b was altered: when $t_b>1/(2.f_n)$, the increase of t_b caused the decreased in d_m, and when $t_b<1/(2.f_n)$, the increase of t_b caused the increase in d_m. This result was very surprising because the increase in t_b caused the decrease in I_{coil} when E_{coil} was kept constant, which eventually decreased the applied electromagnetic force (F_{EM}). The physical reason for this behavior was not well understood, but this physically showed the dynamic limitation of the actuator to provide the reaction force against the applied F_{EM}. The upward and downward d_m were the reaction of the membrane against the applied F_{EM}. From a thermodynamics point of view, the membrane had a rapid acceleration (A_m) that caused the irreversibility of the applied F_{EM}. Some of the applied energy might be lost to the environment in the form of sound waves or transferred to the fluid motion.

The optimal burst time (t_b) for the double-legs design was 1.67 ms, with a maximum displacement (d_{max}) of 28.3 μm and minimum displacement (d_{min}) of -71 μm. The lowest I_{coil} to achieve d_{max} was 0.25 A and the highest I_{coil} to achieve d_{min} was -0.25 A.

The optimal burst time (t_b) for the single-leg design was 5 ms with the upward d_m of 148 μm at I_{coil} = 0.32 A. The minimum displacement (d_{min}) was found to be -108 μm and the highest I_{coil} to achieve d_{min} was -0.1 A.

9.2.5 Bistable and Bidirectional Microactuator with Latching Mechanism

One of the inventions resulting from this research was the development of bistable and bidirectional microactuators with latching mechanism. Even though the actuator was utilized for the microvalve application, it could also be utilized for other purposes, such as: an optical switch, RF relay, or micro mirror.

In order to perform bistable and bidirectional movements, the microactuator was implemented with a CoNiMnP permanent magnet on the soft magnetic membrane. The testing of a particular actuator with a plain single-leg design in air showed that the latching mechanism was achieved at the membrane minimum displacement (d_{min}) of -20.5 μm. An operational current (I_{coil}) and power (P_{coil}) as low as 13.9 mA and 1.39 mW respectively were required to perform the latching mechanism. The membrane maximum displacement (d_{max}) was found to be 29 μm, which was achieved at I_{coil} = 0.13 A and P_{coil} = 130 mW.

Intensive experiments were carried out to find the pulse time (t_b) required for the membrane to latch. There were two different latching times observed from the experiments: static latching time (t_{latch_st}) and dynamic latching time (t_{latch_dy}). The t_{latch_st} of the bistable and bidirectional microactuator was found to be at least 2.5 ms. When t_b was 2.5 ms, there was enough time for the membrane to sit on the bottom coil to align the permanent magnet and achieve latching. The time was enough for the force produced by the permanent magnet to recover the repelling momentum experienced by the membrane as it touched the bottom coil. This repelling momentum tended to bounce the membrane upward and might unlatch the membrane if there was not sufficient force and time.

One idea for solving this problem is to provide just a sufficient amount of energy to bring the membrane close to the bottom coil. The remanence force (F_R) produced by the permanent magnet could then pull the membrane farther, bringing it into contact with the bottom coil, and, finally, latched. In order to obtain this optimum energy, experiments were carried out by setting I_{coil} at a certain value and varying the values of t_b. It was found that for a particular I_{coil}, there was a new t_b that was smaller than the t_{latch_st}, 2.5 ms, at which the membrane is latched. This t_b is called dynamic latching time (t_{latch_dy}). This results showed that when I_{coil} = 0.024 A, it required t_{latch_dy} = 1.1 ms for latching; this corresponded to E_{coil} = 5.2 μJ compared to 11 μJ for static latching. Meanwhile for I_{coil} = 0.13 A, the required t_{latch_dy} was only 0.2 ms for latching; this corresponded to E_{coil} = 25 μJ compared to more than 1 mJ for static latching. Thus dynamic latching mechanism had produced a tremendous reduction in the energy consumption of the microactuator.

Some tests were also carried out to investigate the latching mechanism of the microactuator in water. The minimum required time (t_b) was 10 ms to perform latching in water, which was much larger than in air. This was because the membrane moved at much slower velocity in water due to the large squeeze film damping effect. Some amount of fluid might remain underneath the membrane as it moved closer to the microcoil; this had substantial surface tension that resisted the membrane displacement. During the tests, we did not observe the dynamic latching behavior in water.

9.3 Recommendations for Future Works

These are a list of several issues for further study that could provide a potential thesis topic for the development in the future MS and PhD dissertation work:

9.3.1 Power Reduction

Currently the microvalve developed in this research consumed the operational power, in the range of 0.5 – 1.5 W, for controlling the flow rate of D.I. (deionized) water or 50% diluted methanol, in the range of 1 – 50 μL/min. It is recommended for future efforts to reduce this power consumption to mW level, first by choosing a better selection of soft magnetic material that builds the microvalve structure, and second by designing a more efficient microcoil. The details of these ideas are discussed in the following topics:

9.3.1.1 Better Soft Magnetic Material

The current design of microvalve uses permalloy or orthonol to build its structure; these soft magnetic materials have the magnetic saturation (B_S) in the order of 0.9 T and 1.4 T respectively. In the operation, the microvalve has reached the saturation in the membrane supported legs. If one can introduce a soft magnetic material with much higher B_S, in the level of 2 T, the saturation will be prevented in these supported legs. An electroplated CoFeCu film reported in [87] has shown the B_S in the order of 1.8 – 2 T with the coercivity of about 4 Oe. This results in the reduction of power consumption because lesser reluctance ($\Re$) in the magnetic circuits of the microvalve.

For a larger value of B_S, the thickness of supported legs can be reduced from 3 - 4 μm of the current design to 1 - 2 μm for the future design. These will reduce the stiffness

of the supported legs for the same size of microvalve, thus requiring lesser operational current (I_{coil}) to displace the centered membrane between the opening/closing states of the microvalve.

9.3.1.2 More Efficient Microcoil

An ideal design of microcoil should have a material that has a good electrical conductivity, like gold or copper, and good magnetic properties, like Ni, Fe, or NiFe, and can be easily fabricated by electroplating with a smooth surface. The microcoil produced will have a low resistance and a low magnetic reluctance, which leads to the reduction in the power consumption of the microvalve. Obviously it will be a greater challenge to produce such an ideal material.

Another idea is to replace the current 10μm thickness Au microcoil design with NiFe (permalloy) at twice the thickness. The major drawback of this idea is the surface condition of the electroplated permalloy, which is non-uniform over the entire wafer area. The plated thickness decreases with the distance from the edge of the wafer; the thinnest dimensions are experienced in the wafer center. This will produce nonuniformity for the subsequent layers of photoresists. In order to mitigate this problem, one can plate 30 μm thickness of permalloy in the microcoil mould (based on the dimension on the center of the wafer), and then polish the entire wafer surface by 10 μm reduction (based on the centered dimensions). Finally, the process produces a 20 μm thickness of permalloy microcoil for the entire wafer surface with much better surface roughness, depending on the accuracy of the polishing machine.

The recommended photoresist used for the patterning of the microcoil is a negative photoresist, such as Futurrex or SU8, which has straight side walls for high aspect ratio mould.

9.3.2 Better Sealing/Gasket for Bistable Microvalve

The current design of bistable microvalve experiences a leaking that increases with the latching pressure; this indicates that there is a small gap between the membrane and the microcoil when these two parts are in contact or latched. This gap occurs because of the poor surface roughness of the microcoil. In order to compensate for the surface roughness problem, one can introduce a soft material, such as silicone on the bottom surface of the centered membrane, which will act as a gasket to provide better sealing when it is in contact with the microcoil. The obvious next question is: what should be the best fabrication method be to deposit silicone on the centered membrane?

One idea is to evaporate the silicone on the entire surface of the wafer once the sacrificial layer is defined, and then pattern another photoresist layer to etch the unnecessary silicone and hence define the silicone gasket. This idea seems to be feasible; however it introduces a lot of complexity to the existing fabrication process for the microvalve. Another idea is to vapor deposit the silicones on the entire surface of the finished fabricated microvalve. This idea is similar to the parylene-C that has been applied in this research; but the silicone's properties make it a much better sealant for the microvalve.

9.3.3 Improvements in the Permanent Magnet

The current selections of permanent magnet material in this research are CoPt and CoNiMnP. Both of these materials have excellent magnetic properties as shown in Tables 3.3 and 3.4. However, we experienced tremendous problems in surface cracking and bubbling during CoPt magnet electroplating, and very bad surface roughness during CoNiMnP electroplating. In the future, a material that has better surface roughness would increase the yield and performance of the microvalve. Some material is required that does not have the same problems as experienced in the CoPt and CoNiMnP electroplating, yet still produces good magnetic properties for thick films.

Another avenue for future exploration is improvement of the magnetic anisotropy by introducing an external magnetic field during the electroplating of the permanent magnet. This technique has been applied for CoNiMnP in this dissertation; however the introduced magnetic field is rather small, only 0.08 T, which is less than the remanence of reported CoNiMnP, $B_R = M_R = 0.17 – 0.19$ T. One recommendation is to introduce an external magnetic field 3 to 5 times larger than B_R, i.e. about 0.6 to 1 T, and study the improvement in the magnetic anisotropy. The external field can be introduced by using a permanent magnet that has high $B_R > 1$ T, such as Neodymium magnet that has $B_R = 1 – 1.5$ T and $H_C \approx 10$ kOe. An external field can also be introduced by having an external magnetic coil that produces a continuous magnetic field of more than 2 T.

Another suggestion is to improve the magnetic anisotropy by introducing a thin layer of metal that has (111) a preferred grain orientation, such as Co or a thin layer of Au, before electroplating the actual permanent magnet; this would promote the growth of an hcp structure that has high crystal anisotropy. The combination of this method, at the

same time applying external magnetic during electroplating, is a combinational approach also suggested for the future research work.

9.3.4 Bistable Microvalve with Integrated Switching Mechanism

The latching mechanism of the developed microvalve can also be utilized as a switch mechanism. Thus, the microvalve can serve two functions at the same time; to control the flow rate of liquid, as well as to open or close the electrical connections. This also would be a good topic for future research work.

9.3.5 Dynamic Latching Mechanism for Bistable Microvalve in Liquid Medium

So far in this research, we have observed the dynamic latching behavior of the microvalve actuator in the medium of air. It was found from the experiments that the static latching occurs at t_{latch_st} = 10 ms in water. We have not yet observed the dynamic latching behavior in the liquid mediums such as water or 50% diluted methanol. Theoretically the dynamic latching behavior should also exist in liquid.

After applying improvements to the microcoil design, as suggested in section 9.3.1.2 and improved permanent magnet, as suggested in section 9.3.3, one should explore the possibility of dynamic latching in liquid medium to reduce the required burst time (t_b) from ms to μs levels; this will finally reduce the latching/unlatching energy consumption from mJ to μJ levels.

9.3.6 Integrating the Microvalve for the Micro Fuel Cell Application

The bistable microvalve with latching mechanism has been developed in this research; it has the operational voltage, power, and energy consumptions in the order of 2.5 V, 1 W, and 10 mJ respectively. It only remains to integrate this microvalve into the micro fuel cell application to control the fuel flow rate to the micro channels.

9.3.7 Integrating Arrays of microvalve for Biochemical Applications

The development of microvalves for biomedical applications inspired this PhD work. This lead to development of a micro fluidic controller by combining sets of different microvalves fabricated on top of a single chip. Several different kinds of fluids can be controlled and mixed by utilizing sets of microvalves. There are two different type of microvalves that can be implemented: “on/off” valves, and three-way valves. Each microvalve is able to open and close the fluid flow with a fast response; they are designed for less than 1 ms actuation. The fluidic lines of the system resemble a micro-fluidic mother board, and the device can be implemented for the Lab on chip chemical analysis systems.

9.3.8 Nano Indenter to Measure the Thermo and Mechanical Properties of Different Thin Films

Rapid and large actuation of the electromagnetic bidirectional microactuator, with latching mechanism and bistable positions, as developed in this research, can be utilized

to function as a nano indenter by integrating a nano tip on the center of the membrane. The indentation of the nano tip on the surfaces can be utilized to measure the thermo and mechanical properties and to do writing at nano dimensions.

APPENDIX 1

INTERPOLATION ON THE LEAKING RATE

The procedures as described in section 8.2.2, have given an effective method to measure the leaking of the microvalves ($\dot{V}_{leak}$); with the lowest measured leaking rate of 0.016 μL/min. This method can measure $\dot{V}_{leak}$ in the increment of 0.016 μL/min, with the optimum accuracy of +/- 0.008 μL/min. However, when $\dot{V}_{leak}$ of the microvalve is within this increment, some interpolation is required to determine more accurate $\dot{V}_{leak}$, please refer to Figure A1.1.

Figure A1.1 shows the pressure head across the microvalve (dP) with time, when an experiment is carried out to find out $\dot{V}_{leak}$ of the on/off microvalve at a certain closing pressure (dP_{close}). It turns out that the leaking rate of the microvalve is $0.016 < \dot{V}_{leak} < 0.032$ μL/min. As shown by line 1, dP decreases with time (t) when $\dot{V}$ of the syringe pump is set to 0.016 μL/min. On the other hand, dP increases with time (t) when $\dot{V}$ =0.032 μL/min. In order to determine actual $\dot{V}_{leak}$ of the microvalve, which is indicated by imaginary line 3, the slopes of lines 1 and 2 have to be determined. The time duration (Δt) is set to be 30 minutes, long enough to determine an accurate values of m_1 and m_2. The leaking rate of the microvalve is then determined by Equation A1.1:

$$\dot{V}_{leak} = a + \frac{m_1}{m_1 + m_2} .(b - a) \qquad \text{(A1.1)}$$

Where a = 0.016 μL/min and b = 0.032 μL/min in this case

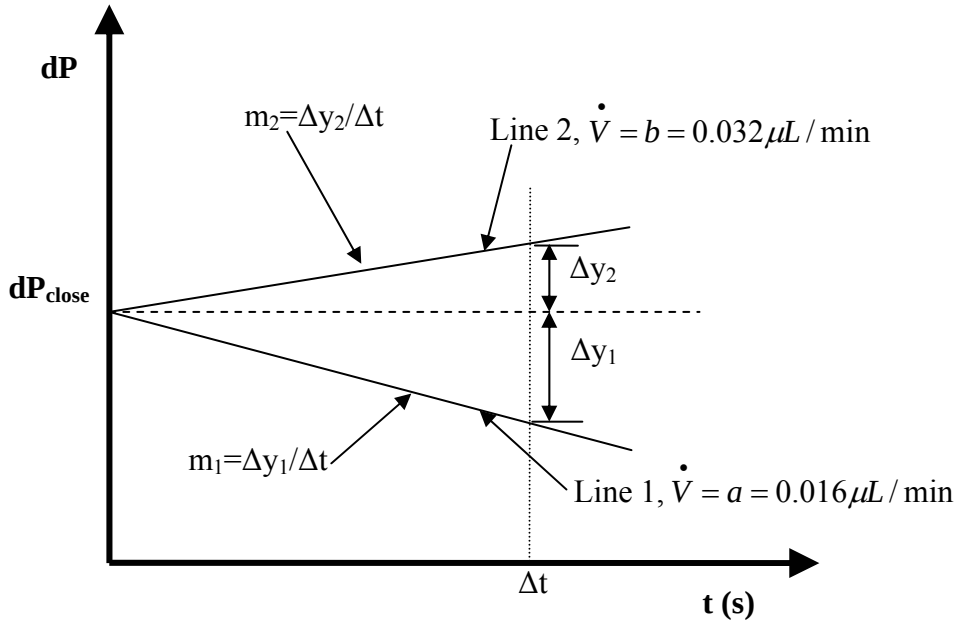

Figure A1.1. The pressure drop (dP) across the microvalve with time (t), showing the attempt to measure the leaking rate ($\dot{V}_{leak}$) of the microvalve at a certain closing pressure (dP_{close}), where $0.016 < \dot{V}_{leak} < 0.032$ μL/min.

REFERENCES

[1] S. Shoji and M. Esashi, "Microflow devices and systems," *J. Micromech. Microeng.* ,vol. 4, pp. 157-171, **1994**

[2] M. Esashi, "Silicon micromachining for integrated microsystems," *Vacuum,* vol. 47, 469-474, **1996**

[3] S. Shoji, "Fluids for Sensor Systems," in *Microsystem Technology in Chemistry and Life Sciences,* Springer Verlag, Berlin, **1999**, (Eds: A. Manz, H. Becker) pp. 163-188.

[4] P.K. Yuen, L.J. Krika, P. Wilding, "Semi-disposable microvalves for use with microfabricated devices or microchips," *J. Micromech. Microeng*. vol. 10, pp. 401-409, **2000**

[5] N.-T. Nguyen and S. Wereley, *Fundamentals and Application of Microfluidics,* Artech House, London, **2002**.

[6] M. Madou, *Micromachining*, CRC Press, **2002.**

[7] M. Elwenspeok, and H. V. Jansen, *Silicon Micromachining,* Cambridge University Press, **1999**.

[8] G. C. Frye-Mason, R. P. Manginell, E. J. Heller, C. M. Matzke, S. A. Casalnuovo, V. M. Heitala, R. J. Kottenstette, P. R. Lewis, C. C. Wong, "Microfabricated gas phase chemical analysis systems," *Proceedings of Microprocess and Nanotechnology Conference*, pp. 60-61, **1999.**

[9] Manz, H. Becker, *Microsystem Technology in Chemistry and Life Sciences,* Springer Verlag, **1999**.

[10] C. W. Moore and P. A. Kohl, "Microfabricated direct methanol fuel cells to power on-board integrated circuits", *Proceedings of Electrochem Soc, Microfabricated Systems and MEMS-VI*, vol. 2002-6, pp. 183-189, **2002**

[11] E. Thielicke, E. Obermeier, "Microactuators and their technologies," *Mechatronics,* vol. 10, pp. 431-455, **2000.**

[12] C. Kittel, H. Kromer, *Thermal Physics,* Freeman and Company, New York, **1980**.

[13] M. Gad-el-Hak, "The fluid mechanics of micodevices – The Freeman Scholar Lecture", *Journal of Fluids Engineering*, vol. 121, pp. 5-33, **1999**.

[14] B. R Munson, D. F. Young., and T. H. Okiishi, *Fundamentals of Fluid Mechanics*, John Wiley &Sons, Inc., **1998**.

[15] F. P. Incropera and D. P. DeWitt, *Fundamentals of Heat and Mass Transfer*, John Wiley &Sons, Inc., **2001**

[16] Beskok, and G. E. Karniadakis, "Simulation of hest and momentum transfer in complex microgeometries", *Journal of Thermophysics and Heat Transfer,* vol. 8, pp. 355-370, **1994**.

[17] D. J. Beebe, G. A. Mensing, G. M. Walker, "Physics and applications of microfluidics in biology," *Annu. Rev. Biomed. Eng.,* vol. 4, pp. 261-286, **2002**

[18] F. M. White, Viscous Fluid Flow, 2nd ed., McGraw Hill, NY, **1991**.

[19] C. C. Wong et al, "Investigation of Gas Flow in Long and Narrow Channels", *Proc. ASME FEDSM'00*, **2000**.

[20] Beskok, G.E. Karniadakis, and W. Trimmer, "Rarefaction and compressibility effects in gas microflows", *Transactions of the ASME. Journal of Fluids Engineering*, vol. 118, pp. 448-56, **1996.**

[21] E. B. Arkilic, M. A. Schmidt, and K. S. Breuer, "Gaseous slip flow in long microchannels", *J. Microelectromech. Syst.*, vol. 6, pp. 167-178, **1997**.

[22] P. Gravesen, J. Branebjerg, O. S. Jensen, "Microfluidics – a review," *J. Micromech. Microeng.,* vol. 3, pp. 168-182, **1993**.

[23] K. Onitsuka, A. Dogan, J. F. Tressler, X. Qichang, S. Yoshikawa, R. E. Newnham, "Metal-cermaic composite transducer, the "Moonie"," *J. Intel Mater. Syst. Struct.,* vol. 6, pp. 447-455, **1995.**

[24] M. Esashi, S. Shoji and A. Nakano, "Normally closed microvalve and micropump fabricated on a silicon wafer," *Sensors and Actuators,* vol. 20, pp. 163-169, **1989.**

[25] S. Shoji and M. Esashi, "Fabrication of a micropump for integrated chemical analyzing systems," *Electronics and Communications in Japan, Part 2,* vol. 72, pp. 52-59, **1989**.

[26] S. Shoji, "Micro total analysis systems," *Electronics and Communications in Japan, Part 2,* vol. 82, pp. 21-29, **1999**.

[27] T. Watanabe, H. Kuwano, "A microvalve matrix using piezoelectric actuators," *Microsystems Technology,* vol. 3, pp. 107-111, **1997**.

[28] Chakroborty, W. C. Tang. D. P. Bame, T.K. Tang, "MEMS micro-valve for space applications" *Sensors and Actuators*, vol. 83, pp. 188-193, **2000**.

[29] D. C. Roberts, H. Li, J. L. Steyn, O. Yaglioglu, S. M. Spearing, M. A. Schmidt, and N. W. Hagood, "A piezoelectric microvalve for compact high-frequency, high-differential pressure hydraulic micropumping system," *J. Microelectromech. Syst.,* vol. 12, 81-92, **2003**

[30] M. A. Huff, J. R. Gilbert, M. A. Schmidt, "Flow characteristics of a pressure-balanced microvalve," *Technical Digest of the 7th International Conference on Solid-State Sensors and Actuators*, pp. 98-101, **1991.**

[31] J. Garcia-Bonito, M. J. Brennan, S. J. Elliott, A. David, R. J. Pinnington, "A novel high-displacement piezoelectric actuator for active vibration control," *Smart. Mater. Struct.,* vol. 7, pp. 31-42, **1998.**

[32] F. Yang, I Kao, "Analysis of fluid flow and deflection for pressure-balanced MEMS diaphragm valves," *Sensors and Actuators A,* vol. 79, pp. 13-21, **2000.**

[33] K. Sato and M. Shikida, "An electrostatically actuated gas valve with an S-shaped film element," *J. Micromech. Microeng.,* vol. 4, pp. 205-209, **1994**

[34] M. Shikida, K. Sato, S. Tanaka, Y. Kawamura, Y. Fujisaki, "Electrostatically driven gas valve with high conductance," *J. Microelectromech. Syst.,* vol. 3, pp. 76-79. **1994**

[35] C. Cabuz, "Dielectric related effects in micromachined electrostatic actuators," *Proceedings of IEEE Conference on Electrical Insulation and Dielectric Phenomena*, pp. 327-332, **1999**.

[36] C. Goll, W. Bacher, B. Bustgens, D. Mass, R. Ruprecht, W. K. Schomburg, "An electrostatically actuated polymer microvalve equipped with a movable membrane electrode," *J. Micromech. Microeng.*, vol. 7, pp. 224-226, **1997.**

[37] N. T. Nguyen, S. Schubert, S. Richter, W. Dotzel, "Hybrid-assembled micro dosing system using silicon-based micropump/valve and mass flow sensor," *Sensors and Actuators A,* vol. *69,* pp. 85-91, **1998.**

[38] T. Ohnstein, T. Fukiura, J. Ridley, U. Bonne, "Micromachined silicon microvalve," *MEMS, Proceedings of IEEE Conference*, pp. 95-98, **1990**.

[39] N. Vandelli, D. Wroblewski, M. Velonis, and T. Bifano, "Development of a MEMS Microvalve Array for Fluid Flow Control," *J. Microelectromech. Syst.,* vol. 7, pp. 395 – 403, **1998.**

[40] L. Yobas, M. A. Huff, F. J. Lisy, and D. M. Durand, "A novel bulk-micromachined electrostatic microvalve with a curved-compliant structure applicable for a pneumatic tactile display," *J. Microelectromech. Syst.*, vol. 10, pp.187-196, **2001**.

[41] Ph. Dubois, B. Guldimann, M.A. Gretillat, N.F. de Rooi, Electrostatically Actuated Gas Microvalve Based On A Ta-Si-N Membrane, *MEMS, 14th IEEE International Conference*, pp. 535-538, **2001**.

[42] W. van der Wijngaart, H. Ask, P. Enoksson, and G. Stemme, "A high-stroke, high-pressure electrostatic actuator for valve applications," *Sensors and Actuators A*, vol. 100, pp. 264-271, **2002**.

[43] D. Jiles, *Introduction to Magnetism and Magnetic Materials,* Chapman Hall, New York, **1998**.

[44] K. I. Arai, T. Honda, "Micromagnetic actuators," *Robotica*, vol. 14, pp. 477-481, **1996**.

[45] M. Tabib-Azar, *Microactuators – Electrical, Magnetic, Thermal, Optical, Mechanical, Chemical and Smart Structures,* Kluwer Academic Pub., **1998**.

[46] R. L. Smith, R. W. Bower, S. D. Collins, "The design and fabrication of a magnetically actuated micromachined flow valve," *Sensors and Actuators A***,** vol. 24, pp. 47-53, **1990**.

[47] D. Bosch, B. Heimhofer, G. Muck, H. Seidel, U. Thumser, W. Wslser, "A silicon microvalve with combined electromagnetic/electrostatic actuation," *Sensors and Actuators A*, vol. 37-38, pp. 684-692, **1993**.

[48] K. Yanagisawa, H. Kuwano, and A. Tago, "Electromagnetically driven microvalve," *Microsystem Technology*, vol. 2, pp. 22-25, **1995.**

[49] Y. Shinozawa, T. Abe, and T. Kondo, "A Proportional Micro Valve Using A Bi Stable Magnetic Actuator, *MEMS, IEEE proceedings,* pp. 233-237, **1997.**

[50] H. Ren, E. Gerhard, "Design and fabrication of a current-pulse-excited bistable magnetic microactuator," *Sensors and Actuators A,* vol. *58,* pp. 259-264, **1997.**

[51] Meckes, J. Behrens, and W. Benecke, "Electromagnetically Driven Microvalve Fabricated in Silicon," *International Conference on Solid-State Sensors and actuators*, Transducers, pp. 821 – 824, **1997.**

[52] Meckes, "Microfluidic system for the integration on cyclic operation of gas sensors," *Sensors and Actuators A***,** vol. 76, pp. 478-483, **1999**.

[53] D. L. Sadler, K. W. Oh, C. H. Ahn, S. Bhansali, H. T. Henderson, "A new magnetically actuated microvalve for liquid and gas control applications," *Proceedings of the 13th International Conference on Solid-State Sensors and Actuators*, pp. 1812-1815, **1999.**

[54] H. J. Cho and C.H. Ahn, 'A Bidirectional Magnetic Microactuator Using Electroplated Permanent Magnet Array," *J. Microelectromech. Syst.***,** vol. 11, pp. 78 – 84*,* **2002.**

[55] S. Bohm, G.J Burger, M.T. Korthorst, F. Roseboom, *"A micromachined silicon valve driven by a miniature bi-stable electro-magnetic actuator," Sensors and Actuators A*, vol. 80, pp. 77-83, **2000**.

[56] M. Capanu, J.G. Boyd IV, and P.J. Hesketh**,** "Design, Fabrication, and Testing of a Bistable Electromagnetically Actuated Microvalve," *J. Microelectromech. Syst.,* vol. 9, pp. 181 – 189, **2000**.

[57] B. Bae, N. Kim, H. Kee, Y. Lee, S. Lee, K. Park, "Feasibility test of an electromagnetically driven valve actuator for glaucoma treatment," *J. Microelectromech. Syst.,* vol. 11, pp. 344-354, **2002**

[58] H. Jerman, "Electrically-activated, normally-closed diaphragm valve," in *Proceedings of Transducers '91, the 1991 International Conference on Solid-State Sensors and Actuators*, pp. 210-216, **1991.**

[59] H. Jerman, "Electrically-activated, normally-closed diaphragm valves," *J. Micromech. Microeng.,* vol. 4, pp. 210-216, **1994.**

[60] H. P. Trah, H. Aumann, C. Doring, H. Goebel, T. Grauer, M. Mettner, "Micromachined valve with hydraulically actuated membrane subsequent to a thermoelectrically controlled bimorph cantilever," *Sensors and Actuators A,* vol. 39, pp. 169-176, **1993**.

[61] T. Lisec, H. J. Quenzer, M. Kreutzer, S. Horschelmann, B. Wagner, W. Benecke, "Thermally Driven Microvalve with Buckling Behavior for Pneumatic Applications, *Sensors and Materials,* vol. 8, pp. 13 – 17, **1996.**

[62] P. W. Barth, "Silicon microvalves for gas flow control," *Proceedings of Transducers '95, the 8th International Conference on Solid-State Sensors and Actuators, and Eurosensors IX*, pp. 276-277, **1995.**

[63] M. J. Zdeblick, R. Anderson, J. Jankowski, B. Kline-Schoder, L. Christel, R. Miles and W. Eber, "Thermopneumatically actuated microvalves and integrated electo-fluidic circuits," *Proceedings of the Solid-State Sensor and Actuator Workshop*, pp. 251-255, **1994**.

[64] D. Y. Sim, T. Kurabayashi, M. Esashi, "A bakable microvalve with a Kovar-glass-silicon-glass structure," *J. Micromech. Microeng.,* vol. 6, pp. 266-271, **1996.**

[65] X.Yang, C. Grosjean, Y.-T. Tai, "Design, fabrication, and testing of micromachined silicone rubber membrane valves," *J. Microelectromech. Syst.*, vol. 8, pp. 393-402, **1999**.

[66] C.A. Rich, K.D. Wise, "A High-Flow Thermopneumatic Microvalve with Improved Efficiency and Integrated State Sensing", Journal of Microelectromechanical Systems, vol. 12, pp. 201-208, **2003**.

[67] E.T. Carlen and C.H. Mastrangelo, "Surface Micromachined Paraffin-Actuated Microvalve," *J. Microelectromech. Syst.,* vol. 11, pp. 408 – 420, **2002**

[68] S. Buttgenbach, S. Butefisch, M. Leester-Schadel, A. Wogersien, "Shape memory microactuators," *Microsystem Technology*, vol. 7, pp. 165-170, **2001**.

[69] P. Krulevitch, A. P. Lee, R. B. Ramsey, J. C. Tevino, J. Hamilton and M. A. Northrup, "Thin film shape memory alloy microactuators," *J. Microelectromech. Syst.,* vol. 5, pp. 270-282, **1996.**

[70] D. Johnson, E. J. Shahoian, "Recent progress in thin film shape memory microactuators," *IEEE Proc. MEMS,* pp. 216, **1995.**

[71] R. H. Wolf, A. H. Heuer, "TiNi (Shape Memory) films on silicon for MEMS applications," *J. Microelectromech. Syst.,* vol. 4, pp. 206-212, **1995.**

[72] D. Johnson, C. A. Ray, "Shape Memory Alloy Film Actuated Microvalve," US Patent 5,325,880, **1994.**

[73] H. Kahn, M. A. Huff, A. H. Heuer, "The TiNi shape-memory alloy and its applications for MEMS," *J. Micromech. Microeng.,* vol. 8, pp. 213-221, **1998**.

[74] C. M. Pemble, B. C. Towe, "A miniature shape memory alloy pinch valve," *Sensors and Actuators A,* vol. 77, pp. 145-148, **1999.**

[75] M. Kohl, K. D. Skrobanek, E. Quandt, P. Schlossmacher, A. Schussler, D. M. Allen, "Development of microactuators based on shape memory effect," *Journal de Physique IV, Colloque C8*, vol. 5, pp. 1167-1192, **1995.**

[76] M. Kohl, K.D. Skrobanek, S. Miyazaki, "Development of Stress-Optimized Shape Memory Microvalve, *Sensors and Actuators A*, vol. 72, pp. 243-250, **1999.**

[77] M. Kohl, B. Krevet, "3D simulation of a shape memory microactuator," *Materials Transactions,* vol. 43, pp. 1030-1036, **2002.**

[78] M. Kohl, D. Dittmann, E. Quandt, B. Winzek, S. Miyazaki, D.M. Allen, "Shape memory microvalves based on thin films or rolled sheets," *Materials Science & Engineering A,* vol. 273-275, pp. 784-788, **1999**.

[79] M. Kohl, D. Dittmann, E. Quandt, B. Winzek, "Thin film shape memory microvalves with adjustable operation temperature," *Sensors and Actuators,* vol. 83, pp. 214-219, **2000**.

[80] D. J. Beebe, J. S. Moore, J. M. Bauer, Q. Yu, R. H. Liu, C. Devadoss, B-H. Jo, "Functional hydrogel structures for autonomous flow control inside microfluidic channels," *Letter to Nature,* vol. 404, pp. 588-590, **2000**.

[81] Q. Yu, J. M. Bauer, J. S. Moore, D. J. Beebe, "Responsive biomimetic hydrogel valve for microfluidics," *Appl. Phys. Lett.,* vol. 78, pp. 2589-2591, **2001.**

[82] Baldi, Y. Gu, P.E. Loftness, R.A. Siegel, and B. Ziaie, "A Hydrogel-Actuated Smart Microvalve with a Porous Diffusion Barrier Back Plate for Active Flow Control," *IEEE Conference*, pp. 105 – 108, **2002.**

[83] R.H. Liu, Q. Yu, and D.J. Beebe, "Fabrication and Characterization of Hydrogel-Based Microvalves," *J. Microelectromech. Syst.,* vol. 11, pp. 45-53, **2002.**

[84] J.S. Bintoro and P.J. Hesketh, "Design, Fabrication, and Testing of a CMOS Compatible Electromagnetic Microvalve Fabricated on Top of A Single Wafer," *J. Micromech. Microeng.*, **2004**, paper under review

[85] J. W. Judy and N. Myung, "Magnetic Materials for MEMS", *MRS Workshop on MEMS Materials*, San Francisco, California, pp.23-26, **2002**

[86] J. Y. Park and M.G. Allen, "Integrated Electroplated Micromachined Magnetic Devices Using Low Temperature Fabrication Processes," *IEEE transactions on electronics packaging manufacturing*, vol. ctions in electroplated materials thin film recording hesds23, pp. 48 – 55, **2000**

[87] P. C. Andricacos and N. Robertson, "Future directions in electroplated materials thin-film recording heads, *IBM Journal of Research and Development*, vol. 42, no. 5, **1998**.

[88] G.T.A. Kovacs, *Micromachined Transducers Sourcebook*, McGraw-Hill, New York, **1998**

[89] J.M. Gere and S.P. Timoshenko, *Mechanics of Material,* PWS Publishing, **1996**

[90] P. Campbell, *Permanent Magnet Materials and Their Application*, Cambridge University Press, New York, p. 104, **1994**

[91] J. Groom, "Design considerations for air core magnetic actuator," *Tech. Memorandum 104229,* NASA, **1992.**

[92] J.S. Bintoro, A. Papania, Y.H. Berthelot, and P.J. Hesketh, "Bi-directional Micro Actuator with Micro Coils Fabricated on a Single Wafer, Part I: Static Characteristic of Membrane Displacements," *J. Micromech. Microeng.*, **2004**, submitted

[93] J.S. Bintoro, A. Papania, Y.H. Berthelot, and P.J. Hesketh, "Bi-directional Micro Actuator with Micro Coils Fabricated on a Single Wafer, Part II: Dynamic Characteristic of Membrane Displacements," *J. Micromech. Microeng.*, **2004**, submitted

[94] T. S. Chin, "Permanent magnet films for applications in microelectromechanical systems," *J. Magnetism and Magnetic Materials*, vol. 209, pp. 75-79, **2000**.

[95] B. Wagner, M. Kreutzer, and W. Benecke, "Permanent Magnet Micromotors on Silicon Substrates," *J. Microelectromech. Syst*, vol. 2, pp. 23 – 29, **1993.**

[96] F. E. Luborsky, "High coercive force films of cobalt-nickel with additions of group VA and VIB element", *IEEE Transactions on Magnetics*, vol. 6, pp. 502-505, **1970.**

[97] R.M. Bozorth, *Ferrormagnetism,* D. Van Nostrand, **1963.**

[98] K. R. Coffey, M. A. Parker, and J. K. Howard, "High anisotropy $L1_0$ thin Films for longitudinal recording, *IEEE Transaction Magnetics*, vol. 31, pp. 2737-2739, **1995.**

[99] C. H. Lee, R. F. C. Farrow, C. J. Lin, and E. E. Marinero, "Molecular beam-epitaxial growth and magnetic properties of Co-Pt superlattices oriented along the (001), (110), and (111) axes of Pt", *Physical Review B*, vol. 42, no. 7, pp. 11384-11386, **1990.**

[100] P. F. Garcia, Z. G. Li, and W. B. Zeper, *J. Magnetism and Magnetic Materials*, vol. 121, pp. 452-460, **1993**

[101] R. F. Farrow and R. F. Marks, U.S. Patent #5,792,510.

[102] J. Horkans, D. J. Seagle, and I. C. H. Chang, "Electroplated magnetic media with vertical anisotropy," *J. Electrochem. Soc*. vol. 137, pp. 2056-2061, **1990**

[103] M. Monew, I. Krastev, and A. Zielonka, "In situ stress measurements during electrodeposition of Ag-Sb and Pt-Co alloy multilayers", *J. Physics: Condensed Matter*, vol. 49, pp. 10033-10040, **1999**

[104] V. Tutovan and V. Georgescu, "The magnetic behavior of thin electrolytically deposited Co-Pt films," *Thin Solid Films*, vol. 61, pp. 133-140, **1979**.

[105] P. L. Cavalotti, N. Lecis, H. Fauser, A. Zielonka, J. P. Celis, G. Wouters, J. Machado de Silva, J. M. Brochado Oliveria, and M. A. Sa, "Electrodeposition of magnetic multilayers," *Surface and Coatings Technology,* vol. 105, pp. 232-239, **1998.**

[106] G. J. Long and F. Grandjean, "Supermagnets, Hard Magnetic Materials," *NATO ASI Series*, vol. 331, Kluwer Academic Publishers, Dordrecht, **1990**.

[107] I. Zana and G. Zangari, "Co-Pt Micromagnets by Electrodeposition," *Journal of Applied Physics*, vol. 91, **2002**

[108] T. J. Garino, T. Christenson, and E. Venturini, "Fabrication of MEMS devices by powder-filling into DXRL-formed molds," *Proceedings of Materials Science of Microelectromechanical systems (MEMS) devices*, Boston, MA, U.S.A, pp. 195-200, **1998**.

[109] N. V. Myung, D. Y. Park, M. Schwartz, K. Nobe, H. Yang, C. K. Yang, and J. W. Judy, *Proceedings of Electrochem. Soc.*, PV. 2000-29 and submitted to J. Electrochem. Soc.

[110] D. Y. Park, N. V. Myung, M. Schwartz, and K. Nobe, "Nanostructured magnetic CoNiP electrodeposits: structure-property relationships," *Electrochimica Acta*, vol. 47, pp. 2893-2900, **2002**

[111] Y. Omata, H. Asai, and T. Shinosaki, "Preparation of soft magnetic properties of pulse-plated permalloy films," *Translation Journal on Magnetic in Japan*, vol. 9, pp. 106-111, **1994**

[112] H. Lemke, T. Lang, T. Goddenhenrich, and C. Heiden, "Micropatterning of thin Nd-Fe-B films," *J. Magn. Mgn. Mater.*, vol. 148, pp. 426-432, **1995**

[113] S. Parhfer, G. Gieres, J. Wecker, and L. Schultz, "Growth characteristics and magnetic properties of sputtered Nd-Fe-B thin films," *J. Magn. Magn. Mater.*, vol. 163, pp.32-38, **1996**

[114] I. Zana and G. Zangari, "Electrodeposition of Co-Pt Films with High Perpendicular Anisotropy," *Electrochemical and Solid-State Letters*, vol. 6, no. 12, pp. C153 – C156, **2003**

[115] http://scienceworld.wolfram.com/physics/CoefficientofRestitution.html

[116] H. E. Merrit, *Hydraulic Control Systems*, Wiley, New York, p. 35, **1967**.

[117] T. Gerlach, "Microdiffusers as dynamic passive valves for micropump applications," *Sensors and Actuators A*, Elsevier, Vol. 69, pp. 181–191, **1998**.

[118] J. S. Bintoro, Y. H. Berthelot, P.J. Hesketh, "CMOS compatible bistable electromagnetic microvalves fabricated on a single wafer," *Proceedings of European Micro and Nano Systems conference*, Noise le Grand (Paris), pp. 219-223, **2004**

[119] http://www.adams-magnetic.com/pdfd/materials_chart1.pdf

[120] unpublished info, private conversation with Jun Li who works in the testing of micro fuel cell